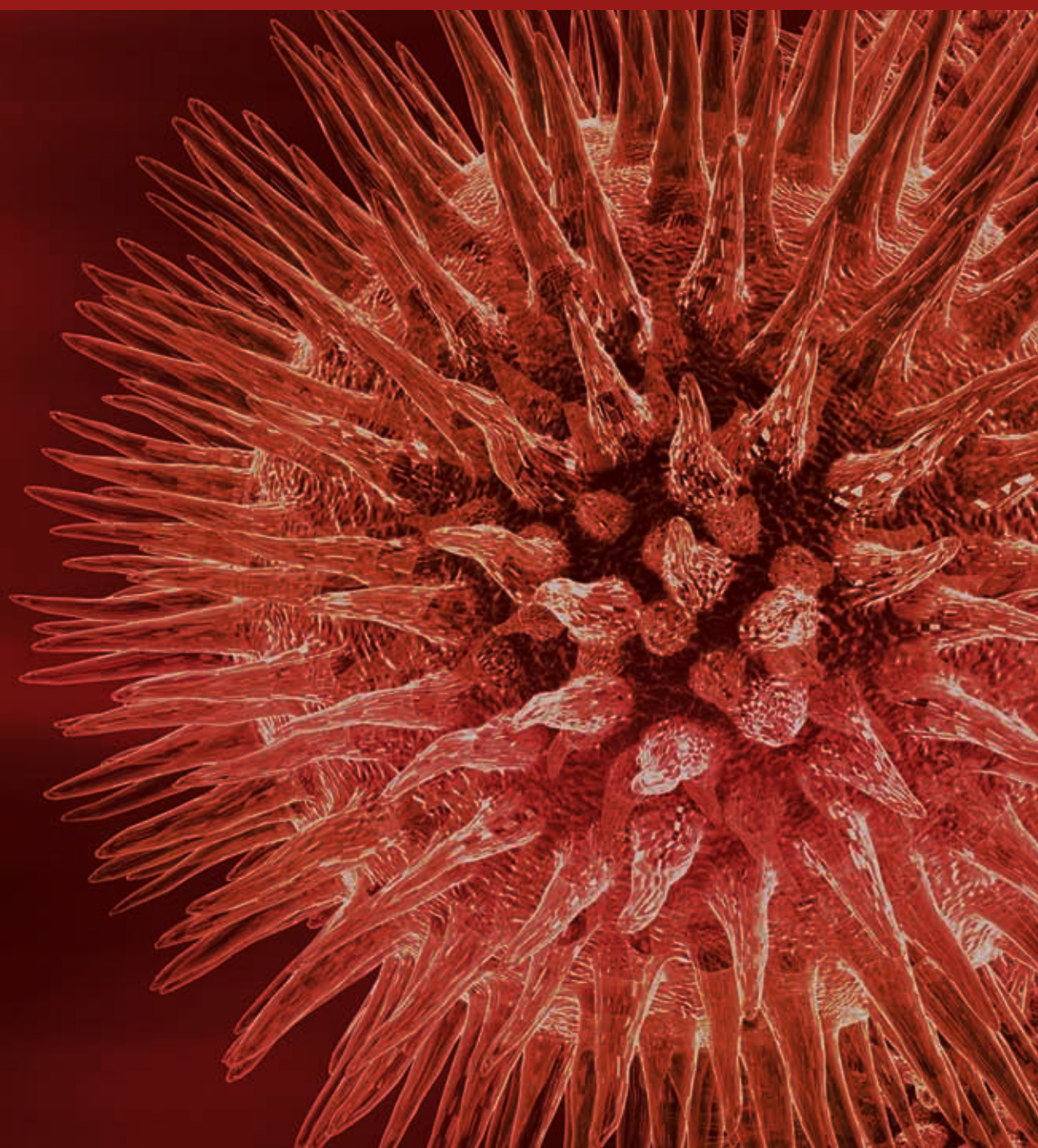


# **Biomedical Applications of Colloidal Nanocrystals**

Guest Editors: Marek Osiński, Thomas M. Jovin,  
and Kenji Yamamoto





---

# **Biomedical Applications of Colloidal Nanocrystals**

## **Biomedical Applications of Colloidal Nanocrystals**

Guest Editors: Marek Osiński, Thomas M. Jovin,  
and Kenji Yamamoto



---

Copyright © 2007 Hindawi Publishing Corporation. All rights reserved.

This is a special issue published in volume 2007 of “Journal of Biomedicine and Biotechnology.” All articles are open access articles distributed under the Creative Commons Attribution License, which permits unrestricted use, distribution, and reproduction in any medium, provided the original work is properly cited.



## Editor-in-Chief

Abdelali Haoudi, Eastern Virginia Medical School, USA

## Advisory Editors

H. N. Ananthaswamy, USA  
Ronald E. Cannon, USA  
Jean Dausset, France  
John W. Drake, USA  
Shyam K. Dube, USA

Marc Fellous, France  
Daniela S. Gerhard, USA  
Mauro Giacca, Italy  
Peter M. Gresshoff, Australia  
Vladimir Larionov, USA

S. B. Petersen, Denmark  
Pierre Tambourin, France  
Michel Tibayrenc, Thailand

## Associate Editors

Claude Bagnis, France  
Halima Bensmail, USA  
Omar Benzakour, France  
Maria A. Blasco, Spain  
Mohamed Boutjdir, USA  
Douglas Bristol, USA  
Virander Singh Chauhan, India  
Hatem El Shanti, USA  
Hicham Fenniri, Canada  
James Huff, USA  
Shahid Jameel, India  
Celina Janion, Poland

Ali A. Khraibi, USA  
Pierre Lehn, France  
Nan Liu, USA  
Yan Luo, USA  
James M. Mason, USA  
John L McGregor, France  
Ali Ouaiissi, France  
Allal Ouhtit, USA  
George Perry, USA  
George Plopper, USA  
Nina Luning Prak, USA  
Kanury V. S. Rao, India

Annie J. J. Sasco, France  
Wolfgang A. Schulz, Germany  
Gerald G. Schumann, Germany  
O. John Semmes, USA  
James L. Sherley, USA  
Mouldy Sioud, Norway  
Mark A. Smith, USA  
Lisa Wiesmuller, Germany  
Leila Zahed, Lebanon  
Steven L. Zeichner, USA

# Contents

**Biomedical Applications of Colloidal Nanocrystals**, Marek Osiński, Thomas M. Jovin, and Kenji Yamamoto  
Volume 2007, Article ID 82752, 2 pages

**Gel Electrophoresis of Gold-DNA Nanoconjugates**, T. Pellegrino, R. A. Sperling, A. P. Alivisatos, and W. J. Parak  
Volume 2007, Article ID 26796, 9 pages

**Design of Biotin-Functionalized Luminescent Quantum Dots**, Kimihiro Susumu, H. Tetsuo Uyeda, Igor L. Medintz, and Hedi Mattoussi  
Volume 2007, Article ID 90651, 7 pages

**Imaging GABA<sub>c</sub> Receptors with Ligand-Conjugated Quantum Dots**, Ian D. Tomlinson, Hélène A. Gussin, Deborah M. Little, Michael R. Warnement, Haohua Qian, David R. Pepperberg, and Sandra J. Rosenthal  
Volume 2007, Article ID 76514, 9 pages

**Fluorescence Intensity and Intermittency as Tools for Following Dopamine Bioconjugate Processing in Living Cells**, Rafael Khatchadourian, Alexia Bachir, Samuel J. Clarke, Colin D. Heyes, Paul W. Wiseman, and Jay L. Nadeau  
Volume 2007, Article ID 70145, 10 pages

**Development of FRET-Based Assays in the Far-Red Using CdTe Quantum Dots**, E. Z. Chong, D. R. Matthews, H. D. Summers, K. L. Njoh, R. J. Errington, and P. J. Smith  
Volume 2007, Article ID 54169, 7 pages


**Fluorescence Resonance Energy Transfer in Quantum Dot-Protein Kinase Assemblies**, Ibrahim Yildiz, Xinxin Gao, Thomas K. Harris, and Francisco M. Raymo  
Volume 2007, Article ID 18081, 5 pages

**Time-Resolved Analysis of a Highly Sensitive Förster Resonance Energy Transfer Immunoassay Using Terbium Complexes as Donors and Quantum Dots as Acceptors**, Niko Hildebrandt, Loïc J. Charbonnière, and Hans-Gerd Löhmannsröben  
Volume 2007, Article ID 79169, 6 pages

**Superparamagnetic Iron Oxide Nanoparticles Coated with Galactose-Carrying Polymer for Hepatocyte Targeting**, Mi Kyong Yoo, In Yong Kim, Eun Mi Kim, Hwan-Jeong Jeong, Chang-Moon Lee, Yong Yeon Jeong, Toshihiro Akaike, and Chong Su Cho  
Volume 2007, Article ID 94740, 9 pages

**Fluorescent Nanoparticle-Based Indirect Immunofluorescence Microscopy for Detection of *Mycobacterium tuberculosis***, Dilan Qin, Xiaoxiao He, Kemin Wang, Xiaojun Julia Zhao, Weihong Tan, and Jiyun Chen  
Volume 2007, Article ID 89364, 9 pages

**Preparation and Characterization of Poly(D,L-Lactide-co-Glycolide) Nanoparticles Containing Ascorbic Acid**, Magdalena M. Stevanović, Branka Jordović, and Dragan P. Uskoković  
Volume 2007, Article ID 84965, 8 pages



---

**Clinical Potential of Quantum Dots**, Arthur M. Iga, John H. P. Robertson, Marc C. Winslet,  
and Alexander M. Seifalian  
Volume 2007, Article ID 76087, 10 pages

**Getting Across the Plasma Membrane and Beyond: Intracellular Uses of Colloidal Semiconductor Nanocrystals**, Camilla Luccardini, Aleksey Yakovlev, Stéphane Gaillard, Marcel van't Hoff, Alicia Piera Alberola, Jean-Maurice Mallet, Wolfgang J. Parak, Anne Feltz, and Martin Oheim  
Volume 2007, Article ID 68963, 9 pages

**Blue-Emitting Small Silica Particles Incorporating ZnSe-Based Nanocrystals Prepared by Reverse Micelle Method**, Masanori Ando, Chunliang Li, Ping Yang, and Norio Murase  
Volume 2007, Article ID 52971, 6 pages

## Editorial

# Biomedical Applications of Colloidal Nanocrystals

**Marek Osinski,<sup>1</sup> Thomas M. Jovin,<sup>2</sup> and K. Yamamoto<sup>3</sup>**

<sup>1</sup> Center for High Technology Materials, University of New Mexico, 1313 Goddard SE, Albuquerque, NM 87106-4343, USA

<sup>2</sup> Department of Molecular Biology, Max Planck Institute for Biophysical Chemistry, 37070 Göttingen, Germany

<sup>3</sup> Research Institute, International Medical Center of Japan, 1-21-1 Toyama, Shinjuku-ku, Tokyo 162-8655, Japan

Correspondence should be addressed to K. Yamamoto, backen@ri.imcj.go.jp

Received 6 May 2008; Accepted 6 May 2008

Copyright © 2007 Marek Osinski et al. This is an open access article distributed under the Creative Commons Attribution License, which permits unrestricted use, distribution, and reproduction in any medium, provided the original work is properly cited.

Because of the high affinity of the thiol groups to a metal such as gold and zinc, we can conjugate metal nanocrystals with chemical compounds which contain thiol such as cysteine, cytein contained peptide, and thiol-modified nucleic acids including DNA. Among them, T. Pellegrino et al. investigated Gold-DNA conjugates in detail by a comprehensive gel-electrophoresis study based on 1200 gels. The investigation contains the following three results: firstly, the precise detection of relative changes in size upon binding of molecules, secondary, comparison of the specific attachment of DNA via gold-thiol bonds to Au nanoparticles with nonspecific adsorption of DNA, and thirdly, determination of the maximum number of DNA molecules bounded per particle. These data might be the essential information for designing a functional nanodevice such as for the nanometer-sized electric circuit and for the carrier for gene delivery system.

A new ligand which readily binds itself to CdSe-ZnS core-shell QDs, via surface ligand exchange, was designed and synthesized by Kimihiro Susumu et al. from tetraethylene glycol (TEG) based bidentate ligand functionalized with dihydrolipoic acid (DHLLA) and biotin (DHLLA-TEG-biotin). Quantum dots capped with DHLLA and DHLLA-TEG-biotin or polyethylene glycol modified DHLLA (DHLLA-PEG600) are dispersed easily in aqueous buffer solutions. Homogenized buffer solutions of QDs capped with mixture of DHLLA-PEG600 and DHLLA-TEG-biotin are stable over broad pH range and showed specific interactions with NeutrAvidin in surface binding assays. The authors say “further studies of these surface functionalized QDs for coupling with a variety of bioreceptors and biological assays are in progress.”

For the study on the ligand-receptor binding, we need fluorescent markers. Ligand conjugated quantum dots are reported here by Ian D. Tomlinson et al. for imaging GABAC receptor on the surface membrane of intact cell. They

have already succeeded in developing serotonin-conjugated quantum dots and the method to reduce nonspecific binding using PEGylated quantum dots. Together with all these works, they have proceeded for imaging GABAC receptors heterologously expressed on *Xenopus laevis* oocytes.

On the other hand, Dopamine conjugated quantum dots are known to be endocytosed by cells bearing dopamine receptors and not by cells without dopamine receptors. Rafael Khatchadourian et al. studied the tools of fluorescence intensity and intermittency for following dopamine bioconjugate processing in living cells.

In this special issue, we have three papers on quantum dots as for the use of Forster (or fluorescent) resonance energy transfer (FRET). The characters of quantum dots such as photostability, high quantum yield broad absorption, and narrow emission spectrum are more useful for probes than organic dyes, especially in the study of molecular imaging.

In the investigation of E. Z. Chong et al., biotinylated DY731-Bio fluorophores with an absorption peak at 720 nm were self-assembled onto Qdot705-STVs that emit the fluorophores at 705 nm using a streptavidin-biotin binding mechanism. They have particular interest on the far-red region to minimize optical region absorption within tissue and to avoid cell autofluorescence and they succeeded in doing so.

In order to identify selective inhibitors of protein kinases efficiently, Ibrahim Yildiz et al. designed a binding assay to probe the interactions of human phosphoinositide-dependent protein kinase-1 with potential ligands using FRET between quantum dots and organic dyes.

Using terbium complexes as donors and quantum dots as acceptors, FRET immunoassay is improved more than two orders of magnitude compared to commercial systems,

which has been investigated by Niko Hildebrandt et al. They say “the presented results demonstrate the great potential of Tb to QD-FRET system for highly sensitive homogenous immunoassays for biological as well as clinical and medical applications.”

For the application of MRI imaging, the following two papers are included. Mi Kyong Yoo et al. developed superparamagnetic iron oxide nanoparticles (SPIONs). SPIONs were coated with agent (PVLA-coated SPIONs) to be recognized by asialoglycoprotein receptors on hepatocytes. Intracellular uptake of this nanoparticle was visualized by confocal laser scanning microscopy and the hepatocyte-specific delivery was also investigated with magnetic resonance image of rat liver. The authors said “the results suggest the potential utility of PVLA-coated SPIONs as liver-targeting MRI contrast agent.”

Quantum dots are absolutely useful for clinical laboratory test. Dilan Qin et al. say “tuberculosis is a global health threatening emergency with the spread of acquired immunodeficiency syndrome and the emergence of a drug-resistant strain of mycobacterium tuberculosis.” They used RuBpy-doped silica nanoparticles as the fluorescent probe to detect the bacteria with an indirect immunofluorescence microscopy. Four-hour assay time is enough including spiked sputum sample pretreatment, which can be done by the advantage of higher luminescence and higher photostability for the nanoparticles.

For the study on the clinical treatment, we have a paper of Magdalena M. Stevanović et al. They produced copolymer poly(D,L-lactide-co-glycolide) (DLPLG) nanoparticles by using physical method with solvent/nonsolvent systems and technique of the centrifugal processing. Encapsulation of ascorbic acids into DLPLG particles can be used for transdermal controlled delivery of ascorbic acids. The authors say “DLPLG nanospheres are very efficient means of transdermal transport of medicament within the polymer matrix.”

Finally, this special issue includes two review articles. One is from Arthur M. Iga et al. They describe the clinical potential of quantum dots focused in sentinel lymph node mapping, cancer imaging, photodynamic therapy in cancer treatment, and drug delivery. The authors examined the hindrances for clinical use and the current progress in abrogating their inherent toxicity. The other review is from Camilla Luccardini et al. They start from the chemical and optical properties of nanocrystals and surface chemistry. They cross the description of plasma membrane section and reach the specific intracellular targets. They also describe a whole animal imaging in vivo with nanocrystals and cytotoxicity of cadmium ion as an example.

Both of the authors of the review articles have taken the topics of toxicity commonly. Silica coating of the quantum dots might be one of the ways to escape from the cytotoxicity. Masanori Ando et al. say “here we report the preparation of silica particle phosphor incorporating ZnSe-based NCs prepared by a reverse micelle method.” The size distribution of the spherical particles is 20–40 nm in diameter. They have already reported the presentation of green- and red-emitting silica particles. “These emitting silica particles are expected to be applicable as fluorescent biomarkers,” they also say. Their

method of silica coating might be applicable for any type of the nanoparticles.

On the other hand, Arthur M. Iga et al. say “with improvements in nanotechnology, nanotoxicology, and chemistry some of the goals could be achieved, however, it will be difficult to replace the toxic core of the QD without losing optical properties or we will redirect our efforts to less toxic elements.” All of us might have to think about it deeply.

Marek Osinski  
Thomas M. Jovin  
K. Yamamoto

## Research Article

# Gel Electrophoresis of Gold-DNA Nanoconjugates

**T. Pellegrino,<sup>1,2,3</sup> R. A. Sperling,<sup>1,4</sup> A. P. Alivisatos,<sup>2</sup> and W. J. Parak<sup>1,2,4</sup>**

<sup>1</sup> Center for Nanoscience, Ludwig Maximilians University Munich, 80799 München, Germany

<sup>2</sup> Department of Chemistry and Lawrence Berkeley National Lab, University of California, Berkeley, CA 94720, USA

<sup>3</sup> National Nanotechnology Laboratory, INFN, 73100 Lecce, Italy

<sup>4</sup> Fachbereich Physik, Philipps Universität Marburg, 35037 Marburg, Germany

Correspondence should be addressed to W. J. Parak, Wolfgang.parak@physik.uni-marburg.de

Received 20 July 2007; Accepted 13 December 2007

Recommended by Marek Osinski

Gold-DNA conjugates were investigated in detail by a comprehensive gel electrophoresis study based on 1200 gels. A controlled number of single-stranded DNA of different length was attached specifically via thiol-Au bonds to phosphine-stabilized colloidal gold nanoparticles. Alternatively, the surface of the gold particles was saturated with single stranded DNA of different length either specifically via thiol-Au bonds or by nonspecific adsorption. From the experimentally determined electrophoretic mobilities, estimates for the effective diameters of the gold-DNA conjugates were derived by applying two different data treatment approaches. The first method is based on making a calibration curve for the relation between effective diameters and mobilities with gold nanoparticles of known diameter. The second method is based on Ferguson analysis which uses gold nanoparticles of known diameter as reference database. Our study shows that effective diameters derived from gel electrophoresis measurements are affected with a high error bar as the determined values strongly depend on the method of evaluation, though relative changes in size upon binding of molecules can be detected with high precision. Furthermore, in this study, the specific attachment of DNA via gold-thiol bonds to Au nanoparticles is compared to nonspecific adsorption of DNA. Also, the maximum number of DNA molecules that can be bound per particle was determined.

Copyright © 2007 T. Pellegrino et al. This is an open access article distributed under the Creative Commons Attribution License, which permits unrestricted use, distribution, and reproduction in any medium, provided the original work is properly cited.

## 1. INTRODUCTION

DNA-functionalized gold nanoparticles are an interesting system with applications ranging from biological sensors to the construction of self-assembled materials. Experiments are based on attaching single-stranded DNA molecules via thiol-gold bonds to the surface of Au nanoparticles and a subsequent self-assembly process of these conjugates by making use of base pairing of complementary DNA molecules [1–5]. For example, by employing Au-DNA conjugates, several groups have developed schemes to detect target DNA sequences [6] and to assemble nanoparticles into macroscopic materials [7, 8]. DNA-functionalized Au nanoparticles are the building blocks for the above-mentioned experiments. Therefore, it is of great interest to investigate the properties of these conjugates in detail.

Due to the high affinity of thiol groups to gold surfaces, thiol-modified DNA molecules can be directly bound to the

surface of citrate- or phosphine-stabilized Au nanoparticles [9, 10]. Although commonly a random number of DNA molecules are attached per Au nanoparticle [1], also particles with an exactly defined number of one, two, or three attached DNA molecules per nanoparticles can be obtained [11–15]. Certainly, several parameters have significant influence on the properties of Au-DNA conjugates, such as coverage of the Au surface with DNA, configuration of the attached DNA molecules, and hybridization efficiency of DNA attached to Au surfaces. These parameters are strongly connected. The degree of DNA coverage will influence the DNA conformation, which, in turn, will affect the hybridization efficiency. Also, nonspecific adsorption has to be considered.

A body of experiments investigating these parameters has been reported for DNA attached to flat Au surfaces using different techniques such as atomic force microscopy (AFM) [16–18], surface plasmon resonance (SPR) spectroscopy [19–21], radioisotopic techniques [22, 23], ellipsometry [23], and X-ray photoelectron spectroscopy (XPS) [23]. These experiments allow for a detailed picture of DNA bound to planar gold surfaces and the results have clarified



the binding mechanism, the surface coverage, the hybridization efficiency, and the role of nonspecific adsorption, all in dependence of the length of the DNA.

Since the effect of surface curvature has to be taken into account [24], the results obtained for planar Au surfaces may be transferred to spherical Au nanoparticles only under certain restrictions. The surface coverage of Au nanoparticles with DNA has been investigated using the displacement of fluorescence-labeled DNA molecules with mercaptoethanol [25] and by gel electrophoresis [26]. Also, the conformation of bound DNA [27, 28], hybridization [29], and the role of nonspecific adsorption [26, 28, 30] have been investigated for Au nanoparticles.

In this report, we present a detailed study of electrophoretic mobility of Au-DNA conjugates. With this study, we want to determine the possibilities and limitations of this technique. Besides our own previous work [27, 31], also other groups [28, 32, 33] have recently reported about the possibility to extract effective diameters for bioconjugated colloidal nanoparticles from electrophoretic mobilities. The aim of this study is, in particular, to investigate the limitations of this analysis.

## 2. MATERIALS AND METHODS

### 2.1. Sample preparation

Citrate-coated gold nanoparticles of 5, 10, and 20 nm diameter were purchased from BBI/TED Pella (Redding, Calif, USA). In order to improve their stability in buffer solution, the adsorbed citrate molecules were replaced by a phosphine (bis(p-sulfonatophenyl)phenylphosphine dehydrate, dipotassium salt) [11]. The concentration of the Au nanoparticles was determined by UV/vis spectroscopy by using the molecular extinction coefficient of their absorption at the plasmon peak. Thiol- and Cy5-modified and unmodified single-stranded DNA were purchased from IDT (Coralville, Iowa, USA) or Metabion (München, Germany). All sequences can be found in the Supplementary Material (available online at doi: 10.1155/2007/26796). The concentration of the DNA was determined by UV/vis spectroscopy by using the molecular extinctions coefficient of their absorption at 260 nm. The thiol-modified and plain DNA were added to the phosphine-coated Au nanoparticles at pH = 7.3,  $c(\text{NaCl}) = 50 \text{ mM}$ , and samples were incubated for some hours up to several days [11, 27]. Generally, in such experiments, DNA is always added in large excess, thus that the number of attached molecules is related but not fully controlled by the stoichiometry of DNA:Au-NP because of the rather low binding yield.

### 2.2. Gel electrophoresis experiments

The resulting Au-DNA conjugates were loaded on 0.5%–6% agarose gels (agarose: Gibco BRL, number 15510-027;  $0.5 \times \text{TBE}$  buffer, pH 9) and run for one hour at 100 V [11, 27]. (Since 6% gels can be inhomogeneous due to their high viscosity, the data obtained with these gels have to be interpreted with care.) As reference, always unconjugated Au nanoparti-

cles of the same diameter were run on the same gel. In addition, gels with unconjugated Au nanoparticles of different diameter and free DNA of different length were run. The bands of the plain and DNA-conjugated Au nanoparticles were directly visible by the red color of the Au colloid and the free DNA was visualized by an attached fluorescence label (fluorescein, Cy3, or Cy5). The bands of the gels were photographed using a digital camera system (Eagle Eye III, Stratagene). The mobility of each sample was determined by measuring the position of each band referring to the start position where the samples had been loaded. This resulted in a comprehensive set of data which relates the mobility of Au-DNA conjugates to the diameter of the Au particles, where the relation between the amount and the length of the attached DNA, nonspecific versus specific attachment via thiol-gold bonds, and the gel percentage was studied.

### 2.3. Calculation of the effective diameter of the Au-DNA conjugates

Since mobility is not an illustrative quantity, we have attempted to convert the mobilities of Au-DNA conjugates in effective diameters. The evaluation of the gels in which plain Au-nanoparticles of known diameter were run yielded a calibration curve in which the mobility is plotted versus the diameter. By using this calibration curve, the mobility of the Au-DNA conjugates could be directly converted into effective diameters [27]. Alternatively, the mobility of Au-DNA conjugates at different agarose concentrations was used to obtain Ferguson plots [34] and fits of the Ferguson plots yielded the retardation coefficients [28]. First, Ferguson plots were made for plain Au-nanoparticles of known diameter and a calibration curve in which the retardation coefficients were plotted versus the particle diameter was obtained [28]. By using this calibration curve, the effective diameters of Au-DNA conjugates could be derived from the retardation coefficients derived from the Ferguson plots of the Au-DNA conjugates [28].

### 2.4. Determination of the maximum number of attached DNA molecules per particle

We have also quantified the maximum number of DNA molecules that can be attached per gold nanoparticle for particles with 5 nm and 10 nm diameter and single-stranded DNA with 8 and 43 bases. For this purpose, single-stranded DNA that had been modified with a thiol group on the 3' and a Cy5 dye on the 5' end has been attached via formation of thiol-Au bonds to the surface of Au particles. DNA was added in different DNA to Au ratios and the conjugates were run on an agarose gel. The more DNA bound per Au nanoparticle, the more the band of this conjugate was retarded on the gel [27]. At a certain amount of added DNA, the retardation of the band of the conjugates did not further increase, which indicates that the Au surface is fully saturated with DNA [27]. The bands were extracted from the gel by cutting out the agarose piece that contained the band and immersing it into  $0.5 \times \text{TBE}$  buffer solution. After two days, the Au-DNA conjugates had diffused out of the gel into the buffer. The

extraction procedure ensures that all DNA is really attached to the Au particles, since free DNA migrates in a much faster band. UV/vis spectra were recorded of the extracted Au-DNA conjugates. For each of the conjugates, the DNA concentration was determined by the Cy5 absorption and the Au concentration was determined by the absorption at the plasmon peak and from both concentrations the number of attached DNA molecules per particles was derived. As we quantified the number of attached Cy5 molecules only with absorption and not with fluorescence measurements, the effect that the fluorescence of Cy5 close to Au surfaces is quenched [35] did not interfere with our analysis.

All methods and additional experiments can be found in detail in the supplementary material.

### 3. RESULTS AND DISCUSSION

#### 3.1. *The attachment of DNA to particles increases the effective diameter and thus lowers the electrophoretic mobility*

The attachment of DNA to Au nanoparticles can be clearly observed by gel electrophoresis [9, 11, 13, 26–28, 36–38]. The mobility of particles on the gel depends on two factors: size and charge. The bigger the size, the slower and the higher the charge, the faster particles will migrate. In the case of negatively charged Au particles (e.g., with citrate or phosphine molecules adsorbed to the particles), the attachment of negatively charged DNA molecules causes in first place an increase of size that can be seen as a retardation of the band of the gel [27]. If the change in charge dominated, then the mobility of the Au particles should be increased (addition of negative charge) or drastically decreased (addition of positive charge) up to change in the direction of migration. Although this effect has been observed for different systems [31, 39], it has not been observed for the Au-DNA conjugates used in this study. Upon attachment of DNA, the mobility of the resulting conjugates was always moderately decreased. Therefore, in agreement with previous reports, we assume throughout this manuscript that attachment of DNA to Au nanoparticles in first order increases the effective diameter of the conjugates which can be directly seen in the retardation of the band of the conjugates in gel electrophoresis experiments [9, 11, 26–28, 36–38].

#### 3.2. *Generation of a calibration curve that relates electrophoretic mobilities to effective diameters*

One aim of this study was to obtain calibration curves in which measured electrophoretic mobilities  $m$  can be related to effective diameters  $d_{\text{eff}}$ . By running phosphine-stabilized Au particles of known diameter (the overall diameter of phosphine-coated Au NP was assumed as the core diameter plus two times 0.5 nm for the thickness of the phosphine layer and the smallest nanoparticle size used for calibration was 6 nm) on gels, by measuring their mobility, by fitting the data empirically with an exponential function, and by using the inverse of the fit function, we obtained a function in which the effective diameter of Au particles and Au-

TABLE 1: Experimentally obtained parameters for deriving effective diameters from electrophoretic mobilities for different gel percentages  $\gamma$ . The data have been derived by fitting an experimentally obtained dataset of electrophoretic mobilities of Au nanoparticles of known diameter and represent the mean values and standard deviations.

$\gamma$	$A_\gamma$	$T_\gamma$ (nm)
0.5%	$1.017 \pm 0.015$	$189 \pm 19$
1%	$1.049 \pm 0.012$	$85.0 \pm 3.7$
2%	$1.120 \pm 0.024$	$37.7 \pm 1.9$
3%	$1.236 \pm 0.025$	$18.8 \pm 0.8$
4%	$1.476 \pm 0.061$	$10.3 \pm 0.9$
5%	$1.759 \pm 0.079$	$7.16 \pm 0.66$
6%	$2.073 \pm 0.083$	$5.77 \pm 0.49$

DNA conjugates can be directly calculated from their electrophoretic mobility:

$$d_{\text{eff}}(m) = -T_\gamma * \ln((m/m_{10\text{ nm},\gamma})/A_\gamma) + 6 \text{ nm}. \quad (1)$$

The parameters for  $\gamma = 0.5\%$ ,  $1\%$ ,  $2\%$ ,  $3\%$ ,  $4\%$ ,  $5\%$ , and  $6\%$  agarose gels are enlisted in Table 1. In order to enhance the accuracy by making relative instead of absolute measurements, we always normalized the mobilities  $m$  to the mobilities  $m_{10\text{ nm},\gamma}$  of plain phosphine-stabilized Au particles of 10 nm core diameter on the same gel. Therefore, although the primary data of all electrophoresis measurements are electrophoretic mobilities, we are discussing the experimental results in terms of effective diameters. The diameters have been obtained with the above-described formula from the mobility data.

Since obviously the effective diameter of Au-DNA conjugates is a fixed physical property, it should not depend on the form of measurement and analysis. We, therefore, compared the effective diameters derived from 1%, 2%, 3% gels via the respective mobility-diameter calibration curves and from Ferguson plots [34]. For the Ferguson plots, the mobility data from all gel percentages are required.

#### 3.3. *Evaluation of the accuracy of effective diameters obtained from electrophoretic mobilities via mobility-diameter calibration curves*

The determined effective diameters for Au-DNA conjugates for Au particles saturated with DNA and for Au particles with only few DNA strands attached per particle are plotted in Figures 1 and 2 for DNA of different length. In all cases, regardless the length of the DNA, whether DNA was attached by specific thiol-gold linkage or by nonspecific adsorption, or whether only a few or a many as possible DNA molecules were bound per Au nanoparticles, the effective diameters derived with the mobility-diameter calibration curves are different for different gel percentages. Though most of the times the effective diameters derived from gels with higher percentage were found to be larger than the ones obtained from gels with lower percentage, also the opposite effect was observed within the experimental error bars (see, e.g., Figure 2). The

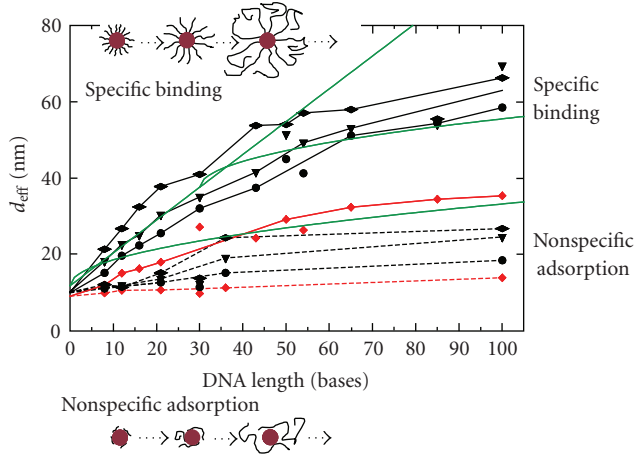


FIGURE 1: Effective diameter  $d_{\text{eff}}$  of Au-DNA conjugates for Au surfaces saturated with DNA. The surface of 10 nm phosphine-stabilized Au nanoparticles was saturated with single-stranded DNA of different lengths and the conjugates were run on 1%, 2%, and 3% gels. From the measured mobilities, the effective diameters of the conjugates were determined. The effective diameters obtained from 1%, 2%, and 3% gels are plotted in black with diamond, triangle, and circle symbols, the effective diameters obtained from Ferguson analysis are plotted in red. The effective diameters of conjugates in which the DNA was linked to the Au particles via specific thiol-gold bonds are connected with straight lines, the effective diameters of conjugates in which the DNA is nonspecifically adsorbed to the Au particles are connected with dotted lines. The green lines correspond to rudimentary theoretical models of the effective diameters of DNA molecules attached via thiol-gold to Au particles [27]. For fully stretched DNA (bottom curve),  $d_{\text{eff,linear}}(N) = 10 \text{ nm} + 2 \cdot (0.92 \text{ nm} + N \cdot 0.43 \text{ nm})$ , for randomly coiled DNA (top curve)  $d_{\text{eff,coil}}(N) = 10 \text{ nm} + 2 \cdot (0.92 \text{ nm} + 2 \cdot [3^{-1} \cdot N \cdot 0.43 \text{ nm} \cdot 2 \text{ nm}]^{1/2})$ , and for DNA partly stretched and partly coiled DNA (middle curve)  $d_{\text{eff,mixed}}(N) = 10 \text{ nm} + 2 \cdot (0.92 \text{ nm} + 30 \cdot 0.43 \text{ nm} + 2 \cdot [3^{-1} \cdot (N - 30) \cdot 0.43 \text{ nm} \cdot 2 \text{ nm}]^{1/2})$  was used [27]. We assumed 0.92 nm for the length of the thiol-hydrocarbon ( $\text{C}_6$ ) spacer at the reactive end of the DNA, 0.43 nm per base for the contour length and 2 nm for the persistence length [42, 43].  $N$  corresponds to the number of bases.

effective diameters derived from Ferguson plots were always smaller than the ones derived from the mobility-diameter calibration curves. This clearly demonstrates a severe limitation of deriving effective diameters from electrophoretic mobilities. If always the effective diameters derived from the gel of higher percentage were smaller than the one derived from gels with lower percentage, one could have argued that the soft DNA shell around the rigid Au cores would be squeezed or compressed more while migrating through the gel of higher agarose concentration, which would lead to smaller effective diameters. However, since no clear correlation between the gel concentration and the derived effective diameters was observed, we have to consider the difference between the effective diameters that have been obtained from gels of different concentrations as error bars. The bigger the Au particles become due to attachment of DNA, the bigger the error in deriving their effective diameter from electrophoretic mobilities becomes. For example, according to Figure 1, the effective diameters of 10 nm Au particles saturated with 100

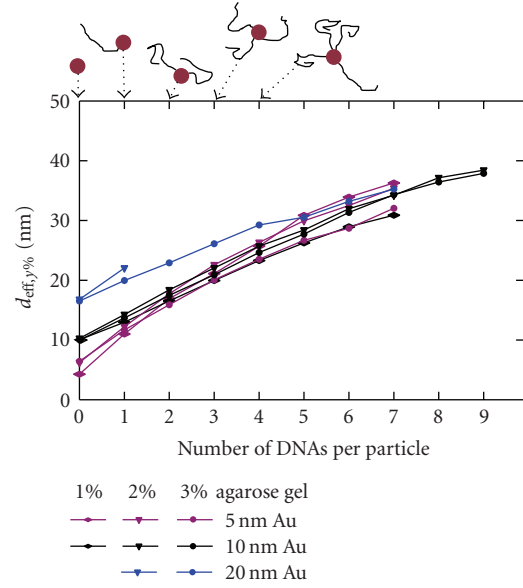


FIGURE 2: Effective diameter of Au-DNA conjugates with a discrete number of DNA molecules attached per Au nanoparticle. 10 nm Au particles were incubated with thiol-modified single-stranded DNA of 43 and 100 bases length and run on 1%, 2%, and 3% agarose gels. On the gels, particles with exactly 0, 1, 3, 4, ... DNA molecules attached per Au particle could be identified as discrete bands. From the mobilities of the bands on the gels, the effective diameters  $d_{\text{eff}}$  were derived by using a calibration curve that relates mobilities and diameters. The effective diameters corresponding to effective diameters derived from 1%, 2%, and 3% gels are plotted in black with diamond, triangle, and circle symbols, respectively. From the mobility data of the gels of different percentage effective diameters were also obtained by the Ferguson method and are plotted in red. The upper and lower sets of curves belong to the Au-DNA conjugates with 100 bases and 43 bases DNA, respectively.

bases DNA that is specifically linked via thiol-Au bonds are 66.3 nm, 69.5 nm, and 58.5 nm as determined from 1%, 2%, and 3% gels. We believe that from these data we can assume that the effective diameter of these conjugates is around 60 nm with an error bar of around 10 nm. From these and additional similar data (not shown), we conclude that deriving absolute effective diameters from electrophoretic mobilities via mobility-diameter calibration curves is possible only under certain restrictions. It is not sufficient to extract the data just from gels of one percentage. Only by using gels of different percentage an average value for the effective diameter and an estimate about the error can be obtained. Part of this limitation might be due to our principal assumption that in the case of phosphine-stabilized Au particles conjugated with DNA, the electrophoretic mobility is in first order only determined by the size of the conjugates. Charge effects may hamper obtaining more precise data for effective diameters. For other systems in which charge effects certainly will play a more important role [39], it might be even impossible to derive effective diameters from electrophoretic mobilities with the here-reported mobility-diameter calibration curves. It also has to be pointed out that the possible application of

the here-reported calibration curves is limited to relatively rigid objects similar in nature to Au nanoparticles. As these objects were used in first order to obtain the experimental data on which the calibration functions are based, the calibration functions certainly will not describe the diameters of soft objects, such as DNA, very well. A likely explanation for the deviation in the effective diameters obtained for the DNA-Au conjugates with the calibration functions for the gels of different percentage can be seen in the fact that the calibration functions are directly only applicable for Au particle-like rigid objects. Attaching soft objects as DNA to the Au particle surface changes their electrophoretic behavior so that the calibration curves can be only applied in a restricted way.

### 3.4. Evaluation of the accuracy of effective diameters obtained from Ferguson plots

We have also evaluated the possibility to obtain effective diameters of Au-DNA conjugates via Ferguson plots, as had already suggested by the group of Hamad-Schifferli [28]. From Figures 1 and 2, it is evident that the effective diameters obtained from Ferguson plots are always significantly smaller than the ones obtained from mobility-diameter calibration curves. It has to be pointed out that both evaluation methods are based on the same set of experimentally obtained mobilities. In a classical Ferguson plot, for example for free DNA, the logarithm of the mobilities is linear to the gel percentage. However, in the case of Au and Au-DNA conjugates, this linearity holds no longer true, in particular for gels of higher percentage [36]. We, therefore, had to restrict our analysis to gels from 1% to 3% although in some cases data for 4% to 6% had also been available. Additional experiments can be found in the supplementary material. Though theories for nonlinear, convex Ferguson plots exist [40, 41], we did not try to apply them here. Due to the significant deviation from the data obtained with the Ferguson plots to the data obtained with mobility-diameter calibration curves and due to the above-mentioned limitations, we conclude that the linear Ferguson analysis is less suited to obtain absolute effective diameters. However, relative increases in size due to binding of molecules can be observed with sufficient resolution with Ferguson analysis.

### 3.5. Specific thiol-Au bond-mediated attachment of DNA versus nonspecific DNA adsorption

Our data clearly indicate that there is also nonspecific adsorption of DNA to the surface of Au particles in case the particles are exposed to many DNA molecules, see Figure 1. It is important to point out that in Figure 1, the data of Au particles that have been exposed to as much DNA as possible and that are, therefore, saturated with DNA are described. This is different from the case in which the Au particles are exposed to only to a few strands of DNA as in Figure 2, where no nonspecific adsorption could be observed, as already reported by Zanchet et al. [11]. Nonspecific adsorption of DNA to Au particles is significantly lower compared to specific thiol-Au bond-mediated attachment and thus can only be observed in

case of exposure of the particles to very high DNA concentrations.

Although the absolute numbers derived for effective diameters for Au-DNA conjugates are afflicted with significant error bars as described above, these data nevertheless contain valuable information about the binding of DNA to Au particles. Any attachment of DNA leads to an increase in the effective diameter, dependent on the nature of attachment, the amount of bound DNA, and the length of each DNA molecule, see Figure 1. With very simple models, we can assume that DNA attached to the surface of Au particles can adopt two basic types of conformation [27]. In the first case, the confirmation of DNA is not effected by the presence of the Au particles and it will form a random coil. In the second case, DNA has to compete for the binding places at the gold surface and thus, in order to bind as many DNA molecules per area as possible, the DNA has to be stretched. Actually, a combination of both models will best describe the reality. In Figure 1, the effective diameters for the different models (randomly coiled DNA, fully stretched DNA, and DNA that is stretched for the first 30 bases and randomly coiled for the rest of the bases) are plotted versus the DNA length for Au particles that are saturated with DNA. Clearly, thiol-gold-bond specific attachment can be distinguished from nonspecific adsorption of DNA. Similar observations have been reported also before by Sandström et al. [26, 37]. First, the increase in the effective diameter tells that also DNA without thiol modification can be adsorbed to the surface of phosphine-stabilized Au nanoparticles. Second, a comparison with the effective diameters of the theoretical models clearly proves that nonspecifically adsorbed DNA does not exist in a stretched configuration perpendicular to the Au surface. The data rather indicate that even when the particle surface is saturated with nonspecifically attached DNA, only parts of the DNA molecules will be randomly coiled, as the experimentally obtained effective diameters are smaller than the diameter of conjugates in which the adsorbed DNA is randomly coiled. From this, one can conclude that due to nonspecific Au-DNA interaction, the adsorbed DNA is at least partly wrapped around the surface of the Au particles, which is in agreement with other studies [44]. In case of Au surfaces saturated with thiol-modified DNA, the effective diameters are significantly bigger compared to nonspecifically adsorbed DNA, see Figure 1. By comparison with basic models, we conclude in agreement to our previous study that specifically bound DNA adopts a stretched configuration so that as many DNA molecules as possible can bind to the Au surface. Due to the spherical geometry, DNA longer than around 30 bases only needs to be stretched due to this space limitation within around the first 30 bases, whereas the parts of the DNA molecules further away from the Au particle are not affected by space limitation and thus can be randomly coiled. These results again show the possibilities and limitations of the here-described method. Though it is complicated to derive accurate absolute effective diameters of Au-DNA conjugates, the binding of DNA molecules can be clearly seen as an increase in the effective diameters and a comparison with theoretical models can give indications about the conformation of the attached DNA. These



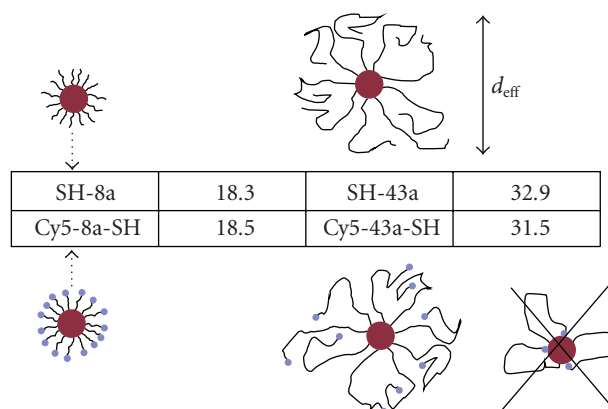


FIGURE 3: 10 nm diameter Au particles have been saturated with thiol-modified single-stranded DNA of 8 and 43 bases lengths and were run on 2% agarose gels. From the resulting mobilities, effective diameters were derived via a mobility-diameter calibration curve (for 2% agarose gels). In the table, the effective diameters of particles are given in nm. In the upper row, the data for DNA modified at one end with an-SH group are shown. In the bottom row, the data for DNA modified at one end with an-SH and at the other end with a -Cy5 organic fluorophore are shown. The results are within the error bars identical for DNA with and without Cy5, which indicates that the Cy5 at the free end does not interfere with the binding process of the DNA to the Au particle surface.

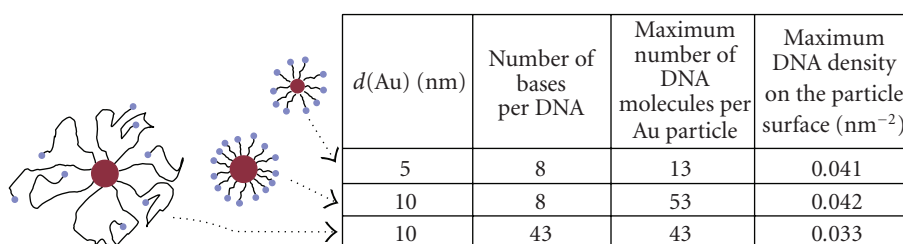


FIGURE 4: Maximum number of thiol-modified single-stranded DNA molecules that can be bound to the surface of phosphine-stabilized Au particles. Au particles of different core-diameter ( $d = 5$  nm, 10 nm) and thiol modified single-stranded DNA of different length (8 and 43 bases) have been used. The maximum possible number of DNA molecules per Au particle and the maximum surface density (in DNA per particle surface) are given.

types of binding assays via gel electrophoresis are an attractive complementary method compared to other techniques, such as light scattering [45]. Presumably a combination of gel electrophoresis, light scattering, and zeta potential measurements of identical samples would give the most accurate analysis about Au-DNA conjugates. It remains to note that although electrophoresis of free DNA is well studied both experimentally and theoretically, the case of Au-DNA conjugates is more complex because several properties (total charge, charge density, and elasticity) are not constant but depend all at the same time on the binding of DNA to the Au nanoparticles. A theoretical model for gel electrophoresis of such conjugates would be helpful for data analysis.

### 3.6. Effect of organic fluorophores linked to DNA on the binding of DNA to Au particles

When organic fluorophores are attached to Au-DNA conjugates at the free end of the DNA, which is pointing towards solution, then energy transfer between the fluorophore and the Au nanoparticle can be observed [35]. This effect can be,

for example, employed for DNA sensors [46]. Since energy transfer depends on the distance between the organic fluorophore and the Au surface [35, 47], certainly the configuration of the bound fluorophore-modified DNA is important for this process. In case of nonspecific adsorption of the fluorophore to the Au surface, the distance between the fluorophore and the Au would be much smaller than for the case in which the DNA is linked with its thiol-modified end, see Figure 3. In this study, we have shown that the attachment of Cy5 to the free end of thiol-modified DNA does not change the effective diameter in the case of Au particles saturated with DNA, see Figure 3. These results demonstrate that the direct adsorption of Cy5 to the Au surface is much less probable than the formation of thiol-Au bonds and that, therefore, the dye points towards the solution.

### 3.7. Determination of the maximum number of DNA molecules that can be bound per one Au particle

The number of bound DNA molecules per Au particle has already been determined with several methods [25, 26, 48].

In comparison to methods in which the number of DNA molecules is quantified by the fluorescence of attached fluorophores, the counting of DNA via absorption measurements (as reported in this study) is not affected by photobleaching and quenching effects. Extracting the Au-DNA conjugates from the gel also helps that no unbound excess DNA is present in the solution, as it still might be possible in the case of purification with filter membranes. The results of this study are summarized in Figure 4 and are in the same range as the results obtained by other groups [25, 26, 48] though our determined DNA densities are rather lower than the ones determined by other groups. This might be due to the fact that the phosphine stabilization is harder to be displaced by DNA than citrate stabilization and in particular due to the fact that our incubation was performed at lower NaCl concentrations [48]. In our measurements, we could not find any effect of the different curvature between 5 nm and 10 nm gold particles on the density of attached DNA molecules. This can be understood as the surface curvature difference between both types of particles is not very high and DNA attachment to both types of particles was done under the same buffer conditions. Recently, Qin and Yung have instead demonstrated that the most relevant parameter for the maximum number of attached DNA molecules per particle is the salt concentration under which the attachment was performed [48]. High salt concentrations reduce electrostatic repulsion and thus allow for higher DNA surface densities.

### 3.8. Attachment of an exactly known number of DNA molecules per Au particle

As already reported in earlier publications, gel electrophoresis allows for a separation of Au-DNA conjugates with 0, 1, 2, ... DNA molecules attached per particle [9, 11]. In Figures 2 and 5, the effective diameters of such conjugates as determined from their electrophoretic mobilities are presented. The dependence of DNA length and Au core diameter on the effective diameter is as expected. The longer the DNA, the more the effective diameter of Au-DNA conjugates upon which attachment of another DNA molecule to one gold particle is increased (see Figure 2). The more long DNA strands are attached per individual gold particle, the fewer the effective diameter of the Au-DNA conjugated depends on the initial diameter of the Au core (see Figure 5). Although no simple model for Au-DNA conjugates is available that could predict the exact mobility in gel electrophoresis, the bands of particles with a defined number of DNA strands can be identified with their structure by relative (qualitative) comparison and control experiments that include hybridization. So far, we are not aware of another separation technique (such as HPLC) that can resolve Au particles with an individual number of attached DNA molecules as it is possible with gel electrophoresis. The concept of separating conjugates of particles with a discrete number of attached molecules by gel electrophoresis could be also be generalized and used besides for Au-DNA conjugates for other systems [49]. Because of their defined composition, we think that such conjugates of particles with a defined number of linked molecules are very

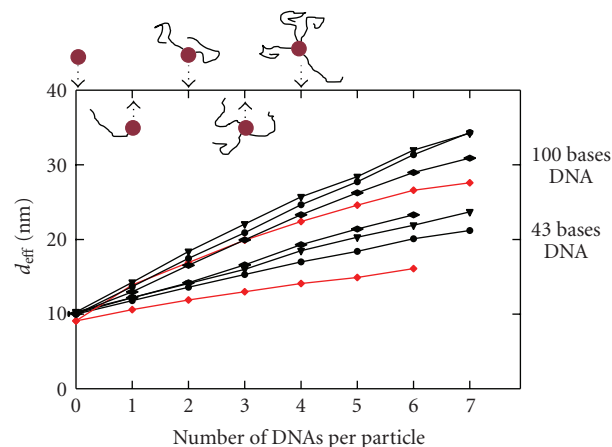


FIGURE 5: Effective diameters  $d_{\text{eff}}$  of Au-DNA conjugates with a discrete number of DNA molecules per particle for Au particles of different diameter. Single-stranded DNA (100 bases) had been specifically attached via thiol-gold bonds to the surface of 5 nm, 10 nm, and 20 nm Au particles. The conjugates were run on 1%, 2%, and 3% agarose gels and their effective diameters  $d_{\text{eff}}$  were derived from the measured electrophoretic mobilities. Here, the effective diameters for Au particles with a discrete number of attached DNA molecules (100 bases) per particle are shown. Data for 5 nm, 10 nm, and 20 nm particles are plotted in violet, black, and blue, respectively. Data derived from 1%, 2%, and 3% gels are plotted with diamond, triangle, and circle symbols.

interesting model systems and several applications have been already demonstrated [50, 51].

## 4. CONCLUSIONS

In this manuscript, the analysis of Au-DNA conjugates by gel electrophoresis is discussed. Whereas the principal effects are already known by our previous studies and reported by other groups, the aim of this work was the detailed analysis about the possibilities and limitations of this technique. For this purpose, an extensive study with 1200 gels was performed. From these data, we can conclude that the determination of absolute effective diameters from electrophoretic mobilities has severe limitations. In order to get an estimate about the accuracy of the data gels of different percentages have to be compared. The deviation between these data sets is an indicator for the error bars in the derived effective diameters. We believe that this strategy leads to more reliable values for effective diameters than Ferguson analysis. Pointing out these limitations is important as several studies exist in which this method has been applied without investigating its limitations first [27, 28, 32]. Though the extraction of absolute values for effective diameters from the mobility data has very limited accuracy, the attachment of molecules to particles can on the other hand be detected with high sensitivity as an increase in the effective diameters. In this way, even the attachment of single molecules can be resolved, which to our knowledge has not been demonstrated yet with an alternative separation technique such as HPLC. Besides such binding assays, also



indications about the conformation of the DNA molecules that are bound to the particles can be derived from the obtained effective diameters. In this way, we believe that gel electrophoresis is a very powerful method to investigate the attachment of DNA molecules to Au nanoparticles though it has also clear limitations. Whereas specific and nonspecific attachment of DNA can be detected with high sensitivity, the quantitative determination of effective hydrodynamic diameters is not possible in a straightforward way.

## ACKNOWLEDGMENTS

The authors are grateful to Dr. Eric Dulkeith for helpful comments. This work was supported in part by the German Research Foundation (DFG, Emmy Noether program), the European Union (STREP program NANO-SA), the Center for Nanoscience (CeNS), and the U.S. Department of Energy (Contract no. DE-AC02-05CH11231).

## REFERENCES

- [1] W. Fritzsche and T. A. Taton, "Metal nanoparticles as labels for heterogeneous, chip-based DNA detection," *Nanotechnology*, vol. 14, no. 12, pp. R63–R73, 2003.
- [2] C. A. Mirkin, "Programming the assembly of two- and three-dimensional architectures with DNA and nanoscale inorganic building blocks," *Inorganic Chemistry*, vol. 39, no. 11, pp. 2258–2272, 2000.
- [3] E. Dujardin and S. Mann, "Bio-inspired materials chemistry," *Advanced Materials*, vol. 14, no. 11, pp. 775–788, 2002.
- [4] Z. Wang, R. Lévy, D. G. Fernig, and M. Brust, "The peptide route to multifunctional gold nanoparticles," *Bioconjugate Chemistry*, vol. 16, no. 3, pp. 497–500, 2005.
- [5] A. G. Kanaras, Z. Wang, A. D. Bates, R. Cosstick, and M. Brust, "Towards multistep nanostructure synthesis: programmed enzymatic self-assembly of DNA/gold systems," *Angewandte Chemie International Edition*, vol. 42, no. 2, pp. 191–194, 2003.
- [6] R. Elghanian, J. J. Storhoff, R. C. Mucic, R. L. Letsinger, and C. A. Mirkin, "Selective colorimetric detection of polynucleotides based on the distance-dependent optical properties of gold nanoparticles," *Science*, vol. 277, no. 5329, pp. 1078–1081, 1997.
- [7] C. A. Mirkin, R. L. Letsinger, R. C. Mucic, and J. J. Storhoff, "A DNA-based method for rationally assembling nanoparticles into macroscopic materials," *Nature*, vol. 382, no. 6592, pp. 607–609, 1996.
- [8] A. Paul Alivisatos, K. P. Johnsson, X. Peng, et al., "Organization of 'nanocrystal molecules' using DNA," *Nature*, vol. 382, no. 6592, pp. 609–611, 1996.
- [9] C. J. Loweth, W. Brett Caldwell, X. G. Peng, A. Paul Alivisatos, and P. G. Schultz, "DNA-based assembly of gold nanocrystals," *Angewandte Chemie International Edition*, vol. 38, no. 12, pp. 1808–1812, 1999.
- [10] R. L. Letsinger, R. Elghanian, G. Viswanadham, and C. A. Mirkin, "Use of a steroid cyclic disulfide anchor in constructing gold nanoparticle-oligonucleotide conjugates," *Bioconjugate Chemistry*, vol. 11, no. 2, pp. 289–291, 2000.
- [11] D. Zanchet, C. M. Micheel, W. J. Parak, D. Gerion, and A. Paul Alivisatos, "Electrophoretic isolation of discrete Au nanocrystal/DNA conjugates," *Nano Letters*, vol. 1, no. 1, pp. 32–35, 2001.
- [12] K.-M. Sung, D. W. Mosley, B. R. Peelle, S. Zhang, and J. M. Jacobson, "Synthesis of monofunctionalized gold nanoparticles by Fmoc solid-phase reactions," *Journal of the American Chemical Society*, vol. 126, no. 16, pp. 5064–5065, 2004.
- [13] S. D. Jhaveri, E. E. Foos, D. A. Lowy, E. L. Chang, A. W. Snow, and M. G. Ancona, "Isolation and characterization of trioxethylene-encapsulated gold nanoclusters functionalized with a single DNA strand," *Nano Letters*, vol. 4, no. 4, pp. 737–740, 2004.
- [14] C. J. Ackerson, M. T. Sykes, and R. D. Kornberg, "Defined DNA/nanoparticle conjugates," *Proceedings of the National Academy of Sciences of the United States of America*, vol. 102, no. 38, pp. 13383–13385, 2005.
- [15] W. J. Qin and L. Y. L. Yung, "Nanoparticle-DNA conjugates bearing a specific number of short DNA strands by enzymatic manipulation of nanoparticle-bound DNA," *Langmuir*, vol. 21, no. 24, pp. 11330–11334, 2005.
- [16] N. Mourougou-Candoni, C. Naud, and F. Thibaudau, "Adsorption of thiolated oligonucleotides on gold surfaces: an atomic force microscopy study," *Langmuir*, vol. 19, no. 3, pp. 682–686, 2003.
- [17] E. Huang, M. Satjapipat, S. Han, and F. Zhou, "Surface structure and coverage of an oligonucleotide probe tethered onto a gold substrate and its hybridization efficiency for a polynucleotide target," *Langmuir*, vol. 17, no. 4, pp. 1215–1224, 2001.
- [18] E. Huang, F. Zhou, and L. Deng, "Studies of surface coverage and orientation of DNA molecules immobilized onto preformed alkanethiol self-assembled monolayers," *Langmuir*, vol. 16, no. 7, pp. 3272–3280, 2000.
- [19] A. W. Peterson, R. J. Heaton, and R. M. Georgiadis, "The effect of surface probe density on DNA hybridization," *Nucleic Acids Research*, vol. 29, no. 24, pp. 5163–5168, 2001.
- [20] A. W. Peterson, L. K. Wolf, and R. M. Georgiadis, "Hybridization of mismatched or partially matched DNA at surfaces," *Journal of the American Chemical Society*, vol. 124, no. 49, pp. 14601–14607, 2002.
- [21] K. A. Peterlinz, R. M. Georgiadis, T. M. Herne, and M. J. Tarlov, "Observation of hybridization and dehybridization of thiol-tethered DNA using two-color surface plasmon resonance spectroscopy," *Journal of the American Chemical Society*, vol. 119, no. 14, pp. 3401–3402, 1997.
- [22] A. B. Steel, R. L. Levicky, T. M. Herne, and M. J. Tarlov, "Immobilization of nucleic acids at solid surfaces: effect of oligonucleotide length on layer assembly," *Biophysical Journal*, vol. 79, no. 2, pp. 975–981, 2000.
- [23] T. M. Herne and M. J. Tarlov, "Characterization of DNA probes immobilized on gold surfaces," *Journal of the American Chemical Society*, vol. 119, no. 38, pp. 8916–8920, 1997.
- [24] D. V. Leff, L. Brandt, and J. R. Heath, "Synthesis and characterization of hydrophobic, organically-soluble gold nanocrystals functionalized with primary amines," *Langmuir*, vol. 12, no. 20, pp. 4723–4730, 1996.
- [25] L. M. Demers, C. A. Mirkin, R. C. Mucic, et al., "A fluorescence-based method for determining the surface coverage and hybridization efficiency of thiol-capped oligonucleotides bound to gold thin films and nanoparticles," *Analytical Chemistry*, vol. 72, no. 22, pp. 5535–5541, 2000.
- [26] P. Sandström, M. Boncheva, and B. Åkerman, "Nonspecific and thiol-specific binding of DNA to gold nanoparticles," *Langmuir*, vol. 19, no. 18, pp. 7537–7543, 2003.
- [27] W. J. Parak, T. Pellegrino, C. M. Micheel, D. Gerion, S. C. Williams, and A. Paul Alivisatos, "Conformation of oligonucleotides attached to gold nanocrystals probed by gel electrophoresis," *Nano Letters*, vol. 3, no. 1, pp. 33–36, 2003.

- [28] S. Park, K. A. Brown, and K. Hamad-Schifferli, "Changes in oligonucleotide conformation on nanoparticle surfaces by modification with mercaptohexanol," *Nano Letters*, vol. 4, no. 10, pp. 1925–1929, 2004.
- [29] K. Hamad-Schifferli, J. J. Schwartz, A. T. Santos, S. Zhang, and J. M. Jacobson, "Remote electronic control of DNA hybridization through inductive coupling to an attached metal nanocrystal antenna," *Nature*, vol. 415, no. 6868, pp. 152–155, 2002.
- [30] J. J. Storhoff, R. Elghanian, C. A. Mirkin, and R. L. Letsinger, "Sequence-dependent stability of DNA-modified gold nanoparticles," *Langmuir*, vol. 18, no. 17, pp. 6666–6670, 2002.
- [31] R. A. Sperling, T. Liedl, S. Duhr, et al., "Size determination of (Bio)conjugated water-soluble colloidal nanoparticles: a comparison of different techniques," *Journal of Physical Chemistry C*, vol. 111, no. 31, pp. 11552–11559, 2007.
- [32] T. Pons, H. Tetsuo Uyeda, I. L. Medintz, and H. Mattoussi, "Hydrodynamic dimensions, electrophoretic mobility, and stability of hydrophilic quantum dots," *Journal of Physical Chemistry B*, vol. 110, no. 41, pp. 20308–20316, 2006.
- [33] M. Hanauer, S. Pierrat, I. Zins, A. Lotz, and C. Sönnichsen, "Separation of nanoparticles by gel electrophoresis according to size and shape," *Nano Letters*, vol. 7, no. 9, pp. 2881–2885, 2007.
- [34] K. A. Ferguson, "Starch-gel electrophoresis—application to the classification of pituitary proteins and polypeptides," *Metabolism*, vol. 13, pp. 985–1002, 1964.
- [35] E. Dulkeith, M. Ringler, T. A. Klar, J. Feldmann, A. Muñoz Javier, and W. J. Parak, "Gold nanoparticles quench fluorescence by phase induced radiative rate suppression," *Nano Letters*, vol. 5, no. 4, pp. 585–589, 2005.
- [36] D. Zanchet, C. M. Micheel, W. J. Parak, D. Gerion, S. C. Williams, and A. Paul Alivisatos, "Electrophoretic and structural studies of DNA-directed Au nanoparticle groupings," *Journal of Physical Chemistry B*, vol. 106, no. 45, pp. 11758–11763, 2002.
- [37] P. Sandström and B. Åkerman, "Electrophoretic properties of DNA-modified colloidal gold nanoparticles," *Langmuir*, vol. 20, no. 10, pp. 4182–4186, 2004.
- [38] M.-E. Aubin, D. G. Morales, and K. Hamad-Schifferli, "Labeling ribonuclease S with a 3 nm Au nanoparticle by two-step assembly," *Nano Letters*, vol. 5, no. 3, pp. 519–522, 2005.
- [39] W. J. Parak, D. Gerion, D. Zanchet, et al., "Conjugation of DNA to silanized colloidal semiconductor nanocrystalline quantum dots," *Chemistry of Materials*, vol. 14, no. 5, pp. 2113–2119, 2002.
- [40] D. Tietz and A. Chrambach, "Analysis of convex ferguson plots in agarose gel electrophoresis by empirical computer modeling," *Electrophoresis*, vol. 7, pp. 241–250, 1986.
- [41] D. Tietz and A. Chrambach, "Concave ferguson plots of DNA fragments and convex ferguson plots of bacteriophages: evaluation of molecular and fiber properties, using desktop computers," *Electrophoresis*, vol. 13, no. 1, pp. 286–294, 1992.
- [42] B. Tinland, A. Pluen, J. Sturm, and G. Weill, "Persistence length of single-stranded DNA," *Macromolecules*, vol. 30, no. 19, pp. 5763–5765, 1997.
- [43] C. Rivetti, M. Guthold, and C. Bustamante, "Scanning force microscopy of DNA deposited onto mica: equilibration versus kinetic trapping studied by statistical polymer chain analysis," *Journal of Molecular Biology*, vol. 264, no. 5, pp. 919–932, 1996.
- [44] G. Han, C. T. Martin, and V. M. Rotello, "Stability of gold nanoparticle-bound DNA toward biological, physical, and chemical agents," *Chemical Biology & Drug Design*, vol. 67, no. 1, pp. 78–82, 2006.
- [45] M. Cárdenas, J. Barauskas, K. Schillén, J. L. Brennan, M. Brust, and T. Nylander, "Thiol-specific and nonspecific interactions between DNA and gold nanoparticles," *Langmuir*, vol. 22, no. 7, pp. 3294–3299, 2006.
- [46] C. K. Kim, R. R. Kalluru, J. P. Singh, et al., "Gold-nanoparticle-based miniaturized laser-induced fluorescence probe for specific DNA hybridization detection: studies on size-dependent optical properties," *Nanotechnology*, vol. 17, no. 13, pp. 3085–3093, 2006.
- [47] E. Dulkeith, A. C. Morteani, T. Niedereichholz, et al., "Fluorescence quenching of dye molecules near gold nanoparticles: radiative and nonradiative effects," *Physical Review Letters*, vol. 89, no. 20, Article ID 203002, 4 pages, 2002.
- [48] W. J. Qin and L. Y. L. Yung, "Efficient manipulation of nanoparticle-bound DNA via restriction endonuclease," *Biomacromolecules*, vol. 7, no. 11, pp. 3047–3051, 2006.
- [49] R. A. Sperling, T. Pellegrino, J. K. Li, W. H. Chang, and W. J. Parak, "Electrophoretic separation of nanoparticles with a discrete number of functional groups," *Advanced Functional Materials*, vol. 16, no. 7, pp. 943–948, 2006.
- [50] J. Sharma, R. Chhabra, Y. Liu, Y. Ke, and H. Yan, "DNA-templated self-assembly of two-dimensional and periodical gold nanoparticle arrays," *Angewandte Chemie International Edition*, vol. 45, no. 5, pp. 730–735, 2006.
- [51] J. Zheng, P. E. Constantinou, C. Micheel, A. Paul Alivisatos, R. A. Kiehl, and N. C. Seeman, "Two-dimensional nanoparticle arrays show the organizational power of robust DNA motifs," *Nano Letters*, vol. 6, no. 7, pp. 1502–1504, 2006.

## Research Article

# Design of Biotin-Functionalized Luminescent Quantum Dots

Kimihiro Susumu,<sup>1</sup> H. Tetsuo Uyeda,<sup>1,2</sup> Igor L. Medintz,<sup>3</sup> and Hedi Mattoussi<sup>1</sup>

<sup>1</sup> Division of Optical Sciences, U.S. Naval Research Laboratory, Washington, DC 20375, USA

<sup>2</sup> Promega Biosciences, Inc., 277 Granada Dr., San Luis Obispo, CA 93401, USA

<sup>3</sup> Center for Bio/Molecular Science and Engineering, U.S. Naval Research Laboratory, Washington, DC 20375, USA

Correspondence should be addressed to Hedi Mattoussi, hedimat@ccs.nrl.navy.mil

Received 25 June 2007; Accepted 21 December 2007

Recommended by Marek Osinski

We report the design and synthesis of a tetraethylene glycol- (TEG-) based bidentate ligand functionalized with dihydrolipoic acid (DHLA) and biotin (DHLA—TEG—biotin) to promote biocompatibility of luminescent quantum dots (QD's). This new ligand readily binds to CdSe—ZnS core-shell QDs via surface ligand exchange. QDs capped with a mixture of DHLA and DHLA—TEG—biotin or polyethylene glycol- (PEG-) (molecular weight average ~600) modified DHLA (DHLA—PEG600) and DHLA—TEG—biotin are easily dispersed in aqueous buffer solutions. In particular, homogeneous buffer solutions of QDs capped with a mixture of DHLA—PEG600 and DHLA—TEG—biotin that are stable over broad pH range have been prepared. QDs coated with mixtures of DHLA/DHLA—TEG—biotin and with DHLA—PEG600/DHLA—TEG—biotin were tested in surface binding assays and the results indicate that biotin groups on the QD surface interact specifically with NeutrAvidin-functionalized microtiter well plates.

Copyright © 2007 Kimihiro Susumu et al. This is an open access article distributed under the Creative Commons Attribution License, which permits unrestricted use, distribution, and reproduction in any medium, provided the original work is properly cited.

## 1. INTRODUCTION

Luminescent semiconductor nanocrystals, such as those made of CdSe—ZnS core-shell quantum dots (QD's), provide substantial advantages for use as stable fluorophores in biological assays and imaging. As synthesized by conventional methods using high-temperature solution reaction from organometallic precursors, highly luminescent QD's are capped with hydrophobic organic ligands primarily made of a mixture of trioctylphosphine/trioctylphosphine oxide (TOP/TOPO). Further surface modification is required to make them water-soluble and biocompatible. Methods reported to date for achieving water solubility of such materials include silica coating [1], encapsulation of the native TOP/TOPO-capped QD's within amphiphilic polymer shells [2] or lipid micelles [3], and cap exchange of the native TOP/TOPO caps with hydrophilic ligands [4–6]. The strategy based on cap exchange with bifunctional ligands is relatively simple to implement and has the potential to provide compact hydrophilic QD's, a desired property in targeted studies, including fluorescence resonance energy transfer (FRET-) based sensing and cellular uptake [7–11].

We have previously utilized readily available thioctic acid and polyethylene glycols (PEGs) in simple esterification schemes, followed by reduction of the 1,2-dithiolane to synthesize a series of PEG-terminated dihydrolipoic acid (DHLA—PEG) capping substrates [12]. The cap exchange reaction of TOP/TOPO-capped QD's with these substrates produced water-soluble nanocrystals that are stable over extended periods of time and over a relatively broad pH range, from weakly acidic to basic conditions (pH 5~12). Though compact and stable, those ligands lack specific functional end groups and do not allow easy implementation of simple conjugation techniques, such as avidin-biotin binding.

In this study, we further expanded those findings and report the design and synthesis of ligands functionalized with a biotin end group. The designed ligands have a central tetraethylene glycol (TEG) segment, a dithiol terminal group for anchoring on the QD surface and a lateral biotin. Appending biotin at the end of surface-attached ligands should permit the use of the ubiquitous avidin-biotin binding motif to conjugate QD's to proteins and other biomolecules via an avidin bridge. Cap exchange reactions were carried out with mixed ligands and preliminary binding assays of the

biotin-coated water-soluble QD's to NeutrAvidin-functionalized substrates showed that specific capture of the QD's due to avidin-biotin interactions was achieved.

## 2. EXPERIMENTAL SECTION

All manipulations were carried out under dry nitrogen and air-sensitive solids were handled in an MBraun Labmaster 130 glovebox. TEG was purchased from Sigma-Aldrich (Milwaukee, Wis, USA). Triphenylphosphine, thioctic acid, 4-(*N,N*-dimethylamino)pyridine, *N,N'*-dicyclohexylcarbodiimide, and *N*-hydroxysuccinimide were purchased from Acros Organics (Morris Plains, NJ, USA). Sodium azide and biotin were purchased from Alfa Aesar (Ward Hill, Mass, USA). Methanesulfonyl chloride was purchased from GFS Chemicals (Powell, Ohio, USA). Sodium borohydride was purchased from Strem Chemicals (Newburyport, Mass, USA). All the other chemicals (including solvents) were purchased from Sigma-Aldrich and Acros Organics. Tetrahydrofuran (THF) was dried over CaH<sub>2</sub> before use. Deuterated solvents employed in all NMR measurements were used as received. Chemical shifts for <sup>1</sup>H NMR spectra are reported relative to tetramethylsilane (TMS) signal in the deuterated solvent (TMS,  $\delta$  = 0.00 ppm). All *J* values are reported in Hertz. Column chromatography was performed on bench top, using silica gel (Bodman Industries, Aston, Pa, USA, 60 Å, 230–400 mesh).

<sup>1</sup>H NMR spectra were recorded on a Bruker SpectroSpin 400 MHz spectrometer. Electronic absorption spectra were recorded using an HP 8453 diode array spectrophotometer (Agilent technologies, Santa Clara, Calif, USA), while fluorescence spectra were collected using a Spex Fluorolog-3 spectrophotometer (Jobin Yvon Inc, Edison, NJ, USA). To account for the nonlinear (wavelength-dependent) quantum efficiency of the PMT detector, the fluorescence spectra were corrected using calibration curves accounting for the wavelength-dependence of the PMT's detection efficiency.

### 2.1. Ligand synthesis

The biotin-terminated ligands were synthesized stepwise using commercially available TEG. The choice of a short TEG segment to test this synthetic scheme was motivated by the well-defined chain length of the TEG molecules compared to longer PEG chains, which is expected to make separation using column chromatography easier. In the following section we detail the synthesis of each intermediate compound necessary for preparation of the final DHLA-TEG-biotin ligand. All the compounds were characterized by thin layer chromatography (TLC) and <sup>1</sup>H NMR.

#### 2.1.1. 1,11-Diazido-3,6,9-trioxaundecane

Diazide-functionalization of TEG (**3**): compound **3** was prepared following published procedures [13]. TEG (40.0 g, 206 mmol), tetrahydrofuran (THF) (350 mL), and methanesulfonyl chloride (53.0 g, 463 mmol) were mixed in a 1 L round bottom flask and cooled to 0°C. A solution of triethylamine (49.0 g, 484 mmol) in THF (50 mL) was added drop-

wise over 30 minutes and the mixture was stirred at room temperature over 20 hours. The reaction was then diluted with water (200 mL) and NaHCO<sub>3</sub> (12.5 g). Sodium azide (36.0 g, 554 mmol) was added and the biphasic reaction mixture was first heated to 65°C to distill off the THF, and then to 70°C for 14 hours. The reaction mixture was cooled to room temperature and extracted with ether (3 × 75 mL). The combined organic extracts were dried over MgSO<sub>4</sub>, filtered, and evaporated to give brownish oil. The product was purified by flash column chromatography (hexane : EtOAc 1 : 1) and the solvent evaporated to give 39 g (a yield of 78%) as a colorless oil. <sup>1</sup>H NMR (400 MHz, CDCl<sub>3</sub>):  $\delta$  (ppm) 3.66–3.71 (m, 12H, –OCH<sub>2</sub>CH<sub>2</sub>–), 3.40 (t, 4H, *J* = 5.1 Hz, –CH<sub>2</sub>N<sub>3</sub>).

#### 2.1.2. 1-Amino-11-azido-3,6,9-trioxaundecane

Transformation to monoamine-terminated TEG (**4**) [13]: 1,11-Diazido-3,6,9-trioxaundecane (**3**) (33.0 g, 135 mmol) and 250 mL of 0.7 M H<sub>3</sub>PO<sub>4</sub> were placed in a 1 L round bottom flask and cooled to 0°C using an ice bath while stirring. A solution of triphenylphosphine (PPh<sub>3</sub>) (29.0 g, 110 mmol) in ether (250 mL) was slowly added via cannula and the temperature of the reaction was maintained below 5°C. Once addition was complete, the reaction mixture was warmed to room temperature and stirred under nitrogen for an additional 16 hours. The biphasic solution was separated and the aqueous layer was washed with ether (3 × 100 mL). Potassium hydroxide (KOH) (30 g) was slowly added to the aqueous layer and cooled to 0°C overnight. The solution was filtered and the filtrate was basified with an additional 40 g of KOH and cooled to room temperature. The reaction mixture was extracted with CHCl<sub>3</sub> (4 × 75 mL) and the combined organic extracts were dried over MgSO<sub>4</sub>, filtered, and the solvent was evaporated to give 18.5 g of an oil with a slight yellow color. The monoamine transformation reaction has a yield of 63%. <sup>1</sup>H NMR (400 MHz, CDCl<sub>3</sub>):  $\delta$  (ppm) 3.57 (m, 10H, –OCH<sub>2</sub>CH<sub>2</sub>–), 3.40 (t, 2H, *J* = 5.2 Hz, –CH<sub>2</sub>CH<sub>2</sub>NH<sub>2</sub>), 3.29 (t, 2H, *J* = 5.0 Hz, –CH<sub>2</sub>N<sub>3</sub>), 2.75 (t, 2H, *J* = 5.2 Hz, –CH<sub>2</sub>CH<sub>2</sub>NH<sub>2</sub>).

#### 2.1.3. 5-([1,2]Dithiolan-3-yl)pentanoic acid-*N*-(3',6',9'-trioxaundecane-11'-azido)amide

Coupling of amino-terminated TEG to thioctic acid: TA-TEG-N<sub>3</sub>, compound **5**: thioctic acid (11.1 g, 53.8 mmol), 1-amino-11-azido-3,6,9-trioxaundecane (**4**) (11.2 g, 51.3 mmol), 4-dimethylaminopyridine (1.26 g, 10.3 mmol), and CH<sub>2</sub>Cl<sub>2</sub> (200 mL) were placed in a 500 mL round bottom flask, cooled to 0°C and stirred under N<sub>2</sub> atmosphere. *N,N'*-Dicyclohexylcarbodiimide (DCC) (11.1 g, 53.8 mmol) was slowly added and reaction mixture was stirred at 0°C for 2 hours, then warmed to room temperature and stirred for an additional 16 hours. The reaction mixture was filtered over a plug of celite and rinsed with EtOAc. The filtrate was evaporated and the crude material was purified by flash column chromatography (CHCl<sub>3</sub> : MeOH 97 : 3 as the eluent) to give 11.7 g (yield of 56%) of a yellow oil. <sup>1</sup>H NMR (400 MHz, CDCl<sub>3</sub>):  $\delta$  (ppm) 6.15 (m, 1H, CO–NH), 3.50–3.62 (m, 11H,



–OCH<sub>2</sub>CH<sub>2</sub>– and CH), 3.47 (t, 2H, *J* = 5.0 Hz, CO–NH–CH<sub>2</sub>CH<sub>2</sub>O–), 3.36 (t, 2H, *J* = 5.5 Hz, CO–NH–CH<sub>2</sub>–), 3.31 (t, 2H, *J* = 5.0 Hz, –CH<sub>2</sub>N<sub>3</sub>), 2.98–3.13 (m, 2H, CH<sub>2</sub>), 2.32–2.42 (m, 1H, CH), 2.10 (t, 2H, *J* = 7.4 Hz, –CH<sub>2</sub>–CO–NH–), 1.77–1.87 (m, 1H, CH), 1.50–1.68 (m, 4H, CH<sub>2</sub>), 1.30–1.45 (m, 2H, CH<sub>2</sub>).

#### 2.1.4. 5-([1,2]Dithiolan-3-yl)pentanoic acid-*N*-(3'6'9'-trioxaundecane-11-amino)amide

Transformation to amine-terminated TA-TEG, compound **6**: compound **5** (11.0 g, 27 mmol) was dissolved in THF (150 mL) in a 300 mL round bottom flask fitted with a condenser and nitrogen inlet. PPh<sub>3</sub> (15.0 g, 81 mmol) was added and the reaction was heated to reflux for 20 hours. The reaction mixture was cooled to room temperature and diluted with 15 mL of water and stirred for an additional 20 hours. The solvent was evaporated and the crude product was purified by flash column chromatography. Unreacted PPh<sub>3</sub> and triphenylphosphine oxide were removed with CHCl<sub>3</sub> and the eluent was switched to CHCl<sub>3</sub> : MeOH : Et<sub>3</sub>N (45 : 45 : 10) to collect the desired product. Removal of the solvent gave 9.0 g (yield of 88%) of gelatinous yellow oil. <sup>1</sup>H NMR (400 MHz, methanol-*d*<sub>4</sub>): δ (ppm) 3.41–3.59 (m, 12H, –OCH<sub>2</sub>CH<sub>2</sub>–), 3.26 (t, 2H, *J* = 5.1 Hz, –CO–NH–CH<sub>2</sub>–), 3.22 (m, 1H, CH–), 2.97–3.12 (m, 2H, CH<sub>2</sub>), 2.71 (t, 2H, *J* = 5.3 Hz, –CH<sub>2</sub>CH<sub>2</sub>–NH<sub>2</sub>), 2.32–2.42 (m, 1H, CH), 2.12 (t, 2H, *J* = 7.4 Hz, –CH<sub>2</sub>–CO–NH–), 1.75–1.85 (m, 1H, CH), 1.47–1.69 (m, 4H, CH<sub>2</sub>), 1.29–1.44 (m, 2H, CH<sub>2</sub>).

#### 2.1.5. TA-TEG-Biotin (7)

Biotinyl-*N*-hydroxysuccinimide was first prepared following the synthetic procedure previously reported [14–16]. Compound **6** (2.3 g, 6.0 mmol), biotinyl-*N*-hydroxysuccinimide (2.05 g, 6.0 mmol) were dissolved in DMF (50 mL) and stirred at room temperature under N<sub>2</sub> atmosphere. Et<sub>3</sub>N (3.0 g, 30 mmol) was added dropwise via syringe and the reaction was stirred for 16 hours. The solvent was evaporated under reduced pressure and the yellow residue was purified by flash column chromatography (using CHCl<sub>3</sub> : MeOH 95 : 5 as the eluent). The solvent was evaporated to give 3.1 g (a yield of 85%) of viscous yellow oil. <sup>1</sup>H NMR (400 MHz, CDCl<sub>3</sub>): δ (ppm) 6.79 (m, 1H, CO–NH), 6.59 (m, 1H, CO–NH), 6.49 (s, 1H, biotin CO–NH), 6.02 (s, 1H, biotin CO–NH), 4.41 (m, 1H, biotin CO–NH–CH), 4.22 (m, 1H, biotin CO–NH–CH), 3.52 (m, 9H, –OCH<sub>2</sub>CH<sub>2</sub>– and CH), 3.45 (m, 4H, CO–NH–CH<sub>2</sub>CH<sub>2</sub>O–), 3.30 (m, 4H, CO–NH–CH<sub>2</sub>), 2.96–3.10 (m, 3H, CH<sub>2</sub> and CH–S), 2.76–2.83 (m, 1H, CH–S), 2.65 (d, 1H, *J* = 12.8 Hz, CH–S), 2.30–2.40 (m, 1H, CH), 2.11 (m, 4H, NH–CO–CH<sub>2</sub>), 1.75–1.85 (m, 1H, CH), 1.45–1.68 (m, 8H, CH<sub>2</sub>), 1.26–1.42 (m, 4H, CH<sub>2</sub>).

#### 2.1.6. DHLA-TEG-biotin (8)

Compound **7** (2.0 g, 3.3 mmol) was dispersed in a mixture of ethanol (40 mL) and water (20 mL) while stirring in a 125 mL flask. NaBH<sub>4</sub> (700 mg, 18.5 mmol) was slowly added and the solution was stirred at room temperature for 4 hours. The

reaction mixture was diluted with water (200 mL) and extracted with CHCl<sub>3</sub> (4 × 50 mL), dried over MgSO<sub>4</sub>, filtered, and the solvent was evaporated. The crude product was purified by flash column chromatography (CHCl<sub>3</sub> : MeOH 95 : 5 as the eluent) to give 1.53 g (a yield of 77%) of colorless viscous oil. <sup>1</sup>H NMR (400 MHz, CDCl<sub>3</sub>): δ (ppm) 6.96 (m, 1H, CO–NH), 6.69 (m, 1H, CO–NH), 6.63 (s, 1H, biotin CO–NH), 6.03 (s, 1H, biotin CO–NH), 4.37 (m, 1H, biotin CO–NH–CH), 4.18 (m, 1H, biotin CO–NH–CH), 3.50 (m, 8H, –OCH<sub>2</sub>CH<sub>2</sub>–), 3.42 (m, 4H, CO–NH–CH<sub>2</sub>CH<sub>2</sub>O–), 3.29 (m, 4H, CO–NH–CH<sub>2</sub>), 2.96–3.06 (m, 1H, CH–S), 2.70–2.84 (m, 2H, CH–S and CH–SH), 2.46–2.66 (m, 3H, CH–S and CH<sub>2</sub>–SH), 2.07 (m, 4H, NH–CO–CH<sub>2</sub>), 1.71–1.83 (m, 1H, CH), 1.35–1.67 (m, 13H, CH<sub>2</sub>), 1.28 (t, 1H, *J* = 8.0 Hz, CH<sub>2</sub>–SH), 1.23 (d, 1H, *J* = 7.6 Hz, CH–SH).

## 2.2. Quantum dot synthesis and cap exchange

The CdSe–ZnS core-shell QD's used were synthesized using high-temperature reaction of organometallic precursors in a mixture of TOP/TOPO and alkylamine, as described in the literature [17–20]. Cap exchange of the TOP/TOPO-capped QD's with the newly synthesized ligands to achieve water solubility (a mixture of **1** and **8**, and a mixture of **2** and **8**) was carried out following procedures described previously [5, 12, 21]. For cap exchange with a mixture of **2** and **8**, ~50–300 mg of TOP/TOPO-capped QD's were precipitated using EtOH and the supernatant was discarded. To the precipitate ~0.5 mL in total of pure or mixed ligands and ~0.5 mL of EtOH were added. The mixture was then heated to 60 ~ 80°C while stirring for a period of 6 to 12 hours. Once homogenized, the sample was then precipitated out with mixtures of hexane, EtOH, and CHCl<sub>3</sub> (approximate ratio is 11 : 10 : 1, this ratio may vary from batch to batch); the precipitate was dispersed in water. The homogenized solution was further purified using 3 ~ 4 cycles of concentration/dilution with an ultrafree centrifugal filtration device (Millipore, *M<sub>w</sub>* cutoff ~50,000 Da) to remove excess ligands and other materials from the solution. Cap exchange with a mixture of **1** and **8** was done similarly though some modifications are required for purification steps. [21] DMF (~5 mL) was added to the reaction mixture after the solution was homogenized. The QD's were precipitated out by adding excess potassium *tert*-butoxide. The mixture was centrifuged and the supernatant was discarded. The precipitate was dispersed in water and the homogenized solution was further purified as described above.

## 2.3. Gel electrophoresis

Samples were separated in agarose gels as described previously [22]. Briefly, samples were mixed with 30% glycerol, loaded into 1.5% agarose gels buffered with 1X Tris borate EDTA (TBE) in TBE running buffer (pH ~8.3) and run at 10 volts/cm for ~1 hour at ambient temperature. The gel-shift bands were visualized using the QD photoluminescence collected on a Kodak 440 Digital Image Station (Rochester, NY, USA) equipped with a long-pass cutoff filter; samples were illuminated with UV light (365 nm excitation).

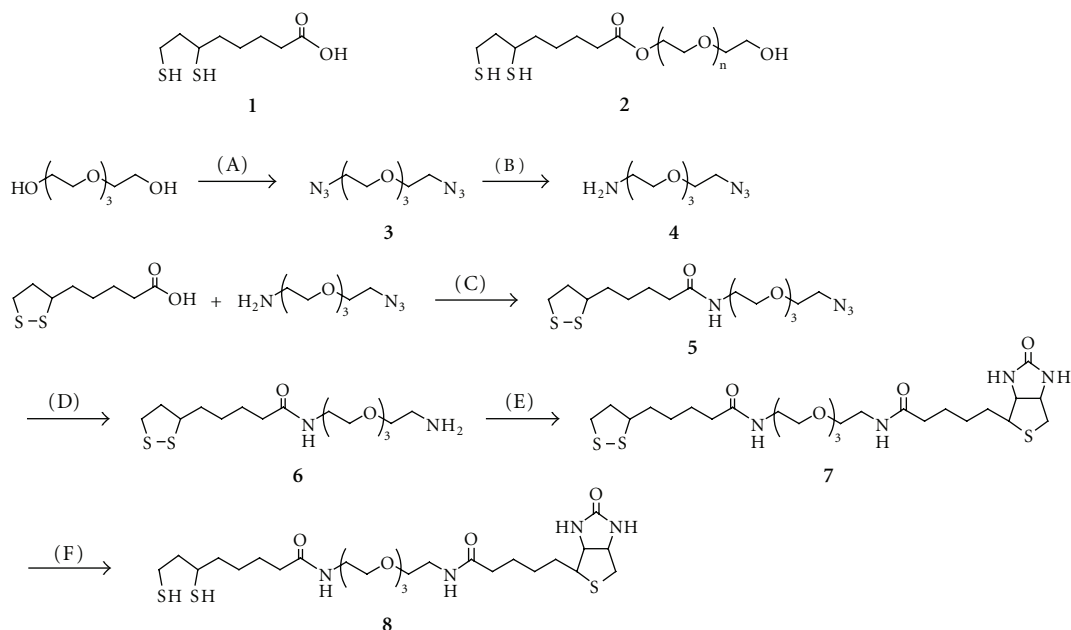


FIGURE 1: Chemical structures and synthetic routes of the surface ligands used in this study: (A) (i)  $\text{MsCl}$ ,  $\text{Et}_3\text{N}$ ,  $\text{THF}$ ,  $0^\circ\text{C} \rightarrow 20^\circ\text{C}$ , 20 hours; (ii)  $\text{NaN}_3$ ,  $\text{NaHCO}_3$ ,  $\text{H}_2\text{O}$ ,  $70^\circ\text{C}$ , 14 hours; (B)  $\text{PPh}_3$ ,  $0.7\text{ M H}_3\text{PO}_4$ ,  $\text{Et}_2\text{O}$ ,  $<5^\circ \rightarrow \text{room temperature}$ , 16 hours; (C)  $\text{DCC}$ ,  $\text{DMAP}$ ,  $\text{CH}_2\text{Cl}_2$ ,  $0^\circ\text{C}$ , 2 hour  $\rightarrow \text{room temperature}$ , 20 hours; (D)  $\text{PPh}_3$ ,  $\text{H}_2\text{O}$ ,  $\text{THF}$ , reflux, 20 hour  $\rightarrow \text{room temperature}$ , 20 hours; (E) Biotin *N*-hydroxysuccinimide ester,  $\text{Et}_3\text{N}$ ,  $\text{DMF}$ , room temperature, 16 hours; (F)  $\text{NaBH}_4$ ,  $\text{EtOH}$ ,  $\text{H}_2\text{O}$ , room temperature, 4 hours.

## 2.4. Surface binding assay

The binding capacity of NeutrAvidin-covered 96-well microtiter flat-bottom plates from Pierce Biotechnology is 60 picomoles of biotin per well. 100  $\mu\text{L}$  aliquots of QD samples (with the desired cap mixture at  $\sim 7\text{ pM}$  concentration) were added to the wells and let incubate overnight at room temperature. The fluorescence intensity was measured using a Tecan Safire Dual Monochromator Multifunction Microtiter Plate Reader (Tecan, Research Triangle Park, NC, USA), then plates were washed 3 times with 10 mM Na tetraborate buffer (pH 9) supplemented with 0.02% Tween and the fluorescence signal was measured again; 300 nm excitation line was used for all the samples. The remaining fluorescence intensities were calculated as approximate binding percentages. Those values were normalized by setting the highest binding percentage to 100%.

## 3. RESULTS AND DISCUSSION

The chemical structures and synthetic schemes of a few representative ligands (namely DHLA, DHLA-PEG600, and DHLA-TEG-biotin) and reaction steps involved are summarized in Figure 1. TEG was first transformed into diazide-terminated-TEG (3) using a two-step reaction with methanesulfonyl chloride and sodium azide. Monosubstitution of one azide into an amine group was carried out in biphasic acidic solution to improve the efficiency of selective formation of the monosubstituted product (4) [13]. Thioglutaric acid (TA) and  $\text{N}_3\text{-TEG-NH}_2$  (4) were coupled with

*N,N'*-dicyclohexylcarbodiimide (DCC) to provide azide-terminated compound 5. The terminal azido group of 5 was reduced with  $\text{PPh}_3$  and  $\text{H}_2\text{O}$  to obtain an amine-terminated TA-TEG ligand (Compound 6). Biotin-functionalized compound 7 was synthesized by coupling between 6 and Biotin *N*-hydroxysuccinimide ester. Finally, the terminal 1,2-dithiolane group in compound 7 was reduced with  $\text{NaBH}_4$  to obtain DHLA terminal group as a bidentate thiol anchoring unit.

We verified quality of the new compounds by collecting  $^1\text{H-NMR}$  spectra throughout the various steps employed. The  $^1\text{H-NMR}$  spectra show that TEG-modified compounds have large peaks around  $\sim 3.6\text{ ppm}$ , which are ascribed to  $\text{CH}_2$  groups of TEG chains. After coupling between 6 and biotin *N*-hydroxysuccinimide ester, new distinct multiplet peaks (2.6  $\sim$  2.9, 4.22, and 4.41 ppm) are measured in the NMR spectra, which were ascribed to biotin-ring protons. In addition, following reduction of the 1,2-dithiolane group with  $\text{NaBH}_4$ , new doublet and triplet peaks appeared at 1.23 and 1.28 ppm, respectively. These two peaks were assigned as thiol protons of DHLA unit (open dithiol) [12]. The observed changes in each collected spectrum indicate that each reaction step produced the desired compound.

We have previously shown that QD's capped with DHLA-PEG600 or DHLA-PEG1000 ligands can be dispersed in buffers with pH ranging between 5  $\sim$  12 [12]. However, cap exchange of TOP/TOPO with DHLA-TEG-biotin alone did not produce water-soluble QD's, a property attributable to the rather short TEG segment combined with the hydrophobic nature of the biotin group [12]. To achieve



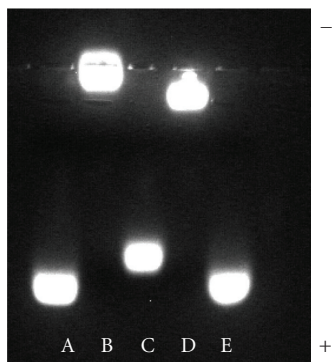


FIGURE 2: Gel shift of 510-nm emitting CdSe-ZnS QD's coated with different ligands in 1.5% agarose gel buffered with TBE buffer: (A,E) DHLA; (B) DHLA-PEG600; (C) DHLA : DHLA-TEG-Biotin (7 : 1); (D) DHLA-PEG600 : DHLA-TEG-Biotin (7 : 1).

water solubility using the new DHLA-TEG-biotin ligands (compound **8**), TOP/TOPO-capped QD's were instead dispersed (during cap exchange) with mixtures of ligand **8** and either DHLA (**1**) or DHLA-PEG600 (**2**). Rather low to modest DHLA-TEG-biotin ratios (5–25%) were used in the mixtures for cap exchange. In addition to promoting easy transfer into buffer solutions, this approach ensures that only controlled and low density of biotin groups are available on each QD. This should also allow control over the number of biological receptors coupled to a single QD and potentially biological activity of the QD-bioconjugates. In this particular study, we used a mixture of compound **1** and compound **8** (at 7 : 1 molar ratio), and a mixture of compound **2** and compound **8** (at 7:1 molar ratio) for the cap exchange.

In the first characterization experiment of the cap exchange, we monitored changes in the electrophoretic mobility of QD's (run on a 1.5% agarose gel) as a function of the capping mixture used. The gel image in Figure 2 shows a side-by-side comparison of the mobility shift of 510 nm emitting QD cap exchanged with either a mixture of DHLA : DHLA-TEG-biotin (7 : 1) (lane C) or a mixture of DHLA-PEG600 : DHLA-TEG-biotin (7 : 1) (lane D), together with control samples made of either QD's capped with DHLA (lanes A and E) or QD's capped with DHLA-PEG600 (lane B). The data clearly show that on the one hand QD's capped with only DHLA experienced the highest mobility shift (towards the positive electrode) in this series; this result is attributed to the presence of carboxyl groups on DHLA molecules, which can be deprotonated and negatively charged in basic buffer solutions. On the other hand, DHLA-PEG600-capped QD's showed no mobility shift under applied voltage (materials did not migrate from the loading well), indicating that these QD's are essentially neutral; water solubility for this sample is mainly promoted by hydrophilicity of the long PEG chains. In comparison, the gel shift of the QD with DHLA : DHLA-TEG-Biotin (7 : 1) was slightly lower than that of the DHLA-capped QD's, whereas QD's capped with DHLA-PEG600 : DHLA-TEG-Biotin (7 : 1) mixture showed a very small shift compared with DHLA-PEG600-capped QD's. For QD's capped with

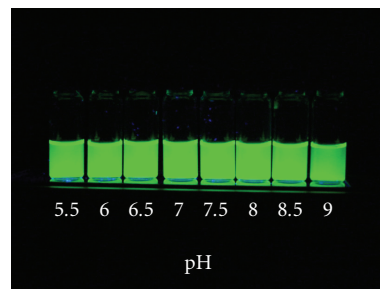


FIGURE 3: Luminescence image set of 540 nm emitting CdSe-ZnS QD with DHLA-PEG600 : DHLA-TEG-Biotin (4 : 1) at pH 5.5 ~ 9 in phosphate buffer saline at various pH values at room temperature. Samples were excited with a handheld UV lamp at 365 nm.

DHLA : DHLA-TEG-Biotin (7 : 1) mixture, partial occupation of the nanocrystal surface by DHLA-TEG-Biotin (compared with DHLA-capped QD's) has led to reduced number of charges per QD and thus small reduction in the gel mobility shift (lane C). The nonzero mobility shift (even though extremely small) measured for QD's capped with a mixture of DHLA-PEG600 : DHLA-TEG-Biotin may be due to a slight/partial charging of biotin or amide groups on the chain under applied voltage. Overall, the present gel electrophoresis data confirm that cap exchange of TOP/TOPO-capped QD's with a ligand mixture produced nanocrystals that have both types of capping ligands; furthermore, the overall relative proportions of each ligand used during cap exchange is preserved in the final QD samples.

Absorption and fluorescence spectra were measured for both the native TOP/TOPO-capped QD's in toluene and the new hydrophilic QD's capped with DHLA-TEG derivatives in H<sub>2</sub>O (data not shown). Absorption spectra measured before and after the cap exchange were essentially unchanged, though a few nm red shift of the lowest absorption maximum of the hydrophilic QD's was occasionally measured compared with that of QD's capped with TOP/TOPO ligands. The fluorescence spectra showed similar trends. These occasional small changes in the optical properties of QD's following transfer into aqueous solutions are commonly observed [1, 12, 23]. The fluorescence quantum yields of the water-dispersed QD's change from batch to batch. The quantum yields in aqueous solutions (after cap exchange and transfer) are ~50% of the original values measured for TOP/TOPO-capped QD's in organic solutions. The overall quantum yield of the hydrophilic QD's thus varies anywhere between 10–40%.

QD's cap-exchanged with mixture containing the new DHLA-TEG-biotin ligands were also stable and aggregate-free over extended periods of time (months). Figure 3 shows solutions of QD's capped with a mixture of compound **2** and compound **8** (7 : 1) in H<sub>2</sub>O of which pH ranged from 5.5 to 9. The new water-soluble QD's were stable and well dispersed in the wide pH range including acidic conditions. This feature is quite different from what we have observed for solutions

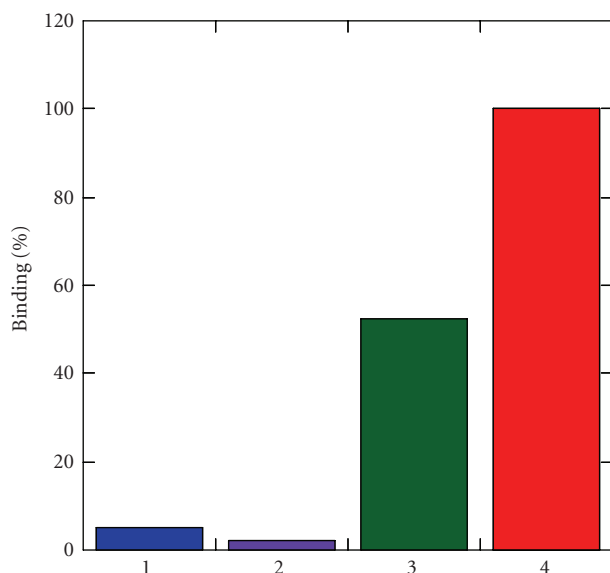


FIGURE 4: Surface binding plate assay of QD's with different surface ligands: (1) DHLA, (2) DHLA-PEG600, (3) DHLA : DHLA-TEG-Biotin (at 4 : 1 ratio), and (4) DHLA-PEG600 : DHLA-TEG-Biotin (at 4 : 1 ratio). 540 nm emitting QD's were used.

of QD's capped with either DHLA or mercaptoundecanoic acid (MUA). The DHLA- or MUA-capped QD solutions were well dispersed in aqueous basic media but showed aggregation and eventual precipitation at pH lower than 7 (data not shown), indicating that deprotonation of carboxyl groups is a crucial factor to solubilize those QD's in aqueous solutions. In contrast, appending a short PEG chain at the end of DHLA molecules extended the stability of QD capped with either 100% DHLA-PEG600 or a mixture of DHLA-PEG600 and Biotin-functionalized DHLA-TEG to acidic buffer solutions.

Once cap exchange with biotin-terminated DHLA-TEG and transfer into aqueous environment was successfully realized, targeted biological assays were carried out. The binding properties of QD's partially capped with biotin-terminated DHLA-TEG (**8**) were investigated for their ability to interact with NeutrAvidin-functionalized substrates [24]. NeutrAvidin, which is a deglycosylated form of avidin, was chosen due to its low nonspecific interactions (compared with avidin or streptavidin) while maintaining the strong binding affinity with biotin [24]. Following incubation of the NeutrAvidin-functionalized substrates with the QD samples, substrates were rinsed 3 times with borate buffer with Tween and the fluorescence signals were collected. Figure 4 shows the fluorescence intensities measured for 4 different QD solutions incubated with NeutrAvidin-coated plates: one capped with DHLA (**1**), one capped with DHLA-PEG600 (**2**), one capped with a mixture of **1** and DHLA-TEG-Biotin (**8**) (at 4 : 1 ratio), and one capped with a mixture of **2** and **8** (at 4 : 1 ratio). The data clearly show that only substrates incubated with QD's that were capped with a mixture of biotin-terminated DHLA-TEG produced a large signal-to-background fluorescence signal. In comparison, the substrates incubated with DHLA- or DHLA-PEG600-capped QD's produced only

background contribution to the signal. This result indicates that efficient and specific interactions between the biotin groups present on the QD surface and NeutrAvidin on the substrate drive the surface capture of the nanocrystals. It is important to note that the QD's capped with DHLA-TEG-biotin alone were, however, not dispersible in buffer solutions, a result we attribute to the poor water compatibility of biotin by itself and the short TEG. We are exploring the use of longer chain PEG segments for insertion between the dithiol group and biotin. This should make dispersion in buffer solution achievable even at high biotin fractions and promote strong interactions with NeutrAvidin. Those findings will be discussed in future reports.

#### 4. CONCLUSION

We have demonstrated simple and efficient synthetic procedures to prepare new biotin-functionalized ligands based on the DHLA motif and employing short TEG segment. The present synthetic route provided high quality and stable compounds, which were further employed to make biotin-functionalized luminescent QD's, using easy-to-implement cap exchange procedure. The new biotin-appended ligand mixed with either DHLA or DHLA-PEG600 effectively cap exchanged with the native TOP/TOPO and provided QD's that are water-soluble over extended periods of time and biologically active. QD's cap-exchanged with a mixture of DHLA-PEG600 (neutral) and DHLA-TEG-biotin showed specific interactions with NeutrAvidin in surface binding assays. The present synthetic methodologies of hydrophilic surface ligands and cap-exchange reactions promise access to a variety of biological entities. Further studies of these surface-functionalized QD's for coupling with a variety of bioreceptors and biological assays are in progress.

#### ACKNOWLEDGMENTS

The authors acknowledge NRL, Office of Naval Research (ONR), and the Army Research Office for financial support.

#### REFERENCES

- [1] M. Bruchez Jr., M. Moronne, P. Gin, S. Weiss, and A. P. Alivisatos, "Semiconductor nanocrystals as fluorescent biological labels," *Science*, vol. 281, no. 5385, pp. 2013–2016, 1998.
- [2] X. Gao, Y. Cui, R. M. Levenson, L. W. K. Chung, and S. Nie, "In vivo cancer targeting and imaging with semiconductor quantum dots," *Nature Biotechnology*, vol. 22, no. 8, pp. 969–976, 2004.
- [3] B. Dubertret, P. Skourides, D. J. Norris, V. Noireaux, A. H. Brivanlou, and A. Libchaber, "In vivo imaging of quantum dots encapsulated in phospholipid micelles," *Science*, vol. 298, no. 5599, pp. 1759–1762, 2002.
- [4] W. C. W. Chan and S. Nie, "Quantum dot bioconjugates for ultrasensitive nonisotopic detection," *Science*, vol. 281, no. 5385, pp. 2016–2018, 1998.
- [5] H. Mattoussi, J. M. Mauro, E. R. Goldman, et al., "Self-assembly of CdSe-ZnS quantum dot bioconjugates using an engineered recombinant protein," *Journal of the American Chemical Society*, vol. 122, no. 49, pp. 12142–12150, 2000.

- [6] Y. A. Wang, J. J. Li, H. Chen, and X. Peng, "Stabilization of inorganic nanocrystals by organic dendrons," *Journal of the American Chemical Society*, vol. 124, no. 10, pp. 2293–2298, 2002.
- [7] I. L. Medintz, A. R. Clapp, H. Mattoussi, E. R. Goldman, B. R. Fisher, and J. M. Mauro, "Self-assembled nanoscale biosensors based on quantum dot FRET donors," *Nature Materials*, vol. 2, no. 9, pp. 630–638, 2003.
- [8] A. R. Clapp, I. L. Medintz, J. M. Mauro, B. R. Fisher, M. G. Bawendi, and H. Mattoussi, "Fluorescence resonance energy transfer between quantum dot donors and dye-labeled protein acceptors," *Journal of the American Chemical Society*, vol. 126, no. 1, pp. 301–310, 2004.
- [9] A. R. Clapp, I. L. Medintz, and H. Mattoussi, "Förster resonance energy transfer investigations using quantum-dot fluorophores," *ChemPhysChem*, vol. 7, no. 1, pp. 47–57, 2006.
- [10] F. Patolsky, R. Gill, Y. Weizmann, T. Mokari, U. Banin, and I. Willner, "Lighting-up the dynamics of telomerization and DNA replication by CdSe-ZnS quantum dots," *Journal of the American Chemical Society*, vol. 125, no. 46, pp. 13918–13919, 2003.
- [11] J. B. Delehanty, I. L. Medintz, T. Pons, F. M. Brunel, P. E. Dawson, and H. Mattoussi, "Self-assembled quantum dot-peptide bioconjugates for selective intracellular delivery," *Bioconjugate Chemistry*, vol. 17, no. 4, pp. 920–927, 2006.
- [12] H. T. Uyeda, I. L. Medintz, J. K. Jaiswal, S. M. Simon, and H. Mattoussi, "Synthesis of compact multidentate ligands to prepare stable hydrophilic quantum dot fluorophores," *Journal of the American Chemical Society*, vol. 127, no. 11, pp. 3870–3878, 2005.
- [13] A. W. Schwabacher, J. W. Lane, M. W. Schiesher, K. M. Leigh, and C. W. Johnson, "Desymmetrization reactions: efficient preparation of unsymmetrically substituted linker molecules," *The Journal of Organic Chemistry*, vol. 63, no. 5, pp. 1727–1729, 1998.
- [14] S. H. Um, G. S. Lee, Y.-J. Lee, K.-K. Koo, C. Lee, and K. B. Yoon, "Self-assembly of avidin and D-biotin-tethering zeolite microcrystals into fibrous aggregates," *Langmuir*, vol. 18, no. 11, pp. 4455–4459, 2002.
- [15] N. Charvet, P. Reiss, A. Roget, et al., "Biotinylated CdSe/ZnSe nanocrystals for specific fluorescent labeling," *Journal of Materials Chemistry*, vol. 14, no. 17, pp. 2638–2642, 2004.
- [16] D. Tong, J. Yao, H. Li, and S. Han, "Synthesis and characterization of thermo- and pH-sensitive block copolymers bearing a biotin group at the poly(ethylene oxide) chain end," *Journal of Applied Polymer Science*, vol. 102, no. 4, pp. 3552–3558, 2006.
- [17] C. B. Murray, D. J. Norris, and M. G. Bawendi, "Synthesis and characterization of nearly monodisperse CdE (E = S, Se, Te) semiconductor nanocrystallites," *Journal of the American Chemical Society*, vol. 115, no. 19, pp. 8706–8715, 1993.
- [18] M. A. Hines and P. Guyot-Sionnest, "Synthesis and characterization of strongly luminescing ZnS-capped CdSe nanocrystals," *Journal of Physical Chemistry*, vol. 100, no. 2, pp. 468–471, 1996.
- [19] B. O. Dabbousi, J. Rodriguez-Viejo, F. V. Mikulec, et al., "(CdSe)ZnS core-shell quantum dots: synthesis and characterization of a size series of highly luminescent nanocrystallites," *Journal of Physical Chemistry B*, vol. 101, no. 46, pp. 9463–9475, 1997.
- [20] Z. A. Peng and X. Peng, "Formation of high-quality CdTe, CdSe, and CdS nanocrystals using CdO as precursor," *Journal of the American Chemical Society*, vol. 123, no. 1, pp. 183–184, 2001.
- [21] A. R. Clapp, E. R. Goldman, and H. Mattoussi, "Capping of CdSe-ZnS quantum dots with DHLA and subsequent conjugation with proteins," *Nature Protocols*, vol. 1, no. 3, pp. 1258–1266, 2006.
- [22] I. L. Medintz, L. Berti, T. Pons, et al., "A reactive peptidic linker for self-assembling hybrid quantum dot-DNA bioconjugates," *Nano Letters*, vol. 7, no. 6, pp. 1741–1748, 2007.
- [23] F. Pinaud, D. King, H.-P. Moore, and S. Weiss, "Bioactivation and cell targeting of semiconductor CdSe/ZnS nanocrystals with phytochelatin-related peptides," *Journal of the American Chemical Society*, vol. 126, no. 19, pp. 6115–6123, 2004.
- [24] G. T. Hermanson, *Bioconjugate Techniques*, Academic Press, San Diego, Calif, USA, 1996.

Since their introduction into biology as imaging agents in 1998 [16, 17], qdots have increasingly found applications as fluorescent probes in biology. To be useful as fluorescent probes in biological systems, qdots must be soluble in water and commonly used buffers. Additionally, they must have colloidal stability and low nonspecific adsorption to cellular membranes. These properties have been achieved using a number of techniques, including encapsulation in micelles [18], silanization [19], encapsulation in amphiphilic polymers [20, 21], and encapsulation in proteins such as streptavidin [22]. To further reduce nonspecific adsorption to cellular membranes, a number of techniques may be used to modify the surface chemistry of qdots. For example, we have recently demonstrated that nonspecific binding can be significantly reduced by attaching polyethylene glycol chains (i.e., by PEGylating) qdots coated in an amphiphilic modified polyacrylic acid polymer (AMP) [23]. The length of the PEG chain and the PEG loading were demonstrated to be important in reducing nonspecific adsorption to cellular



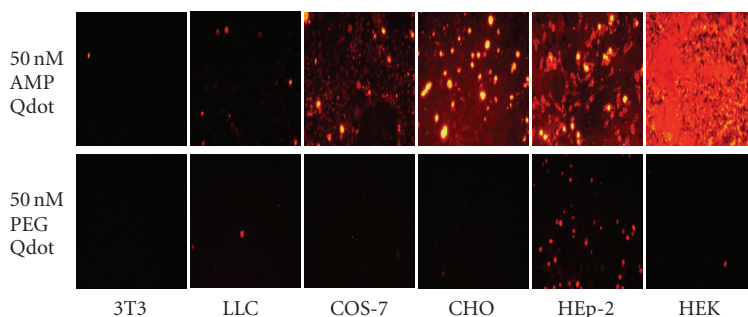


FIGURE 1: A comparison of nonspecific adsorption of AMP-coated qdots to the surfaces of 6 different cell types. These experiments employed AMP-coated qdots that were either unconjugated (upper row) or conjugated to PEG2000 (lower row).

membranes. When PEGs with short (less than 12) repeat units were conjugated to qdots, a small reduction in nonspecific adsorption to cellular membranes was observed. This reduction increased in magnitude when larger PEGs were used. Figure 1 shows the effects of PEGylation (PEG2000) on nonspecific adsorption to 6 different cell types. These cells were treated with a 50 nM solution of PEGylated AMP-coated qdots or a 50 nM solution of AMP-coated qdots. A significant reduction in nonspecific adsorption to cellular membranes was obtained by the addition of PEG2000. The nonspecific adsorption is cell-type specific, as can be seen in the relatively low nonspecific adsorption of AMP-coated qdots to the surfaces of 3T3 cells compared to the high levels of nonspecific adsorption to HEK cells.

In addition to surface modification techniques such as PEGylation, a wide variety of biologically active molecules have been attached to qdots, including proteins [24–31], peptides [32–34], DNA [35–43], RNA [44], peptide nucleic acid (PNA) [45], cytokines [46], viruses [47], and antibodies [48–54]. The qdots-based imaging applications that have been reported in the literature are extensive and encompass a wide variety of imaging applications. Of these, live cell imaging [51] and whole animal imaging [52] have received a great deal of interest. In addition to qdots that emit in the visible region of the electromagnetic spectrum, near-infrared qdots have been developed that have a cadmium telluride core instead of a cadmium selenide core. These near-IR dots have found applications in the clinic as tools for imaging sentinel lymph nodes during surgery [53].

Our research efforts focus on the central nervous system. We are interested in using qdots that have been conjugated with small molecules [55–60], antibodies [61], and peptides [34] to image receptors and transporters in cell cultures, oocytes, and, ultimately, neurons. In our early work, we used qdots to image the serotonin transporter (SERT) using PEGylated serotonin ligands [62] attached to the surfaces of qdots via an acid-base interaction (see Figure 2). These conjugates antagonized the serotonin transporter protein (SERT) with an  $IC_{50}$  of 115  $\mu$ M in transfected HEK-293 cells. Using these conjugates we were able to image SERT expressed in HEK-293 cells [55].

Numerous biofunctionalization methods for qdots have been reported in recent years. Qdot preparations that con-

tain an amphiphilic coating on the qdots surface are commercially available, and a variety of methodologies, including those involving sulfo-SMCC [63] and adaptor proteins [64], have been used to conjugate ligands to the coated qdot. Our current strategy uses commercially available qdots that have either an amphiphilic coating (AMP) on the surface of the dots, or AMP qdots with an additional coating of streptavidin. PEGylated ligands may be attached to the surface of these dots using two different methodologies. Either they may be covalently attached to the AMP coating using 1-[3-(dimethylamino)propyl]-3-ethylcarbodiimide hydrochloride (EDC) coupling chemistry, or a biotinylated derivative of the biologically active ligand may be attached to the surface of streptavidin-coated qdots via a streptavidin-biotin interaction. Using the PEGylated ligand approach, we have synthesized a novel qdot conjugate and tested its binding activity to the GABA<sub>C</sub> receptor, a ligand-gated ion channel that is found in retina and other central nervous system tissue and that is activated *in vivo* by  $\gamma$ -aminobutyric acid (GABA). Specifically, we have investigated a PEG derivative of muscimol, a known agonist of both GABA<sub>C</sub> and GABA<sub>A</sub> receptors (see Figure 3). Multiple copies of this ligand have been conjugated to the surface of AMP-coated qdots and used to image GABA<sub>C</sub> receptors expressed in *Xenopus laevis* oocytes [65].

## 2. METHODOLOGY

Streptavidin-coated qdots and AMP-coated qdots with maximum emissions of 605 and 585 nm were obtained from Invitrogen (Carlsbad, Calif, USA). *N*-Hydroxy urea, dimethyl acetylenedicarboxylate, 1,5-diazabicyclo[5.4.0] undec-7-ene (DBU), borane dimethyl sulfide, and *N*-hydroxy succinimide (NHS) were obtained from Sigma-Aldrich (St. Louis, Mo, USA). Trifluoroacetic acid (TFA), potassium hydroxide, and hydrazine monohydrate were obtained from VWR (West Chester, Pa, USA). All reagents were used without further purification. Borate buffer was obtained from PolySciences, Inc. (Warrington, Pa, USA), and Sephadex G-50 was obtained from Amersham Biosciences (Uppsala, Sweden). *t*-Butyloxycarbamate (BOC)-protected *N*-hydroxy succinimide-activated PEG3400 ester (BOC-PEG-NHS) was obtained from Nektar Therapeutics (Huntsville, Ala, USA).

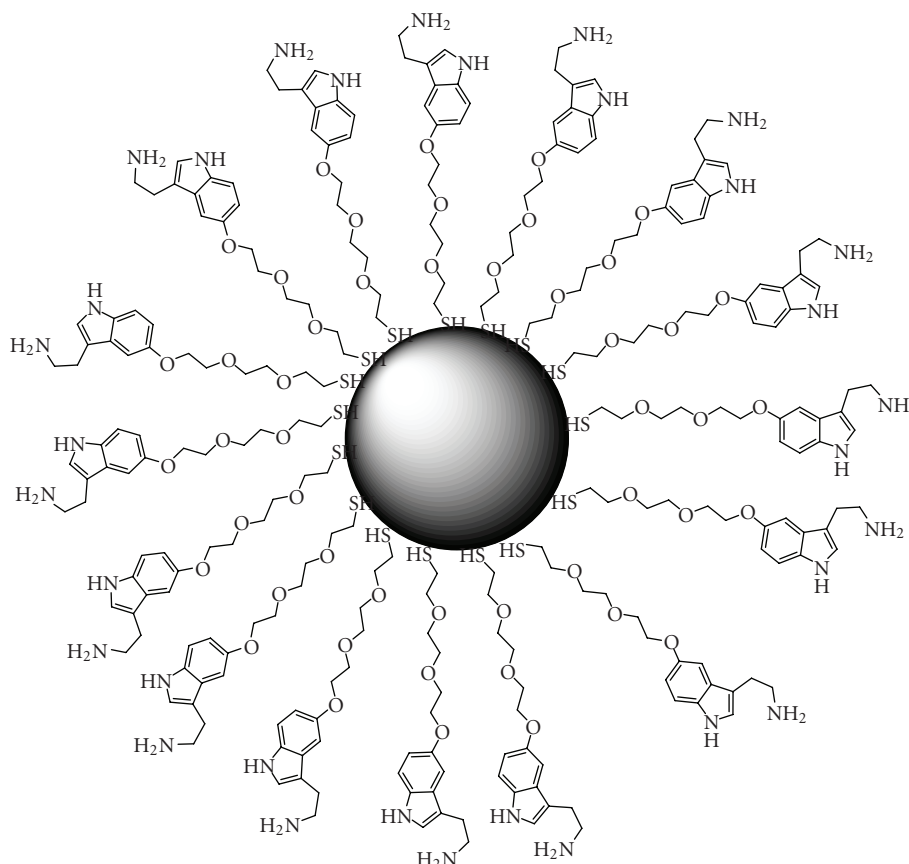
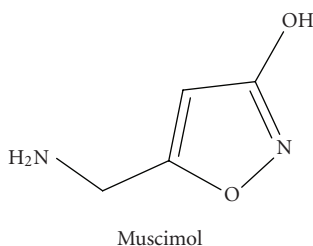


FIGURE 2: Serotonin-coated qdots used to label SERT-expressing cells.

FIGURE 3: Muscimol, a GABA<sub>C</sub> and GABA<sub>A</sub> receptor agonist.

## 2.1. Synthesis of the muscimol ligand

Muscimol was synthesized using the method described by Frey and Jäger [66]. This was then coupled to the PEG linker via an aminohexanoyl NHS ester to give the PEGylated muscimol ligand. The ligand was characterized by matrix-assisted laser desorption/ionization time-of-flight (MALDI-TOF) mass spectroscopy and conjugated to AMP-coated qdots via an EDC coupling.

### 2.1.1. Muscimol synthesis

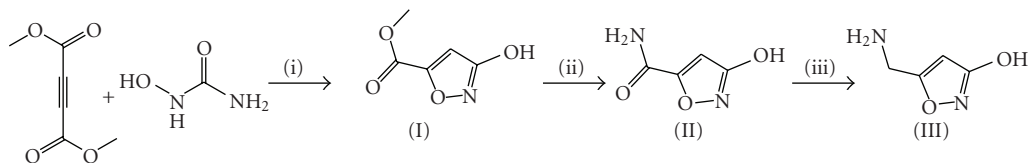
Muscimol was synthesized using the synthetic methodology shown in Scheme 1. Dimethyl acetylenedicarboxylate (3.1 mL) was added dropwise to a solution of *N*-hydroxy urea

(1.9 g, 25 mmols) and DBU (4.19 g, 28 mmols) in methanol (25 mL) at 0°C. The resulting solution was stirred at 0°C for 10 minutes, and then evaporated under reduced pressure. Concentrated hydrochloric acid was added until a pH of 1 was obtained. This solution was extracted with diethyl ether, dried over magnesium sulfate, filtered, and then evaporated. The resulting solid was recrystallized from methylene chloride to yield 1.1 g of methyl 3-hydroxy isoxazole-5-carboxylate (I) in a 32% yield. This was converted to (II) by stirring 0.84 g of (I) in ammonium hydroxide (3 mL) and methanol (3 mL) for 1 hour, followed by recrystallization from ethanol to give 0.75 g of 3-hydroxyisoxazole-5-carboxamide (II) in 88% yield as the ammonium salt. Muscimol (III) was obtained from 1 g of (II) by reduction with borane dimethyl sulfide in tetrahydrofuran (THF) to give 0.2 g of (III) in a 22% yield after purification by ion exchange chromatography.

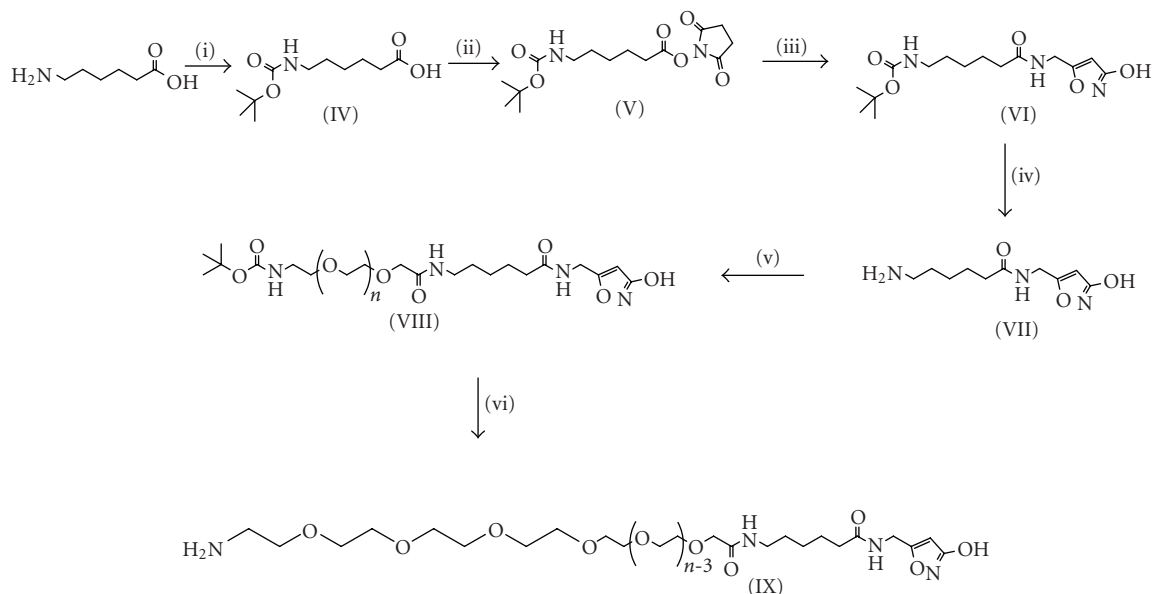
### 2.1.2. Synthesis of PEGylated muscimol ligand

The synthetic route used to synthesize the PEGylated muscimol ligand is shown in Scheme 2. Initially, the aminohexanoyl spacer was synthesized by reacting 6-amino hexanoic acid with <sup>t</sup>BOC anhydride in methanol to give 6-(*tert*-butoxycarbonylamino)hexanoic acid (IV) in a 58% yield. This was converted to 2,5-dioxopyrrolidin-1-yl





SCHEME 1: Synthesis of Muscimol: (i) DBU, (ii)  $\text{NH}_3$ , and (iii)  $\text{BH}_3$ .



SCHEME 2: Synthesis of muscimol ligand: (i) BOC anhydride, (ii) NHS, DCC, (iii) Muscimol, (iv) TFA, (v) BOC-PEG3400-NHS, and (vi) TFA.

6-(*tert*-butoxycarbonylamino)hexanoate (V) by reacting (IV) with NHS in the presence of dicyclo carbodiimide (DCC). The product was recrystallized from ether/hexanes resulting in a 38% yield of (V). This was coupled to muscimol in pyridine to give *tert*-butyl 6-((3-hydroxyisoxazol-5-yl)methylamino)-6-oxahexylcarbamate (VI) in a 54% yield. The BOC protecting group was removed using TFA to give 6-amino-*N*-((3-hydroxyisoxazol-5-yl)methyl)hexanamide (VII) in a 100% yield. This was coupled to <sup>1</sup>BOC protected PEG3400 NHS ester to give (VIII) in 100% yield. The BOC protecting group was removed using TFA to give (IX).

### 2.1.3. MALDI-TOF mass spectroscopy

Compounds (VIII) and (IX) were characterized by MALDI-TOF mass spectroscopy (Applied Biosystems Voyager mass spectrometer equipped with a 337 nm nitrogen laser) using an acceleration voltage of 25 kV, and the spectra were obtained by averaging of 30–64 scans [65]. The samples were prepared using a saturated matrix stock solution, consisting of 2,5-dihydroxybenzoic acid and 0.01 M sodium iodide dissolved in methanol. The PEG derivatives (VIII) and (IX) were prepared (5 mM) in methanol. The sample was added to the matrix by mixing the sample and stock solutions in a 2 : 5 : 2 ratio of sample to matrix to salt

(v/v). A 1- $\mu\text{L}$  aliquot of each sample solution was placed on the sample plate. Mass calibration of the instrument employed a PEG standard, and was prepared using the same protocol as that employed for the other samples. Analysis of the resulting spectra indicated that compounds (VIII) and (IX) were polydisperse. Compound (VIII) exhibited masses ranging from 3241 Da to 4188 Da (indicative of muscimol conjugation to PEGs of different lengths), and a primary peak at 3726 Da. The treatment of (VIII) with TFA to yield compound (IX) resulted in a MALDI-TOF spectrum shift of 100 Da (primary peak at 3626 Da), consistent with loss of the BOC protecting group.

### 2.1.4. Ligand conjugation

The ligand was conjugated to qdots using an EDC coupling in which 1000 equivalents of ligand were mixed with 750 equivalents of NHS and EDC in borate buffer at pH 8.5. To this was added a solution of AMP-coated qdots (8.4  $\mu\text{M}$ ). This mixture was stirred for 1 hour at ambient temperature. Unbound ligand was removed by Sephadex G-50 chromatography. The coupling of amino-terminated PEG2000 to AMP-coated qdots using EDC has been studied in an earlier publication, and the efficiency of coupling has been reported to be ~20% when 2000 equivalents of methoxy-terminated

aminoPEG2000 are reacted with 1 equivalent of AMP-coated qdots [23]. Since the terminating muscimol of the present ligand is attached to PEG3400, the coupling efficiency is likely to be similar. On this basis, we estimate the number of muscimol ligands to be around 150–200 per qdot [65]. The derivatized qdots were characterized by electrophoresis in 1% agarose gel (see Figure 4). The gel demonstrates that the muscimol-conjugated qdots (Lane 3), as well as qdots conjugated with PEG2000 (Lane 4), have a wide distribution in the number of ligands attached to their surface, as they streak on the gel more than unconjugated qdots (Lane 2). It is important to note that mobility in the gel does not depend merely on mass, but rather on mass-to-charge ratio. Thus, despite the substantial difference in mass of the PEG2000 versus the muscimol-terminated PEG3400 ligand, the bands representing the qdots conjugates that contain (numerous copies of) these ligands exhibit similar mobilities (Lanes 3 and 4). The present experimental conditions (1% agarose gel) do not separate protein standards that span a molecular weight range of 10–250 kDa (data not shown).

## 2.2. Oocyte imaging

The oocytes used in this study were obtained from adult female *X. laevis* toads. The oocytes were stored in physiological saline (Ringer solution; 100 mM NaCl, 2 mM KCl, 2 mM CaCl<sub>2</sub>, 1 mM MgCl<sub>2</sub>, 10 mM glucose, and 5 mM HEPES, pH 7.4). Using previously reported procedures, we expressed GABA<sub>C</sub> receptors (human  $\rho 1$  and perch  $\rho 1B$ ) in *X. laevis* oocytes [67, 68]. cRNA (50 nL) for each of the receptor subunits was injected into the oocyte, and the oocytes were assayed after 18–72-hour incubation in Ringer solution containing 0.1 mg/mL gentamycin at 16–19°C to allow for expression of the GABA<sub>C</sub> receptors. Oocyte imaging was carried out in a glass-bottom dish into which GABA<sub>C</sub> expressing oocytes and oocytes that did not express GABA<sub>C</sub> were placed. These oocytes were incubated for 5–10 minutes in a drop (~25  $\mu$ L) of solution containing either 34 nM AMP-coated qdots conjugated to the muscimol ligand, or 34 nM AMP-coated qdots that lacked conjugated muscimol ligand. The oocytes were then imaged using a confocal microscope (Leica model DM-IRE2 with 20x objective) with excitation at 476 nm, and with detection of fluorescence emission over a wavelength range (580–620 nm) that included the qdot emission peak (605 nm). At the beginning of experiments conducted on a given day, we established microscope settings relevant to excitation illumination and detection of fluorescence emission (gain and offset) with use of either a human  $\rho 1$  GABA<sub>C</sub>-expressing or perch  $\rho 1B$  GABA<sub>C</sub>-expressing oocyte incubated with 34 nM muscimol-conjugated AMP-coated qdots. These settings were maintained without change for the entire day's measurements [65].

## 3. RESULTS

### 3.1. Labeling of GABA<sub>C</sub>-expressing oocytes with muscimol-conjugated qdots

Figure 5 shows the binding of muscimol-conjugated AMP-coated qdots and unconjugated AMP-coated qdots to oocytes

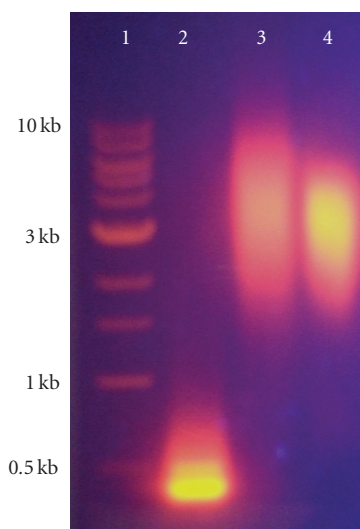


FIGURE 4: Agarose gel electrophoresis of qdots conjugates (1% agarose gel; Tris-acetate-EDTA buffer containing ethidium bromide for DNA visualization; 80 V potential difference). A 1-kb DNA ladder (Lane 1; New England Biolabs, Ipswich, Mass, USA), with DNA fragments ranging from 0.5–10 kilobases (kb) as indicated, was utilized to illustrate relative electrophoretic mobility of the qdot conjugates. Unconjugated AMP-coated qdots (Lane 2) have an increased mobility by comparison with both muscimol-conjugated qdots (Lane 3) and qdots conjugated with methoxy terminated PEG2000 (Lane 4), indicating successful functionalization of the qdot surface.

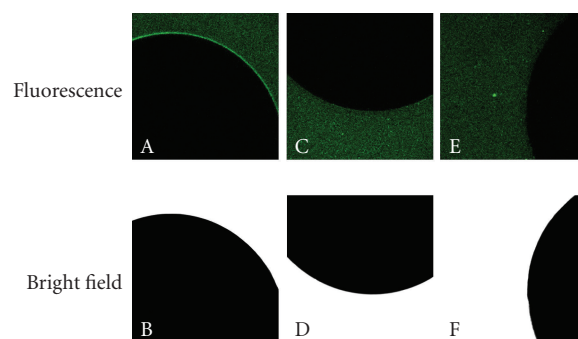


FIGURE 5: Fluorescence images (top row) and bright-field images (bottom row) of oocytes incubated with qdot-containing compounds for 10 minutes. The bright-field images illustrate the plane of focus of the opaque oocyte. Panels A and B show results from a human  $\rho 1$  GABA<sub>C</sub>-expressing oocyte incubated with 34 nM muscimol-conjugated AMP-coated qdots. Panels C and D show a human  $\rho 1$  GABA<sub>C</sub>-expressing oocyte incubated with a 34 nM solution of unconjugated AMP-coated qdots. Panels E and F show a nonexpressing oocyte incubated with 34 nM muscimol-conjugated AMP-coated qdots. Adapted from Gussin et al. [65].

expressing the human  $\rho 1$  GABA<sub>C</sub> receptor, and to non-expressing control oocytes (see Figure 5 legend). When GABA<sub>C</sub>-expressing oocytes were incubated with a 34 nM solution of muscimol-conjugated dots for 10 minutes, a fluorescent halo was observed at the oocyte surface membrane

(panel A). The intensity of this halo exceeded that of the surrounding extracellular medium. The fluorescent image can be compared with the corresponding bright-field image (panel B), which shows the position and focus of the oocyte. By comparison with panel A, no fluorescence halo was observed upon similar incubation of a  $\rho 1$  GABA<sub>C</sub>-expressing oocyte with AMP-coated qdots, that is, with a structure that lacked muscimol (panel C). Halo fluorescence of the oocyte surface membrane was also absent when a nonexpressing oocyte was incubated with 34 nM muscimol-conjugated dots (panel E). These results indicate that the muscimol ligand is necessary for binding of the conjugate to the oocyte surface membrane.

As noted in Section 2.1.4, the muscimol-conjugated AMP-coated qdot preparation used in the oocyte imaging experiments contained ~150–200 muscimol-terminated chains per qdot. In some preparations (not illustrated) of these muscimol-conjugated AMP-coated qdots, the extracellular medium surrounding the oocytes exhibited aggregation of the fluorescent particles. In developing the method of preparation of the conjugate, we observed that if 2000 equivalents of the muscimol ligand were reacted with AMP-coated qdots in the presence of 1500 equivalents of EDC and NHS, aggregates formed that subsequently precipitated from solution. It is likely that this aggregation is due to hydrogen bonding between muscimol ligands on adjacent qdots. The size and solubility of these aggregates likely depended on the number of ligands conjugated to the qdots.

### 3.2. Image analysis

To quantify the extent of binding of muscimol-conjugated AMP-coated qdots to the oocytes, we analyzed the surface membrane and extracellular regions of a given fluorescence image [65]. Using MetaMorph software (Offline Version 6.3r0; Universal Imaging Corp., Downingtown, Pa, USA), we determined the intensities of pixels underlying a multisegmented line that traced the arc-like border of the oocyte (15–25 straight-line segments; 450–750 pixels), and tabulated the resulting pixel values in relation to a 0–255 gray scale. We similarly determined the intensities of pixels that corresponded with an identical multisegment line constructed within the extracellular region of the image; tabulated intensities for this control extracellular region were taken as a measure of background (i.e., surround) fluorescence. For the image shown in Figure 5A, fluorescence intensities determined for the halo (henceforth termed “border”) at the oocyte surface membrane and the surrounding extracellular medium (background) were  $67.31 \pm 36.79$  (mean  $\pm$  SD) and  $22.30 \pm 21.18$ , respectively. As reported by Gussin et al. [65], results obtained in experiments similar in design to that described in Figures 5A, 5B (human  $\rho 1$  GABA<sub>C</sub>-expressing oocytes; incubation with 34 nM muscimol-conjugated dots) indicated a border fluorescence of  $88.84 \pm 64.84$  and a background fluorescence of  $31.60 \pm 35.50$  ( $n = 11$ ), respectively. Additional experiments of the same design (not illustrated), conducted on oocytes expressing the perch  $\rho 1B$  receptor [65], yielded border and background fluorescence intensities of  $109.58 \pm 58.42$  and  $18.54 \pm 16.47$  ( $n = 4$ ), respec-

tively. Aggregate results obtained in 4 experiments in which GABA<sub>C</sub>-expressing oocytes were incubated with unconjugated AMP-coated qdots (see Figures 5C, 5D) yielded border and background fluorescence intensities of  $15.79 \pm 23.18$  and  $13.13 \pm 18.17$ , respectively. Among 14 experiments that involved the incubation of 34 nM muscimol-conjugated dots with nonexpressing oocytes (see Figures 5E, 5F), border and background fluorescence intensities were  $15.14 \pm 22.35$  and  $16.78 \pm 22.17$ , respectively, [65]. Two-way ANOVA analysis of results obtained with the muscimol-conjugated AMP-coated qdots showed that for both human  $\rho 1$  GABA<sub>C</sub>-expressing and perch  $\rho 1B$  GABA<sub>C</sub>-expressing oocytes, the fluorescence intensity of the border differed significantly from that of the background. For nonexpressing oocytes incubated with the conjugate, there was no significant difference between border and background values. In addition, the treatment of GABA<sub>C</sub>-expressing oocytes with free (i.e., non-qdot-conjugated) GABA, muscimol, or PEGylated muscimol significantly reduced binding of the muscimol-qdots conjugate to the oocyte surface membrane (see Gussin et al. [65] for further details).

## 4. DISCUSSION

The primary finding of the experiments involving the incubation of muscimol-conjugated AMP-coated qdots with GABA<sub>C</sub>-expressing oocytes is that these conjugates exhibit specific binding at GABA<sub>C</sub> receptors. This binding depends on the presence of muscimol in the conjugate, as (unconjugated) AMP-coated qdots show no significant binding to oocytes expressing GABA<sub>C</sub> receptors. The approach described here builds on our earlier work with PEGylated serotonin attached to qdots in which we found that these conjugates exhibited binding at serotonin transporters expressed in HeLa and HEK cells. These findings indicate that it is possible to specifically label transporter proteins and ligand-gated receptors with qdots that have multiple copies of a membrane receptor or membrane transporter ligand attached through a PEG linker.

The presence of numerous copies of ligand in the muscimol-qdot conjugate described here raises the possibility that these conjugates bind to multiple GABA<sub>C</sub> receptors in a cross-linking fashion. Indeed, it is reasonable to hypothesize that the multiplicity of the muscimol ligand, as well as the length of the PEG linker that tethers each ligand to the qdot, favors such cross-linking. However, experiments conducted to date, while clearly establishing the ability of this conjugate to bind to cell-surface-expressed GABA<sub>C</sub> receptors, do not address the extent to which receptor cross-linking affects this binding activity. Other investigators have used fluorescent probes to track the diffusion dynamics of single receptors (single-particle tracking (SPT)), and such an SPT approach could be useful for evaluating the cross-linking activity of the present muscimol-qdot conjugate. For example, Dahan et al. [50] have examined the diffusion dynamics of glycine receptors in neuronal membranes by labeling the receptor with a conjugate consisting of a primary antireceptor antibody, biotinylated secondary antibody, and streptavidin-coated qdots. To test the extent

of receptor cross-linking by this conjugate, they investigated, as a comparison system, an Fab fragment of the primary antibody that had been linked to an organic fluorophore (Cy-3). Dahan et al. [50] found that the receptor dynamics determined with the qdot conjugate and the Cy-3-containing molecule were similar, indicating that neither the presence of the SA-qdots nor some other feature of the qdot-containing conjugate promoted significant receptor cross-linking. It should be emphasized that the structure of the presently described muscimol-qdot conjugate (see Figure 2) differs from the qdot-containing conjugate studied by Dahan et al. [50] in several respects, including the presence of a small-molecule ligand (muscimol) rather than an antibody as the receptor-reactive moiety, a high valency (copy number) of ligands per qdot, and a separation of each ligand from the qdot by a long linking chain (PEG3400). In future experiments, it may be possible to test for cross-linking by the muscimol-qdot conjugate using an approach in which GABA<sub>C</sub> receptor dynamics determined with the muscimol-qdots conjugate are compared with those determined using a structure optimized for SPT, for example, a fluorescent probe attached to a single receptor [26, 27].

## ACKNOWLEDGMENTS

Liz Bentzen and David Wright assisted in the studies of nonspecific binding of qdots shown in this paper. The authors thank Niraj J. Muni for the helpful discussions. This research was supported by Grants EY016094, EY13693, EY05494, EY01792, EB003728, EM72048, and AG028662 from the National Institutes of Health, grants from the Daniel F. and Ada L. Rice Foundation (Skokie, Ill, USA), the American Health Assistance Foundation (Clarksburg, Md, USA), and the CINN Foundation (Chicago, Ill, USA), and an unrestricted departmental award from Research to Prevent Blindness (NewYork, NY, USA). Dr. Pepperberg is a Senior Scientific Investigator of Research to Prevent Blindness.

## REFERENCES

- [1] A. Watson, X. Wu, and M. Bruchez, "Lighting up cells with quantum dots," *BioTechniques*, vol. 34, no. 2, pp. 296–303, 2003.
- [2] W. W. Yu, L. Qu, W. Guo, and X. Peng, "Experimental determination of the extinction coefficient of CdTe, CdSe, and CdS nanocrystals," *Chemistry of Materials*, vol. 15, no. 14, pp. 2854–2860, 2003.
- [3] A. Striolo, J. Ward, J. M. Prausnitz, et al., "Molecular weight, osmotic second virial coefficient, and extinction coefficient of colloidal CdSe nanocrystals," *Journal of Physical Chemistry B*, vol. 106, no. 21, pp. 5500–5505, 2002.
- [4] J. M. Tsay, M. Pflughoeft, L. A. Bentolila, and S. Weiss, "Hybrid approach to the synthesis of highly luminescent CdTe/ZnS and CdHgTe/ZnS nanocrystals," *Journal of the American Chemical Society*, vol. 126, no. 7, pp. 1926–1927, 2004.
- [5] J. Zheng, J. T. Petty, and R. M. Dickson, "High quantum yield blue emission from water-soluble Au<sub>8</sub> nanodots," *Journal of the American Chemical Society*, vol. 125, no. 26, pp. 7780–7781, 2003.
- [6] P. Yang, M. Lü, D. Xü, D. Yuan, and G. Zhou, "Photoluminescence properties of ZnS nanoparticles co-doped with Pb<sup>2+</sup> and Cu<sup>2+</sup>," *Chemical Physics Letters*, vol. 336, no. 1-2, pp. 76–80, 2001.
- [7] A. Agostiano, M. Catalano, M. L. Curri, M. Della Monica, L. Manna, and L. Vasanelli, "Synthesis and structural characterisation of CdS nanoparticles prepared in a four-components "water-in-oil" microemulsion," *Micron*, vol. 31, no. 3, pp. 253–258, 2000.
- [8] A. Schroedter, H. Weller, R. Eritja, W. E. Ford, and J. M. Wessels, "Biofunctionalization of silica-coated CdTe and gold nanocrystals," *Nano Letters*, vol. 2, no. 12, pp. 1363–1367, 2002.
- [9] J. McBride, J. Treadway, L. C. Feldman, S. J. Pennycook, and S. J. Rosenthal, "Structural basis for near unity quantum yield core/shell nanostructures," *Nano Letters*, vol. 6, no. 7, pp. 1496–1501, 2006.
- [10] M. Bäuml, D. Stamou, J.-M. Segura, R. Hovius, and H. Vogel, "Highly fluorescent streptavidin-coated CdSe nanoparticles: preparation in water, characterization, and micropatterning," *Langmuir*, vol. 20, no. 10, pp. 3828–3831, 2004.
- [11] X. Gao, L. Yang, J.A. Petros, J.W. Simons, and S. Nie, "In vivo molecular and cellular imaging with quantum dots," *Current Opinion in Biotechnology*, vol. 16, no. 1, pp. 63–72, 2005.
- [12] A. P. Alivisatos, "Perspectives on the physical chemistry of semiconductor nanocrystals," *Journal of Physical Chemistry*, vol. 100, no. 1, pp. 13226–13239, 1996.
- [13] C. B. Murray, D. J. Norris, and M. G. Bawendi, "Synthesis and characterization of nearly monodisperse CdE (E = S, Se, Te) semiconductor nanocrystallites," *Journal of the American Chemical Society*, vol. 115, no. 19, pp. 8706–8715, 1993.
- [14] M. A. Hines and P. Guyot-Sionnest, "Synthesis and characterization of strongly luminescing ZnS-capped CdSe nanocrystals," *Journal of Physical Chemistry*, vol. 100, no. 2, pp. 468–471, 1996.
- [15] W. Cai, D.-W. Shin, K. Chen, et al., "Peptide-labeled near-infrared quantum dots for imaging tumor vasculature in living subjects," *Nano Letters*, vol. 6, no. 4, pp. 669–676, 2006.
- [16] M. Bruchez Jr., M. Moronne, P. Gin, S. Weiss, and A. P. Alivisatos, "Semiconductor nanocrystals as fluorescent biological labels," *Science*, vol. 281, no. 5385, pp. 2013–2016, 1998.
- [17] W. C. W. Chan and S. Nie, "Quantum dot bioconjugates for ultrasensitive nonisotopic detection," *Science*, vol. 281, no. 5385, pp. 2016–2018, 1998.
- [18] B. Dubertret, P. Skourides, D. J. Norris, V. Noireaux, A. H. Brivanlou, and A. Libchaber, "In vivo imaging of quantum dots encapsulated in phospholipid micelles," *Science*, vol. 298, no. 5599, pp. 1759–1762, 2002.
- [19] D. Gerion, F. Pinaud, S. C. Williams, et al., "Synthesis and properties of biocompatible water-soluble silica-coated CdSe/ZnS semiconductor quantum dots," *Journal of Physical Chemistry B*, vol. 105, no. 37, pp. 8861–8871, 2001.
- [20] T. M. Jovin, "Quantum dots finally come of age," *Nature Biotechnology*, vol. 21, no. 1, pp. 32–33, 2003.
- [21] X. Gao, Y. Cui, R. M. Levenson, L. W. K. Chung, and S. Nie, "In vivo cancer targeting and imaging with semiconductor quantum dots," *Nature Biotechnology*, vol. 22, no. 8, pp. 969–976, 2004.
- [22] X. Wu, H. Liu, J. Liu, et al., "Immunofluorescent labeling of cancer marker Her2 and other cellular targets with semiconductor quantum dots," *Nature Biotechnology*, vol. 21, no. 1, pp. 41–46, 2003.



- [23] E. L. Bentzen, I. D. Tomlinson, J. N. Mason, et al., "Surface modification to reduce nonspecific binding of quantum dots in live cell assays," *Bioconjugate Chemistry*, vol. 16, no. 6, pp. 1488–1494, 2005.
- [24] Z. Chunyang, M. Hui, D. Yao, J. Lei, C. Dieyan, and N. Shuming, "Quantum dot-labeled trichosanthin," *The Analyst*, vol. 125, no. 6, pp. 1029–1031, 2000.
- [25] O. Minet, C. Dressler, and J. Beuthan, "Heat stress induced redistribution of fluorescent quantum dots in breast tumor cells," *Journal of Fluorescence*, vol. 14, no. 3, pp. 241–247, 2004.
- [26] M. Howarth, K. Takao, Y. Hayashi, and A. Y. Ting, "Targeting quantum dots to surface proteins in living cells with biotin ligase," *Proceedings of the National Academy of Sciences of the United States of America*, vol. 102, no. 21, pp. 7583–7588, 2005.
- [27] M. Howarth, D. J.-F. Chinnapen, K. Gerrow, et al., "A monovalent streptavidin with a single femtomolar biotin binding site," *Nature Methods*, vol. 3, no. 4, pp. 267–273, 2006.
- [28] M.-V. Ehrensperger, C. Hanus, C. Vannier, A. Triller, and M. Dahan, "Multiple association states between glycine receptors and gephyrin identified by SPT analysis," *Biophysical Journal*, vol. 92, no. 10, pp. 3706–3718, 2007.
- [29] I. L. Medintz and J. R. Deschamps, "Maltose-binding protein: a versatile platform for prototyping biosensing," *Current Opinion in Biotechnology*, vol. 17, no. 1, pp. 17–27, 2006.
- [30] A. Månsson, M. Sundberg, M. Balaz, et al., "In vitro sliding of actin filaments labelled with single quantum dots," *Biochemical and Biophysical Research Communications*, vol. 314, no. 2, pp. 529–534, 2004.
- [31] S. Le Gac, I. Vermes, and A. van den Berg, "Quantum dots based probes conjugated to annexin V for photostable apoptosis detection and imaging," *Nano Letters*, vol. 6, no. 9, pp. 1863–1869, 2006.
- [32] M. E. Åkerman, W. C. W. Chan, P. Laakkonen, S. N. Bhatia, and E. Ruoslahti, "Nanocrystal targeting in vivo," *Proceedings of the National Academy of Sciences of the United States of America*, vol. 99, no. 20, pp. 12617–12621, 2002.
- [33] D. S. Lidke, P. Nagy, R. Heintzmann, et al., "Quantum dot ligands provide new insights into erbB/HER receptor-mediated signal transduction," *Nature Biotechnology*, vol. 22, no. 2, pp. 198–203, 2004.
- [34] I. D. Tomlinson, J. N. Mason, R. D. Blakely, and S. J. Rosenthal, "Peptide-conjugated quantum dots: imaging the angiotensin type 1 receptor in living cells," *Methods in Molecular Biology*, vol. 303, pp. 51–60, 2005.
- [35] P. Alivisatos, "The use of nanocrystals in biological detection," *Nature Biotechnology*, vol. 22, no. 1, pp. 47–52, 2004.
- [36] F. Patolsky, R. Gill, Y. Weizmann, T. Mokari, U. Banin, and I. Willner, "Lighting-up the dynamics of telomerization and DNA replication by CdSe-ZnS quantum dots," *Journal of the American Chemical Society*, vol. 125, no. 46, pp. 13918–13919, 2003.
- [37] D. Gerion, W. J. Parak, S. C. Williams, D. Zanchet, C. M. Mischeel, and A. P. Alivisatos, "Sorting fluorescent nanocrystals with DNA," *Journal of the American Chemical Society*, vol. 124, no. 24, pp. 7070–7074, 2002.
- [38] Y. Xiao and P. E. Barker, "Semiconductor nanocrystal probes for human metaphase chromosomes," *Nucleic Acids Research*, vol. 32, no. 3, p. e28, 2004.
- [39] W. J. Parak, D. Gerion, D. Zanchet, et al., "Conjugation of DNA to silanized colloidal semiconductor nanocrystalline quantum dots," *Chemistry of Materials*, vol. 14, no. 5, pp. 2113–2119, 2002.
- [40] C. Srinivasan, J. Lee, F. Papadimitrakopoulos, L. K. Silbart, M. Zhao, and D. J. Burgess, "Labeling and intracellular tracking of functionally active plasmid DNA with semiconductor quantum dots," *Molecular Therapy*, vol. 14, no. 2, pp. 192–201, 2006.
- [41] E. Tholouli, J. A. Hoyland, D. Di Vizio, et al., "Imaging of multiple mRNA targets using quantum dot based *in situ* hybridization and spectral deconvolution in clinical biopsies," *Biochemical and Biophysical Research Communications*, vol. 348, no. 2, pp. 628–636, 2006.
- [42] C.-Y. Zhang, H.-C. Yeh, M. T. Kuroki, and T.-H. Wang, "Single-quantum-dot-based DNA nanosensor," *Nature Materials*, vol. 4, no. 11, pp. 826–831, 2005.
- [43] A. Fu, C. M. Mischeel, J. Cha, H. Chang, H. Yang, and A. P. Alivisatos, "Discrete nanostructures of quantum dots/Au with DNA," *Journal of the American Chemical Society*, vol. 126, no. 35, pp. 10832–10833, 2004.
- [44] W. B. Tan, S. Jiang, and Y. Zhang, "Quantum-dot based nanoparticles for targeted silencing of HER2/neu gene via RNA interference," *Biomaterials*, vol. 28, no. 8, pp. 1565–1571, 2007.
- [45] R. Chakrabarti and A. M. Klibanov, "Nanocrystals modified with peptide nucleic acids (PNAs) for selective self-assembly and DNA detection," *Journal of the American Chemical Society*, vol. 125, no. 41, pp. 12531–12540, 2003.
- [46] S. Bryde, I. Grunwald, A. Hammer, et al., "Tumor necrosis factor (TNF)-functionalized nanostructured particles for the stimulation of membrane TNF-specific cell responses," *Bioconjugate Chemistry*, vol. 16, no. 6, pp. 1459–1467, 2005.
- [47] M. Manchester and P. Singh, "Virus-based nanoparticles (VNPs): platform technologies for diagnostic imaging," *Advanced Drug Delivery Reviews*, vol. 58, no. 14, pp. 1505–1522, 2006.
- [48] L. Dyadyusha, H. Yin, S. Jaiswal, et al., "Quenching of CdSe quantum dot emission, a new approach for biosensing," *Chemical Communications*, no. 25, pp. 3201–3203, 2005.
- [49] E. R. Goldman, A. R. Clapp, G. P. Anderson, et al., "Multiplexed toxin analysis using four colors of quantum dot fluororeagents," *Analytical Chemistry*, vol. 76, no. 3, pp. 684–688, 2004.
- [50] M. Dahan, S. Lévi, C. Luccardini, P. Rostaing, B. Riveau, and A. Triller, "Diffusion dynamics of glycine receptors revealed by single-quantum dot tracking," *Science*, vol. 302, no. 5644, pp. 442–445, 2003.
- [51] J. N. Mason, H. Farmer, I. D. Tomlinson, et al., "Novel fluorescence-based approaches for the study of biogenic amine transporter localization, activity, and regulation," *Journal of Neuroscience Methods*, vol. 143, no. 1, pp. 3–25, 2005.
- [52] B. Ballou, B. C. Lagerholm, L. A. Ernst, M. P. Bruchez, and A. S. Waggoner, "Noninvasive imaging of quantum dots in mice," *Bioconjugate Chemistry*, vol. 15, no. 1, pp. 79–86, 2004.
- [53] S. Kim, Y. T. Lim, E. G. Soltesz, et al., "Near-infrared fluorescent type II quantum dots for sentinel lymph node mapping," *Nature Biotechnology*, vol. 22, no. 1, pp. 93–97, 2004.
- [54] C. Bouzigues, M. Morel, A. Triller, and M. Dahan, "Asymmetric redistribution of GABA receptors during GABA gradient sensing by nerve growth cones analyzed by single quantum dot imaging," *Proceedings of the National Academy of Sciences of the United States of America*, vol. 104, no. 27, pp. 11251–11256, 2007.
- [55] S. J. Rosenthal, I. D. Tomlinson, E. M. Adkins, et al., "Targeting cell surface receptors with ligand-conjugated nanocrystals,"



- Journal of the American Chemical Society*, vol. 124, no. 17, pp. 4586–4594, 2002.
- [56] I. D. Tomlinson, A. P. Gies, P. J. Gresch, et al., “Universal polyethylene glycol linkers for attaching receptor ligands to quantum dots,” *Bioorganic & Medicinal Chemistry Letters*, vol. 16, no. 24, pp. 6262–6266, 2006.
- [57] I. D. Tomlinson, J. L. Grey, and S. J. Rosenthal, “A synthesis of 6-(2,5-dimethoxy-4-(2-aminopropyl)phenyl)-hexylthiol. A ligand for conjugation with fluorescent cadmium selenide/zinc sulfide core/shell nanocrystals and biological imaging,” *Molecules*, vol. 7, no. 11, pp. 777–790, 2002.
- [58] I. D. Tomlinson, J. Mason, J. N. Burton, R. Blakely, and S. J. Rosenthal, “The design and synthesis of novel derivatives of the dopamine uptake inhibitors GBR 12909 and GBR 12935. High-affinity dopaminergic ligands for conjugation with highly fluorescent cadmium selenide/zinc sulfide core/shell nanocrystals,” *Tetrahedron*, vol. 59, no. 40, pp. 8035–8047, 2003.
- [59] I. D. Tomlinson, J. N. Mason, R. D. Blakely, and S. J. Rosenthal, “Inhibitors of the serotonin transporter protein (SERT): the design and synthesis of biotinylated derivatives of 3-(1,2,3,6-tetrahydro-pyridin-4-yl)-1H-indoles. High-affinity serotonergic ligands for conjugation with quantum dots,” *Bioorganic & Medicinal Chemistry Letters*, vol. 15, no. 23, pp. 5307–5310, 2005.
- [60] I. D. Tomlinson, J. N. Mason, R. D. Blakely, and S. J. Rosenthal, “High affinity inhibitors of the dopamine transporter (DAT): novel biotinylated ligands for conjugation to quantum dots,” *Bioorganic & Medicinal Chemistry Letters*, vol. 16, no. 17, pp. 4664–4667, 2006.
- [61] J. N. Mason, I. D. Tomlinson, S. J. Rosenthal, and R. D. Blakely, “Labeling cell-surface proteins via antibody quantum dot streptavidin conjugates,” *Methods in Molecular Biology*, vol. 303, pp. 35–50, 2005.
- [62] I. D. Tomlinson, T. Kippeny, L. Swafford, N. H. Siddiqui, and S. J. Rosenthal, “Novel polyethylene glycol derivatives of melatonin and serotonin. Ligands for conjugation to fluorescent cadmium selenide/zinc sulfide core shell nanocrystals,” *Journal of Chemical Research*, vol. 2002, no. 5, pp. 203–204, 2002.
- [63] A. Wolcott, D. Gerion, M. Visconte, et al., “Silica-coated CdTe quantum dots functionalized with thiols for bioconjugation to IgG proteins,” *Journal of Physical Chemistry B*, vol. 110, no. 11, pp. 5779–5789, 2006.
- [64] E. R. Goldman, G. P. Anderson, P. T. Tran, H. Mattoussi, P. T. Charles, and J. M. Mauro, “Conjugation of luminescent quantum dots with antibodies using an engineered adaptor protein to provide new reagents for fluoroimmunoassays,” *Analytical Chemistry*, vol. 74, no. 4, pp. 841–847, 2002.
- [65] H. A. Gussin, I. D. Tomlinson, D. M. Little, et al., “Binding of muscimol-conjugated quantum dots to GABA<sub>C</sub> receptors,” *Journal of the American Chemical Society*, vol. 128, no. 49, pp. 15701–15713, 2006.
- [66] M. Frey and V. Jäger, “Synthesis of *N*-substituted muscimol derivatives including *N*-glycylmuscimol,” *Synthesis*, vol. 1985, no. 12, pp. 1100–1104, 1985.
- [67] H. Qian, J. E. Dowling, and H. Ripps, “Molecular and pharmacological properties of GABA- $\rho$  subunits from white perch retina,” *Journal of Neurobiology*, vol. 37, no. 2, pp. 305–320, 1998.
- [68] T. Q. Vu, S. Chowdhury, N. J. Muni, H. Qian, R. F. Standaert, and D. R. Pepperberg, “Activation of membrane receptors by a neurotransmitter conjugate designed for surface attachment,” *Biomaterials*, vol. 26, no. 14, pp. 1895–1903, 2005.

## Research Article

# Fluorescence Intensity and Intermittency as Tools for Following Dopamine Bioconjugate Processing in Living Cells

Rafael Khatchadourian,<sup>1</sup> Alexia Bachir,<sup>2</sup> Samuel J. Clarke,<sup>1</sup> Colin D. Heyes,<sup>3</sup>  
Paul W. Wiseman,<sup>2,3</sup> and Jay L. Nadeau<sup>1</sup>

<sup>1</sup> Department of Biomedical Engineering, McGill University, 3775 Rue University, 316 Lyman Duff Medical Building, Montréal, Canada QC H3A 2B4

<sup>2</sup> Department of Chemistry, McGill University, 801 Sherbrooke Street West, Montréal, Canada QC H3A 2K6

<sup>3</sup> Department of Physics, McGill University, 3600 Rue University, Montréal, Canada QC H3A 2T8

Correspondence should be addressed to Jay L. Nadeau, jay.nadeau@mcgill.ca

Received 10 April 2007; Revised 11 August 2007; Accepted 24 December 2007

Recommended by Marek Osinski

CdSe/ZnS quantum dots (QDs) conjugated to biomolecules that quench their fluorescence, particularly dopamine, have particular spectral properties that allow determination of the number of conjugates per particle, namely, photoenhancement and photobleaching. In this work, we quantify these properties on a single-particle and ensemble basis in order to evaluate their usefulness as a tool for indicating QD uptake, breakdown, and processing in living cells. This creates a general framework for the use of fluorescence quenching and intermittency to better understand nanoparticle-cell interactions.

Copyright © 2007 Rafael Khatchadourian et al. This is an open access article distributed under the Creative Commons Attribution License, which permits unrestricted use, distribution, and reproduction in any medium, provided the original work is properly cited.

## 1. INTRODUCTION

The interactions of semiconductor quantum dots (QDs) with living cells remain poorly understood. QDs of different materials (e.g., CdSe and CdTe), sizes, colors, and surface coatings demonstrate very different toxic effects to cells in culture [1, 2]. Much of the toxicity differences associated with a given type of nanoparticle are attributable to whether the particles are able to enter the cell, escape from endosomes, and enter the nucleus or mitochondria. No satisfactory explanation exists for differences in these properties among batches of particles although there appear to be loose correlations with particle size, particularly for nuclear entry [3]. However, these experiments were performed using thiol-capped particles, and because the small size correlates with thiol coating stability [4], no firm conclusions can be drawn from the results.

A quantitative understanding of the fate of conjugated QDs in biological systems is therefore critical if these particles are to be used in *in vitro* diagnostics or *in vivo* systems. Our previous work demonstrated that QD-dopamine conjugates (see Figure 1) can be used not only as static fluorescent labels, but also as sensors for intracellular redox processes such as endocytosis, lysosomal processing, and mitochon-

drial depolarization [5]. This is due to the electron-donating properties of dopamine (DA), which permit this molecule to act as an electron shuttle between the nanoparticle and other molecules.

The goal of this work is to improve the spatial and temporal resolution of the QD-dopamine redox sensor by determining, in as quantitative as possible a fashion, the relationship between the number of dopamine molecules on the particle and two optical properties which can be measured within the cell: photoenhancement and photobleaching.

The eventual goal is to make an intracellular redox sensor that can yield nanometer spatial resolution. The possibility of several-nanometer resolution would become a reality if the photophysical properties of *single* QDs could be regulated by their immediate environment in a controllable fashion [6]. Fluorescence intermittency, or blinking, is a classic example of a poorly-understood feature of QD fluorescence that is often neglected or suppressed rather than exploited. Under continuous illumination, single QDs exhibit blinking over a wide range of timescales [7–12]. A number of studies have been reported which look at various effects on blinking, such as excitation power [8, 9, 11, 13, 14], the shell material around the QDs [7, 8, 10], as well as environmental conditions such as temperature [8, 15] and surrounding

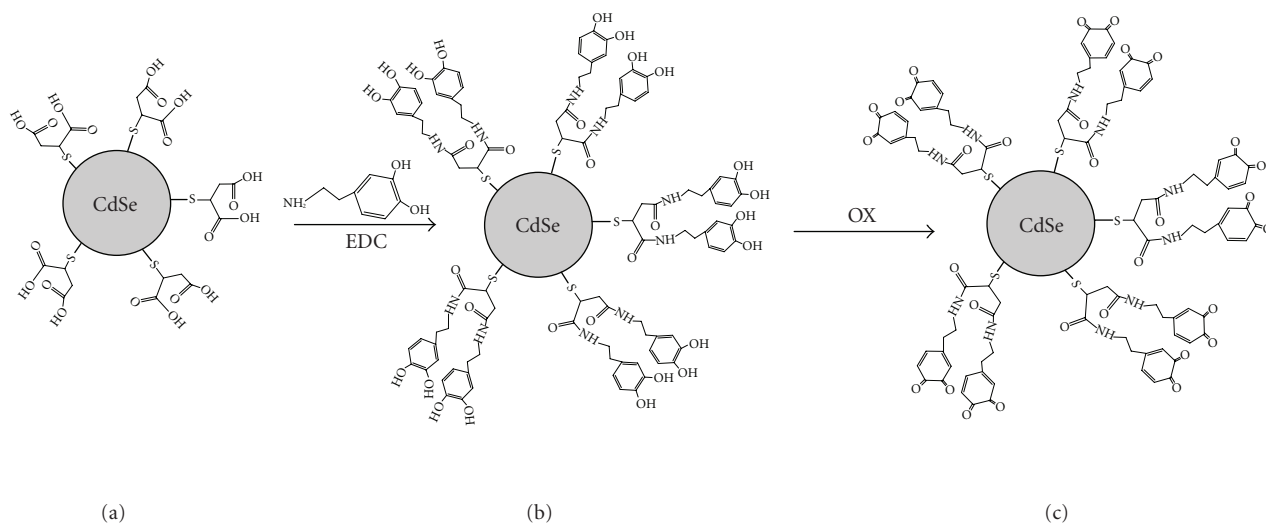


FIGURE 1: Schematic of QD-dopamine conjugate preparation and mechanism of redox sensitivity. (a) MSA-capped QD. (b) Upon addition of dopamine (structure shown above arrow) and the zero-length cross-linker EDC, an amide bond is formed between the amine of dopamine and the carboxylate groups of MSA. This schematic shows 100% linkage of dopamine to MSA termini; however, we show here that this ratio can be controlled. (c) Upon oxidation ("OX"), the catechol becomes a less-soluble quinone.

medium [16, 17]. From these studies, two physical models have been advanced which attempt to explain the inverse power law behavior of the blinking statistics. The first model assumes a fluctuating distribution of electron traps in the immediate vicinity of, but external to, the QD [18]. Tunneling of the electron out of the QD results in a charged particle, quenching any emission and, thus, resulting in an off state. Neutralization of the QD by recapture of the electron recovers the emission, resulting in an on state. The second model does not assume external traps, but rather posits internal hole traps, presumably at surface states or crystal imperfection sites [19]. Energetic diffusion of the electronic states results in a time-dependent resonance condition in which Auger-assisted trapping of the hole results in an off state. Given the variability of the possible mechanisms, it is not possible to predict the effects of conjugation of a redox-active molecule such as dopamine. In this work, we evaluate the effects of dopamine of blinking and evaluate the possibility of the use of intermittency as a tool for the ultrasensitive detection of subcellular environments and biochemical processing of QD-bioconjugates.

## 2. RESULTS

### 2.1. Quantifying numbers of conjugates per particle

In this study, we used red-emitting CdSe/ZnS QDs (QD605, emission peak  $605 \pm 20$  nm) for photoenhancement and blinking studies, and green-emitting QDs (QD560, emission peak  $560 \pm 20$  nm) for cellular uptake studies. QDs were conjugated to the neurotransmitter dopamine via the primary amine located on the opposite end of the molecule from the redox-active catechol (see Figure 1). The number of bound ligands was quantified in EDC-coupling reactions containing varying concentrations of dopamine and/or of 1-ethyl-3-(3-

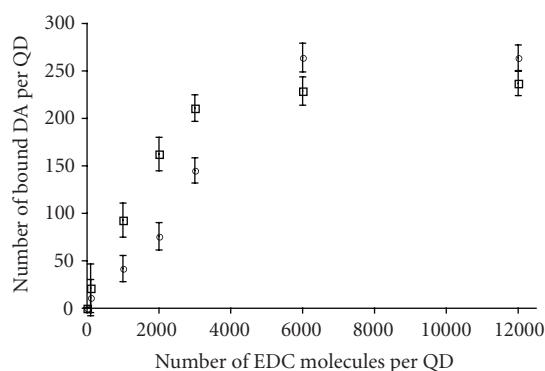


FIGURE 2: Number of bound dopamine molecules as a function of the number of EDC added to the coupling reaction for QD560 (squares) and QD605 (circles) as measured by OPA assay. Data are an average of three experiments with error bars indicating the standard error of the mean.

dimethylaminopropyl) carbodiimide hydrochloride (EDC), using the o-phthalaldehyde (OPA) assay as described previously [20]. A strong dependence was observed of the number of EDCs per QD on the number of dopamine molecules that bound. The number of bound ligands increased linearly with the number of EDC molecules until a certain breakpoint and a plateau was reached, which was considered as the saturation point for the QDs (see Figure 2). Indirectly, we can interpret the saturation point as an indicator of the number of functional groups available on the surface of the QDs. This appears to be slightly smaller for green QDs than for red, as expected due to the smaller size of these particles, although it is the same within error at the maximum EDC concentration.

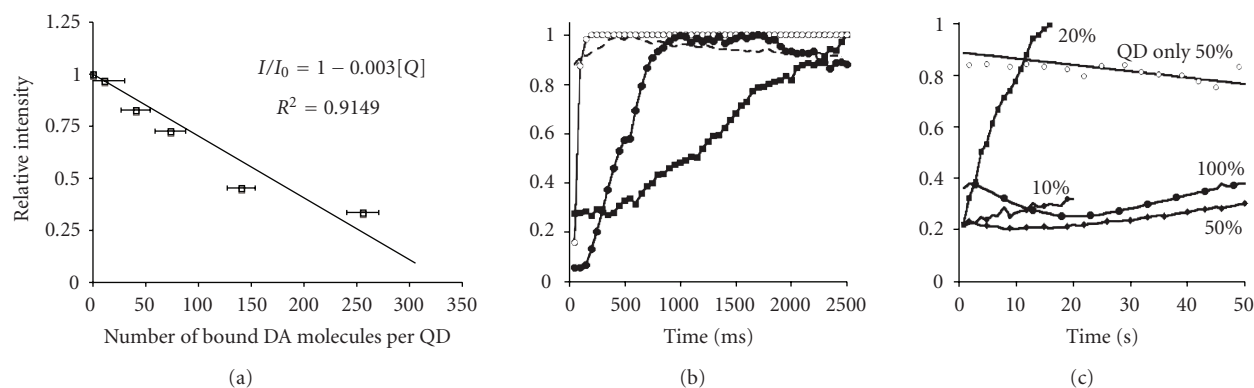


FIGURE 3: Relationship between the number of dopamine molecules bound to the surface of QD605 and the resulting emission intensity. (a) The quenching observed upon conjugation is nearly logarithmic. Data are an average of three experiments with error bars indicating the standard error of the mean. (b) Unquenching of QD-dopamine conjugates with varying amounts of coverage under Hg-lamp exposure (QD filter set, see Methods). Each symbol is a data point, with error bars smaller than symbols ( $n = 3$ ). Bare QDs alone (dashed line) show essentially constant fluorescence over a 2.5-second exposure period; they begin to photobleach near the end. QDs, to which dopamine was added but not conjugated (no EDC) (open circles), achieve maximum fluorescence within 50 milliseconds. Conjugates with  $40 \pm 14$  DA/particle (filled circles) brighten over a time course of  $\sim 700$  milliseconds. The conjugates with the greatest coverage (filled squares,  $255 \pm 14$  DA/particle) have just begun to plateau at 2.5 seconds. (c) Confocal laser illumination of samples with  $255 \pm 14$  DA/particle. Photoenhancement showed a strong dependence upon laser power, with efficient enhancement at 20% but limited or no enhancement at 10%, 50%, and 100% power. Each symbol is a data point, with error bars smaller than symbols ( $n = 5$ ). Unconjugated QDs showed similar bleaching curves for all powers tested (shown: 50%).

## 2.2. QD-dopamine fluorescence properties

Manipulating the extent of ligand coverage of the QD surface can be an effective way to modulate fluorescent properties if the ligands can act as energy or electron donors or acceptors to or from the QDs. In our previous work, we have shown that dopamine can be used to modulate the emission characteristics of QDs by a mechanism of electron transfer. In Figure 3(a), we demonstrate the effect of the number of bound dopamine ligands and the subsequent reduction in the emission intensity of the QDs. To distinguish this type of quenching from the Stern-Volmer collisional quenching, we purified the conjugates from excess unbound ligand. Our results showed a large decrease in intensity when a relatively small number of ligands were bound to the surface, owing to the electron transfer from dopamine to the QDs [5].

Oxidation of these quenched QDs, either by photoexposure or chemical means, led to a restoration of fluorescence from the QD. In addition, oxidized dopamine emitted fluorescence in the blue regime (peak emission 460 nm). Thus, there were three parameters that could be used to indicate the number of dopamine conjugates on the particle surface: (a) blue fluorescence from oxidized dopamine; (b) brightness of QD fluorescence without UV pre-exposure; and (c) time course of QD fluorescence under photooxidation.

This latter quantity must be determined for each light source; broad Hg-lamp excitation (through a QD or DAPI filter, see Figure 3(b)) yielded very different results than 488 nm laser-line excitation, showing essentially all-or-nothing dependence on illumination power (see Figure 3(c)). Similarly, lifetime measurements with time-correlated single photon counting (TCSPC) and 400 nm

laser illumination revealed extreme sensitivity to illumination power. A full study with laser powers varying from tens of microwatts to several milliwatts is forthcoming.

## 2.3. Improved spatial resolution of redox sensing in living cells

QD-dopamine was readily endocytosed by cells bearing dopamine receptors. Little or no binding was seen to cells without dopamine receptors, and the QD conjugates were readily washed away [5]. We investigated the effect of dopamine ligand coverage and corresponding uptake in DA-receptor-expressing PC12 cells. As expected, cells that were treated with QDs alone did not show any detectable QD association. For the QD560-DA conjugates, particles with fewer than 100 DA/particle were not taken up in significant amounts after 15–30 minutes of incubation (not shown). Thus, particles that were effectively taken up began with slow photoenhancement curves. The variation of photoenhancement properties with position in the cell was then used to semiquantitatively identify regions where oxidation had occurred.

The location and appearance of various organelles in cells were determined by labeling with specific dyes such as LysoTracker and Mitotracker (see Figure 4). Studies of unquenching time-courses of the simultaneously loaded QD-dopamine were then performed under 488 nm laser illumination. The results showed a consistent and reproducible pattern with three distinctive QD behaviors. In fixed cells, with depolarized mitochondria, QDs did not show overlap with the mitochondrial-targeting dye MitoTracker. QD fluorescence brightened slightly under light exposure

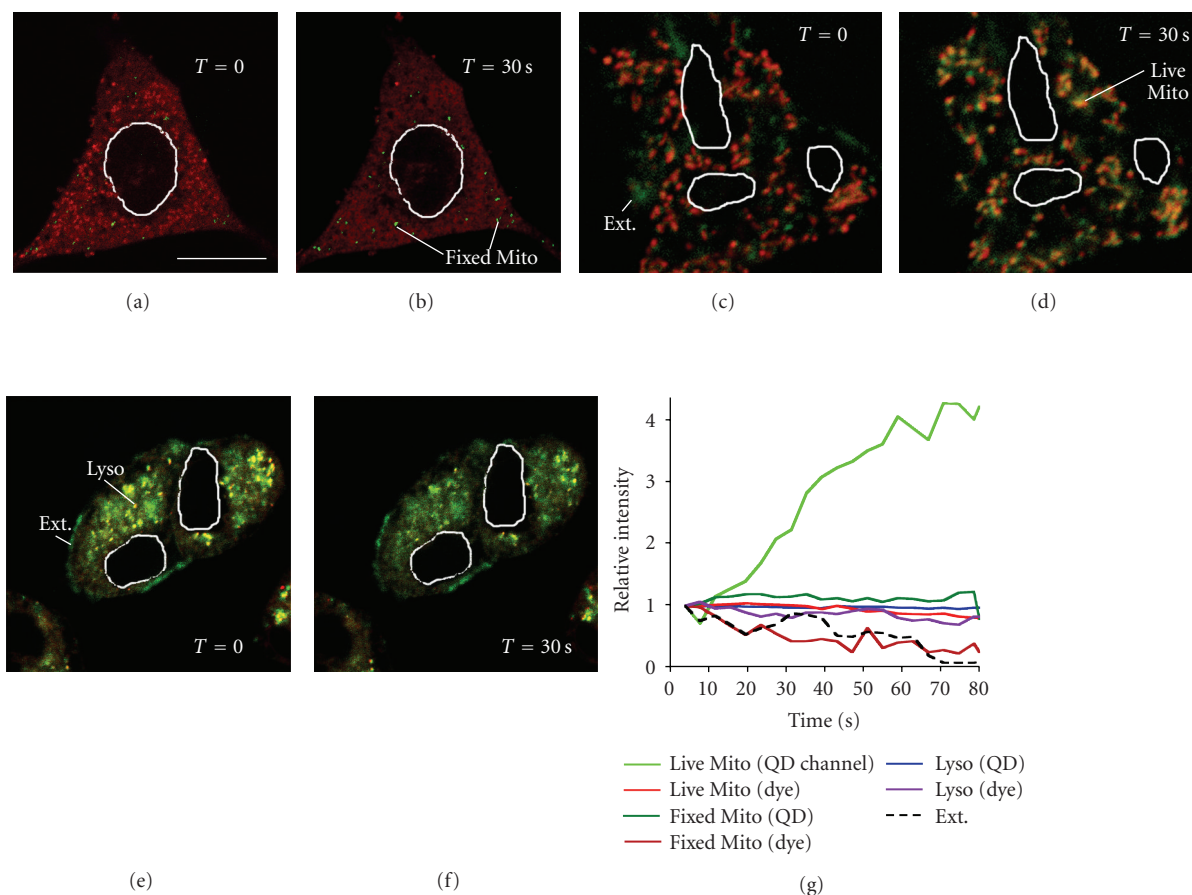


FIGURE 4: Confocal images and time courses of QD-dopamine with  $100 \pm 10$  DA/particle in PC12-dopamine receptor cells colabeled with organelle dyes. Scale bar =  $10 \mu\text{m}$  for all panels; in all panels, the green channel indicates the QDs and the red channel the organelle dye. The white lines indicate the cell nuclei. (a) Paraformaldehyde-fixed cell labeled with MitoTracker and QDs. (b) The same cell after 30 seconds of laser-light exposure. (c) Live cells labeled with MitoTracker and QDs. (d) The same cells after 30 seconds of laser-light exposure. (e) Live cell labeled with LysoTracker and QDs. (f) The same cell after 30 seconds of light exposure. (g) Relative intensities from the indicated regions over 100 seconds of exposure time.

(see Figures 4(a), 4(b), and 4(g)). In live cells, however, the mitochondrial region brightened quickly and intensely, with QD-MitoTracker overlap becoming apparent (see Figures 4(c), 4(d), and 4(g)). In both live and fixed cells, a good deal of QD fluorescence was seen colocalized with lysosomes. QD fluorescence within lysosomes shows only bleaching with time (see Figures 4(e), 4(f), and 4(g)). QDs that were outside the cell, in aggregates outside the membrane, exhibited no brightening but only photobleaching over time (see Figures 4(e), 4(f), and 4(g)).

Observation of the blue QD-dopamine fluorescence confirmed what was suggested by the time-course spectra. QDs outside the cells showed no blue emission, confirming the absence of dopamine, whereas those in the cytoplasm and mitochondria showed visible 460 nm emission (see Figure 5).

#### 2.4. Effect of dopamine on fluorescence intermittency

Blinking is conveniently studied by taking an image series with time of a number of immobilized QDs [9–11]. Details

of the analysis may be found in the methods section and in previous publications [9, 10]. The result of the analysis is that the fluorescence time trace for each identified QD is extracted from the image series, and the durations of on and off times (time durations for which the signal is above and below the threshold level, resp.) are extracted. A typical image and extracted fluorescence trace of a single, immobile QD are shown in Figure 6.

We studied the effect of conjugating dopamine to QDs on their blinking statistics. The probability distributions of on times,  $P(\text{on})$ , and off times,  $P(\text{off})$ , for QDs with and without conjugated dopamine are shown in Figures 7(a) and 7(b), respectively, as measured by extracting fluorescence time traces, such as shown in Figure 6(b), setting a threshold and calculating on and off times. Approximately 500 QDs were analyzed from 5 sets of movies, taken at 50-millisecond resolution for 100 seconds. Except for the dopamine, the QDs and the experimental conditions were identical. Clearly, under these conditions, the conjugation of dopamine to the QD reduced the on times and increased the off times.



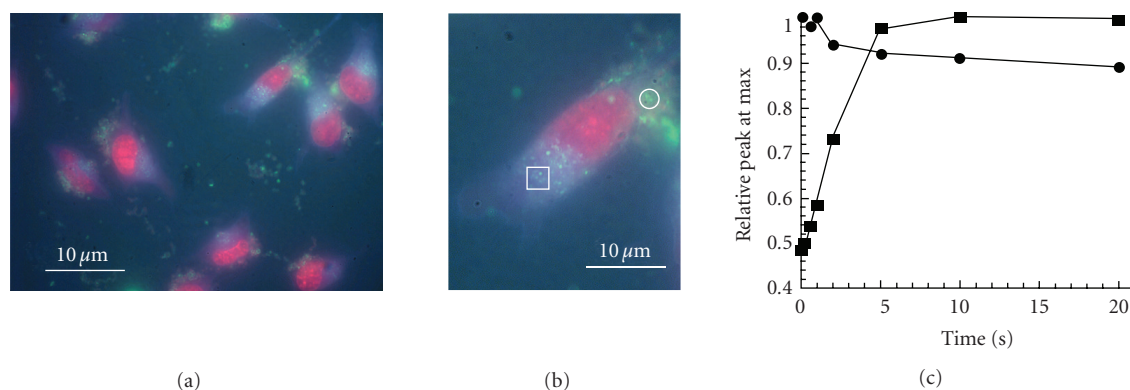


FIGURE 5: Subcellular differences in QD-dopamine fluorescence. (a) Image under DAPI filter of cells labeled with QD-dopamine (and with SYTO red to show nuclei). The green regions (540–580 nm emission) show QD fluorescence but no dopamine fluorescence. The blue areas (460–500 nm emission) show dopamine fluorescence and no initial QD fluorescence; QD fluorescence appears after UV illumination. Double-labeling experiments identified the green areas as lysosomes (not shown) or as regions exterior to the cell. (b) Closeup of a single cell from panel A showing blue spots (square) and green spots (circle). (c) Time course of QD peak fluorescence under UV illumination (QD filter) for a blue region (squares) and a green region (circles).

### 3. DISCUSSION

#### 3.1. Tracking QD oxidation with fluorescence changes

We previously showed [5] that QD-dopamine conjugates show altered fluorescence in living cells in accordance with the cellular and subcellular redox potential with brighter fluorescence corresponding to more oxidizing conditions. However, two of the observed phenomena were not fully explained. First, different colors, batches of QDs, and conjugate preparations showed widely varying degrees of uptake. Second, the mechanism of brightening in response to oxidation was not elucidated although it was presumed to be related to cap decay [21].

In this work, we explain the differing levels of uptake by showing that using standard MSA-EDC coupling techniques, approximately 100 dopamines per particle are required to obtain efficient uptake in our stably transfected dopamine-receptor cell lines. Future work will explore variations on solubilizing-agent chain length and the addition of spacers [22] to improve the presentation of the dopamine to its receptor, as this high requirement probably reflects biological inactivity of most of the dopamines on these particles.

Of general interest is the observation that controlling the average number of dopamine molecules bound to QDs affects the photoenhancement of ensembles of particles in a measurable fashion. This makes these conjugates a more useful tool than one based upon quenching alone, as the presence of fully-quenched particles can obviously not be detected under fluorescence microscopy. On slides, more dopamines per particle correspond to slower photoenhancement (see Figure 3(b)); QDs without dopamine show bleaching without enhancement.

Confocal laser illumination shows a quite different pattern from Hg-lamp illumination; this could be due to several factors. The illumination is at a single wavelength; the most commonly used line (488 nm) will not excite the dopamine

quinone, eliminating issues of signal confusion as well as eliminating the possibility that excitation of the quinone affects the QD enhancement or bleaching. Finally, laser illumination is intermittent due to scanning, perhaps permitting QDs to recover in-between pulses.

In cells, a minimum number of dopamines, corresponding to slow enhancement, is necessary for uptake. However, as the particles travel through the cell, particularly to oxidizing regions, enhancement becomes more rapid suggesting that the cap decay mechanism is in fact correct. These data could be used for a semiquantitative model of QD processing in cells (Schematic in Figure 8).

#### 3.2. Blinking analysis

It is immediately obvious from Figure 7 that the addition of dopamine to the QD surface affects blinking by reducing on times and increasing off times. Many groups have found that the distribution of off times fits to a power law function [8–10, 12, 18, 23], whereas the on times distribution is the source of some debate. Some have found that the on times fit to a power law function [18, 24]; whereas others have found that they fit better to a power law function convoluted with an exponential function at long on times [8, 10, 19]. The effect of coating the CdSe with a ZnS shell on the blinking has also been studied by several groups. Nirmal et al. found that a thick ZnS shell results in the observation of longer on and off events [7]. Subsequently, a more thorough statistical analysis revealed that the power law slopes for both the on times and the off times distributions are not affected by ZnS capping, but that the exponential cutoff time in the on times slightly increases by ZnS capping [8]. Heyes et al. found that, within experimental error, there was no effect in both the power law slope and the exponential cutoff upon increasing the ZnS capping thickness [10]. This lack of dependence was explained as the physical origin of blinking lying in hole-trap states at the surface or core-shell interface.

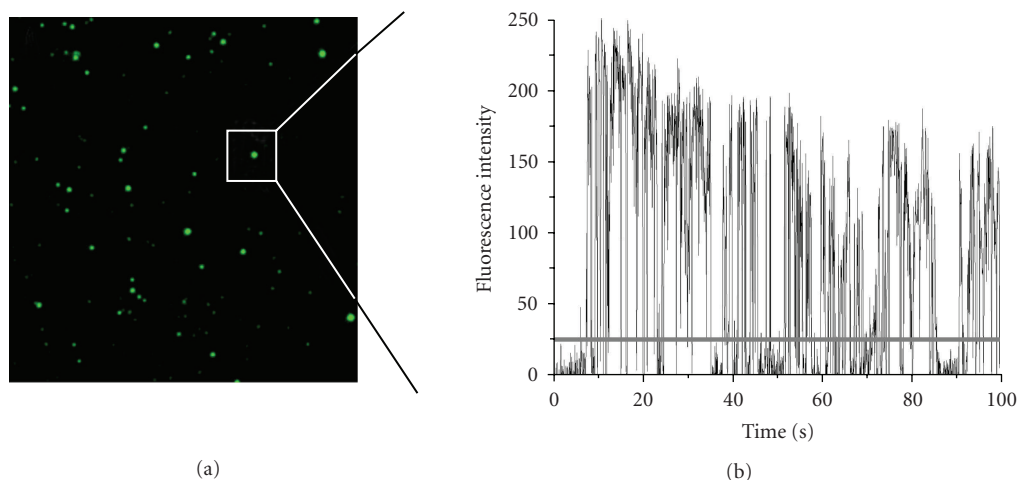


FIGURE 6: Evaluation of QD blinking. (a) Typical image of immobilized QDs. Due to their different brightness, some spots appear larger than others. Single QDs are identified by the size of their point spread function and selected for subsequent analysis. Image size is  $40 \times 40 \mu\text{m}^2$ . (b) Typical intensity trace of a single QD under continuous excitation. The grey line indicates an arbitrary threshold used to separate on-events from off-events. The threshold is usually set to 2–3 standard deviations above the background noise level, which is determined from nearby pixels containing no QD.

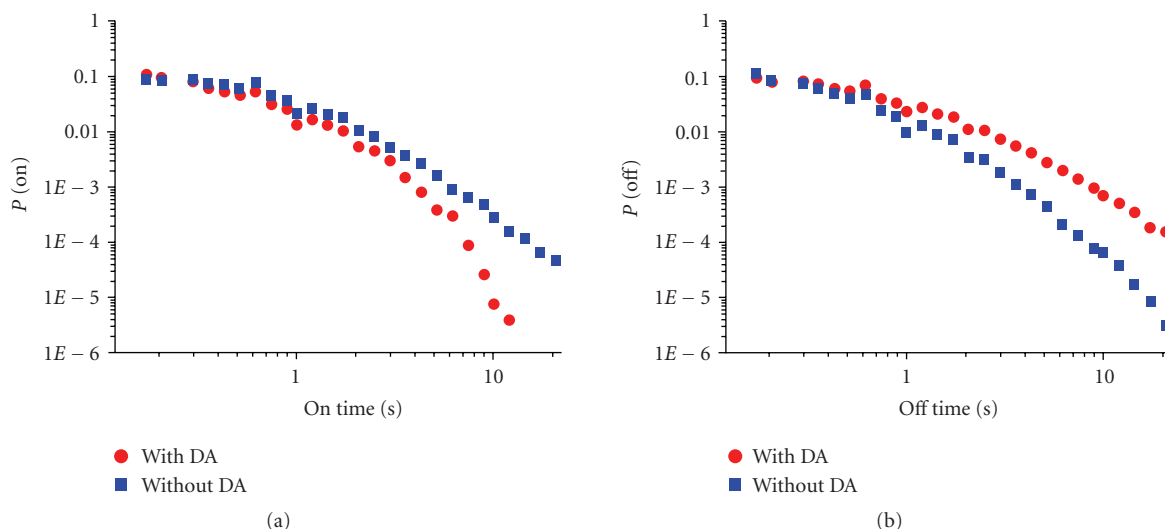


FIGURE 7: Probability histograms for (a) on-times and (a) off-times durations with (red) and without (blue) dopamine conjugated to the QD surface. A strong effect of dopamine in both on-times and off-times durations is evident. The addition of dopamine reduces the probability of observing long on-times and increases the probability of observing long off-times.

In the study of Heyes et al. [10], all blinking probability distributions fit to an inverse power law for off times. For on times, the functions fit to an inverse power law with exponential cutoff at longer on times, in agreement with previous observations and a previously published model, which did not assume the presence of external trap states [19]. The data presented here do not fit to the same functions as previous observations (power law for off times and a power law convoluted with an exponential cutoff at longer times) suggesting that the underlying mechanisms of blinking differ. At

the current time, we cannot identify the source of these differences and much more work is needed to further investigate the physical origins. We have identified several possible sources that may be responsible for the observed difference in blinking statistics. One such source may be that the difference in chemical environment of the QD is responsible. The QDs used here are coated with mercaptosuccinic acid (MSA) ligands, which carry both a negative charge and a coordinating sulfur group which may both affect the blinking statistics. Most previous studies have investigated QDs

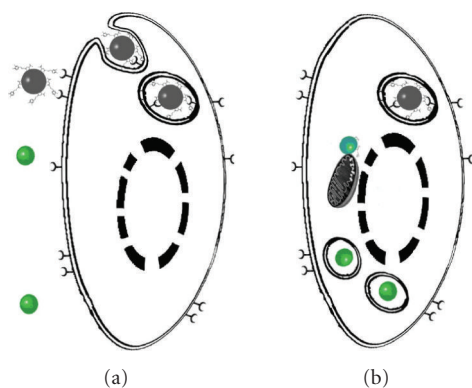


FIGURE 8: Fluorescent tracking of QD uptake and breakdown in cells (cellular structures not to scale). (a) QDs conjugated to an electron donor can bind to specific receptors (gray sphere) but are not immediately fluorescent. QDs that have lost this surface cap are immediately green-fluorescent (green spheres) but do not bind to receptors and are rarely endocytosed. (b) Processing through the cell leads to changes in surface cap and resulting alterations of fluorescence. Areas of normal cellular redox potential such as endosomes (gray) are not fluorescent unless illuminated for significant amounts of time. Highly oxidizing areas such as lysosomes, in contrast, show immediate green fluorescence and no blue fluorescence without photoenhancement, indicating that the conjugate has been removed from the particle, probably due to proteases in the lysosome. Particles near mitochondria show varying degrees of green and blue fluorescence with slow photoenhancement.

that are either coated with uncharged organic ligands or are coated with large amphiphilic polymers. The chemical environment may be further affected by the conjugation of dopamine which may result in the presence of different trap (off) states. Another source for the difference may lie in the fact that in the experiments presented here, polychromatic excitation from a halogen lamp, passed through a QD filter cube, which results in excitation with a range of wavelengths from 380 nm to 460 nm, was used. While this excitation configuration is a common one for biological detection of QDs in cellular environments, both the CdSe core and the ZnS shell are excited (as well as dopamine when it is present) whereas most previous blinking experiments have been performed using monochromatic excitation at either 488 nm, 514 nm, or 532 nm [7–12] where only the CdSe core is excited. Excitations formed following excitation of the QDs using the present excitation configuration are more easily exposed to the QD surface or surrounding environment. Further work is currently underway in our lab to identify the effects of both the ligand properties and the excitation energy on the blinking mechanism.

Bleaching of QDs is also affected by the addition of dopamine. The average intensity of the images decreases faster for QD-dopamine conjugates than for QDs not conjugated with dopamine. However, the decrease in average intensity is relatively small compared to the total intensity due to the contribution from the background signal arising from the many pixels in which no QDs are present. This is constant throughout the experiment, which contributes to a nonzero

offset in the integrated intensity of the image. On the other hand, the fraction of particles in the on state decreases by approximately 3 orders of magnitude for the QD-dopamine conjugates, whereas QDs without dopamine show a relatively constant on fraction during the experiment. This reduction in the fraction of emitting QDs indicates that either they are trapped in a long off time or that they are permanently bleached. Chung and Bawendi argued that there must exist a saturation in the maximum off time duration in order to explain the observation that, under continuous illumination, QD emission does not reach zero intensity due to all QDs eventually becoming trapped in a very long off state [25]. Indeed, using ensemble fluorescence spectroscopy, they determined that the maximum off time is on the order of thousands of seconds—a timescale that is generally not reached using single molecule experiments. In order to determine if the nonfluorescent particles would turn “on” again at later times (i.e., the particles are in an extended off period), we turned off the excitation source for several minutes. We then imaged the same area to determine if the particles were once again fluorescent. We found that almost none of the particles regained their fluorescence, indicating that the photobleaching was indeed permanent rather than the particles residing in an extended off period. It has been shown that QDs are much more photostable than other fluorophores, and are generally photostable for timescales much longer than our experiments. Dopamine itself must be a significant source of the photobleaching. One possible mechanism may be that radicals are formed by the dopamine, which may then eventually diffuse through the solution and react with the QD surface forming trap states. This may repeat until a significant number of trap states are formed which results in preferential nonradiative decay rather than radiative decay of any formed excitons. It must also be noted here that, under these excitation conditions, dopamine is also directly excited. The initial increase in on fraction of QDs may be the result of an initial bleaching of dopamine on the QDs which results in more on particles. This may be then followed by reaction of radicals with the QD to once again turn them off. Further chemical characterization of the bleached particles is necessary to test these hypotheses.

The changes in blinking statistics upon conjugation of QDs to specific ligands such as dopamine suggest that such an assay may be used in the future as ultrasensitive sensors for chemical and biological characterization of subcellular environments and biological processing pathways. However, it is necessary for the underlying mechanisms contributing to the observed changes to be fully understood in order to interpret these types of experimental results.

### 3.3. Conclusion

Conjugation of QDs to an electron donor such as dopamine leads to changes in optical properties beyond simply quenching. These properties, such as photoenhancement and blinking, may be used in biological studies as novel means to probe subcellular environments. The use of other electron donors, such as any of the biological catechols, should show equally interesting properties when conjugated

to QDs, creating a general principle upon which new fluorescent indicators may be created.

## 4. METHODS

### 4.1. QD synthesis

All chemicals were purchased from Sigma-Aldrich Canada (Oakville, ON, Canada). CdSe/ZnS core-shell nanocrystals were synthesized as previously described [26, 27]. In brief, CdSe/ZnS QDs were synthesized as follows: 0.024 g CdO was added to a reaction flask containing 0.44 g stearic acid and heated to 180°C under inert conditions, forming a colorless solution. The solution was allowed to cool, and afterwards 5 g TOPO and 2 g octadecylamine were added to the flask. The flask was then evacuated and filled with inert gas several times, and the solution was heated to 200°C–300°C (exact temperature depends on the desired size). 0.2 g Se was then dissolved in 2–4 mL TOPO under inert conditions, and added to the reaction flask. Finally, 0.4 mL of  $\text{Zn}(\text{Me})_2$  was added to 0.07 mL  $(\text{TMSi})_2$  under an inert atmosphere, and added to the reaction flask. Finally the solution was allowed to cool, dissolved in  $\text{CHCl}_3$ , and precipitated with MeOH. The precipitate was collected by centrifugation and washed several times with MeOH. These TOPO-passivated nanocrystals were then dispersed in the desired solvent, including toluene,  $\text{CHCl}_3$ , and hexane. QDs were solubilized using MSA. Aqueous QD solutions were diluted in  $\text{H}_2\text{O}$  to an optical density (OD) of 0.1 at the exciton peak. This corresponds to an approximate concentration of 1  $\mu\text{M}$  [26]. All QDs were stored in the dark until ready for use.

### 4.2. Conjugation to dopamine

One mg EDC was added to 0.2 mL of QDs in aqueous solution and 0.3 mL phosphate-buffered saline (PBS) solution. The tubes were covered in foil and put on a shaker for one hour. Afterwards dopamine was added to a final concentration of 2 mM, and PBS was added to a final volume of 1 mL. The tube was again covered in foil, and agitated on a shaker for 2 hours. Solutions were dialyzed against PBS for 1 hour in order to remove excess dopamine. All handling of dopamine solutions and QD-dopamine was performed in a glove bag under nitrogen to avoid oxidation of dopamine and further stored under an inert atmosphere until ready for use.

### 4.3. Incubation of QDs with cells

Experiments with cell lines were performed using PC12 cells stably transfected with human D2 dopamine receptors (gift of Stuart Sealton, Mount Sinai School of Medicine). Cells were maintained in high glucose Dulbecco's Modified Eagle's Medium (DMEM) (Invitrogen Canada, Burlington, ON, Canada) supplemented with 10% fetal bovine serum, 5% horse serum, 0.2 mM glutamine, 100 U/mL penicillin, and 100  $\mu\text{g}/\text{mL}$  streptomycin in a 5%  $\text{CO}_2$  atmosphere at 37°C. For passage, cells were rinsed first with phosphate-buffered saline (PBS) and then with Hanks balanced salt solution containing 0.05% trypsin and 0.02% EDTA, incu-

bated for 2 minutes at room temperature, and resuspended in supplemented DMEM. Cells were passaged onto glass bottom dishes (MatTek Co., Ashland, Mass, USA) the day before use at 50–80% confluency. Just prior to labeling, growth medium was removed by 2 washes in sterile PBS, and then replaced with 1 mL serum-free medium without phenol red (OptiMem, Invitrogen Canada). In preliminary studies, incubation times were varied between 15 minutes to 2 hours, and it was found that some uptake of unconjugated QDs could occur at longer timescales. Thus, all data presented show cells incubated for 15 minutes. QD-dopamine conjugates were applied directly into serum-free medium at a concentration of ~5–10 nm particles. For co-labeling with MitoTracker Red or LysoTracker Orange (Invitrogen Canada), dyes were added to cells at a concentration of 1  $\mu\text{M}$  at least 30 minutes before QD addition. All cells were washed several times with sterile PBS after labeling, and live cells were imaged in PBS. Fixed cells were incubated in 3.7% paraformaldehyde in PBS for 30 minutes, rinsed twice in PBS, and imaged in PBS.

### 4.4. Spectroscopy and microscopy of cells

Absorbance and emission spectra were recorded on Spectra-Max Plus and SpectraMax Gemini readers (Molecular Devices, Sunnyvale, Calif, USA). For Hg-lamp exposure experiments, cells and QDs were examined and imaged with an Olympus IX-71 inverted microscope and a Nuance multi-spectral imaging system, which provides spectral data from 420–720 nm in 10-nm steps (CRI Instruments, Cambridge, Mass, USA). The objective lens was a Nikon PlanFluor 100 $\times$  (N.A. = 1.30). Illumination was through a “QD” filter cube set (excitation = 380–460 nm, dichroic = 475 nm, emission = 500 LP), a “DAPI” filter cube set (excitation = 350/50nm, dichroic = 400 nm, emission = 420 LP), or a “TRITC” filter set (excitation = 540 nm, dichroic = 565 nm, emission 605 LP) (Chroma Technologies, Rockingham, Vt, USA). For evaluation of photoenhancement on slides, a droplet of QD solution was placed on a glass slide and illuminated at full lamp power from below using the QD filter. Data were excluded if the sample dried out during imaging.

Confocal imaging and time-course experiments were performed on a Zeiss 510 LSM with a Plan Apo 100 $\times$  oil objective. QDs were excited with an Ar ion laser with output power held at 55% for all experiments, corresponding to 6 A of tube current to reduce laser flicker, and the percent transmission of the 488 nm line was adjusted between 10% and 100%. LysoTracker Red and MitoTracker Orange were excited with a HeNe laser (543 nm line). Cells labeled with >1 probe were examined for channel bleed-through before imaging. For cell imaging studies, the 488 nm line was kept at 50% of maximum power.

Samples were prepared for blinking studies by aminosilanizing a glass coverslip with aminopropyl trichlorosilane to which a drop of ~100 pM QD solution was added. QDs were immobilized by electrostatic forces between the positively charged amino groups of the silane and the negatively charged carboxylates on the QD. The QDs were measured with the liquid still above them to reduce possible



effects from oxygen in the atmosphere. Drying out of the solution was reduced by placing a reservoir of water next to the sample, and covering the sample stage, which resulted in a humid environment around the sample. Blinking studies of QDs were performed in an epifluorescence configuration on an Olympus IX70 inverted microscope using a halogen-lamp source. A QD filter cube set was used for excitation and emission (excitation = 380–460 nm, dichroic = 475 nm, emission = 500 LP). The excitation light was passed through an Olympus PlanApo oil-immersion objective (60 $\times$ , 1.45 NA) and the emission collected into the same objective. The light is then focused onto a Photometrics Cascade 512 B EM-CCD camera, and a time-stack of images taken at 20 fps (50-millisecond exposure) for 2000 frames using the RSImage software (Roper Scientific, Tucson, Ariz, USA). The images are stored in 16-bit TIFF format for subsequent analysis. Homemade software was written by Dr. Andrei Kobitski at the University of Ulm (Germany) using Matlab 6.5 (Mathworks, Natick, Mass, USA), from which traces of individual QDs are extracted and probability distributions of on and off times are determined. The details of the analysis may be found in previous publications [9, 10]. Briefly, the algorithm aligns each frame of the series and integrates the image stack. Thus, QDs that are on at least once in the time series will be identified. Then, the software measures the integrated signal from the  $3 \times 3$  pixels around the center of the emission (the  $3 \times 3$  pixels is approximately equal to the point spread function of the microscope, and may be manually set by the user of the software) as a function of frame number (time). The local background signal is found from the pixels surrounding the QD in each frame and subtracted. If another QD is too close that the local background cannot be determined, then this QD is ignored. Due to the low QD concentration, this occurs very seldom. This results in a set of traces similar to that shown in Figure 6(b). A threshold is set to  $2\sigma$  of the background signal. It was previously found that if the signal:noise is strong enough, the actual threshold level used (from  $2-4\sigma$ ) does not affect the resulting statistics [10]. Then the durations of times spent in the off state and on state are calculated from all the extracted traces and plotted as a probability histogram (Figure 7, normalized to a total probability of 1).

## ACKNOWLEDGMENTS

This research is funded by U.S. EPA—Science to Achieve Results (STAR) program, Grant no. R831712, by the National Science and Engineering Research Council of Canada (NSERC) Individual Discovery, Grants no. RGPIN 312970 and RGPIN 250013, as well as NanoInnovation Platform. The authors wish to thank Dr. Andrei Kobitski at the University of Ulm for the Matlab codes used for blinking analysis.

## REFERENCES

- [1] J. P. Ryman-Rasmussen, J. E. Riviere, and N. A. Monteiro-Riviere, "Surface coatings determine cytotoxicity and irritation potential of quantum dot nanoparticles in epidermal keratinocytes," *Journal of Investigative Dermatology*, vol. 127, no. 1, pp. 143–153, 2007.
- [2] R. Hardman, "A toxicologic review of quantum dots: toxicity depends on physicochemical and environmental factors," *Environmental Health Perspectives*, vol. 114, no. 2, pp. 165–172, 2006.
- [3] J. Lovrić, H. S. Bazzi, Y. Cuie, G. R. Fortin, F. M. Winnik, and D. Maysinger, "Differences in subcellular distribution and toxicity of green and red emitting CdTe quantum dots," *Journal of Molecular Medicine*, vol. 83, no. 5, pp. 377–385, 2005.
- [4] S. K. Poznyak, N. P. Osipovich, A. Shavel, et al., "Size-dependent electrochemical behavior of thiol-capped CdTe nanocrystals in aqueous solution," *Journal of Physical Chemistry B*, vol. 109, no. 3, pp. 1094–1100, 2005.
- [5] S. J. Clarke, C. A. Hollmann, Z. Zhang, et al., "Photophysics of dopamine-modified quantum dots and effects on biological systems," *Nature Materials*, vol. 5, no. 5, pp. 409–417, 2006.
- [6] B. C. Lagerholm, L. Averett, G. E. Weinreb, K. Jacobson, and N. L. Thompson, "Analysis method for measuring submicron distances with blinking quantum dots," *Biophysical Journal*, vol. 91, no. 8, pp. 3050–3060, 2006.
- [7] M. Nirmal, B. O. Dabbousi, M. G. Bawendi, et al., "Fluorescence intermittency in single cadmium selenide nanocrystals," *Nature*, vol. 383, no. 6603, pp. 802–804, 1996.
- [8] K. T. Shimizu, R. G. Neuhauser, C. A. Leatherdale, S. A. Empedocles, W. K. Woo, and M. G. Bawendi, "Blinking statistics in single semiconductor nanocrystal quantum dots," *Physical Review B*, vol. 63, no. 20, Article ID 205316, 5 pages, 2001.
- [9] A. Y. Kobitski, C. D. Heyes, and G. U. Nienhaus, "Total internal reflection fluorescence microscopy—a powerful tool to study single quantum dots," *Applied Surface Science*, vol. 234, no. 1–4, pp. 86–92, 2004.
- [10] C. D. Heyes, A. Y. Kobitski, V. V. Breus, and G. U. Nienhaus, "Effect of the shell on the blinking statistics of core-shell quantum dots: a single-particle fluorescence study," *Physical Review B*, vol. 75, no. 12, Article ID 125431, 8 pages, 2007.
- [11] A. Bachir, N. Durisic, B. Hebert, P. Grütter, and P. W. Wiseman, "Characterization of blinking dynamics in quantum dot ensembles using image correlation spectroscopy," *Journal of Applied Physics*, vol. 99, no. 6, Article ID 064503, 2006.
- [12] M. Kuno, D. P. Fromm, H. F. Hammann, A. Gallagher, and D. J. Nesbitt, "Nonexponential "blinking" kinetics of single CdSe quantum dots: a universal power law behavior," *Journal of Chemical Physics*, vol. 112, no. 7, pp. 3117–3120, 2000.
- [13] S. Doose, J. M. Tsay, F. Pinaud, and S. Weiss, "Comparison of photophysical and colloidal properties of biocompatible semiconductor nanocrystals using fluorescence correlation spectroscopy," *Analytical Chemistry*, vol. 77, no. 7, pp. 2235–2242, 2005.
- [14] R. F. Heuff, J. L. Swift, and D. T. Cramb, "Fluorescence correlation spectroscopy using quantum dots: advances, challenges and opportunities," *Physical Chemistry Chemical Physics*, vol. 9, no. 16, pp. 1870–1880, 2007.
- [15] U. Banin, M. Bruchez, A. P. Alivisatos, T. Ha, S. Weiss, and D. S. Chemla, "Evidence for a thermal contribution to emission intermittency in single CdSe/CdS core/shell nanocrystals," *Journal of Chemical Physics*, vol. 110, no. 2, pp. 1195–1201, 1999.
- [16] M. Pelton, D. G. Grier, and P. Guyot-Sionnest, "Characterizing quantum-dot blinking using noise power spectra," *Applied Physics Letters*, vol. 85, no. 5, pp. 819–821, 2004.
- [17] A. Issac, C. von Borczyskowski, and F. Cichos, "Correlation between photoluminescence intermittency of CdSe quantum dots and self-trapped states in dielectric media," *Physical Review B*, vol. 71, no. 16, Article ID 161302, 4 pages, 2005.



- [18] M. Kuno, D. P. Fromm, S. T. Johnson, A. Gallagher, and D. J. Nesbitt, "Modeling distributed kinetics in isolated semiconductor quantum dots," *Physical Review B*, vol. 67, no. 12, Article ID 125304, 15 pages, 2003.
- [19] P. A. Frantsuzov and R. A. Marcus, "Explanation of quantum dot blinking without the long-lived trap hypothesis," *Physical Review B*, vol. 72, no. 15, Article ID 155321, 10 pages, 2005.
- [20] S. J. Clarke, C. A. Hollmann, F. A. Aldaye, and J. L. Nadeau, "Effect of ligand density on the spectral and affinity characteristics of quantum dot conjugates," *Bioconjug Chem*, vol. 19, no. 2, pp. 8–562, 2008.
- [21] J. Aldana, Y. A. Wang, and X. Peng, "Photochemical instability of CdSe nanocrystals coated by hydrophilic thiols," *Journal of the American Chemical Society*, vol. 123, no. 36, pp. 8844–8850, 2001.
- [22] F. Pinaud, D. King, H. P. Moore, and S. Weiss, "Bioactivation and cell targeting of semiconductor CdSe/ZnS nanocrystals with phytochelatin-related peptides," *Journal of the American Chemical Society*, vol. 126, no. 19, pp. 6115–6123, 2004.
- [23] R. Verberk, A. M. van Oijen, and M. Orrit, "Simple model for the power-law blinking of single semiconductor nanocrystals," *Physical Review B*, vol. 66, no. 23, Article ID 233202, 4 pages, 2002.
- [24] M. Kuno, D. P. Fromm, H. F. Hamann, A. Gallagher, and D. J. Nesbitt, "'On'/'off' fluorescence intermittency of single semiconductor quantum dots," *Journal of Chemical Physics*, vol. 115, no. 2, pp. 1028–1040, 2001.
- [25] I. Chung and M. G. Bawendi, "Relationship between single quantum-dot intermittency and fluorescence intensity decays from collections of dots," *Physical Review B*, vol. 70, no. 16, Article ID 165304, 5 pages, 2004.
- [26] J. A. Kloepfer, R. E. Mielke, M. S. Wong, K. H. Nealson, G. Stucky, and J. L. Nadeau, "Quantum dots as strain- and metabolism-specific microbiological labels," *Applied and Environmental Microbiology*, vol. 69, no. 7, pp. 4205–4213, 2003.
- [27] J. A. Kloepfer, R. E. Mielke, and J. L. Nadeau, "Uptake of CdSe and CdSe/ZnS quantum dots into bacteria via purine-dependent mechanisms," *Applied and Environmental Microbiology*, vol. 71, no. 5, pp. 2548–2557, 2005.

## Research Article

# Development of FRET-Based Assays in the Far-Red Using CdTe Quantum Dots

E. Z. Chong,<sup>1</sup> D. R. Matthews,<sup>1</sup> H. D. Summers,<sup>1</sup> K. L. Njoh,<sup>2</sup> R. J. Errington,<sup>2</sup> and P. J. Smith<sup>2</sup>

<sup>1</sup> School of Physics and Astronomy, Cardiff University, Cardiff, Wales CF24 3AA, UK

<sup>2</sup> School of Medicine, Cardiff University, Cardiff, Wales CF14 4XN, UK

Correspondence should be addressed to E. Z. Chong, chongez@cf.ac.uk

Received 29 March 2007; Accepted 11 October 2007

Recommended by Marek Osinski

Colloidal quantum dots (QDs) are now commercially available in a biofunctionalized form, and Förster resonance energy transfer (FRET) between bioconjugated dots and fluorophores within the visible range has been observed. We are particularly interested in the far-red region, as from a biological perspective there are benefits in pushing to ~700 nm to minimize optical absorption (ABS) within tissue and to avoid cell autofluorescence. We report on FRET between streptavidin- (STV-) conjugated CdTe quantum dots, Qdot705-STV, with biotinylated DY731-Bio fluorophores in a donor-acceptor assay. We also highlight the changes in DY731-Bio absorptivity during the streptavidin-biotin binding process which can be attributed to the structural reorientation. For fluorescence beyond 700 nm, different alloy compositions are required for the QD core and these changes directly affect the fluorescence decay dynamics producing a marked biexponential decay with a long-lifetime component in excess of 100 nanoseconds. We compare the influence of the two QD relaxation routes upon FRET dynamics in the presence of DY731-Bio.

Copyright © 2007 E. Z. Chong et al. This is an open access article distributed under the Creative Commons Attribution License, which permits unrestricted use, distribution, and reproduction in any medium, provided the original work is properly cited.

## 1. INTRODUCTION

Förster (or fluorescence) resonance energy transfer was first explored in the 1920s [1] and is increasingly gaining the attention of multidisciplinary researchers. FRET is a technique widely used in probing the conformational changes of biomolecules, examining the structural constitution of a targeted cell and monitoring intracellular processes and many other *in vivo* biological applications [2]. The main attraction of FRET is its sensitivity to very small spatial changes, typically in the nanometer range.

FRET is based on the near field interaction between two molecules (dipoles) in very close proximity, at a distance much smaller than the fluorescence wavelength [3, 4]. The excited state energy of the donor molecule can be transferred to the acceptor molecule in the ground state if there is a considerable overlap between the donor emission and the acceptor absorption. In the past, a variety of organic fluorescent labels were used as probes in FRET measurements [3–5]. However, photobleaching effects have impaired their function as reliable fluorescent markers especially in single-molecule spectroscopic applications. With the discovery of new robust fluorescent material such as semiconduc-

tor quantum dots, the possibility of photobleaching the inorganic markers over extended excitation is no longer an issue. QDs are well known for their photostability, high quantum yield (QY), broad absorption spectrum, and narrow emission spectrum [6–8]. In contrast to the standard organic dyes, these favourable features provide a new route to optically pump different size QDs using the same photoexcitation energy, thus promoting multicolour microscopic imaging. The specific application area which we seek to address is *in vitro* cell cycle and cell lineage studies. In this context we have confirmed that there is no discernible toxic effect of core/shell QDs on the cells over typical analysis period of 1–5 days which corroborates the fact that the release of free ions from the core lattice is largely obviated by the surface passivation [9]. Furthermore, with the advent of the commercial core-shell QDs, a variety of emissions that cover the visible and the infrared spectra are readily available. Therefore, in view of the superior photostability, the biocompatibility and the wide selection of commercial core/shell QDs, the potential of QDs as fluorescent labels is very promising.

In this work, we explored the potential of far-red CdTe/ZnS core-shell Qdot705 (Invitrogen) as an efficient donor in a FRET assay. From the bioimaging perspective,

this avoids the detection of autofluorescence, allows the usage of red excitation which has greater depth of penetration into targeted tissue, and facilitates multiphoton absorption/excitation. From a material point of view, the compositional change from selenide to telluride in Qdot705 also makes it an interesting experimental test subject. Broader emission/absorption spectra and a fluorescence decay lifetime well in excess of 100 nanoseconds at room temperature were seen. In our QD FRET investigation, biotinylated DY731-Bio fluorophores with an absorption peak at 720 nm were self-assembled onto Qdot705-STVs that emit at 705 nm using a streptavidin-biotin binding mechanism in the similar conjugation route as that in [10, 11]. Due to the strong spectral overlap between Qdot705-STV emission and DY731-Bio absorption, FRET signatures were detected in the steady state and also in the time domain spectroscopic measurements.

## 2. MATERIALS AND METHODS

### 2.1. DY731-Bio-STV preparation

1 mg of streptavidin powder (Sigma-Aldrich, Dorset, UK) was dissolved in 100  $\mu$ L phosphate buffered saline (PBS 0.01 M, pH 7.4) to make  $\sim 170$   $\mu$ M streptavidin solution. 5  $\mu$ L of the solution was added to 400  $\mu$ L of 2.5  $\mu$ M DY731-Bio to give a loading ratio of 1 with respect to DY731-Bio. As a result, the total biotin binding sites outnumbered DY731-Bio. Hence, only streptavidin bound DY731-Bio were generated. The steady-state absorption profile of DY731-Bio-STV bio-complex was recorded with a UV/Vis/NIR Jasco V570 spectrometer (Tokyo, Japan) for determining DY731-Bio-STV molar extinction coefficient.

### 2.2. Qdot705-STV and DY731-Bio mixture by titrations

10  $\mu$ L of 1  $\mu$ M Qdot705-STV stock (Invitrogen, Calif, USA) was dissolved in 400  $\mu$ L PBS (pH 7.4) in a 10 mm optical path cell. 2  $\mu$ L of 30  $\mu$ M DY731-Bio (MoBiTec, Göttingen, Germany) was first dispensed into the QD solution and then followed by 10 successive titrations of 4  $\mu$ L DY731-Bio. Steady-state photoluminescence (PL) measurements were taken after each titration using a Varian Cary Eclipse fluorimeter (Palo Alto, Calif, USA). For comparison, identical procedures were repeated for control experiments which involved DY731-Bio without the presence of Qdot705-STV.

### 2.3. Qdot705-STV-DY731-Bio conjugates preparation

5 separate PBS diluted Qdot705-STV solutions (220  $\mu$ L,  $\sim 90$  nM) were mixed with increasing amount (4  $\mu$ L to 200  $\mu$ L) of 30  $\mu$ M DY731-Bio to produce Qdot705-STV-DY731-Bio donor-acceptor assay with different labelling ratios. It is estimated that a Qdot705-STV is chemically coupled to 5–10 streptavidin [12]. As streptavidin is a tetrameric protein, approximately 20–40 biotinylated molecules which include DY731-Bio can be arrayed around a single Qdot705-STV. The samples were left to sit at room temperature for 15 minutes. By ultrafiltration with Microcon YM50 spin column (Millipore, Billerica, Mass, USA), the unbound DY731-

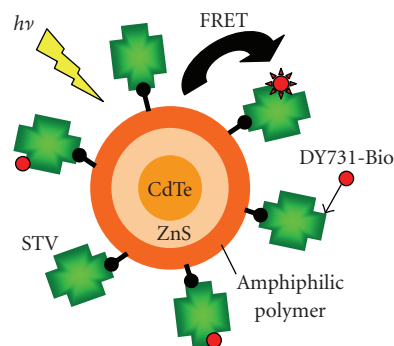


FIGURE 1: Schematic diagram of Qdot705-STV and DY731-Bio in self-assembled assay where energy can be transferred nonradiatively from QD to DY731-Bio upon excitation.

Bio (molecular weight, MW of  $\sim 1$  kDa) were separated from the conjugated pairs. The column with cutoff MW of 50 kDa was spun at a centrifugal speed of  $2000 \times g$  three times for 20 minutes per wash. The collected conjugates were then dissolved in 100  $\mu$ L PBS in 10 mm path length cuvette for time-resolved PL measurements. The average numbers of DY731-Bio per Qdot705-STV were estimated by steady-state absorption using a UV/Vis/NIR Jasco V570 spectrometer in accordance to the molar extinction coefficient at 663 nm for DY731-Bio-STV.

### 2.4. Steady-state absorption and photoluminescence measurements

Steady-state absorptions of Qdot705-STV, DY731-Bio, DY731-Bio-STV and Qdot705-STV-DY731-Bio in PBS (pH 7.4) were measured using a UV/Vis/NIR Jasco V570 spectrometer. Ensemble photoluminescence spectra were recorded with a Varian Cary Eclipse fluorimeter. To measure the photoluminescence spectrum of DY731-Bio, 680 nm excitation was chosen. However, the excitation was set to 425 nm for all FRET experiments in order to reduce the direct excitation of DY731-Bio fluorophores. All measurements were performed under ambient conditions.

### 2.5. Time-resolved photoluminescence measurements

Qdot705-STV-DY731-Bio samples (from Section 2.3) were photoexcited using a Ti:Sapphire laser (Coherent, Santa Clara, Calif, USA) with a repetition rate of 1.1 MHz in order to achieve a longer time window for detecting rather long lived Qdot705-STV photoluminescence. The laser was tuned to 850 nm and was frequency doubled to 425 nm so that direct excitation of DY731-Bio was kept to a minimum. The temporal behaviour of Qdot705-STV in a donor-acceptor assembly was investigated with a Hamamatsu C5680 universal streak camera system (Japan). The photoluminescence of dot ensemble was spectrally filtered using a 700 nm shortpass filter to cutoff unwanted DY731-Bio fluorescence and a 630 nm longpass filter to attenuate any scattered laser. The acquisition of time-resolved photoluminescence was processed using high-performance digital temporal analyser (HPD-TA)

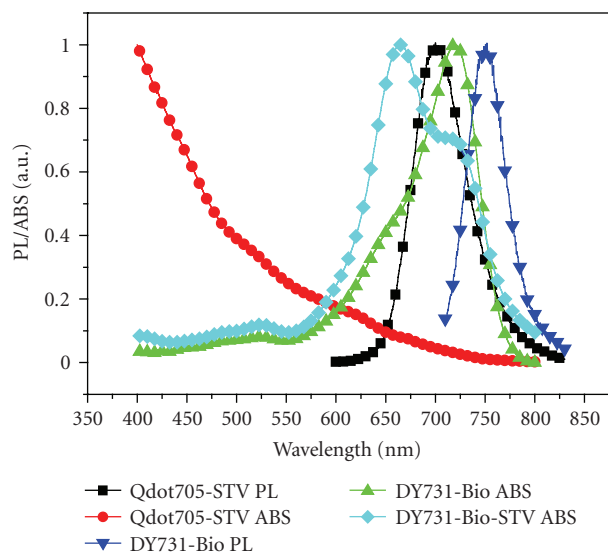


FIGURE 2: Normalised absorption and photoluminescence spectra of Qdot705-STV, DY731-Bio, and DY731-Bio-STV.

software (Hamamatsu, Japan). All measurements were conducted under ambient environmental conditions.

### 3. RESULTS

#### 3.1. Steady-state spectral measurements

##### 3.1.1. Qdot705-STV and DY731-Bio

As shown in Figure 2, Qdot705-STV sample exhibits a broad, continuous absorption spectrum with no pronounced excitonic peak being resolved. The bulk-like spectrum is due to the relative large size variation in the Qdot705-STV ensemble which have a mean diameter of  $\sim 20$  nm [12]. These QDs fluoresce at 705 nm with a full width at half maximum (FWHM) of 70 nm (-■- in Figure 2). The FWHM of Qdot705-STV emission is approximately 3 times broader than that of the commercial CdSe/ZnS Qdots. The inhomogeneous size distribution is likely to be the reason behind the broad photoluminescence spectrum, however, the crystalline geometry and the lattice defects can also be the cofactors to the line width broadening [13].

Unlike Qdot705-STV, pure DY731-Bio have a narrow absorption spectrum that peaks at 720 nm with a weaker secondary absorption at 660 nm. This strongly coincides with the photoluminescence of Qdot705-STV which spreads across the absorption band of DY731-Bio. However, the absorptivity was modified when DY731-Bio were attached to streptavidin, as depicted in Figure 2. The 660 nm absorption strength rose above that of 720 nm peak. This is possibly due to the conformational changes in bound DY731-Bio molecules. The molar extinction coefficients of DY731-Bio-STV at respective 660 nm and 720 nm were found to be  $100\,000\text{ M}^{-1}\text{cm}^{-1}$  and  $70\,000\text{ M}^{-1}\text{cm}^{-1}$  instead of  $50\,000\text{ M}^{-1}\text{cm}^{-1}$  and  $120\,000\text{ M}^{-1}\text{cm}^{-1}$  for pure DY731-Bio.

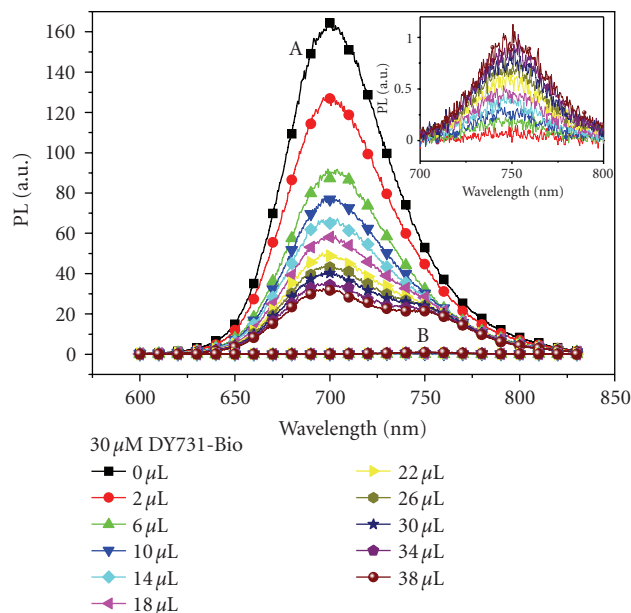


FIGURE 3: Spectra A are the composite photoluminescence of the Qdot705-STV and DY731-Bio mixtures in a series of DY731-Bio titrations. Spectra B are the control photoluminescence of pure DY731-Bio solutions with the equal molar concentration of DY731 as that in the former mixtures. An expanded view of the control spectra is shown in the inset.

The strong overlap between the DY731-Bio absorption and the Qdot705-STV photoluminescence favours the non-radiative energy transfer within the donor-acceptor assay. With the large Stokes shift ( $\sim 30$  nm), DY731-Bio are spectrally well separated from Qdot705-STV and hence, the composite photoluminescence spectrum of a mixed donor-acceptor ensemble can be resolved and deconvoluted into respective spectra for further quantitative FRET analysis.

##### 3.1.2. Qdot705-STV and DY731-Bio mixture by titration

Successive titrations with  $30\text{ }\mu\text{M}$  DY731-Bio solution resulted in the progressive quenching of Qdot705-STV photoluminescence. Initially, the fluorescence signal at 705 nm dropped abruptly but then gradually levelled off after a total of  $\sim 26\text{ }\mu\text{L}$  DY731-Bio have been dispensed into the QD solution. Since the optical densities in the first few titrations ( $2\text{ }\mu\text{L}$ - $22\text{ }\mu\text{L}$ ) were below 0.2, the luminescence quenching in Qdot705-STV was primarily attributed to FRET. The reabsorption of Qdot705-STV photoluminescence by DY731-Bio was anticipated to be less effective. In concomitant with the quenching of Qdot705-STV fluorescence, a systematic enhancement of DY731-Bio photoluminescence was detected as shown in Figure 3(A) with the appearance of a 750 nm peak. The enhanced fluorescence of DY731-Bio in the mixture was many times more intense than the control signal of pure DY731-Bio (see the inset of Figure 3) as the absorption of the solution was dominated by the strong optical interaction with the QD excitons at the excitation wavelength of 425 nm. The quenching of Qdot705-STV emission and the concurrent

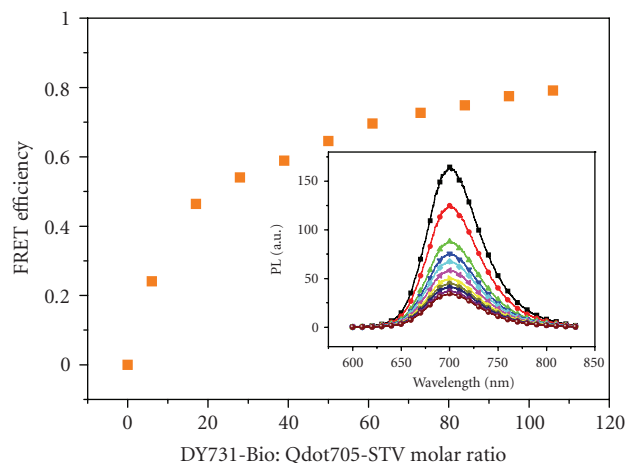


FIGURE 4: The scattered plot represents the FRET efficiency as a function of DY731-Bio to Qdot705-STV molar concentration ratio of nonfiltered mixture. The efficiency calculated is based on the extracted Qdot705-STV spectra (from Spectra A in Figure 3) shown in the inset.

enhancement of DY731-Bio emission signify the occurrence of FRET from the photoexcited Qdot705-STV donors to the ground-state DY731-Bio acceptors.

Since FRET theory is formulated based on proximal dipole-dipole interaction, the excited QDs were generalised as the oscillating dipoles because of the strong electron-hole wavefunction overlap in the core and the weak carrier tunnelling into the wide band gap ZnS shell [14]. FRET efficiency was calculated in accordance to the following equation:

$$E = 1 - \frac{F_{DA}}{F_D}, \quad (1)$$

where  $F_{DA}$  is the integrated donor fluorescence in the presence of the acceptor and  $F_D$  is the integrated donor fluorescence alone. As the equation is only dependent upon the changes of donor emission intensity with acceptor, the relevant Qdot705-STV spectra were extracted from the composite spectra in Figure 3(A), provided that the spectral shape of Qdot705-STV stayed unchanged throughout the measurements. As depicted in Figure 4, despite the undesirable size, a reasonably high-efficient energy transfer ( $\sim 70\%$ ) can be achieved by Qdot705-STV as the FRET donor since its surface area is large enough to interact with multiple DY731-Bio acceptors. However, the plot of FRET efficiency against acceptor/donor ratio shows some signs of saturation when the molar ratio exceeded 50 : 1. After the 50 : 1 molar ratio, the incremental step in FRET efficiency for successive DY731-Bio titrations scaled down dramatically. Unlike the inorganic QD, the conventional organic dyes are generally confined to single donor-acceptor pairing in a FRET assay because of their comparatively small molecular sizes, which in turn impose strict spatial separation condition between the interacting donor-acceptor molecules (typically less than 100 Å) for achieving high FRET efficiency.

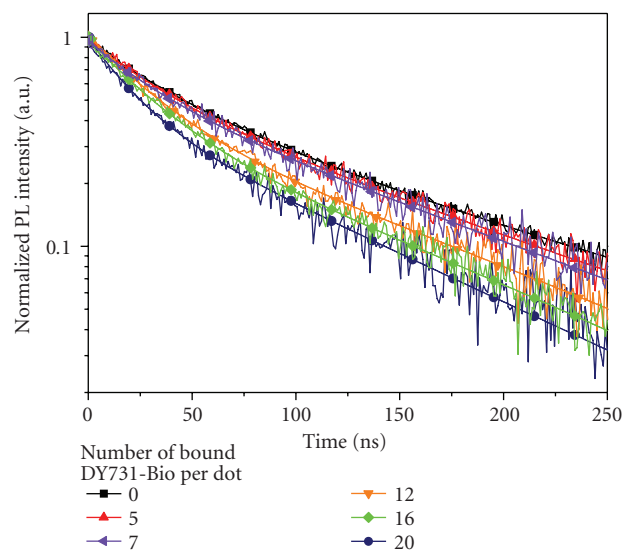


FIGURE 5: Photoluminescence decay of Qdot705-STV with increasing number of labelled DY731-Bio after centrifugation.

### 3.2. Temporal photoluminescence measurements

#### 3.2.1. Qdot705-STV-DY731-Bio conjugates by ultrafiltration

Due to the partial crosstalk, the Qdot705-STV emission was spectrally separated from DY731-Bio using a 700 nm short-pass filter. By monitoring the temporal changes in the fluorescence spectrum below 700 nm, the interaction dynamics of Qdot705-STV ensembles in the presence of bound acceptors were studied. As illustrated in Figure 5, with increasing number of bound DY731-Bio from 5 to 20 per dot, the QD fluorescence decay was progressively shortened. Henceforth, it would appear that an additional nonradiative relaxation pathway was introduced when DY731-Bio fluorophores were self-assembled around Qdot705-STV: the photoexcited QD excitons recombined at a faster rate by coupling to the radiationless transitions. In view of the fact that a Qdot705-STV can be chemically coupled up to 10 tetrameric streptavidin [12], the highest elicited number of labelled DY731-Bio per QD from the absorption measurement was relatively low compared with the prediction that a maximum 40 biotinylated biomolecules can be possibly assembled around a Qdot705-STV. Therefore, this elucidates, in practise, the average number of streptavidin per QD maybe less than 10, and also the obscuration of some of the binding sites due to the compactness of large streptavidin proteins around the QD is not unlikely.

The fluorescence decay curves shown in Figure 5 depict a complex, multiexponential relaxation of the dots and so a specific method of analysis must be adopted in interpreting the data. We use a biexponential fitting that (i) is the simplest approach outside of a monoexponential model and (ii) provides a conceptual framework for interpretation relating to QD photophysics. There are of course alternative measures that could be adopted, for example, the definition of



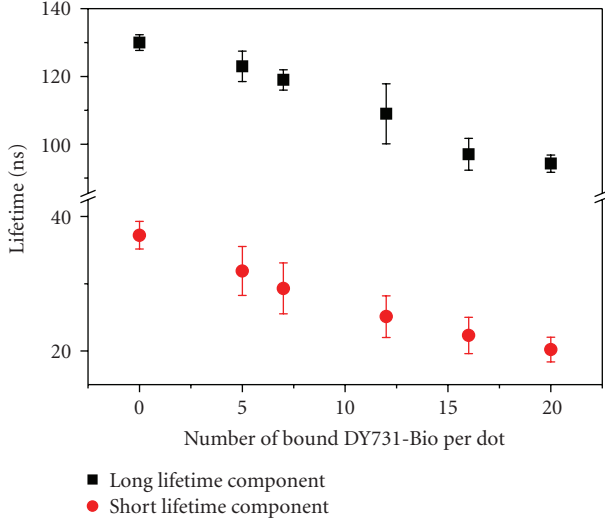


FIGURE 6: Plot of the lifetime components derived from the biexponential fit of Qdot705-STV fluorescence decay versus the number of conjugated DY731-Bio per Qdot705-STV.

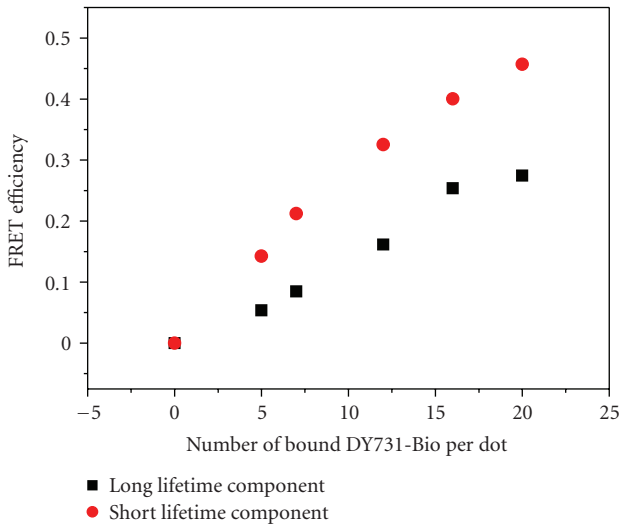


FIGURE 7: FRET efficiency based on Qdot705-STV photoluminescence lifetime measurements plotted against DY731-Bio to Qdot705-STV labelling ratio.

an effective  $1/e$  lifetime. Our main purpose in this paper is to highlight the complexity of the QD decay dynamics and assess the ramifications of this in quantifying FRET-based analyses. The fluorescence dynamic of Qdot705-STV was fitted with the decay function:

$$I(t) = A_1 \exp\left(\frac{-t}{\tau_1}\right) + A_2 \exp\left(\frac{-t}{\tau_2}\right) + Z \quad (2)$$

with  $Z$  as the baseline. Two distinct lifetime components were derived from the fit.  $\tau_1$  fell within 100-nanosecond range and  $\tau_2$  fell within 30-nanosecond range. We associate each lifetime component to different, spatially distinct excitonic relaxation paths [15]. From the two lifetime components,

FRET efficiency was explicitly calculated for each dynamic process using the equation below:

$$E = 1 - \frac{\tau_{DA}}{\tau_D}, \quad (3)$$

where  $\tau_{DA}$  is the donor fluorescence lifetime in the presence of the acceptors and  $\tau_D$  is the donor fluorescence lifetime without the acceptors. Since FRET is the inverse sixth power to  $R$  (donor-acceptor separation), it is intuitive that the efficiency from spatially separated recombination paths will differ. As reflected in Figure 7, the short-lifetime component achieved higher FRET efficiency as compared to that of the long-lifetime component. In this FRET study, we were able to obtain an approximate 46% efficiency from the short-lifetime component at an average 20 bound DY731-Bio per QD. On the contrary, the efficiency was merely 27% for the long-lifetime component at the same labelling ratio. The marked variation asserts the close proximity of the fast decay pathway to the DY731-Bio acceptors.

#### 4. DISCUSSION

Qdot705-STV is a core-shell QD coated with a layer of amphiphilic polymer for water solubility and further surface functionalized with streptavidin for biolinking purposes [16]. Its core is made of direct gap II-VI CdTe with band gap energy of 1.44 eV (at room temperature) [17] which coarsely dictates the emission wavelength of QD. By surface passivation with a larger band gap material like ZnS (3.54 eV at room temperature), the quantum yield of the QDs can be significantly enhanced by suppressing the surface states which may arise from the lattice reconstructions at the final stage of nucleation [6, 7, 18]. However, a perfect passivation is difficult to achieve due to appreciable lattice mismatch between CdTe and ZnS. The lattice constants for CdTe and ZnS are 4.57 Å and 3.81 Å (wurtzite) [17], respectively, which accounts for a total of 17% difference in bond length. In comparison to the visible QDs which are typically made of CdSe, the mismatch is less, at about 12% [6, 19]. So, the surface defects are more predominant in CdTe/ZnS core-shell QDs. The presence of carrier traps near the CdTe/ZnS interface can weaken the oscillator strength of the dipole moment by decreasing the spatial overlap of the exciton wavefunction [20]. Photoexcited electrons are quickly delocalized by surface states, but due to a reduced mobility, the heavier hole is restricted to the inner core. Other factors such as geometrical characteristics of QD (shape and size) can influence the optical absorption as well [13]. Qdot705-STV may not experience the same quantum confinement effects in all dimensions like other commercial visible range Qdots (i.e., Qdot565 and Qdot585) since it adopts a slightly elongated geometry which means that the photoinduced carriers have greater degree of freedom compared to the symmetric spherical QDs [21]. Therefore, the quantization of excited states is less pronounced in the Qdot705-STV absorption spectrum.

Bacterial derivative streptavidin is known to have exceptionally high biotin binding affinity ( $K_a \approx 2.5 \times 10^{13} \text{ M}^{-1}$ ) [22]. Lower nonspecific binding as compared to analogous egg white derivative avidin is an added advantage

in developing superior bioassays for nanosensing devices. In this work, we study the near-field interactions in Qdot705-STV-DY731-Bio self-assembled assay with the use of streptavidin-biotin noncovalent linkers. With the capacity of accommodating multiple bioconjugations and the good spectral overlap between donor emission and acceptor absorption, FRET can occur between large QDs and bioquenchers [23]. In this QD FRET investigation, we were able to achieve high FRET transfer between large Qdot705-STV and DY731-Bio. Besides that, we also observed some drastic changes in the absorption properties of DY731-Bio when they were bound to streptavidin. The 660 nm absorbance was much stronger than the absorbance at 720 nm. The fluorophore probably reoriented itself during the association of streptavidin-biotin and hence, induced some structural changes to accommodate the binding site. It is unlikely that the changes in the absorption were caused by the surface charge of streptavidin since the same spectral shift was detected when DY731-Bio were dispensed in either ethanol or PBS solvents. The analytical interpretation of the FRET-based assay becomes more complicated if the molar extinction coefficient of the acceptor is undesirably modified upon binding. It could possibly influence the overlap integral  $J$ , Förster distance  $R_0$  down to the theoretical FRET efficiency prediction.

Strong enhancement in DY731-Bio emission due to radiationless energy transfer from photoexcited Qdot705-STV was observed. Direct excitation at 425 nm was minimal as shown in Figure 3(B). In contrast to the DY731-Bio acceptor, the photoluminescence of Qdot705-STV was quenched drastically during the initial stage of titrations when the majority of the added DY731-Bio should have attached onto QD surface via streptavidin-biotin affinity. Based on the findings in Section 3.2, after the centrifugation with a Microcon filter device, one Qdot705-STV can bind up to 20 biotinylated acceptors. In regard to that information, for a nonfiltered solution, further titrations (between  $\sim 20 : 1$  and  $\sim 60 : 1$  molar ratio) should only saturate the outermost surface area of the QDs with free DY731-Bio. As a result, the diffused free and the immobilised DY731-Bio were competing for FRET which inherently led to the enhanced efficiency after the molar ratio of  $20 : 1$ . We speculate that the slow growth in the efficiency after  $22 \mu\text{L}$  of DY731-Bio could be the onset of effective radiative quenching by DY731-Bio. It is clear that Qdot705-STV can serve as an efficient donor if the interactions with multiple acceptors are permitted.

The photoluminescence decay of a QD ensemble is multiexponential. The photophysical characteristics in QD ensembles have been correlated to decay-time fluctuations in single QDs [24, 25]. Since the measurements here were taken over an extended period of time, the intensity-dependent effect and the size dispersion in the QD ensemble have averaged out the decay lifetime. The photoluminescence decay can be considered as the collective dynamic behaviour of excited QDs. We statistically fitted the Qdot705-STV photoluminescence decay with discrete biexponential function. The fitted lifetimes were significantly different, 30 nanoseconds and 100 nanoseconds, respectively. Due to a 17% lattice mismatch at the core-shell interface, the formation of fast re-

sponse, carrier trapping states at the surface is highly probable. These surface states provide nonradiative relaxation pathways for the photoinduced electron-hole pairs. Since exciton quenching by surface states usually occurs within sub-nanosecond times, we attribute the fast decay to carrier trapping by surface states and the slow decay to radiative recombination from the band edge. Besides the QD excitonic state, surface states can also couple to DY731-Bio excited state for radiationless energy transfer provided that the surface-state energy level is within the strong absorption band of DY731-Bio. Instead of taking the amplitude-weighted mean lifetime, FRET generated from two separate transitions were studied independently. From Figure 7, the reduction of the long-lifetime component was less significant than that of the short-lifetime component with increasing conjugation ratio. FRET from surface states was apparently more efficient than that from the band edge level. Assuming that this is due to the  $R^{-6}$  relation of FRET, the results are consistent with the interpretation based on the biexponential decay model that the surface states are spatially nearer to labelled DY731-Bio and the band edge recombination primarily occurs within the inner core.

## 5. CONCLUSIONS

We explored the possibility of FRET in a Qdot705-STV-DY731-Bio assembly with the application of strong streptavidin-biotin binding affinity. By careful selection, we minimized the spectral crosstalk between QD donor and fluorophore acceptor emissions but maximized the spectral overlap between donor emission and acceptor absorption. FRET was derived as the resultant of the quenching effect on QD steady-state fluorescence in stepwise DY731-Bio titrations. An efficiency of  $\sim 70\%$  was easily achieved at a molar ratio of 50 acceptors to one QD owing to QD's large surface area. We also recorded the differences in the absorptivity between DY731-Bio and DY731-Bio-STV which could be related to the structural reorientation of fluorophores when molecular complex was formed. However, no further structural studies were conducted to examine the conformation of streptavidin bound DY731-Bio. Any variation in the absorption strength of conjugated acceptor can render FRET less efficient than predicted, if it is based on the optical density of the noninteracting acceptor. By size exclusion filtration, excess DY731-Bio were removed and only Qdot705-STV-DY731-Bio were collected. We achieved  $\sim 20$  acceptors per QD which resulted in  $\sim 50\%$  FRET efficiency. Lifetime measurements on the Qdot705-STV-DY731-Bio assay have further confirmed that FRET can be realized despite the undesirable size of QD. However, the highest efficiency obtainable is limited by the number of streptavidin attached to Qdot705-STV.

## ACKNOWLEDGMENTS

The authors would like to express their gratitude to EPSRC-GSK for the financial support. E. Z. Chong is funded by GSK under DHPA scheme. They also thank RCUK for the support under the "Optical Biochips" Basic Technology project.

## REFERENCES

- [1] R. M. Clegg, "The history of FRET: from conception through the labors of birth," in *Reviews in Fluorescence*, J. R. Lakowicz and C. D. Geddes, Eds., vol. 3, pp. 1–45, Springer, New York, NY, USA, 2006.
- [2] J. R. Lakowicz, *Principles of Fluorescence Spectroscopy*, Springer, Berlin, Germany, 2006.
- [3] I. Z. Steinberg, "Long-range nonradiative transfer of electronic excitation energy in proteins and polypeptides," *Annual Review of Biochemistry*, vol. 40, pp. 83–114, 1971.
- [4] L. Stryer, "Fluorescence energy transfer as a spectroscopic ruler," *Annual Review of Biochemistry*, vol. 47, pp. 819–846, 1978.
- [5] P. G. Wu and L. Brand, "Resonance energy-transfer—methods and applications," *Analytical Biochemistry*, vol. 218, no. 1, pp. 1–13, 1994.
- [6] M. A. Hines and P. Guyot-Sionnest, "Synthesis and characterization of strongly luminescing ZnS-capped CdSe nanocrystals," *Journal of Physical Chemistry*, vol. 100, no. 2, pp. 468–471, 1996.
- [7] B. O. Dabbousi, J. Rodriguez-Viejo, F. V. Mikulec, et al., "(CdSe)ZnS core-shell quantum dots: Synthesis and characterization of a size series of highly luminescent nanocrystallites," *Journal of Physical Chemistry B*, vol. 101, no. 46, pp. 9463–9475, 1997.
- [8] X. Peng, M. C. Schlamp, A. V. Kadavanich, and A. P. Alivisatos, "Epitaxial growth of highly luminescent CdSe/CdS core/shell nanocrystals with photostability and electronic accessibility," *Journal of the American Chemical Society*, vol. 119, no. 30, pp. 7019–7029, 1997.
- [9] W. J. Parak, T. Pellegrino, and C. Plank, "Labelling of cells with quantum dots," *Nanotechnology*, vol. 16, no. 2, pp. R9–R25, 2005.
- [10] D. M. Willard, L. L. Carillo, J. Jung, and A. Van Orden, "CdSe-ZnS quantum dots as resonance energy transfer donors in a model protein-protein binding assay," *Nano Letters*, vol. 1, no. 9, pp. 469–474, 2001.
- [11] E. Oh, M. Y. Hong, D. Lee, S. H. Nam, H. C. Yoon, and H. S. Kim, "Inhibition assay of biomolecules based on fluorescence resonance energy transfer (FRET) between quantum dots and gold nanoparticles," *Journal of the American Chemical Society*, vol. 127, no. 10, pp. 3270–3271, 2005.
- [12] Invitrogen, "Qdot streptavidin conjugates user manual," 2006.
- [13] A. P. Alivisatos, "Perspectives on the physical chemistry of semiconductor nanocrystals," *Journal of Physical Chemistry*, vol. 100, no. 31, pp. 13226–13239, 1996.
- [14] A. R. Clapp, I. L. Medintz, and H. Mattoussi, "Förster resonance energy transfer investigations using quantum-dot fluorophores," *ChemPhysChem*, vol. 7, no. 1, pp. 47–57, 2006.
- [15] L. A. Padilha, A. A.-R. Neves, C. L. Cesar, L. C. Barbosa, and C. H. Brito-Cruz, "Recombination processes in CdTe quantum-dot-doped glasses," *Applied Physics Letters*, vol. 85, no. 15, pp. 3256–3258, 2004.
- [16] X. Y. Wu, H. J. Liu, J. Q. Liu, et al., "Immunofluorescent labeling of cancer marker Her2 and other cellular targets with semiconductor quantum dots," *Nature Biotechnology*, vol. 21, no. 1, pp. 41–46, 2003.
- [17] D. R. Lide, Ed., *CRC Handbook of Chemistry and Physics*, CRC Press, Boca Raton, FL, USA, 2001.
- [18] A. P. Alivisatos, "Semiconductor clusters, nanocrystals, and quantum dots," *Science*, vol. 271, no. 5251, pp. 933–937, 1996.
- [19] M. Nirmal and L. Brus, "Luminescence photophysics in semiconductor nanocrystals," *Accounts of Chemical Research*, vol. 32, no. 5, pp. 407–414, 1999.
- [20] Y. Wang and N. Herron, "Nanometer-sized semiconductor clusters: materials synthesis, quantum size effects, and photophysical properties," *Journal of Physical Chemistry*, vol. 95, no. 2, pp. 525–532, 1991.
- [21] B. N.-G. Giepmans, T. J. Deerinck, B. L. Smarr, Y. Z. Jones, and M. H. Ellisman, "Correlated light and electron microscopic imaging of multiple endogenous proteins using Quantum dots," *Nature Methods*, vol. 2, no. 10, pp. 743–749, 2005.
- [22] A. Chilkoti and P. S. Stayton, "Molecular origins of the slow streptavidin-biotin dissociation kinetics," *Journal of the American Chemical Society*, vol. 117, no. 43, pp. 10622–10628, 1995.
- [23] A. R. Clapp, I. L. Medintz, J. M. Mauro, B. R. Fisher, M. G. Bawendi, and H. Mattoussi, "Fluorescence resonance energy transfer between quantum dot donors and dye-labeled protein acceptors," *Journal of the American Chemical Society*, vol. 126, no. 1, pp. 301–310, 2004.
- [24] G. Schlegel, J. Bohnenberger, I. Potapova, and A. Mews, "Fluorescence decay time of single semiconductor nanocrystals," *Physical Review Letters*, vol. 88, no. 13, pp. 1374011–1374014, 2002.
- [25] B. R. Fisher, H.-J. Eisler, N. E. Stott, and M. G. Bawendi, "Emission intensity dependence and single-exponential behavior in single colloidal quantum dot fluorescence lifetimes," *Journal of Physical Chemistry B*, vol. 108, no. 1, pp. 143–148, 2004.

## Research Article

# Fluorescence Resonance Energy Transfer in Quantum Dot-Protein Kinase Assemblies

Ibrahim Yildiz,<sup>1</sup> Xinxin Gao,<sup>2</sup> Thomas K. Harris,<sup>2</sup> and Francisco M. Raymo<sup>1</sup>

<sup>1</sup> Center for Supramolecular Science, Department of Chemistry, University of Miami, 1301 Memorial Drive, Coral Gables, FL 33146-0431, USA

<sup>2</sup> Department of Biochemistry and Molecular Biology, Miller School of Medicine, University of Miami, Miami, FL 33101-6129, USA

Correspondence should be addressed to Francisco M. Raymo, framo@miami.edu

Received 31 May 2007; Revised 4 September 2007; Accepted 24 December 2007

Recommended by Marek Osinski

In search of viable strategies to identify selective inhibitors of protein kinases, we have designed a binding assay to probe the interactions of human phosphoinositide-dependent protein kinase-1 (PDK1) with potential ligands. Our protocol is based on fluorescence resonance energy transfer (FRET) between semiconductor quantum dots (QDs) and organic dyes. Specifically, we have expressed and purified the catalytic kinase domain of PDK1 with an N-terminal histidine tag [His<sub>6</sub>-PDK1( $\Delta$ PH)]. We have conjugated this construct to CdSe-ZnS core-shell QDs coated with dihydrolipoic acid (DHLLA) and tested the response of the resulting assembly to a molecular dyad incorporating an ATP ligand and a BODIPY chromophore. The supramolecular association of the BODIPY-ATP dyad with the His<sub>6</sub>-PDK1( $\Delta$ PH)-QD assembly encourages the transfer of energy from the QDs to the BODIPY dyes upon excitation. The addition of ATP results in the displacement of BODIPY-ATP from the binding domain of the His<sub>6</sub>-PDK1( $\Delta$ PH) conjugated to the nanoparticles. The competitive binding, however, does not prevent the energy transfer process. A control experiment with QDs, lacking the His<sub>6</sub>-PDK1( $\Delta$ PH), indicates that the BODIPY-ATP dyad adsorbs nonspecifically on the surface of the nanoparticles, promoting the transfer of energy from the CdSe core to the adsorbed BODIPY dyes. Thus, the implementation of FRET-based assays to probe the binding domain of PDK1 with luminescent QDs requires the identification of energy acceptors unable to interact nonspecifically with the surface of the nanoparticles.

Copyright © 2007 Ibrahim Yildiz et al. This is an open access article distributed under the Creative Commons Attribution License, which permits unrestricted use, distribution, and reproduction in any medium, provided the original work is properly cited.

## 1. INTRODUCTION

The outstanding photophysical properties of semiconductor quantum dots (QDs) have encouraged the development of binding assays, based on fluorescence resonance energy transfer (FRET), for the detection of a diversity of biorelevant analytes [1–5]. Some of these sensing protocols are aimed at the investigation of protein-ligand interactions relying on FRET in QD-protein-dye assemblies. For example, the maltose binding protein (MBP) was expressed with a C-terminal oligohistidine segment to promote its adsorption on the surface of CdSe-ZnS core-shell QDs coated with dihydrolipoic acid (DHLLA) [6, 7]. By conjugating the dark quencher QSY9 to  $\beta$ -cyclodextrin, it was shown that titration of the solution containing QD-bound MBP with  $\beta$ -cyclodextrin-QSY9 effectively quenched the nanoparticle luminescence. Such a system was further demonstrated to function as a prototype nanosensor. In fact, the QD luminescence could be re-

stored on subsequent titration with maltose, which competitively displaced  $\beta$ -cyclodextrin-QSY9 from the sugar binding pocket. In principle, a similar strategy could be invoked for the detection of compounds that competitively displace an enzyme-bound dye-labeled substrate for use in high-throughput drug screening assays.

Discovering potent and selective inhibitors of individual members of the protein kinase superfamily has proved to be a long and arduous task. Whereas a large number of high affinity inhibitors have been identified, the majority of such compounds exhibit broad specificity since they typically bind in the ATP-binding cleft shared among all kinase enzymes [8–10]. The matter is further complicated by the fact that the protein kinase superfamily is the largest enzyme family with an estimated 518 members in the human genome [11]. The broad specificity kinase inhibitors are commonly identified in high-throughput enzymatic screening assays, whereby kinase activity is monitored by phosphorylation-induced



fluorescence changes in model peptide substrates. Such enzymatic assays demand active forms of the kinase, which require one or more critical residues to be phosphorylated. Inspection of X-ray structures available for the catalytic domains of different kinases in their phosphorylated and active forms shows highly homologous structures, especially in the ATP-binding cleft [12]. However, known structures of catalytic kinase domains in their unphosphorylated and inactive forms reveal greater divergence of conformational space, which may better accommodate selective binding of compounds that stabilize inactive conformations [12]. Thus, we sought to determine whether competitive displacement of dye-labeled ATP from protein kinase-QD assemblies could be used as a sensitive assay for the detection of compounds that bind either active or inactive forms of kinases.

The human phosphoinositide-dependent protein kinase-1 (PDK1) is particularly well suited to initiate development of QD-mediated competitive binding assays. PDK1 is a member of the AGC subfamily of serine-threonine protein kinases and is comprised of an N-terminal catalytic kinase domain and a C-terminal pleckstrin homology (PH) domain [13]. Baculovirus-mediated expression in Sf9 insect cells and affinity purification of the recombinant catalytic domain construct of PDK1 (residues 51–359) with an N-terminal His<sub>6</sub> tag is well established, and this construct [His<sub>6</sub>-PDK1( $\Delta$ PH)] exhibits high solution stability [14–16]. His<sub>6</sub>-PDK1( $\Delta$ PH) catalyzes autophosphorylation of Ser-241 located in its activation or T-loop, which is the only post-translational modification required for its kinase function [14–16]. Most interestingly, Ser-241 monophosphorylated His<sub>6</sub>-PDK1( $\Delta$ PH) remains relatively inactive, and it is ultimately activated by allosteric interaction with a phosphorylated hydrophobic motif (HM) at the C-terminus of its protein substrate [14–16]. The phosphorylated HM has been termed the “PDK1 interacting fragment” or PIF, and it binds to the PIF pocket on the N-lobe of the PDK1 kinase domain [17–20]. Kinetic studies indicate that His<sub>6</sub>-PDK1( $\Delta$ PH) approximates a Rapid Equilibrium Random Bi Bi System so that it readily forms a high-affinity complex with ATP in the absence of protein substrate [15], as exemplified by the X-ray structure reported for the binary enzyme-nucleotide complex [14]. In this article, we report the ability of His<sub>6</sub>-PDK1( $\Delta$ PH) to adsorb on the surface of CdSe-ZnS core-shell QDs coated with DHLA and the interactions of the resulting assemblies with a compound incorporating an ATP ligand and a BODIPY chromophore within its molecular skeleton.

## 2. MATERIALS AND METHODS

CdSe-ZnS core-shell QDs were prepared following literature procedures [21, 22] and then coated with DHLA according to an established protocol [23]. His<sub>6</sub>-PDK1( $\Delta$ PH) was expressed using the Bac-to-Bac Baculovirus Expression System (Invitrogen, Inc., Carlsbad, Calif, USA) and purified as reported earlier [24]. BODIPY TR adenosine 5'-triphosphate (BODIPY-ATP) was purchased from commercial sources (Invitrogen, Inc.). Visible absorption spectra were recorded with a Varian Cary 100 Bio spectrometer using quartz cells with a path length of 0.5 cm. Emission spectra were recorded

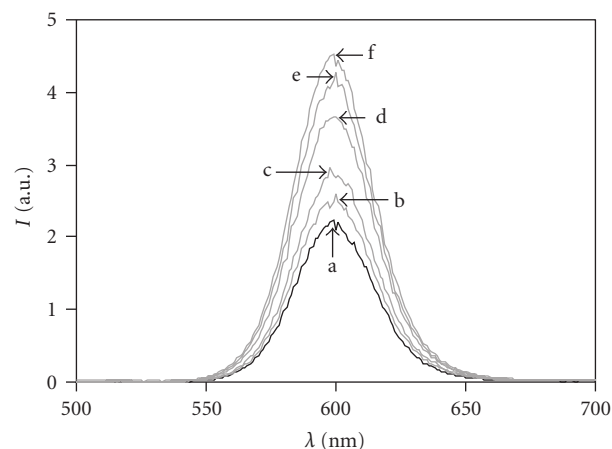


FIGURE 1: Emission spectra of CdSe-ZnS core-shell QDs (0.1  $\mu$ M in borate buffer, pH = 7.4,  $T = 20^\circ\text{C}$ ,  $\lambda_{\text{EX}} = 442\text{ nm}$ ) coated with DHLA in the absence (a) and presence of 0.5 (b), 1.0 (c), 2.0 (d), 5.0 (e), and 10.0 (f)  $\mu$ M of His<sub>6</sub>-PDK1( $\Delta$ PH).

with a Varian Cary Eclipse spectrometer in aerated solutions and are uncorrected with the exception of those shown in Figure 8.

## 3. RESULTS AND DISCUSSION

The emission spectrum (a in Figure 1) of CdSe-ZnS core-shell QDs coated with DHLA in borate buffer (pH = 7.4) shows an intense band centered at 600 nm with a quantum yield of 0.2. The addition of His<sub>6</sub>-PDK1( $\Delta$ PH) to this dispersion affects the emissive behavior of the nanoparticles. Specifically, the luminescence increases with the concentration of His<sub>6</sub>-PDK1( $\Delta$ PH) (a–f in Figure 1) in agreement with the adsorption of the protein on the surface of the QDs. Indeed, literature reports [6] demonstrate that the coating of CdSe-ZnS core-shell QDs with histidine-tagged proteins leads to a luminescence enhancement, as a result of the significant change in the local environment around the emissive inorganic particles. In particular, the plot (see Figure 2) of the emission intensity of our QDs at 600 nm against the relative concentration of His<sub>6</sub>-PDK1( $\Delta$ PH) shows that saturation is reached at a protein/QD ratio of ca. 30. Under these conditions, the luminescence quantum yield of the nanoparticles is 0.4.

The absorption spectrum (a in Figure 3) of BODIPY-ATP shows an intense band for the fluorescent component of this dyad in the visible region. This absorption is positioned in the same range of wavelengths where our QDs emit (b in Figure 3) with an overlap integral of  $5.3 \cdot 10^{-13} \text{ M}^{-1} \text{ cm}^3$ , suggesting that the BODIPY dye can accept the excitation energy of these nanoparticles. The overlap integral ( $J$ ) was calculated from the emission intensity ( $I$ ) of the quantum dots, the molar extinction coefficient ( $\epsilon$ ) of the BODIPY dye and the wavelength ( $\lambda$ ) using

$$J = \frac{\int_0^\infty \epsilon \lambda^4 d\lambda}{\int_0^\infty I d\lambda}. \quad (1)$$

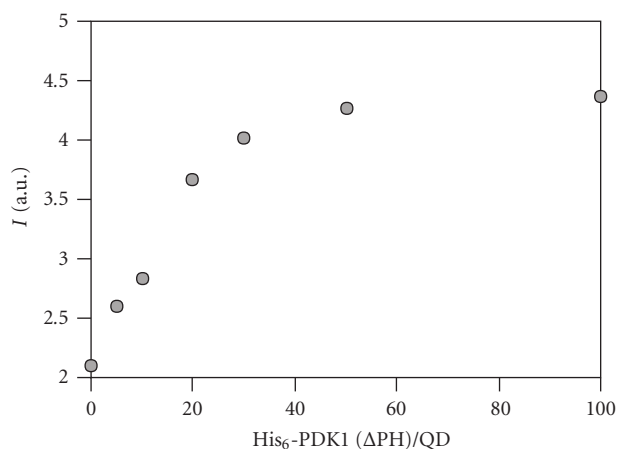


FIGURE 2: Emission intensity at 600 nm of CdSe-ZnS core-shell QDs ( $0.1 \mu\text{M}$  in borate buffer,  $\text{pH} = 7.4$ ,  $T = 20^\circ\text{C}$ ,  $\lambda_{\text{EX}} = 442 \text{ nm}$ ) coated with DHLA against the ratio between the concentration of His<sub>6</sub>-PDK1(ΔPH) and that of the QDs.

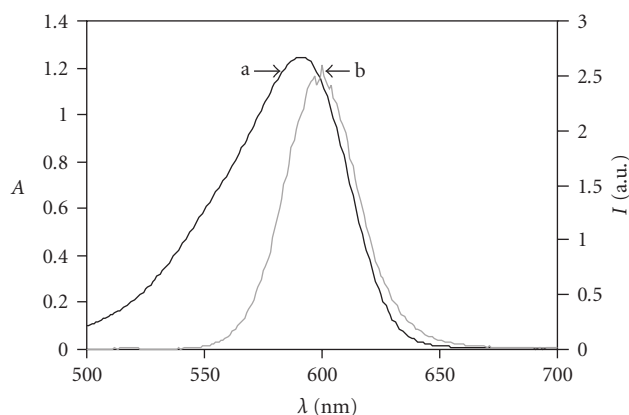


FIGURE 3: Absorption spectrum (a) of BODIPY-ATP ( $30 \mu\text{M}$ ) and emission spectrum (b) of CdSe-ZnS core-shell QDs ( $0.1 \mu\text{M}$ ) and His<sub>6</sub>-PDK1(ΔPH) in borate buffer ( $\text{pH} = 7.4$ ,  $T = 20^\circ\text{C}$ ,  $\lambda_{\text{EX}} = 442 \text{ nm}$ ).

Thus, the supramolecular association of the ATP fragment of the dyad with the His<sub>6</sub>-PDK1(ΔPH) coating of the QDs can be exploited to bring the BODIPY fluorophore in close proximity to the nanoparticles and encourage the transfer of energy from the emissive CdSe core to the organic dye (a in Figure 4). Indeed, the addition of increasing amounts of BODIPY-ATP to the His<sub>6</sub>-PDK1(ΔPH)-QD conjugate alters significantly the emission spectrum (a–g in Figure 5). In particular, the emission band of the QDs at 600 nm fades with an increase in the concentration of BODIPY-ATP. Concomitantly, a second band for the BODIPY fluorophore grows at 624 nm in agreement with the expected transfer of energy from the nanoparticles to the organic dye upon excitation.

In principle, the addition of a ligand able to displace BODIPY-ATP from the complementary recognition site of the His<sub>6</sub>-PDK1(ΔPH)-QD conjugate should result in the physical separation of the nanoparticle donor from the BOD-

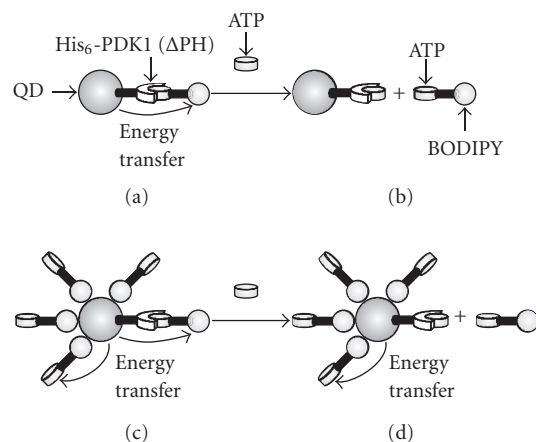


FIGURE 4: The supramolecular association of BODIPY-ATP with His<sub>6</sub>-PDK1(ΔPH)-QD encourages the transfer of energy from QD to BODIPY upon excitation (a). ATP displaces BODIPY-ATP from the recognition site of His<sub>6</sub>-PDK1(ΔPH)-QD and is expected to prevent energy transfer (b). The nonspecific adsorption of BODIPY-ATP on the surface of QD, however, can also encourage energy transfer (c). Under these conditions, the displacement of BODIPY-ATP by ATP is not sufficient to prevent energy transfer.

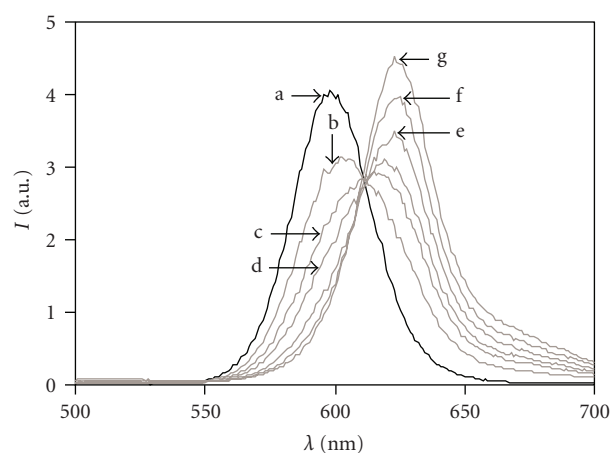


FIGURE 5: Emission spectra of a dispersion of CdSe-ZnS core-shell QDs ( $0.1 \mu\text{M}$ ) and His<sub>6</sub>-PDK1(ΔPH) ( $10 \mu\text{M}$ ) in borate buffer ( $\text{pH} = 7.4$ ,  $T = 20^\circ\text{C}$ ,  $\lambda_{\text{EX}} = 442 \text{ nm}$ ) in the absence (a) and presence of 1.0 (b), 3.0 (c), 5.0 (d), 10.0 (e), 20.0 (f), and 30.0 (g)  $\mu\text{M}$  of BODIPY-ATP.

IPY acceptor and, therefore, suppress the energy transfer processes (b in Figure 4). Consistently, the addition of increasing amounts of ATP to a solution of the complex formed between BODIPY-ATP and His<sub>6</sub>-PDK1(ΔPH)-QD causes a decrease in emission intensity with a concomitant hypsochromic shift (a–f in Figure 6). Instead, the titration of a dispersion of the QDs ( $0.1 \mu\text{M}$ ) with ATP ( $0$ – $30 \mu\text{M}$ ) has no influence on their emission spectrum. The deconvolution of the final spectrum (a in Figure 7) shows the observed emission to be the sum of two distinct bands (b and c in Figure 7). One of them (b in Figure 7) is centered at 600 nm, corresponds to the emission

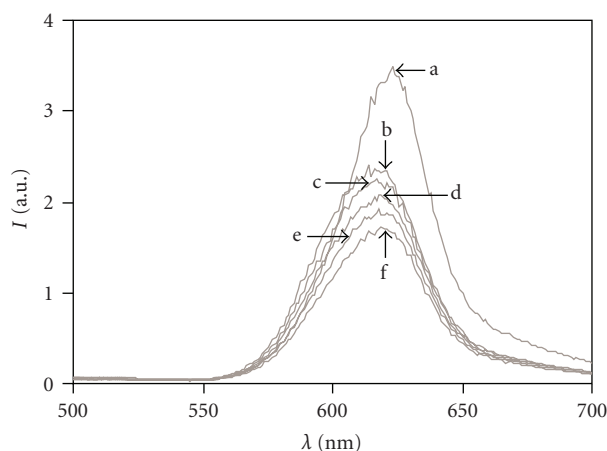


FIGURE 6: Emission spectra of a mixture of CdSe-ZnS core-shell QDs ( $0.1 \mu\text{M}$ ), His<sub>6</sub>-PDK1( $\Delta\text{PH}$ ) ( $10 \mu\text{M}$ ) and BODIPY-ATP ( $10 \mu\text{M}$ ) in borate buffer ( $\text{pH} = 7.4$ ,  $T = 20^\circ\text{C}$ ,  $\lambda_{\text{EX}} = 442 \text{ nm}$ ) in the absence (a) and presence of 1 (b), 3 (c), 11 (d), 31 (e), and 301 (f)  $\mu\text{M}$  of ATP.

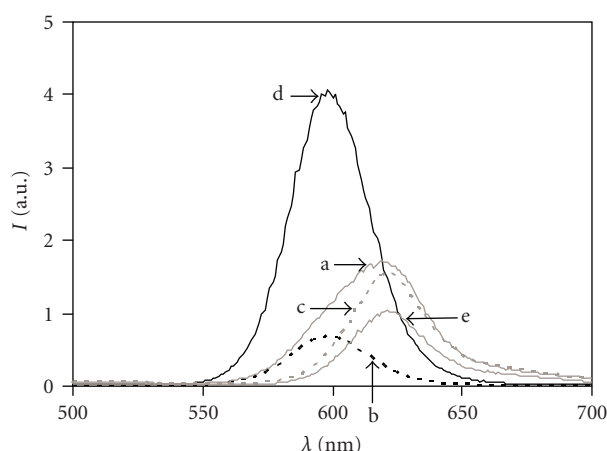


FIGURE 7: Emission spectra of a mixture of CdSe-ZnS core-shell QDs ( $0.1 \mu\text{M}$ ), His<sub>6</sub>-PDK1( $\Delta\text{PH}$ ) ( $10 \mu\text{M}$ ), BODIPY-ATP ( $10 \mu\text{M}$ ) and ATP ( $301 \mu\text{M}$ ) (a) CdSe-ZnS core-shell QDs ( $0.1 \mu\text{M}$ ) (d) and BODIPY-ATP ( $10 \mu\text{M}$ ) (e) in borate buffer ( $\text{pH} = 7.4$ ,  $T = 20^\circ\text{C}$ ,  $\lambda_{\text{EX}} = 442 \text{ nm}$ ). Deconvolution (b and c) of trace a.

of the QDs, and its intensity is significantly smaller than that recorded for a dispersion of the QDs alone (d in Figure 7) under otherwise identical conditions. The other band (c in Figure 7) is centered at 624 nm, corresponds to the emission of the BODIPY dyes, and its intensity is greater than that recorded for BODIPY-ATP alone (e in Figure 7) under otherwise identical conditions. Thus, the QDs recover their luminescence only in part, even after the addition of a relatively large amount of ATP, and still sensitize the emission of the BODIPY dyes under these conditions. These observations suggest that a fraction of the BODIPY-ATP conjugates remains associated with the QDs even in the presence of an excess of ATP (c and d in Figure 4). In agreement with this interpretation, the addition of increasing amounts of

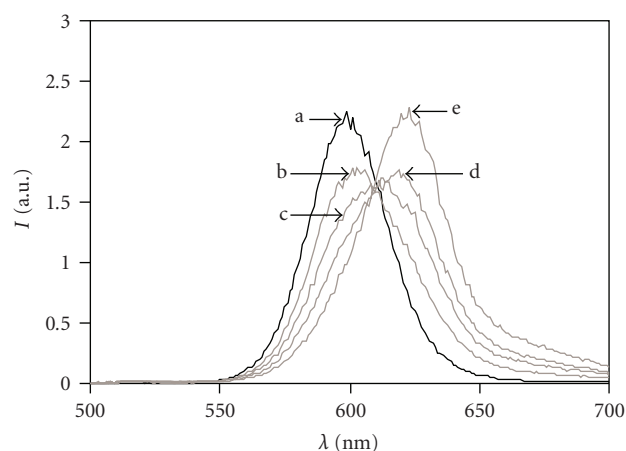


FIGURE 8: Emission spectra of CdSe-ZnS core-shell QDs ( $0.1 \mu\text{M}$  in borate buffer,  $\text{pH} = 7.4$ ,  $T = 20^\circ\text{C}$ ,  $\lambda_{\text{EX}} = 442 \text{ nm}$ ) in the absence (a) and presence of 1.0 (b), 3.0 (c), 5.0 (d), and 10.0 (e)  $\mu\text{M}$  of BODIPY-ATP.

BODIPY-ATP to a dispersion of QDs leads to the disappearance of the nanoparticle emission at 600 nm with the concomitant appearance of the BODIPY emission at 624 nm (a–e in Figure 8). Hence, the BODIPY-ATP can accept the excitation energy of the QDs despite the absence of the His<sub>6</sub>-PDK1( $\Delta\text{PH}$ ) coating around the nanoparticles. These results suggest that the BODIPY-ATP conjugate can adsorb non-specifically on the QDs, presumably, as a result of interactions between the chromophoric component and the surface of the nanoparticles.

#### 4. CONCLUSIONS

The incubation of CdSe-ZnS core-shell QDs, coated with DHLA, and His<sub>6</sub>-PDK1( $\Delta\text{PH}$ ) in borate buffer ( $\text{pH} = 7.4$ ) leads to the adsorption of proteins on the surface of the nanoparticles with a concomitant luminescence enhancement. The dependence of the emission intensity on the protein concentration suggests that an average of ca. 30 proteins adsorb on each QD. The exposure of the His<sub>6</sub>-PDK1( $\Delta\text{PH}$ )-QD conjugate to a BODIPY-ATP dyad brings the inorganic nanoparticle in close proximity to the BODIPY chromophore, encouraging the transfer of energy from the former to the latter. Consistently, the emission band of the QDs fades, as the concentration of BODIPY-ATP increases, with the concomitant growth of an emission band for organic dye. The competitive binding of ATP, however, restores the nanoparticle luminescence only in part. Indeed, control experiments show the occurrence of energy transfer between QDs lacking the His<sub>6</sub>-PDK1( $\Delta\text{PH}$ ) shell and BODIPY-ATP. These observations suggest that the organic chromophore adsorbs nonspecifically on the surface of the nanoparticles. Thus, the development of binding assays for PDK1 based on QDs and FRET demands the identification of strategies to prevent the direct adsorption of the energy acceptor on the surface of the nanoparticle donor.

## ACKNOWLEDGMENT

This work was supported by the National Institutes of Health (GM-69868 to T.K.H.) and National Science Foundation (CAREER Award CHE-0237578 to F.M.R.).

## REFERENCES

- [1] K. E. Sapsford, L. Berti, and I. L. Medintz, "Materials for fluorescence resonance energy transfer analysis: beyond traditional donor-acceptor combinations," *Angewandte Chemie International Edition*, vol. 45, no. 28, pp. 4562–4588, 2006.
- [2] A. R. Clapp, I. L. Medintz, and H. Mattoussi, "Förster resonance energy transfer investigations using quantum-dot fluorophores," *ChemPhysChem*, vol. 7, no. 1, pp. 47–57, 2006.
- [3] A. C. S. Samia, S. Dayal, and C. Burda, "Quantum dot-based energy transfer: perspectives and potential for applications in photodynamic therapy," *Photochemistry and Photobiology*, vol. 82, no. 3, pp. 617–625, 2006.
- [4] R. C. Somers, M. G. Bawendi, and D. G. Nocera, "CdSe nanocrystal based chem-/bio-sensors," *Chemical Society Reviews*, vol. 36, no. 4, pp. 579–591, 2007.
- [5] F. M. Raymo and I. Yildiz, "Luminescent chemosensors based on semiconductor quantum dots," *Physical Chemistry Chemical Physics*, vol. 9, no. 17, pp. 2036–2043, 2007.
- [6] I. L. Medintz, A. R. Clapp, H. Mattoussi, E. R. Goldman, B. Fisher, and J. M. Mauro, "Self-assembled nanoscale biosensors based on quantum dot FRET donors," *Nature Materials*, vol. 2, no. 9, pp. 630–638, 2003.
- [7] E. R. Goldman, I. L. Medintz, J. L. Whitley, et al., "A hybrid quantum dot-antibody fragment fluorescence resonance energy transfer-based TNT sensor," *Journal of the American Chemical Society*, vol. 127, no. 18, pp. 6744–6751, 2005.
- [8] M. E. M. Noble, J. A. Endicott, and L. N. Johnson, "Protein kinase inhibitors: insights into drug design from structure," *Science*, vol. 303, no. 5665, pp. 1800–1805, 2004.
- [9] S. P. Davies, H. Reddy, M. Caivano, and P. Cohen, "Specificity and mechanism of action of some commonly used protein kinase inhibitors," *Biochemical Journal*, vol. 351, no. 1, pp. 95–105, 2000.
- [10] J. Bain, H. McLauchlan, M. Elliott, and P. Cohen, "The specificities of protein kinase inhibitors: an update," *Biochemical Journal*, vol. 371, no. 1, pp. 199–204, 2003.
- [11] G. Manning, D. B. Whyte, R. Martinez, T. Hunter, and S. Sudarsanam, "The protein kinase complement of the human genome," *Science*, vol. 298, no. 5600, pp. 1912–1934, 2002.
- [12] M. Huse and J. Kuriyan, "The conformational plasticity of protein kinases," *Cell*, vol. 109, no. 3, pp. 275–282, 2002.
- [13] D. R. Alessi, M. Deak, A. Casamayor, et al., "3-phosphoinositide-dependent protein kinase-1 (PDK1): structural and functional homology with the *drosophila* DSTPK61 kinase," *Current Biology*, vol. 7, no. 10, pp. 776–789, 1997.
- [14] R. M. Biondi, D. Komander, C. C. Thomas, et al., "High resolution crystal structure of the human PDK1 catalytic domain defines the regulatory phosphopeptide docking site," *The EMBO Journal*, vol. 21, no. 16, pp. 4219–4228, 2002.
- [15] X. Gao and T. K. Harris, "Steady-state kinetic mechanism of PDK1," *Journal of Biological Chemistry*, vol. 281, no. 31, pp. 21670–21681, 2006.
- [16] X. Gao and T. K. Harris, "Role of the PH domain in regulating in vitro autophosphorylation events required for reconstitution of PDK1 catalytic activity," *Bioorganic Chemistry*, vol. 34, no. 4, pp. 200–223, 2006.
- [17] R. M. Biondi, P. C. F. Cheung, A. Casamayor, M. Deak, R. A. Currie, and D. R. Alessi, "Identification of a pocket in the PDK1 kinase domain that interacts with PIF and the C-terminal residues of PKA," *The EMBO Journal*, vol. 19, no. 5, pp. 979–988, 2000.
- [18] R. M. Biondi, A. Kieloch, R. A. Currie, M. Deak, and D. R. Alessi, "The PIF-binding pocket in PDK1 is essential for activation of S6K and SGK, but not PKB," *The EMBO Journal*, vol. 20, no. 16, pp. 4380–4390, 2001.
- [19] M. Frödin, T. L. Antal, B. A. Dümmler, et al., "A phosphoserine/threonine-binding pocket in AGC kinases and PDK1 mediates activation by hydrophobic motif phosphorylation," *The EMBO Journal*, vol. 21, no. 20, pp. 5396–5407, 2002.
- [20] M. Engel, V. Hindie, L. A. Lopez-Garcia, et al., "Allosteric activation of the protein kinase PDK1 with low molecular weight compounds," *The EMBO Journal*, vol. 25, no. 23, pp. 5469–5480, 2006.
- [21] B. O. Dabbousi, J. Rodriguez-Viejo, F. V. Mikulec, et al., "(CdSe)ZnS core-shell quantum dots: synthesis and characterization of a size series of highly luminescent nanocrystallites," *Journal of Physical Chemistry B*, vol. 101, no. 46, pp. 9463–9475, 1997.
- [22] Z. A. Peng and X. Peng, "Formation of high-quality CdTe, CdSe, and CdS nanocrystals using CdO as precursor," *Journal of the American Chemical Society*, vol. 123, no. 1, pp. 183–184, 2001.
- [23] H. Mattoussi, J. M. Mauro, E. R. Goldman, et al., "Self-assembly of CdSe-ZnS quantum dot bioconjugates using an engineered recombinant protein," *Journal of the American Chemical Society*, vol. 122, no. 49, pp. 12142–12150, 2000.
- [24] X. Gao, P. Yo, and T. K. Harris, "Improved yields for baculovirus-mediated expression of human His<sub>6</sub>-PDK1 and His<sub>6</sub>-PKB $\beta$ /Akt2 and characterization of phospho-specific isoforms for design of inhibitors that stabilize inactive conformations," *Protein Expression and Purification*, vol. 43, no. 1, pp. 44–56, 2005.



## Research Article

# Time-Resolved Analysis of a Highly Sensitive Förster Resonance Energy Transfer Immunoassay Using Terbium Complexes as Donors and Quantum Dots as Acceptors

Niko Hildebrandt,<sup>1</sup> Loïc J. Charbonnière,<sup>2</sup> and Hans-Gerd Löhmannsröben<sup>1</sup>

<sup>1</sup>Physikalische Chemie, Institut für Chemie und Interdisziplinäres Zentrum für Photonik, Universität Potsdam, Karl-Liebknecht-Straße 24-25, 14476 Potsdam-Golm, Germany

<sup>2</sup>Laboratoire de Chimie Moléculaire, Ecole Européenne de Chimie, Polymères, Matériaux (ECPM), UMR 7509 CNRS, 25 rue Becquerel, 67087 Strasbourg Cedex, France

Correspondence should be addressed to Niko Hildebrandt, hildebr@uni-potsdam.de

Received 2 April 2007; Accepted 16 July 2007

Recommended by Marek Osinski

CdSe/ZnS core/shell quantum dots (QDs) are used as efficient Förster Resonance Energy Transfer (FRET) acceptors in a time-resolved immunoassays with Tb complexes as donors providing a long-lived luminescence decay. A detailed decay time analysis of the FRET process is presented. QD FRET sensitization is evidenced by a more than 1000-fold increase of the QD luminescence decay time reaching ca. 0.5 milliseconds, the same value to which the Tb donor decay time is quenched due to FRET to the QD acceptors. The FRET system has an extremely large Förster radius of approx. 100 Å and more than 70% FRET efficiency with a mean donor-acceptor distance of ca. 84 Å, confirming the applied biotin-streptavidin binding system. Time-resolved measurement allows for suppression of short-lived emission due to background fluorescence and directly excited QDs. By this means a detection limit of 18 attomol QDs within the immunoassay is accomplished, an improvement of more than two orders of magnitude compared to commercial systems.

Copyright © 2007 Niko Hildebrandt et al. This is an open access article distributed under the Creative Commons Attribution License, which permits unrestricted use, distribution, and reproduction in any medium, provided the original work is properly cited.

## 1. INTRODUCTION

CdSe/ZnS semiconductor nanocrystals or quantum dots (QDs) possess unrivalled photophysical properties, such as size tunable emission wavelengths, extremely high extinction coefficients over a broad absorption spectrum and enhanced photostability compared to organic fluorophores [1–4]. Moreover, several concepts have been introduced in order to develop water soluble and biocompatible QDs [5–9]. Homogeneous Förster resonance energy transfer (FRET) immunoassays with QDs as energy acceptors are of particular interest because of the extremely high-extinction coefficients of the QDs over a broad absorption spectrum. This special optical property gives rise to large Förster radii leading to efficient FRET over long distances [10–12]. However, the use of QDs as FRET acceptors with organic dye donors is problematic, probably due to the short-lived emission of these donors, hence FRET could not be shown for these donor-

acceptor pairs [13]. Only very few publications deal with QDs as acceptors within the biological context, for example, by using bioluminescence energy transfer [14, 15], or with FRET donors of Tb and Eu complexes [16, 17]. In this contribution, we extend these investigations by a thorough analysis of donor and acceptor luminescence decay times, which are important parameters for understanding the dynamic parameters of the FRET process [11, 18]. Within a fluoroimmunoassay of a Tb complex streptavidin conjugate and biotinylated QDs, the sensitized QD acceptor as well as the Tb donor should change their luminescence decay times once they are brought to close proximity by the biotin-streptavidin binding process. For both QD as well as Tb luminescence decay times, we provide further evidence of efficient QD sensitization by FRET from Tb. Previously reported large Förster radii, the high FRET efficiency, and the assumed biotin-streptavidin binding model are confirmed. Moreover, taking advantage of the time-resolved measurement for suppressing

the short-lived background emission and QD fluorescence (from directly excited QDs), and optimizing laser excitation (new laser system with low background emission) and solvent conditions (azide-free solvent leading to decreased luminescence quenching of Tb), a very low detection limit is obtained. This means that a sensitivity improvement of more than two orders of magnitude is accomplished, taking the well established and extensively studied Eu-TBP (Eu<sup>3+</sup>-tris(bipyridine) and APC (allophycocyanin) donor-acceptor system [19–21], used within the same streptavidin-biotin assay format, for comparison. The presented results demonstrate the great potential of the Tb to QD FRET system for highly sensitive homogeneous immunoassays for biological as well as clinical and medical applications.

## 2. MATERIALS AND METHODS

### 2.1. FRET donors and acceptors

The FRET donors are conjugates of the tetrameric protein streptavidin (Strep) labeled with Tb complexes (TbL), produced as described in the literature [17, 22]. A labeling ratio of  $(10 \pm 1)$  TbL per Strep was determined by UV-Vis absorption spectroscopy [22].

The FRET acceptors are commercially available biotinylated CdSe/ZnS core/shell quantum dot nanocrystals emitting at 655 nm (Biot-QD) purchased from Invitrogen Corporation (Carlsbad, Calif, USA). A ratio of ca. 6 biotin molecules per QD is specified by the supplier.

Strep has a very high binding affinity towards biotin with a first dissociation constant of the complex of  $10^{-13}$  M [23]. The biological FRET system is obtained by the strong recognition process between biotin and streptavidin leading to a close proximity of donor and acceptor.

### 2.2. Fluoroimmunoassay

The fluoroimmunoassay (FIA) was performed by adding increasing amounts (0–150  $\mu$ l) of Biot-QD stock solution (concentration  $c = 1 \cdot 10^{-9}$  M) to a stock of  $1 \cdot 10^{-9}$  M TbL-Strep (150–0  $\mu$ l) leading to a total assay volume of 150  $\mu$ l for each TbL-Strep + Biot-QD mixture. The used solvent was 50 mM borate buffer (pH 8.3) with 2% bovine serum albumin (BSA) and 0.5 M potassium fluoride (KF).

The assay was excited at 315 nm by a Nd:YAG-OPO laser system (Nd:YAG-Laser: Spectra-Physics, Mountain View, Calif, USA; OPO: GWU-Lasertechnik, Erftstadt, Germany) working at 20 Hz repetition rate, with an average pulse energy of ca. 15  $\mu$ J, fibre coupled to the fluoroimmunoreader.

The reader system is a commercially available Kryptor immunoreader (Cezanne, Nîmes, France) modified for 315 nm excitation wavelength. Luminescence intensities were collected at  $(665 \pm 5)$  nm (channel A – QD emission) and at  $(545 \pm 5)$  nm (channel B – Tb emission). Time-resolved detection is performed by single photon counting with 2 microsecond integration steps over 8 milliseconds using one photon multiplier tube (PMT) for each channel [22].

### 2.3. Time-resolved FRET calculations

Luminescence decay curves for the different mixtures of TbL-Strep + Biot-QD are collected for both QD (channel A) and Tb (channel B) luminescence.

The time-dependent luminescence intensity in channel A ( $I_A(t)$ ) is the sum of a background emission (due to directly excited QDs ( $I(\text{BgQD})$ ), a weak Tb emission ( $I(\text{BgTb})$ ) occurring from the  $^5\text{D}_4 \rightarrow ^7\text{F}_{2-0}$  transitions) and the QD emission arising from Tb to QD energy transfer given by FRET theory [11]:

$$I_A(t) = a \cdot I(\text{BgQD}) + b \cdot I(\text{BgTb}) + c \cdot \exp\left[-\frac{t}{\tau_D} - \frac{t}{\tau_D} \cdot \left(\frac{R_0}{r}\right)^6\right], \quad (1)$$

where  $\tau_D$  is the Tb luminescence decay time of pure TbL-Strep (absence of the QD acceptor),  $R_0$  is the Förster radius of the donor-acceptor pair,  $c$  is the amount of transferred energy or FRET intensity, and  $r$  is the average donor-acceptor distance. For the decay curves obtained from our experiments,  $I(\text{BgQD})$  is the time-dependent luminescence intensity of 0.1 nM pure Biot-QD in channel A,  $I(\text{BgTb})$  is the time-dependent luminescence intensity of 1 nM pure TbL-Strep in channel A, and  $a$  and  $b$  are correction factors depending on the actual concentration of Biot-QD and TbL-Strep (including donor emission decrease due to FRET) within the different mixtures.

The two variable parameters  $r$  and  $c$  are fitted (using the Microsoft Excel Solver option) so that (1) fits the respective decay function of each TbL-Strep + Biot-QD mixture. This means that the donor-acceptor distance  $r$  and the FRET intensity  $c$  are determined. Assuming that the luminescence decay time of pure QDs is very fast compared to the decay time of the pure Tb donor, the luminescence decay time of QDs upon FRET sensitization ( $\tau_{AD}$ ) is the same as the Tb decay time in presence of QD ( $\tau_{DA}$ ) [24].  $\tau_{AD}$  and  $\tau_{DA}$  can be calculated using:

$$\frac{1}{\tau_{AD}} = \frac{1}{\tau_{DA}} = \frac{1}{\tau_D} + \frac{1}{\tau_D} \cdot \left(\frac{R_0}{r}\right)^6. \quad (2)$$

In order to verify the fitting procedure used for channel A (QD emission channel), a different method was used for channel B, where a simple bi-exponential fit (using the Origin fit procedure) is performed without using any fixed parameters. The luminescence decay in this channel (Tb emission channel) is determined by  $\tau_D$  (no FRET) and  $\tau_{DA}$  (FRET). QD luminescence does not occur in this channel. The time-dependent luminescence intensity in channel B is given by:

$$I_B(t) = I_0 + x \cdot \exp\left[-\frac{t}{\tau_D}\right] + y \cdot \exp\left[-\frac{t}{\tau_{DA}}\right], \quad (3)$$

where  $I_0$  is an intensity offset and:

$$\int_0^\infty x \cdot \exp\left[-\frac{t}{\tau_D}\right] dt = x \cdot \tau_D, \quad (4)$$

$$\int_0^\infty y \cdot \exp\left[-\frac{t}{\tau_{DA}}\right] dt = y \cdot \tau_{DA}$$

represent the dimensionless luminescence intensities of Tb in absence and presence of QD, respectively. In this case, the FRET intensity can be described by  $y \cdot \tau_{DA}$  (increasing with Biot-QD addition) or by  $x \cdot \tau_D$  (decreasing with Biot-QD addition).

#### 2.4. Immunoassay detection limit

For calculation of the limit of detection (LOD) for Biot-QD in this type of FIA, the luminescence intensity ratio ( $R_I$ ) of channel A and channel B integrated from 0.1 to 1.2 milliseconds after the excitation laser pulse (time gating) was used:

$$R_I = \frac{\int_{0.1\text{ms}}^{1.2\text{ms}} I_A(t) dt}{\int_{0.1\text{ms}}^{1.2\text{ms}} I_B(t) dt}. \quad (5)$$

$R_I$  is displayed as a function of Biot-QD concentration for the different mixtures of TbL-Strep + Biot-QD within the FIA. The linear part of the rising  $R_I$  over [Biot-QD] is then used to calculate the LOD by three times the standard deviation of 12  $R_I$  values at [Biot-QD] = 0 ( $\sigma_0$ ) divided by the slope of  $R_I$  over [Biot-QD]:

$$\text{LOD} = 3 \cdot \sigma_0 \cdot \frac{\Delta[\text{Biot-QD}]}{\Delta R_I}. \quad (6)$$

### 3. RESULTS AND DISCUSSION

#### 3.1. Luminescence decay time analysis

Besides the pure TbL-Strep stock solution ( $c = 1 \cdot 10^{-9}$  M) and two pure Biot-QD solutions ( $c = 1 \cdot 10^{-9}$  M and  $c = 1 \cdot 10^{-10}$  M), 13 mixtures of TbL-Strep + Biot-QD with ratios ranging 0.007–2.0 Biot-QD per TbL-Strep were measured. Figures 1 and 2 show some representative luminescence as well as QD background decay curves for the two detection channels.

Regarding the increasing QD emission in channel A (Figure 1), FRET sensitization of QDs by Tb becomes already obvious for low ratios of Biot-QD/TbL-Strep, whereas the QD emission decreases again for ratios higher than 0.5 due to the decreasing TbL-Strep donor concentration with Biot-QD addition (cf. Section 2).

Higher amounts of Biot-QD are necessary for a clearly visible FRET influence in the Tb channel B (Figure 2). There are two reasons for this behavior, the high labeling ratio of 10 TbL per Strep, and the binding of up to six TbL-Strep per Biot-QD, as suggested in previous publications [16, 17, 22]. This means that Biot-QD is saturated with TbL-Strep for low ratios and there is still a majority of free TbL-Strep in solution. Hence, the influence on QD emission is strong whereas it is negligible for Tb. At higher amounts of Biot-QD in the assay, Tb emission is quenched due to FRET and a second decay time becomes obvious in the decay curves.

In order to perform time-resolved FRET calculations using (1), the Förster radius  $R_0$  (in Å) has to be determined by [11]:

$$R_0^6 = 8.79 \cdot 10^{-5} \cdot n_r^{-4} \cdot \Phi_{\text{Tb}} \cdot \kappa^2 \cdot J(\lambda) \quad (7)$$

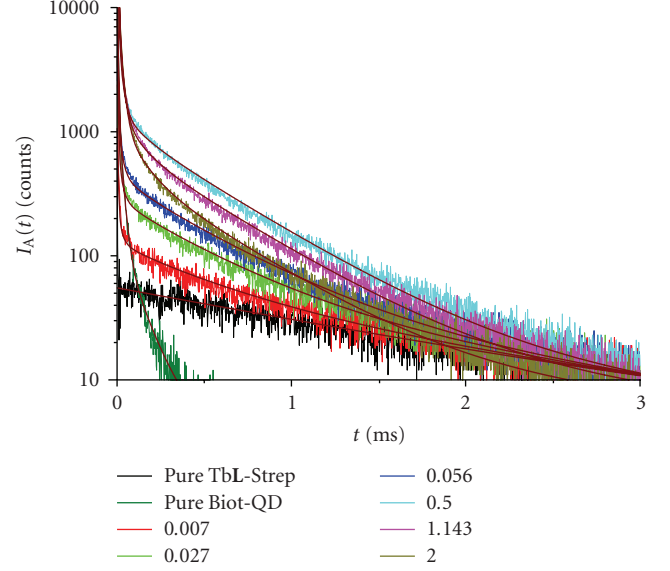


FIGURE 1: Luminescence decay curves for pure TbL-Strep ( $c = 1 \cdot 10^{-9}$  M) and mixtures of TbL-Strep + Biot-QD with ratios between 0.007 and 2.0 Biot-QD per TbL-Strep measured in channel A ( $(665 \pm 5)$  nm). A background decay curve of pure Biot-QD ( $c = 1 \cdot 10^{-10}$  M) arising from a strong detector saturation of short-lived directly excited QD fluorescence is also displayed. Fits according to (1) displayed as thick solid lines.

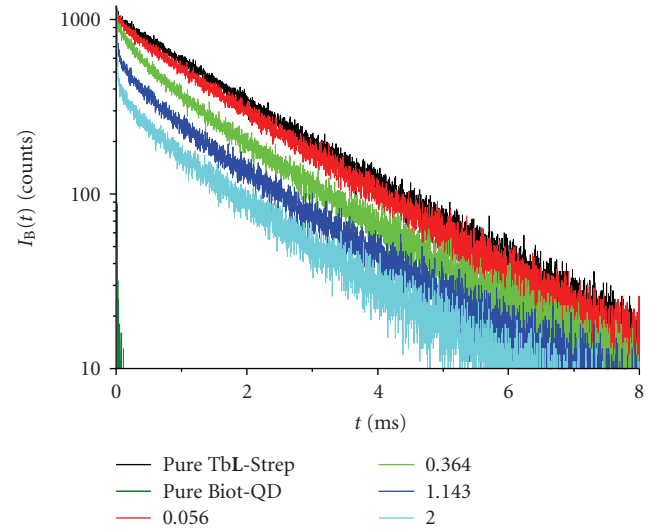


FIGURE 2: Luminescence and background decay curves (for description, see Figure 1) measured in channel B ( $(545 \pm 5)$  nm).

with:

$$J(\lambda) = \int F_{\text{Tb}}(\lambda) \cdot \epsilon_{\text{QD}}(\lambda) \cdot \lambda^4 d\lambda, \quad (8)$$

where  $n_r$  is the refractive index of the surrounding medium (1.4 for aqueous media [11]),  $\Phi_{\text{Tb}}$  is the Tb centered luminescence quantum yield [25],  $\kappa^2$  is the dipole orientation factor (2/3 for randomly oriented systems in solution [11, 25]),  $J(\lambda)$  is the overlap integral in  $\text{M}^{-1} \text{cm}^{-1} \text{nm}^4$ ,  $F_{\text{Tb}}$  is the normalized TbL-Strep luminescence spectrum in  $\text{nm}^{-1}$  (with

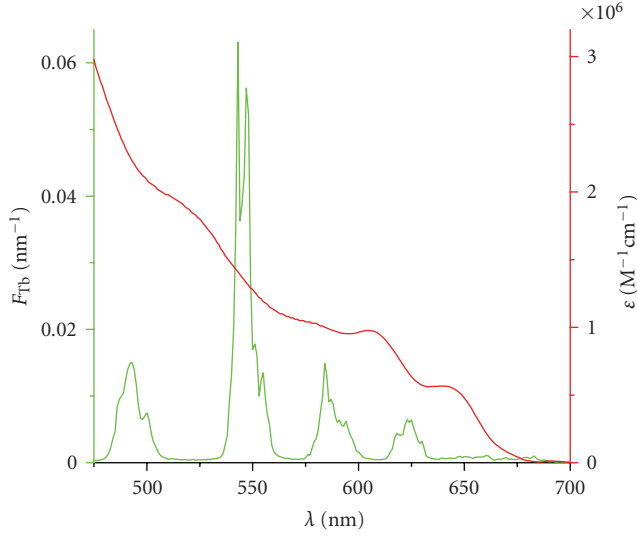


FIGURE 3: Normalized emission spectrum of TbL-Strep (green) and extinction coefficient spectrum of Biot-QD (red).

$\int F_{Tb}(\lambda)d\lambda = 1$ ), and  $\epsilon_{QD}(\lambda)$  is the Biot-QD extinction coefficient spectrum in  $M^{-1} cm^{-1}$ . Taking the luminescence decay time ( $\tau^0 = 1.48$  ms) and the quantum yield ( $\Phi_{Tb}^0 = 0.49$ ) of TbL in pure water [26] and the Tb luminescence decay time of pure TbL-Strep within the assay ( $\tau_D = 1.83$  milliseconds), a value of  $\Phi_{Tb} = 0.61$  can be calculated by [17, 22]:

$$\Phi_{Tb} = \Phi_{Tb}^0 \cdot \frac{\tau_D}{\tau^0}. \quad (9)$$

Regarding the TbL-Strep luminescence spectrum and the Biot-QD extinction coefficient spectrum in Figure 3, the very good overlap becomes obvious, resulting in an extremely large Förster radius of  $R_0 = (100 \pm 2) \text{ \AA}$ .

Taking this value for fitting  $r$  and  $c$  in (1) for each luminescence decay (measured in channel A) of the different TbL-Strep + Biot-QD mixtures leads to a mean donor-acceptor distance of  $r = (84 \pm 1) \text{ \AA}$  (in good agreement with the proposed TbL-Strep + Biot-QD binding model [16, 17, 22]) and an average FRET sensitized QD luminescence decay time of  $\tau_{AD} = (0.47 \pm 0.03)$  milliseconds, which is an increase of more than three orders of magnitude compared to the luminescence decay times of pure Biot-QD, which are in the 100-nanosecond range [16, 17].

These values lead to a FRET efficiency of  $(74 \pm 6)\%$  calculated by [11]:

$$\eta_{FRET} = \frac{R_0^6}{R_0^6 + r^6} = 1 - \frac{\tau_{AD}}{\tau_D}. \quad (10)$$

The calculations of  $\tau_{AD}$  and  $r$  could be confirmed (Figure 4) by fitting the luminescence decay curves of channel B using (3). Values of  $\tau_{DA} = (0.46 \pm 0.07)$  milliseconds and  $r = (83 \pm 3) \text{ \AA}$  are obtained.

As mentioned above, the influence of FRET on the emission signal in channel B starts at higher Biot-QD/TbL-Strep ratios. Hence, only decay curves for ratios above 0.04 are taken into account for the calculations.

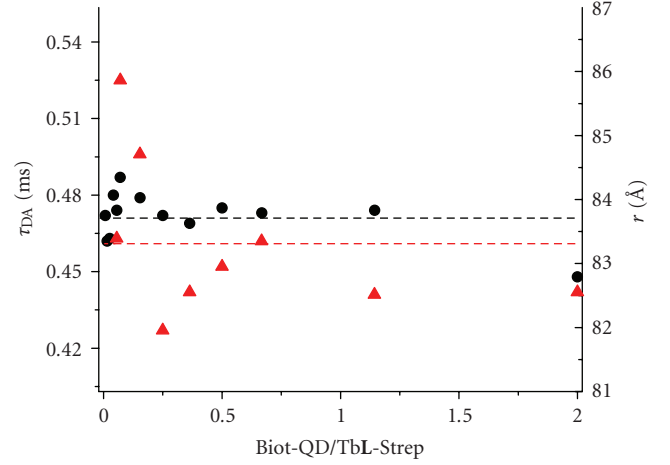


FIGURE 4: Luminescence decay times of Tb and QDs ( $\tau_{DA}$ ) due to QD FRET sensitization by Tb and donor-acceptor distances ( $r$ ) calculated from luminescence decay curves of channel A (black dots) and channel B (red triangles), respectively. The dashed lines represent mean values of  $\tau_{DA}$  and  $r$ .

Regarding the  $r^{-6}$  dependence of FRET, it can be assumed that mainly donors which are close to the QD acceptor contribute to the measured FRET signals. As the QD luminescence decay is several orders of magnitude faster than the one of TbL, absorption saturation by direct QD excitation is negligible and a single QD acceptor can interact with several TbL donors. This does not influence the FRET efficiency but lead to a higher FRET signal intensity which has positive impact on assay sensitivity. Nevertheless, due to the distribution of several TbL donors labeled to streptavidin,  $\tau_{AD}$ ,  $r$  and  $\eta_{FRET}$  are average values.

Further evidence of FRET from Tb to QD is given by the FRET intensities ( $c$  from (1) and  $x \cdot \tau_D$  as well as  $y \cdot \tau_{DA}$  from (3)) obtained from fitting the decays of channel A and B. In order to compare the FRET intensities arising from the different signals, they were normalized to unity at a Biot-QD/TbL-Strep ratio of 0.25 and the decreasing (FRET quenched) donor intensity ( $x \cdot \tau_D$ ) was subtracted from the concentration-dependent pure TbL-Strep donor signal (Tb signal in absence of QD). Figure 5 shows the very good correlation of the FRET intensities calculated from the three different signals.

A strong increase is first observed, up to the saturation of the six biotins on the QD surface by TbL-Strep and is followed by a decrease due to the reduced donor concentration in the assay volume. This confirms the strong increase of FRET up to a ratio of 1/6 Biot-QD/TbL-Strep and the proposed TbL-Strep + Biot-QD binding model [16, 17, 22]. Moreover, it shows that large QD aggregates bridged by TbL-Strep are not formed at these low concentrations, as it would result in a signal increase up to much higher Biot-QD/TbL-Strep, regarding the number of ten Tb donors per Strep.

For understanding the dynamic parameters of FRET, investigation of luminescence decay times is of great importance. This luminescence decay time analysis over a broad range of Biot-QD/TbL-Strep ratio gives clear evidence of



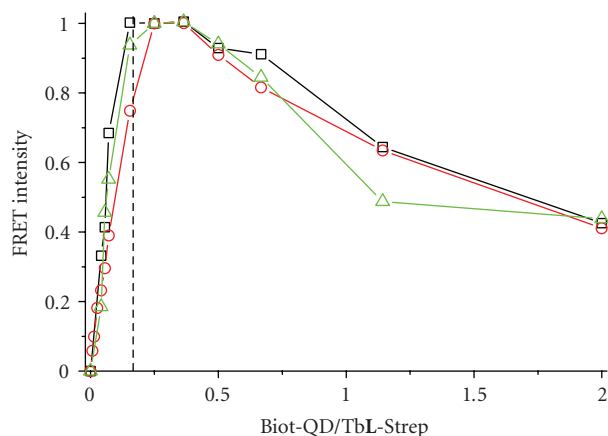


FIGURE 5: Normalized FRET intensities calculated with (1) and (3) from sensitized QD emission (red circles), short-lived Tb emission due to FRET quenching (black squares), and long-lived Tb emission of unquenched Tb (green triangles). The dotted line indicates a ratio of 6 TbL-Strep per Biot-QD.

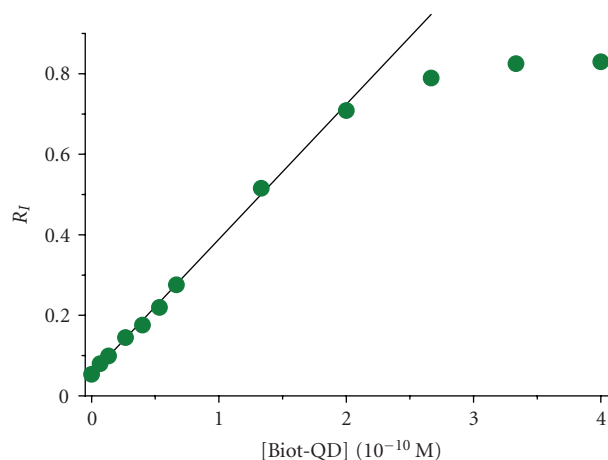


FIGURE 6: Intensity ratio  $R_I$  (cf. (5)) over Biot-QD concentration for the TbL-Strep + Biot-QD immunoassay after 8 hours incubation. Linear fit for LOD calculation shown as solid line.

FRET from Tb to QD within the homogeneous streptavidin-biotin immunoassay and confirms the results accomplished with time-gated emission intensity detection in earlier publications [16, 17, 22].

### 3.2. Immunoassay sensitivity

In order to evaluate the sensitivity of the assay,  $R_I$  (cf. (5)) is displayed over Biot-QD concentration and the LOD is determined from the linear part of the rising  $R_I$  calibration curve obtained from the different TbL-Strep + Biot-QD mixtures (Figure 6).

The  $R_I$  function shows excellent linearity up to a concentration of ca.  $2 \cdot 10^{-10}$  M Biot-QD. The zero concentration standard deviation has a value of  $\sigma_0 = 0.00013$  which leads to an LOD of 0.12 pM Biot-QD (18 attomol of Biot-QD within

the 150  $\mu$ l assay volume) taking the slope of the linear fit in Figure 6.

Comparing this detection limit to earlier results using the same assay with azide containing solutions displays an improvement of one order of magnitude and an LOD decrease of more than two orders of magnitude compared to the homogeneous FRET FIA “gold standard” donor-acceptor pair of Eu-TBP and APC [21] using the same streptavidin-biotin assay [17].

These results underline the very high sensitivity of the Tb to QD FRET system to be used as powerful tool in biomedical analysis, with the possibility of applications in long-distance biological measurements, for example, in high throughput screening for in vitro diagnostics. However, it has to be taken into account that real-life immunoassays can be complicated biological systems and intensive optimization of antibody labeling and measuring conditions is required. First results with good evidence for FRET in a human chorionic gonadotropin (HCG) assay (e.g., applied as pregnancy test) demonstrate the feasibility [22]. In order to achieve the detection limits demonstrated here, these real-life assays are currently under investigation for further optimization.

### ACKNOWLEDGMENTS

This research was supported by the European Community (Specific targeted research project LSHB-CT-2007-037933), the German Bundesministerium für Wirtschaft und Technologie (InnoNet program 16N0225), and the French Centre National de la Recherche Scientifique.

### REFERENCES

- [1] B. O. Dabbousi, J. Rodriguez-Viejo, F. V. Mikulec, et al., “(CdSe)ZnS core-shell quantum dots: synthesis and characterization of a size series of highly luminescent nanocrystallites,” *Journal of Physical Chemistry B*, vol. 101, no. 46, pp. 9463–9475, 1997.
- [2] D. Gerion, F. Pinaud, S. C. Williams, et al., “Synthesis and properties of biocompatible water-soluble silica-coated CdSe/ZnS semiconductor quantum dots,” *Journal of Physical Chemistry B*, vol. 105, no. 37, pp. 8861–8871, 2001.
- [3] M. A. Hines and P. Guyot-Sionnest, “Synthesis and characterization of strongly luminescing ZnS-capped CdSe nanocrystals,” *Journal of Physical Chemistry*, vol. 100, no. 2, pp. 468–471, 1996.
- [4] A. R. Kortan, R. Hull, R. L. Opila, et al., “Nucleation and growth of CdSe on ZnS quantum crystallite seeds, and vice versa, in inverse micelle media,” *Journal of the American Chemical Society*, vol. 112, no. 4, pp. 1327–1332, 1990.
- [5] W. C. W. Chan and S. M. Nie, “Quantum dot bioconjugates for ultrasensitive nonisotopic detection,” *Science*, vol. 281, no. 5385, pp. 2016–2018, 1998.
- [6] W. J. Parak, D. Gerion, D. Zanchet, et al., “Conjugation of DNA to silanized colloidal semiconductor nanocrystalline quantum dots,” *Chemistry of Materials*, vol. 14, no. 5, pp. 2113–2119, 2002.
- [7] P. T. Tran, E. R. Goldman, G. P. Anderson, J. M. Mauro, and H. Mattoussi, “Use of luminescent CdSe-ZnS nanocrystal bioconjugates in quantum dot-based nanosensors,” *Physica Status Solidi (B)*, vol. 229, no. 1, pp. 427–432, 2002.

- [8] S. P. Wang, N. Mamedova, N. A. Kotov, W. Chen, and J. Studer, "Antigen/antibody immunocomplex from CdTe nanoparticle bioconjugates," *Nano Letters*, vol. 2, no. 8, pp. 817–822, 2002.
- [9] W. Z. Guo, J. J. Li, Y. A. Wang, and X. G. Peng, "Conjugation chemistry and bioapplications of semiconductor box nanocrystals prepared via dendrimer bridging," *Chemistry of Materials*, vol. 15, no. 16, pp. 3125–3133, 2003.
- [10] R. M. Clegg, "Fluorescence resonance energy transfer," in *Fluorescence Imaging Spectroscopy and Microscopy*, X. F. Wang and B. Herman, Eds., pp. 179–252, John Wiley & Sons, New York, NY, USA, 1996.
- [11] J. R. Lakowicz, *Principles of Fluorescence Spectroscopy*, Kluwer Academic/Plenum, New York, NY, USA, 2nd edition, 1999.
- [12] B. W. van der Meer, G. Coker, and S. Y. S. Chen, *Resonance Energy Transfer: Theory and Data*, VCH, New York, NY, USA, 1994.
- [13] A. R. Clapp, I. L. Medintz, B. R. Fisher, G. P. Anderson, and H. Mattoussi, "Can luminescent quantum dots be efficient energy acceptors with organic dye donors?" *Journal of the American Chemical Society*, vol. 127, no. 4, pp. 1242–1250, 2005.
- [14] M.-K. So, C. J. Xu, A. M. Loening, S. S. Gambhir, and J. H. Rao, "Self-illuminating quantum dot conjugates for in vivo imaging," *Nature Biotechnology*, vol. 24, no. 3, pp. 339–343, 2006.
- [15] Y. Zhang, M.-K. So, A. M. Loening, H. Q. Yao, S. S. Gambhir, and J. H. Rao, "HaloTag protein-mediated site-specific conjugation of bioluminescent proteins to quantum dots," *Angewandte Chemie International Edition*, vol. 45, no. 30, pp. 4936–4940, 2006.
- [16] N. Hildebrandt, L. J. Charbonnière, M. Beck, R. F. Ziessel, and H.-G. Löhmannsröben, "Quantum dots as efficient energy acceptors in a time-resolved fluoroimmunoassay," *Angewandte Chemie International Edition*, vol. 44, no. 46, pp. 7612–7615, 2005.
- [17] L. J. Charbonnière, N. Hildebrandt, R. F. Ziessel, and H.-G. Löhmannsröben, "Lanthanides to quantum dots resonance energy transfer in time-resolved fluoro-immunoassays and luminescence microscopy," *Journal of the American Chemical Society*, vol. 128, no. 39, pp. 12800–12809, 2006.
- [18] Th. Förster, "Zwischenmolekulare Energiewanderung und Fluoreszenz," *Annalen der Physik*, vol. 437, no. 1-2, pp. 55–75, 1948.
- [19] K. Enomoto, T. Nagasaki, A. Yamauchi, et al., "Development of high-throughput spermidine synthase activity assay using homogeneous time-resolved fluorescence," *Analytical Biochemistry*, vol. 351, no. 2, pp. 229–240, 2006.
- [20] M. Gabourdes, V. Bourguin, G. Mathis, H. Bazin, and B. Alpha-Bazin, "A homogeneous time-resolved fluorescence detection of telomerase activity," *Analytical Biochemistry*, vol. 333, no. 1, pp. 105–113, 2004.
- [21] G. Mathis, "Rare earth cryptates and homogeneous fluoroimmunoassays with human sera," *Clinical Chemistry*, vol. 39, no. 9, pp. 1953–1959, 1993.
- [22] N. Hildebrandt, "Lanthanides and quantum dots: time-resolved laser spectroscopy of biochemical Förster resonance energy transfer (FRET) systems," Dissertation, Universität Potsdam, Potsdam, Germany, 2006.
- [23] A. Loosli, U. E. Rusbandi, J. Gradinaru, et al., "(Strept)avidin as host for biotinylated coordination complexes: stability, chiral discrimination, and cooperativity," *Inorganic Chemistry*, vol. 45, no. 2, pp. 660–668, 2006.
- [24] B. Valeur, *Molecular Fluorescence: Principles and Applications*, Wiley-VCH, New York, NY, USA, 2002.
- [25] M. Xiao and P. R. Selvin, "Quantum yields of luminescent lanthanide chelates and far-red dyes measured by resonance energy transfer," *Journal of the American Chemical Society*, vol. 123, no. 29, pp. 7067–7073, 2001.
- [26] N. Weibel, L. J. Charbonnière, M. Guardigli, A. Roda, and R. Ziessel, "Engineering of highly luminescent lanthanide tags suitable for protein labeling and time-resolved luminescence imaging," *Journal of the American Chemical Society*, vol. 126, no. 15, pp. 4888–4896, 2004.

## Research Article

# Superparamagnetic Iron Oxide Nanoparticles Coated with Galactose-Carrying Polymer for Hepatocyte Targeting

Mi Kyong Yoo,<sup>1</sup> In Yong Kim,<sup>1</sup> Eun Mi Kim,<sup>2</sup> Hwan-Jeong Jeong,<sup>2</sup> Chang-Moon Lee,<sup>2</sup> Yong Yeon Jeong,<sup>3</sup> Toshihiro Akaike,<sup>4</sup> and Chong Su Cho<sup>1</sup>

<sup>1</sup> School of Agricultural Biotechnology, Seoul National University, Seoul 151-921, South Korea

<sup>2</sup> Department of Nuclear Medicine, Chonbuk National University School of Medicine, Jeonju 561-712, South Korea

<sup>3</sup> Department of Diagnostic Radiology, Chonnam National University Medical School, Gwangju 501-746, South Korea

<sup>4</sup> Department of Biomolecular Engineering, Tokyo Institute of Technology, Yokohama 226-8501, Japan

Correspondence should be addressed to Chong Su Cho, chocs@plaza.snu.ac.kr

Received 2 April 2007; Accepted 24 December 2007

Recommended by Marek Osinski

Our goal is to develop the functionalized superparamagnetic iron oxide nanoparticles (SPIONs) demonstrating the capacities to be delivered in liver specifically and to be dispersed in physiological environment stably. For this purpose, SPIONs were coated with polyvinylbenzyl- *O*- $\beta$ -D-galactopyranosyl-D-gluconamide (PVLA) having galactose moieties to be recognized by asialoglycoprotein receptors (ASGP-R) on hepatocytes. For use as a control, we also prepared SPIONs coordinated with 2-pyrrolidone. The sizes, size distribution, structure, and coating of the nanoparticles were characterized by transmission electron microscopy (TEM), electrophoretic light scattering spectrophotometer (ELS), X-ray diffractometer (XRD), and Fourier transform infrared (FT-IR), respectively. Intracellular uptake of the PVLA-coated SPIONs was visualized by confocal laser scanning microscopy, and their hepatocyte-specific delivery was also investigated through magnetic resonance (MR) images of rat liver. MRI experimental results indicated that the PVLA-coated SPIONs possess the more specific accumulation property in liver compared with control, which suggests their potential utility as liver-targeting MRI contrast agent.

Copyright © 2007 Mi Kyong Yoo et al. This is an open access article distributed under the Creative Commons Attribution License, which permits unrestricted use, distribution, and reproduction in any medium, provided the original work is properly cited.

## 1. INTRODUCTION

In the last decade, many investigations with several types of iron oxides have been carried out in the field of nanosized magnetic particles (mostly, magnetite ( $\text{Fe}_3\text{O}_4$ ) or maghemite ( $\gamma\text{-Fe}_2\text{O}_3$ ) single domains of about 5~20 nm in diameter) [1]. These iron oxide particles of nanometer size present superparamagnetic property and are ideal for magnetic resonance imaging (MRI) contrast agent by enhancement of proton relaxation in the tissue microenvironment [2–4].

For the MRI application, these SPIONs must have high magnetization values, stability in physiological environment, and size smaller than 20 nm with overall narrow particle size distribution so that the particles have uniform physical and chemical properties [5]. However, the iron oxide magnetic nanoparticles have several problems such as aggregation in water, chemical instability in air, biodegradability in physiological environment, and toxicity, which limit their use to the medical diagnostic agent. Ferrofluids are colloidal sus-

pensions of magnetic nanoparticles, forming magnetizable fluids that remain liquid in the most intense magnetic fields [6]. Even though the stability of the ferrofluid is of utmost importance for its biomedical applications, the nanoparticles in colloidal suspension are likely to agglomerate and form large cluster due to hydrophobic interactions between the magnetic iron oxide particles with a large hydrophobic surface area to volume ratio [1]. These problems of naked iron oxide nanoparticles have been overcome by coating the surface of magnetic particles with synthetic polymers such as polyethylene glycol (PEG) [7], polyvinyl alcohol (PVA) [8], polyvinyl pyrrolidone (PVP) [9], and natural polymers like dextran [10], chitosan [11], and pullulan [12]. However, the nanoparticles coated with the above-mentioned polymers were nonspecifically accumulated into tissues and organs, resulting in the poor availability in the imaging of specific tissues and organs [13, 14]. Therefore, targeted delivery of MRI contrast agent is a highly desirable strategy for enhancing efficiency and reducing unintended side-effects and toxicity





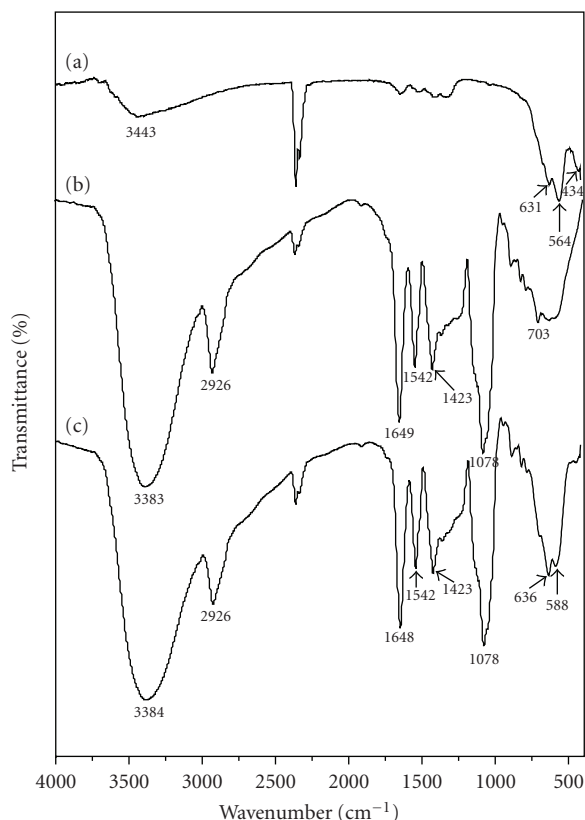


FIGURE 2: FTIR spectra of SPIONs (a), PVLA (b), and PVLA-coated SPIONs (c).

using a JEOL Model JEM 1010 at 80 kV. For sample preparation, a diluted drop of SPIONs suspension was placed on a carbon-coated copper grid. The grid was allowed in air to dry further for 15 minutes and was then examined with the electron microscope.

To investigate the nanocrystallinity of SPIONs, X-ray diffraction (XRD) data were collected on an X-ray diffractometer (Bruker-AXS GmbH D8 Advance, Karlsruhe, Germany) equipped with a rotating anode, Sol-X energy dispersive detector, and Cu-K $\alpha$  radiation source ( $\lambda = 0.1542$  nm).

#### 2.4. Hepatocyte isolation and culture

Hepatocytes were prepared by noncirculation perfusion of male ICR mouse liver with a two-step collagenase perfusion technique of Seglen [28]. Briefly, the male ICR mice (5–7 weeks of age) employed in this study were purchased from Jungang Lab. Animal, Inc. (Seoul, Korea). The liver was perfused by 0.5 mM of ethylene glycol-bis[ $\beta$ -amino ethyl ether]-N,N,N'',N'''-tetraacetic acid (EGTA) in Hanks' balanced salt solution (HBSS) without CaCl<sub>2</sub> and  $5 \times 10^{-3}\%$  (wt./wt.) collagenase in HBSS with CaCl<sub>2</sub> (5 mM) through a disposable needle (25G-1) aligned along the inferior vena cava. The collagenase-perfused liver was dissected, suspended in HBSS, and filtered through cheesecloth and 100- $\mu$ m nylon membrane to remove connective tissue debris and cell clumps. Hepatocytes were purified by a density-gradient centrifuga-

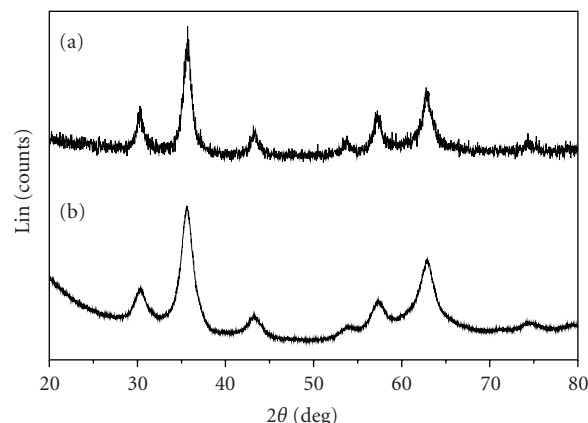


FIGURE 3: X-ray diffraction patterns of 2-pyrrolidone-coated SPIONs (a), PVLA-coated SPIONs (b).

tion (50 g force, 10 minutes) using 45% Percoll solution (Pharmacia, Piscataway, NJ, USA) at 4°C. Cell viability measured by trypan blue exclusion was more than 90%.

Isolated hepatocytes were suspended in a serum-free Williams' E (WE) medium (Gibco BRL, NY, USA) containing 50  $\mu$ g/mL penicillin and 50  $\mu$ g/mL streptomycin.

#### 2.5. Observation of phase contrast, fluorescence, and confocal laser scanning micrographs

The isolated hepatocytes were plated on collagen-coated glass cover slips in 12-well plates (Iwaki Glass Co., Tokyo, Japan) at  $1 \times 10^5$  cells per well. The hepatocytes were incubated at 37°C for 2 hours. Then, the old medium was removed and WE medium containing FITC-PVLA-coated SPIONs (1 mg/mL) was added to cells. After 15-, 30-, and 60-minute incubation, cells were rinsed twice with 0.1 M PBS. The coverslips were enclosed in 1 mL of glycerol and visualized by confocal laser scanning microscope (Micro Systems LSM 410, Carl Zeiss, Germany). Gallery mode of optical sections was used for checking internalization of complexes into cells [29, 30].

#### 2.6. In vivo MR image

For all rats, liver MR images were taken prior and 1 hour after injection of contrast agents. PVLA-coated SPIONs and pyrrolidone-coated SPIONs were intravenously injected through the tail vein. Rats (SD, female, 6 weeks) were anesthetized with the use of a general inhalation anesthesia (1.5% isoflurane in a 1 : 2 mixture of O<sub>2</sub>/N<sub>2</sub>) during MR examination. MR imagings were performed with a 1.5 T MR scanner (GE Signa Exite Twin-speed, GE Health Care, Milwaukee, WI, USA) using an animal coil (4.3 cm Quadrature volume coil, Nova Medical System, Wilmington, Del, USA). For fast spin echo (FSE) T<sub>2</sub>-weighted MR imaging, the following parameters were adopted: repetition time (ms/echo) time milliseconds of 4,800/102, flip angle of 90°, echo train length of 8, field of view of 6 cm, section thickness of 2 mm, intersection gap of 0.1 mm, and 256  $\times$  160 matrix.

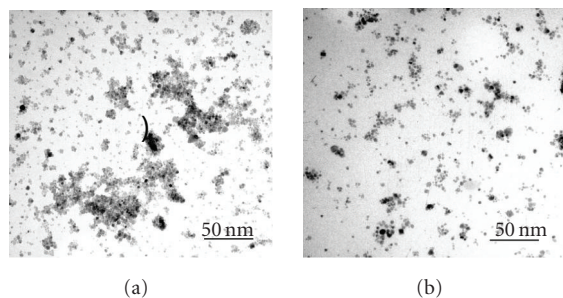


FIGURE 4: Transmission electron micrograph of 2-pyrrolidone-coated SPIONs (a), PVLA-coated SPIONs (b).

The quantitative analysis was performed by one radiologist for MR imaging. The signal intensity (SI) was measured in defined regions of interest (ROI) in identical site of liver before (SI pre of liver) and after (SI post of liver) contrast injection. In addition, the SI in the ROI of back muscle adjacent to the liver was measured before (SI pre of BM) and after (SI post of BM). SI of back muscle is not affected by the SPIONs injection. Relative signal enhancement of liver was calculated by using the formula  $[(SI \text{ post of liver}/SI \text{ post of BM} - SI \text{ pre of liver}/SI \text{ pre of BM})/SI \text{ post of liver}/SI \text{ post of BM}] \times 100$ .

### 3. RESULTS AND DISCUSSION

#### 3.1. Preparation and characterization of PVLA-coated SPIONs

Surface modification of iron oxide nanoparticles with biocompatible polymers is potentially beneficial to prepare MRI contrast agents for in vivo applications. In particular, targeted delivering, nonaggregating, and nontoxic properties are required for the nanoparticles to achieve the accumulation in liver. To produce well-dispersed iron oxide colloidal solutions with hepatocytes targeting properties, we prepared SPIONs coated with PVLA having galactose residues as hepatocyte-specific ligand and serving as an emulsifier due to its amphiphilic property [22]. The parent nanoparticles were synthesized by coprecipitation of ferrous and ferric ions in an aqueous solution upon addition of ammonium hydroxide. Common problems of the naked magnetic nanoparticles are their tendency to agglomerate once formed and their chemical instability with respect to oxidation in air [25]. The final iron oxide compositions are very often intermediate between magnetite ( $Fe_3O_4$ ) and maghemite ( $\gamma\text{-}Fe_2O_3$ ), due to the oxidation of the particles during the synthesis [31]. The problem of oxidation-sensitive magnetite could be overcome by the deliberate introduction of a second oxidation step [25]. Stable ferrofluids for liver targeting can be prepared by adsorption of PVLA on the surface of magnetic nanoparticles after the second oxidation step. Polymer can be adsorbed by electrostatic, covalent, hydrophobic, and hydrogen bonding mechanism [32]. Hydrogen bonding is assumed to be the predominant mechanism for the adsorption of nonionic polymer such as PVLA on oxide surface. The hydrogen bonding result from the interaction between polar

functional groups of PVLA and hydroxylated and protonated surface sides of the oxide [25]. The importance of surface hydroxyl functions in hydrogen bonding has been further verified by adsorbing the polymer onto pure gold sol, the surface of which is not oxidized and, therefore, does not carry any hydroxyl groups; in this case, no adsorption of the polymer is detected [33]. Accordingly, it is believed that the hydrogen bonding may be strengthened by the second oxidation step mentioned above.

FTIR analysis was performed to confirm the coating on SPIONs surface with PVLA. Figure 2 shows a comparison between the FTIR spectra of the SPIONs (a) the pure PVLA itself (b), and the PVLA-coated SPIONs (c). The presence of magnetic iron oxide nanoparticles can be seen by two strong absorption bands at around  $631$  and  $564\text{ cm}^{-1}$ . These bands result from split of the  $\nu_1$  band at  $570\text{ cm}^{-1}$ , which corresponds to the Fe–O bond of bulk magnetite [34]. Furthermore, an adsorption band was observed at around  $434\text{ cm}^{-1}$ , which corresponds to the shifting of the  $\nu_2$  band of the Fe–O bond of bulk magnetite (at  $375\text{ cm}^{-1}$ ) to a higher wave number [34]. The strong band at  $1078\text{ cm}^{-1}$  as shown in the FTIR spectrum of PVLA (b) is attributed to the skeletal vibrations and C–O stretch of oligosaccharide [35], and the band at  $2926\text{ cm}^{-1}$  and a pair of bands at  $1542$  and  $1423\text{ cm}^{-1}$  are attributed to the stretch of  $-\text{CH}_2$  and aromatic C=C of polystyrene backbone, respectively [12, 36]. In addition, the N–H bending and C=O stretching bands are overlapped at  $1647\text{ cm}^{-1}$  [37]. Comparing the FTIR spectrum of SPIONs (a) and that of PVLA-coated SPIONs (c), the characteristic bands resulted from the oligosaccharide and polystyrene containing PVLA appeared near  $2926$  and  $1078\text{ cm}^{-1}$ , respectively, for PVLA-coated SPIONs, indicating that PVLA was coated at the nanoparticle surface. After the adsorption of PVLA, the characteristic bands of Fe–O bond of bulk magnetite ( $631$  and  $564\text{ cm}^{-1}$ ) shifted to the higher wave numbers of about  $636$  and  $588\text{ cm}^{-1}$ , an indication of the occurrence of hydrogen bonding between hydroxyl groups of PVLA and hydroxylated and protonated surface sides of the oxide.

We compared the structure, size, and uniformity of the PVLA-coated SPIONs with those of the 2-pyrrolidone-coated SPIONs prepared for use as a control.

Figure 3 shows the XRD patterns for the 2-pyrrolidone-coated and PVLA-coated SPIONs. Six characteristic peaks ( $2\theta = 30.1, 35.5, 43.1, 53.4, 57.0$ , and  $62.6^\circ$ ), marked by their indices [(220), (311), (400), (422), (511), and (440)], were observed for 2-pyrrolidone-coated SPION samples. The positions and relative intensities of all diffraction peaks in Figure 3(a) match well with those from the JCPDS file (PCPDFWIN v.2.02, PDF No. 85-1436) for magnetite and reveal that the resultant nanoparticles were pure magnetite with spinel structure [11]. As shown in Figure 3(b), the XRD pattern of PVLA-coated SPIONs also proved its highly crystalline nature and the peaks are consistent with standard maghemite reflections [38, Supporting Information], being an indication of the magnetite-maghemite transformation due to second oxidation step. It is already known that magnetite is transformed to maghemite at pH 2 upon addition of ferric ions. Jolivet and Tronc have reported on the

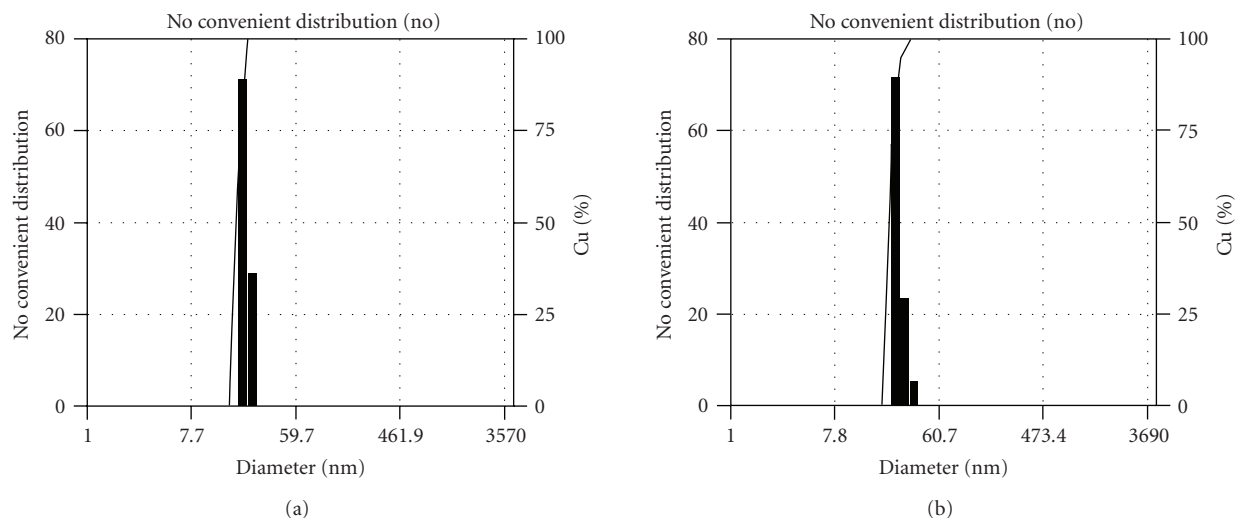


FIGURE 5: Particle size distribution profiles of 2-pyrrolidone-coated SPIONs (a), PVLA-coated SPIONs (b).

behavior of colloidal magnetite in acidic medium in the presence of iron nitrate and studied the phenomena that induce the magnetite-maghemite transformation [25, 39]. Further, XRD confirmed the high degree of crystallinity of the both types of particles.

The shape, size, and uniformity of the 2-pyrrolidone-coated and PVLA-coated SPIONs were observed by means of TEM. The TEM images of these both particles show ellipsoidal iron oxide particles with an average size less than 10 nm as shown in Figure 4. As well known, a representative TEM image of naked magnetic nanoparticles showed that the particles strongly agglomerated [6, 25]. On the other hand, our samples that were obtained after monomer or polymer coating reveal well-separated particles. Especially, in PVLA-coated particles (b), the particle distribution is more homogeneous than the 2-pyrrolidone-coated particles (a).

Figure 5 shows number average sizes and size distribution of synthesized magnetite and PVLA-coated SPIONs by ELS. It was clear that size distributions of both the 2-pyrrolidone-coated and PVLA-coated SPIONs were unimodal and particles were uniformly prepared. The average particle sizes were  $20.8 \pm 4.4$  and  $25.8 \pm 6.1$  nm for 2-pyrrolidone-coated and PVLA-coated SPIONs, respectively. The average diameters obtained by ELS were larger than the sizes determined from the TEM image for corresponding samples. This may presumably be because ELS gives a mean hydrodynamic diameter of magnetic nanoparticles surrounded by PVLA layer in aqueous solution whereas TEM gives the diameter of magnetic nanoparticles alone in dry state [40].

### 3.2. Observation of confocal laser scanning micrographs

The FITC on the nanoparticles allowed direct visualization of the nanoparticle uptakes into cells. Figure 6 shows fluorescence (a) and phasecontrast (b) micrographs of hepatocytes cultured in medium containing SPIONs coated with

FITC-labeled PVLA according to treatment time. The fluorescence micrograph demonstrates a time-dependent uptake of FITC-PVLA-coated SPIONs into hepatocytes as shown in Figure 6(a). A significant uptake of the nanoparticles was clearly observed after 1 hour of culture. We performed a quantitative evaluation of uptake in the in vivo although only qualitative evaluation was performed in the in vitro, because the specific interaction between galactose moieties of PVLA and asialoglycoprotein receptors in the hepatocytes has been already reported.

It was also checked whether the PVLA-coated SPIONs existed in the cytosol or was only attached to the plasma membrane of hepatocyte. The cell was sectioned at various depths from cell surface by confocal laser scanning microscopy, and each fluorescence distribution was observed (see Figure 7). Fluorescence of the magnetic nanoparticles was observed more intensively inside the cell membrane and uniformly distributed in the cytosol. These results suggest that the many nanoparticles were internalized in the cytosol through a receptor-mediated endocytosis. The affinity of AS-GPR to natural and synthetic oligosaccharides having nonreducing galactose residues had been reported by Lee et al. [17].

### 3.3. In vivo MR imaging of liver

We examined an applicability of the PVLA-coated SPIONs for in vivo liver imaging based on a  $T_2$ -weighted FSE echo imaging, which is a useful way to the liver accumulation of the magnetic nanoparticles [14]. We examined three rats to obtain the preliminary data. Liver signal intensity of all animals showed similar degree of signal drop. We described the typical case in our experiment. However, we did not calculate the statistical analysis due to small number of animals.

At 1 hour postinjection of the PVLA-coated SPIO, signal intensity of liver was hypointense compared to SI of back muscle FSE  $T_2$ -weighted MR image (data not shown). The relative signal enhancement on the FSE  $T_2$ -weighted



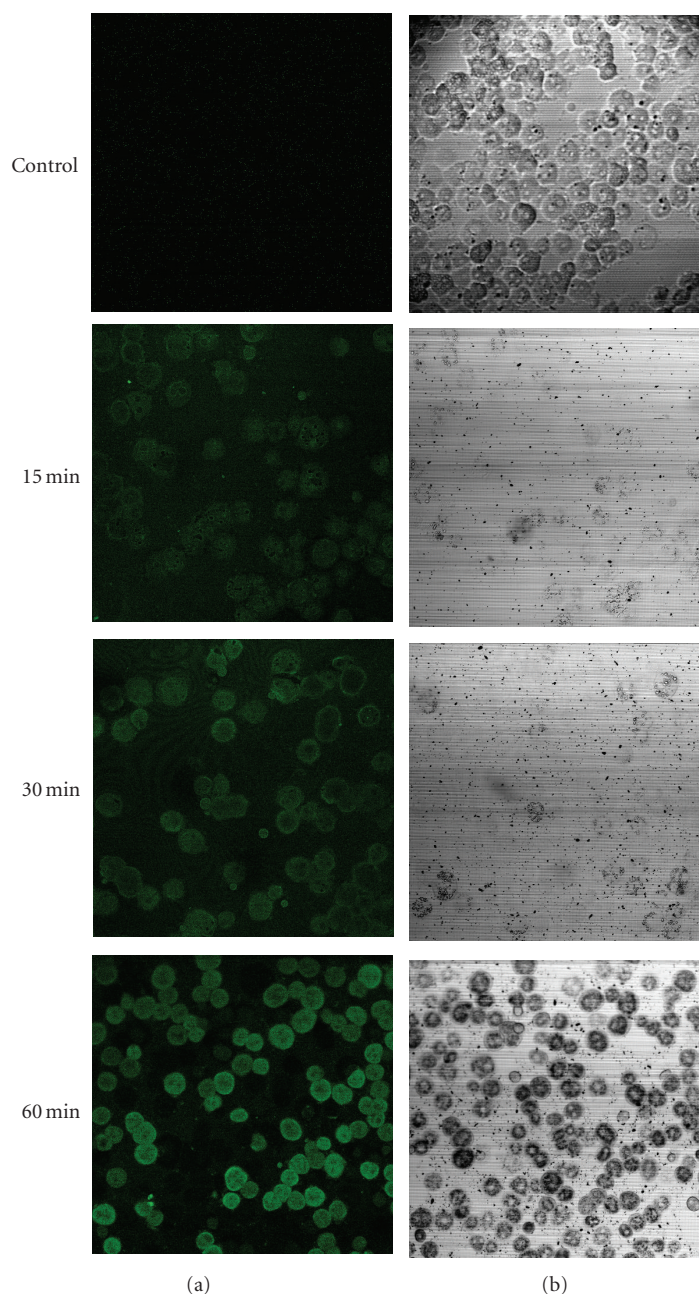


FIGURE 6: Fluorescence (a) and phase-contrast (b) microphotographs of hepatocytes incubated with FITC-PVLA-coated SPIONs (1 mg/mL) against time at 37°C.

MR image was observed in the liver with a  $T_2$  signal drop of 70.9% for PVLA-coated SPIO, indication of the accumulation of nanoparticle in liver. Figure 8 shows the  $T_2$ -weighted MR images of middle part of liver before and after injection of SPIONs through tail vein. After injection of the PVLA-coated SPIONs, the SI of liver clearly dropped on  $T_2$ -weighted MR image. The relative signal enhancement of the  $T_2$ -weighted MR image was observed in the liver with a  $T_2$  signal drop of 75.4% for PVLA-coated SPIONs and 36% for pyrrolidone-coated SPIONs. SI of liver on  $T_2$ -weighted MR image after injection of PVLA-coated SPIONs

was darker than that after pyrrolidone-coated SPIONs (see Figures 8(b) and 8(d)). Thus, PVLA-coated SPIONs were more successfully targeted the liver than pyrrolidone-coated SPIONs. PVLA-coated SPIONs can be used as the hepatocyte targeted contrast agent such as mangafodipir trisodium, formerly known as Mn-DPDP [41]. Additionally, we observed accumulation in kidneys after injection of PVLA-coated SPIONs (data not shown). We think that the nanoparticles will be cleared from kidney. Renal excretion of nanoparticles is beneficial to develop nontoxic MR nanoparticles in the clinical use.



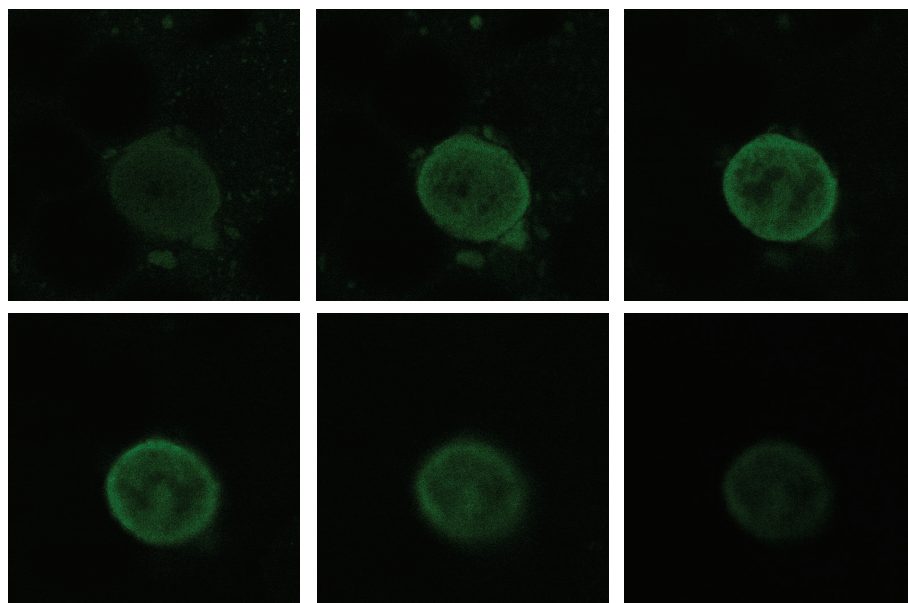


FIGURE 7: Confocal laser micrograph of hepatocytes incubated with FITC-PVLA coated SPIONs (1 mg/mL) for 1 hour (gallery mode observation).

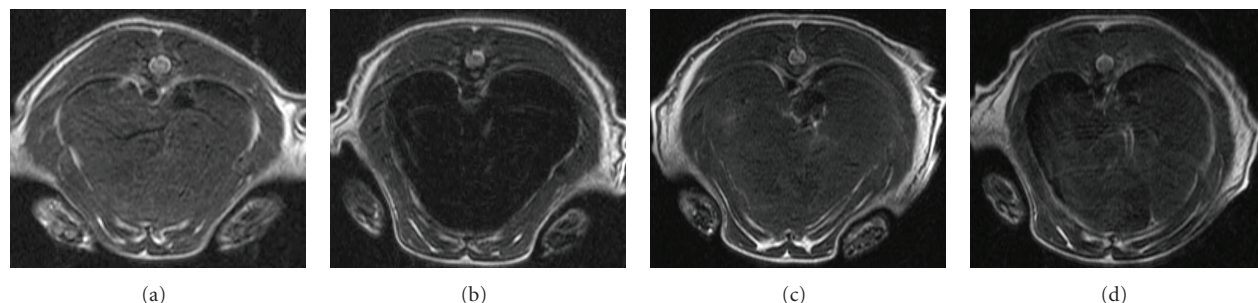


FIGURE 8:  $T_2$ -weighted MR image (b) after 1-hour injection of PVLA-coated SPIONs shows marked signal drop (darkening) of liver compared to  $T_2$ -weighted MR image of preinjection (a). Degree of signal drop is mild between  $T_2$ -weighted MR image of pre- (c) and postinjection (d) of pyrrolidone-coated SPIONs.

#### 4. CONCLUSION

We have demonstrated that PVLA can serve as the coating material for SPIONs to achieve the stabilization and liver-specific delivery of ferrofluid. The PVLA-coated SPIONs of about 10 nm diameter having a core-shell structure with magnetic core and polymeric shell have been successfully prepared. The FTIR experimental results proved that the PVLA is adsorbed onto the surface of SPIONs through the hydrogen bonding between polar functional alcohol groups of PVLA and hydroxylated and protonated surface sides of the oxide. Hence the resultant nanoparticles possess an excellent solubility and stability in ferrofluid. In vivo experimental result indicated that the PVLA-coated SPIONs were accumulated in liver appreciably. Therefore, PVLA as a coating material not only prevented the aggregation between SPIONs in physiological medium but also provided a capacity to be delivered in liver specifically, which suggests the potential utility of PVLA-coated SPIONs as a contrast agent for liver diagnosis.

#### ACKNOWLEDGMENTS

This research was supported by a fund provided by the Ministry of Science and Technology of Korea (M10414030002-05N1403-00210). The authors also acknowledge National Instrumentation Center for Environmental Management for permission to take ELS, FTIR, TEM, and confocal microscopy. M. K. Yoo was supported by the Brain Korea 21 Project.

#### REFERENCES

- [1] A. K. Gupta and M. Gupta, "Synthesis and surface engineering of iron oxide nanoparticles for biomedical applications," *Biomaterials*, vol. 26, no. 18, pp. 3995–4021, 2005.
- [2] R. Weissleder, A. Bogdanov, E. A. Neuwelt, and M. Papisov, "Long circulating iron oxides for MR imaging," *Advanced Drug Delivery Review*, vol. 16, no. 2-3, pp. 321–334, 1995.
- [3] L. Babes, B. Denizot, G. Tanguy, J. J. Le Jeune, and P. Jallet, "Synthesis of iron oxide nanoparticles used as MRI contrast

- agents: a parametric study," *Journal of Colloid and Interface Science*, vol. 212, no. 2, pp. 474–482, 1999.
- [4] C. Chouly, D. Pouliquen, I. Lucet, J. J. Jeune, and P. Jallet, "Development of superparamagnetic nanoparticles for MRI: effect of particle size, charge and surface nature on biodistribution," *Journal of Microencapsulation*, vol. 13, no. 3, pp. 245–255, 1996.
  - [5] Y.-X. J. Wang, S. M. Hussain, and G. P. Krestin, "Superparamagnetic iron oxide contrast agents: physicochemical characteristics and applications in MR imaging," *European Radiology*, vol. 11, no. 11, pp. 2319–2331, 2001.
  - [6] C.-L. Lin, C.-F. Lee, and W.-Y. Chiu, "Preparation and properties of poly(acrylic acid) oligomer stabilized superparamagnetic ferrofluid," *Journal of Colloid and Interface Science*, vol. 291, no. 2, pp. 411–420, 2005.
  - [7] Y. Zhang, N. Kohler, and M. Zhang, "Surface modification of superparamagnetic magnetite nanoparticles and their intracellular uptake," *Biomaterials*, vol. 23, no. 7, pp. 1553–1561, 2002.
  - [8] A. Petri-Fink, M. Chastellain, L. Juillerat-Jeanneret, A. Ferrari, and H. Hofmann, "Development of functionalized superparamagnetic iron oxide nanoparticles for interaction with human cancer cells," *Biomaterials*, vol. 26, no. 15, pp. 2685–2694, 2005.
  - [9] A. J. M. D'Souza, R. L. Schowen, and E. M. Topp, "Polyvinylpyrrolidone-drug conjugate: synthesis and release mechanism," *Journal of Controlled Release*, vol. 94, no. 1, pp. 91–100, 2004.
  - [10] C. C. Berry, S. Wells, S. Charles, G. Aitchison, and A. S. G. Curtis, "Cell response to dextran-derivatised iron oxide nanoparticles post internalisation," *Biomaterials*, vol. 25, no. 23, pp. 5405–5413, 2004.
  - [11] Y.-C. Chang and D.-H. Chen, "Preparation and adsorption properties of monodisperse chitosan-bound  $\text{Fe}_3\text{O}_4$  magnetic nanoparticles for removal of  $\text{Cu(II)}$  ions," *Journal of Colloid and Interface Science*, vol. 283, no. 2, pp. 446–451, 2005.
  - [12] A. K. Gupta and M. Gupta, "Cytotoxicity suppression and cellular uptake enhancement of surface modified magnetic nanoparticles," *Biomaterials*, vol. 26, no. 13, pp. 1565–1573, 2005.
  - [13] I. Raynal, P. Prigent, S. Peyramaure, A. Najid, C. Rebuzzi, and C. Corot, "Macrophage endocytosis of superparamagnetic iron oxide nanoparticles: mechanisms and comparison of ferumoxides and ferumoxtran-10," *Investigative Radiology*, vol. 39, no. 1, pp. 56–63, 2004.
  - [14] M. Kumagai, Y. Imai, T. Nakamura, et al., "Iron hydroxide nanoparticles coated with poly(ethylene glycol)-poly(aspartic acid) block copolymer as novel magnetic resonance contrast agents for in vivo cancer imaging," *Colloids and Surfaces B*, vol. 56, no. 1-2, pp. 174–181, 2007.
  - [15] H. Choi, S. R. Choi, R. Zhou, H. F. Kung, and I.-W. Chen, "Iron oxide nanoparticles as magnetic resonance contrast agent for tumor imaging via folate receptor-targeted delivery," *Academic Radiology*, vol. 11, no. 9, pp. 996–1004, 2004.
  - [16] A. Moore, J. P. Basilion, E. A. Chiocca, and R. Weissleder, "Measuring transferrin receptor gene expression by NMR imaging," *Biochimica et Biophysica Acta*, vol. 1402, no. 3, pp. 239–249, 1998.
  - [17] R. T. Lee, R. W. Myers, and Y. C. Lee, "Further studies on the binding characteristics of rabbit liver galactose/N-acetylgalactosamine-specific lectin," *Biochemistry*, vol. 21, no. 24, pp. 6292–6298, 1982.
  - [18] S.-J. Seo, H.-S. Moon, D.-D. Guo, S.-H. Kim, T. Akaike, and C. S. Cho, "Receptor-mediated delivery of all-*trans*-retinoic acid (ATRA) to hepatocytes from ATRA-loaded poly(*N*-*P*-vinylbenzyl-4-*o*- $\beta$ -D-galactopyranosyl-D-gluconamide) nanoparticles," *Materials Science and Engineering C*, vol. 26, no. 1, pp. 136–141, 2006.
  - [19] C. S. Cho, S. J. Seo, I. K. Park, et al., "Galactose-carrying polymers as extracellular matrices for liver tissue engineering," *Biomaterials*, vol. 27, no. 4, pp. 576–585, 2006.
  - [20] R. L. Hudgin, W. E. Pricer Jr., G. Ashwell, R. J. Stockert, and A. G. Morell, "The isolation and properties of a rabbit liver binding protein specific for asialoglycoproteins," *Journal of Biological Chemistry*, vol. 249, no. 17, pp. 5536–5543, 1974.
  - [21] S. Hirose, H. Ise, M. Uchiyama, C. S. Cho, and T. Akaike, "Regulation of asialoglycoprotein receptor expression in the proliferative state of hepatocytes," *Biochemical and Biophysical Research Communications*, vol. 287, no. 3, pp. 675–681, 2001.
  - [22] A. Maruyama, T. Ishihara, N. Adachi, and T. Akaike, "Preparation of nanoparticles bearing high density carbohydrate chains using carbohydrate-carrying polymers as emulsifier," *Biomaterials*, vol. 15, no. 13, pp. 1035–1042, 1994.
  - [23] K. Kobayashi, H. Sumitomo, and Y. Ina, "Synthesis and functions of polystyrene derivatives having pendent oligosaccharides," *Polymer Journal*, vol. 17, no. 4, pp. 567–575, 1985.
  - [24] G. A. Van Ewijk, G. J. Vroeghe, and A. P. Philipse, "Convenient preparation methods for magnetic colloids," *Journal of Magnetism and Magnetic Materials*, vol. 201, no. 1–3, pp. 31–33, 1999.
  - [25] M. Chastellain, A. Petri, and H. Hofmann, "Particle size investigations of a multistep synthesis of PVA coated superparamagnetic nanoparticles," *Journal of Colloid and Interface Science*, vol. 278, no. 2, pp. 353–360, 2004.
  - [26] X. Hong, W. Guo, H. Yuan, et al., "Periodate oxidation of nanoscaled magnetic dextran composites," *Journal of Magnetism and Magnetic Materials*, vol. 269, no. 1, pp. 95–100, 2004.
  - [27] Z. Li, H. Chen, H. Bao, and M. Gao, "One-pot reaction to synthesize water-soluble magnetic nanocrystals," *Chemistry of Materials*, vol. 16, no. 8, pp. 1391–1393, 2004.
  - [28] P. O. Seglen, "Preparation of isolated rat liver cell," *Methods in Cell Biology*, vol. 13, pp. 29–83, 1976.
  - [29] M. Aubele, H. Zitzelsberger, S. Szücs, et al., "Comparative FISH analysis of numerical chromosome 7 abnormalities in 5- $\mu\text{m}$  and 15- $\mu\text{m}$  paraffin-embedded tissue sections from prostatic carcinoma," *Histochemistry and Cell Biology*, vol. 107, no. 2, pp. 121–126, 1997.
  - [30] C. S. Cho, A. Kobayashi, R. Takei, T. Ishihara, A. Maruyama, and T. Akaike, "Receptor-mediated cell modulator delivery to hepatocyte using nanoparticles coated with carbohydrate-carrying polymers," *Biomaterials*, vol. 22, no. 1, pp. 45–51, 2001.
  - [31] C. Cannas, D. Gatteschi, A. Musinu, G. Piccaluga, and C. Sangregorio, "Structural and magnetic properties of  $\text{Fe}_2\text{O}_3$  nanoparticles dispersed over a silica matrix," *Journal of Physical Chemistry B*, vol. 102, no. 40, pp. 7721–7726, 1998.
  - [32] D. H. Napper, *Polymeric Stabilisation of Colloidal Dispersions*, Academic Press, New York, NY, USA, 1983.
  - [33] L. T. Lee and P. Somasundaran, "Adsorption of polyacrylamide on oxide minerals," *Langmuir*, vol. 5, no. 3, pp. 854–860, 1989.
  - [34] M. Yamaura, R. L. Camilo, L. C. Sampaio, M. A. Macêdo, M. Nakamura, and H. E. Toma, "Preparation and characterization of (3-aminopropyl)triethoxysilane-coated magnetite nanoparticles," *Journal of Magnetism and Magnetic Materials*, vol. 279, no. 2-3, pp. 210–217, 2004.

- [35] C. V. Luyen and D. M. Huong, "Chitin and derivatives," in *Polymeric Materials Encyclopedia*, J. C. Salomone, Ed., vol. 2, pp. 1208–1217, CRC Press, Boca Raton, Fla, USA, 1996.
- [36] P. Galgali, M. Agashe, and A. J. Varma, "Sugar-linked biodegradable polymers: regio-specific ester bonds of glucose hydroxyls in their reaction with maleic anhydride functionalized polystyrene and elucidation of the polymer structures formed," *Carbohydrate Polymers*, vol. 67, no. 4, pp. 576–585, 2007.
- [37] Y.-C. Chang, S.-W. Chang, and D.-H. Chen, "Magnetic chitosan nanoparticles: studies on chitosan binding and adsorption of Co(II) ions," *Reactive and Functional Polymers*, vol. 66, no. 3, pp. 335–341, 2006.
- [38] T. H. Hyeon, S. S. Lee, J. N. Park, Y. H. Chung, and H. B. Na, "Synthesis of highly crystalline and monodisperse maghemite nanocrystallites without a size-selection process," *Journal of the American Chemical Society*, vol. 123, no. 51, pp. 12798–12801, 2001.
- [39] J. P. Jolivet and E. Tronc, "Interfacial electron transfer in colloidal spinel iron oxide. Conversion of  $\text{Fe}_3\text{O}_4$ - $\gamma$ - $\text{Fe}_2\text{O}_3$  in aqueous medium," *Journal of Colloid and Interface Science*, vol. 125, no. 2, pp. 688–701, 1988.
- [40] K. M. Kamruzzaman Selim, Y.-S. Ha, S.-J. Kim, et al., "Surface modification of magnetite nanoparticles using lactobionic acid and their interaction with hepatocytes," *Biomaterials*, vol. 28, no. 4, pp. 710–716, 2007.
- [41] U. Kettritz, J. F. Schlund, K. Wilbur, L. B. Eisenberg, and R. C. Semelka, "Comparison of gadolinium with manganese-DPDP of liver lesion detection and characterization: preliminary results," *Magnetic Resonance Imaging*, vol. 14, no. 10, pp. 1185–1190, 1996.

## Research Article

# Fluorescent Nanoparticle-Based Indirect Immunofluorescence Microscopy for Detection of *Mycobacterium tuberculosis*

Dilan Qin,<sup>1,2</sup> Xiaoxiao He,<sup>1,2</sup> Kemin Wang,<sup>1,2</sup> Xiaojun Julia Zhao,<sup>3</sup> Weihong Tan,<sup>1,2</sup> and Jiyun Chen<sup>1,2</sup>

<sup>1</sup> State Key Laboratory of Chemo/Biosensing and Chemometrics, Biomedical Engineering Center, College of Chemistry and Chemical Engineering, Hunan University, Changsha, Hunan 410082, China

<sup>2</sup> Key Laboratory for Bio-Nanotechnology and Molecule Engineering of Hunan Province, Hunan University, Changsha 410082, China

<sup>3</sup> Department of Chemistry, University of North Dakota, Grand Forks, ND 58202, USA

Correspondence should be addressed to Kemin Wang, kmwang@hnu.cn

Received 24 March 2007; Revised 10 July 2007; Accepted 10 October 2007

Recommended by Marek Osinski

A method of fluorescent nanoparticle-based indirect immunofluorescence microscopy (FNP-IIFM) was developed for the rapid detection of *Mycobacterium tuberculosis*. An anti-*Mycobacterium tuberculosis* antibody was used as primary antibody to recognize *Mycobacterium tuberculosis*, and then an antibody binding protein (Protein A) labeled with Tris(2,2-bipyridyl)dichlororuthenium(II) hexahydrate (RuBpy)-doped silica nanoparticles was used to generate fluorescent signal for microscopic examination. Prior to the detection, Protein A was immobilized on RuBpy-doped silica nanoparticles with a coverage of  $\sim 5.1 \times 10^2$  molecules/nanoparticle. With this method, *Mycobacterium tuberculosis* in bacterial mixture as well as in spiked sputum was detected. The use of the fluorescent nanoparticles reveals amplified signal intensity and higher photostability than the direct use of conventional fluorescent dye as label. Our preliminary studies have demonstrated the potential application of the FNP-IIFM method for rapid detection of *Mycobacterium tuberculosis* in clinical samples.

Copyright © 2007 Dilan Qin et al. This is an open access article distributed under the Creative Commons Attribution License, which permits unrestricted use, distribution, and reproduction in any medium, provided the original work is properly cited.

## 1. INTRODUCTION

Tuberculosis (TB) is a global public health emergency, fueled by the spread of human immunodeficiency virus (HIV)/Acquired Immune Deficiency Syndrome (AIDS) and the emergence of drug-resistant strains of *Mycobacterium tuberculosis* (*M. tuberculosis*). Approximately 2 billion people—one third of the human population—are currently infected with TB, with one new infection occurring every second. Each year there are more than 8.8 million cases and close to 2 million deaths attributed to TB worldwide. Experts at the World Health Organization (WHO) predicted these numbers would escalate in coming decades, nearly 1 billion people would become newly infected, over 150 million would become sick, and 36 million would die worldwide between now and 2020—if control was not further strengthened [1]. Rapid and accurate diagnosis of tuberculosis is a critical step in the management and control of TB. For decades, diagnosis has largely relied on acid-fast staining and culture of bacilli. However, the sensitivity of acid-fast staining is poor, and culture is a relatively time-consuming process. Many ef-

forts have been directed toward developing techniques for rapid diagnosis of tuberculosis with higher sensitivity and reliability [2], including methods based on molecular biology (molecular diagnosis techniques) [3], such as nucleic acid amplification tests (NAA tests) [4, 5], DNA probes [6, 7]; and methods based on immunology (serodiagnosis techniques) [8], such as enzyme-linked immunosorbent assay (ELISA) [9, 10], immunochromatographic assay [11], latex agglutination assay [12]. Recently, more simple, direct, and visually detectable assays have been developed for rapid diagnosis of TB with Au nanoparticles [13, 14]. These approaches have contributed much on the improvement of sensitivity and accuracy of the detection but still exhibit deficiencies in some extent [15]. NAA tests have been the subject of a number of investigations. Many commercial kits are available including the Amplicor and MTD tests which are currently US FDA approved. The NAA tests have high specificity and work better to rule-in TB. However, sensitivity of NAA tests is lower and it is less good to rule-out TB. Serological tests for the diagnosis of tuberculosis have been attempted for decades. Dozens of commercial kits are available, most of which are focused



on antibody detection. However, assays based on antibodies detection are hard to distinguish active TB from BCG vaccination and past infection. Therefore, more studies are needed to develop and improve the detection methods for tuberculosis.

Dye-doped silica nanoparticles [16, 17], exhibiting such important advantages as high luminescence and photostability compared to conventional fluorescent dyes, have been widely applied in biological imaging and ultrasensitive bioanalyses, including cell staining [18], DNA detection [19, 20], cell surface receptor targeting [21–24], and ultrasensitive detection of *Escherichia coli* O157:H7 [25]. Owing to the dye-encapsulated structure, thousands of dye molecules embedded in one nanoparticle contribute to the luminescence of one particle, causing significant signal amplification. In this paper, we establish a rapid immunological method for detection of *M. tuberculosis* by combining highly luminescent RuBpy-doped nanoparticles with indirect immunofluorescence microscopy. Since direct anchoring of antibodies onto solid supports via covalence methods is always faced with the loss of activity of the antibodies, Protein A was applied as an affinitive adsorber. In order to obtain full antibody activity, *M. tuberculosis* was first recognized with the specific antibody in solution then signaled by Protein A functionalized fluorescent nanoparticles. This method was used to detect *M. tuberculosis* in mixed bacterial samples and spiked sputum samples. Meanwhile, signal intensity and photostability of the method were compared with conventional fluorescent dye fluorescein isothiocyanate labeling method.

## 2. MATERIALS AND METHODS

### 2.1. Bacteria

The H37Ra strain of *M. tuberculosis* was obtained from the National Institute for the Control of Pharmaceutical and Biological Products (Beijing, China). *M. tuberculosis* was cultured by Dr. Songlin Yi (Hunan Tuberculosis Hospital, Hunan, China) on modified Lowenstein-Jenson medium at 37°C for 3–4 weeks to obtain pure bacterial culture for use in establishing detection method. *M. tuberculosis* was harvested in pH 7.4, 0.01 M phosphate buffered saline (PBS) to form predominantly single-cell suspension using previously described method [26]. *E. coli* strain DH5 $\alpha$  (Microbial Culture Collection Center of Guangdong Institute of Microbiology, Guangdong, China) was grown overnight in Luria-Bertani broth at 37°C. The bacterial suspensions were counted in a Petroff-Hausser chamber, and the concentrations of bacteria were adjusted for use in experiments.

### 2.2. Materials

Tris(2,2-bipyridyl)dichlororuthenium(II) hexahydrate (RuBpy), Triton X-100, fluorescein isothiocyanate (FITC), and Protein A from *Staphylococcus aureus* were purchased from Sigma-Aldrich. Sodium carbonate, sodium bicar-

bonate, sodium dihydrogen phosphate, disodium hydrogen phosphate, sodium hydroxide, sodium citrate, acetonitrile, glycine, and N-acetyl-L-cysteine (NALC) of analytical grade were obtained from China National Medicines Group Shanghai Chemical Reagents Company (Shanghai, China). Cyanogen Bromide (CNBr) was synthesized using previously described method [27]. Purified rabbit anti-*M. tuberculosis* IgG and FITC-conjugated rabbit anti-*M. tuberculosis* IgG were supplied by Biodesign International (Me, USA). Rabbit anti-p53 IgG was purchased from Boster Biological Technology (Wuhan, China).

### 2.3. Instrumentation

The morphology and uniformity of RuBpy-doped silica nanoparticles were measured with an atomic force microscope (AFM) SPI3800N-SPA400 (Seiko). Size distribution analysis of RuBpy-doped silica nanoparticles was determined at 25°C by dynamic light scattering (DLS) using Zetasizer 3000HS<sub>A</sub> (Malvern). The volume-weighted average diameter obtained by the manufacturer's software was used for the calculation of the average nanoparticle volume. A refractive index of 1.47 was used for nanoparticles (the refractive index of silica). Viscosity was determined at 30°C using a cone plate digital viscometer LVDV-III+CP (Brookfield). Determination of protein concentration according to the Bradford method was done with a UV-Vis spectrophotometer DU-800 (Beckman) [28].

### 2.4. Biological modification of the RuBpy-doped silica nanoparticles

RuBpy-doped silica nanoparticles were prepared using the water-in-oil (W/O) microemulsion method that had been described before [21]. In order to immobilize Protein A onto the nanoparticles, the surface of the RuBpy-doped silica nanoparticles was first activated with CNBr. Nanoparticles (11.2 mg) were suspended in 2 ml of 2 M sodium carbonate solution by ultrasonication. A solution of CNBr in acetonitrile (0.78 g of CNBr dissolved in 2 ml of acetonitrile) was then added dropwise to the particle suspension under stirring at room temperature for 5 minutes. After the activation reaction, the particles were washed twice with ice-cold water and twice with pH 7.4, 0.01 M PBS buffer. For covalently coupling of Protein A onto the nanoparticle surface, a 40  $\mu$ l portion of aqueous solution of 2 mg/ml Protein A was added to 1 ml of 1.1 mg/ml freshly activated nanoparticles in PBS, and stirring was continued for 24 hours at 4°C. The Protein A immobilized nanoparticles were then blocked with 6 ml of 0.3 M glycine solution (pH 8.0) 4°C for 16 hours in order to reduce the effect of nonspecific binding in the subsequent immunoassay. The final product was washed, resuspended in PBS, and stored at 4°C for future usage. The surface coverage of Protein A on nanoparticles was determined by measuring the decrease of Protein A concentration in the coupling solution by the Bradford method [28, 29].

## 2.5. Indirect immunofluorescence detection of *M. tuberculosis* with bioconjugated nanoparticles

Rabbit anti-*M. tuberculosis* antibody was added to a 500  $\mu$ l suspension of *M. tuberculosis* in PBS (antibody final concentration: 5  $\mu$ g/ml) and incubated at 37°C for 1 hour. The suspension was subsequently washed with PBS twice. Nanoparticle-Protein A conjugates (0.1 mg/ml) were then added, and the mixture was incubated at 37°C for 1 hour. To remove the free nanoparticle-Protein A conjugates that did not bind to the bacteria, the mixture was centrifuged at 8000 rpm for 2 minutes, and then the supernatant was discarded. The pellet was washed twice again. Smear slide was made by spreading the pellet on glass slide and observed with fluorescence microscopy or confocal microscopy. For controls, the rabbit anti-p53 antibody or PBS only was substituted for the primary antibody. Another bacterium *E. coli* DH5 $\alpha$  was treated with the same strategy to test the cross-reaction with bioconjugated nanoparticles.

For immunofluorescence detection of *M. tuberculosis* with FITC-labeled antibody, the FITC-conjugated rabbit anti-*M. tuberculosis* antibody was added to a 500  $\mu$ l suspension of *M. tuberculosis* in PBS (antibody final concentration: 25  $\mu$ g/ml) and the mixture was incubated at 37°C for 1 hour. The suspension was subsequently washed with PBS for three times and then spread on glass slide for microscopic examination.

## 2.6. Preparation of mixed bacterial sample

The mixed bacterial sample was prepared by mixing FITC-labeled *E. coli* and unlabeled *M. tuberculosis*. The FITC-labeled *E. coli* was first obtained according to the following method. *E. coli* was incubated at a concentration of 10<sup>9</sup> cells/ml with 0.5 mg of FITC in 0.1 M Na<sub>2</sub>CO<sub>3</sub>-NaHCO<sub>3</sub> buffer (pH 9.2) at 37°C for 2 hours in the dark. The *E. coli* was then washed for three times with PBS to remove free FITC and resuspended in PBS. A 500  $\mu$ l of mixed bacterial sample was prepared by easily mixing 1.8  $\times$  10<sup>6</sup> cells/ml FITC-labeled *E. coli* and 3.6  $\times$  10<sup>5</sup> cells/ml unlabeled *M. tuberculosis*. The mixture was detected with the FNP-IIFM method.

## 2.7. Preparation of spiked sputum sample

Sputum (2 ml) from healthy individual was collected and equally divided into two portions. One portion was spiked with *M. tuberculosis*, whereas the other portion was used as the unspiked sample. Then samples were liquefied with the NALC-NaOH method. In brief, the samples were mixed with equal volumes of NALC-NaOH solution (2% NaOH, 1.45% Na-citrate, and 0.5% NALC), shaken vigorously for digestion, and the mixtures were allowed to stand for 15 minutes at room temperature. Then the samples were diluted with 8 ml of water. To remove big agglomerates in the sputum, the mixtures were centrifuged at 1000 rpm for 2 minutes. The precipitates were disposed and the supernatants were centrifuged at 4000 g for 15 minutes. After the supernatant fluids were carefully decanted, the sediments were resuspended in

10 ml of PBS and centrifuged again at 4000 g for 15 minutes. The supernatants were discarded. The resulting pellets were suspended in 500  $\mu$ l of PBS and detected with the FNP-IIFM method.

## 2.8. Microscopy imaging

An inverted fluorescence microscope ECLIPSE TE300 (Nikon) equipped with a 100 W mercury lamp, a filter block (consisting of a 450–490 nm bandpass excitation and a 515 nm longpass emission filter), and a color CCD (Digital Camera DXM1200, Nikon) was used for common smear microscopic examination. Confocal microscopy was performed on an inverted Olympus IX70 microscope with an argon/krypton laser emitting at 488 nm to excite both RuBpy-doped nanoparticles and FITC fluorescence. We used a dichroic beam splitter (DCB) around 560 nm, together with either a longpass (LP) 560 nm filter for RuBpy-doped nanoparticles signal or an LP 505 nm filter for FITC signal. The RuBpy-doped nanoparticles signal was displayed in the pseudocolor red and the FITC signal in green. To study the differentiation between *M. tuberculosis* and *E. coli* in mixed bacterial samples with the FNP-IIFM method, the smears were scanned by sequential excitation mode. In brief, an argon/krypton laser emitting at 488 nm and a helium/neon laser emitting at 543 nm were used to excite FITC and RuBpy-doped silica nanoparticles fluorescence, respectively. We used a DCB around 560 nm, together with the following emission filter: either a bandpass (BP) 505–525 nm when the argon/krypton laser (FITC signal) was used or an LP 560 nm when the helium/neon laser (RuBpy-doped silica nanoparticles signal) was used. A  $\times$ 60 objective (Olympus PlanApo NA 1.4 oil) was used for routine studies. Pixel format was 512  $\times$  512.

# 3. RESULTS AND DISCUSSION

## 3.1. Highly luminescent and photostable fluorescent nanoparticles

We used an easy and efficient water-in-oil microemulsion method to synthesize RuBpy-doped silica nanoparticles. The obtained nanoparticles were uniform and well dispersed as shown in the AFM image (Figure 1(a)). Dynamic light scattering (DLS) measurements for the nanoparticles showed that the size distribution of RuBpy-doped nanoparticles was narrow and the volume-weighted mean hydrodynamic diameter determined was 63.8 nm (Figure 1(b)). For the structure of dye-doped silica nanoparticles, dye molecules are trapped inside the silica matrix, which endows the nanoparticles with two important merits. For one thing, the fluorescence emitted by one nanoparticle is contributed by thousands of dye molecules embedded in the silica matrix. So it is easy to see that one dye-doped nanoparticle is much more luminescent than one dye molecule, which is called the significant signal amplification effect. This attribute makes the dye-doped nanoparticles be advantageous

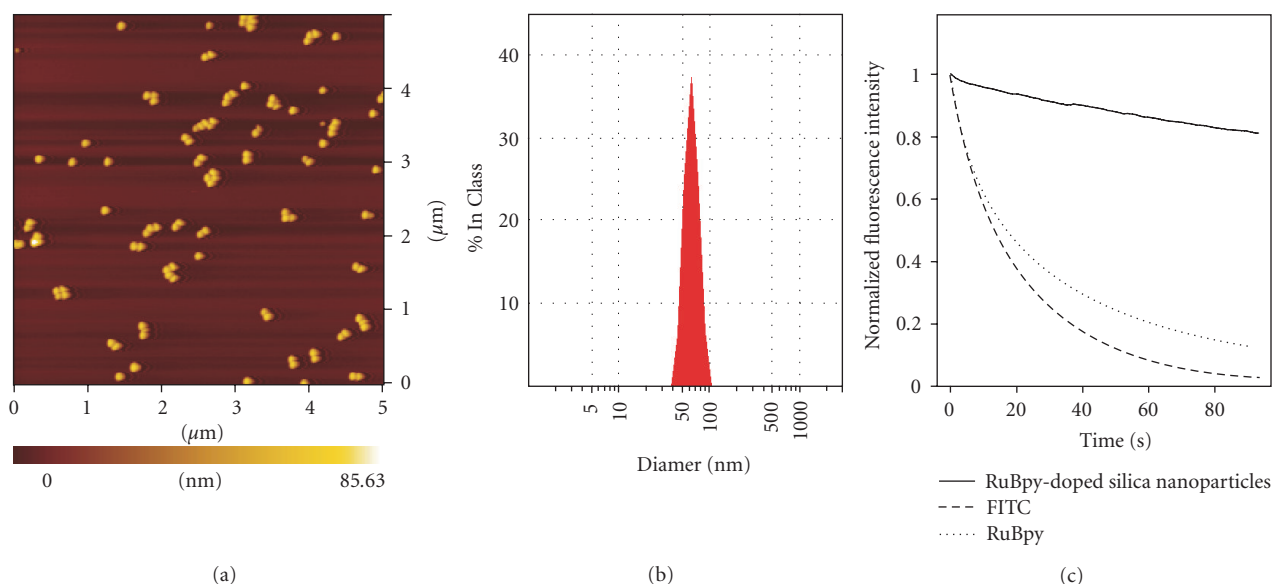


FIGURE 1: Properties of RuBpy-doped silica nanoparticles. (a) AFM micrograph of the RuBpy-doped silica nanoparticles. Particle size is determined to be  $65 \pm 2$  nm. (b) Size distribution analysis of RuBpy-doped silica nanoparticles in water by dynamic light scattering (DLS). The volume-weighted average diameter determined is 63.8 nm. (c) Photostability of RuBpy-doped silica nanoparticles versus pure RuBpy dye molecules and FITC dye molecules. Realtime measurements of fluorescence intensities were performed on a confocal microscope with an intensive argon/krypton laser as the excitaton source.

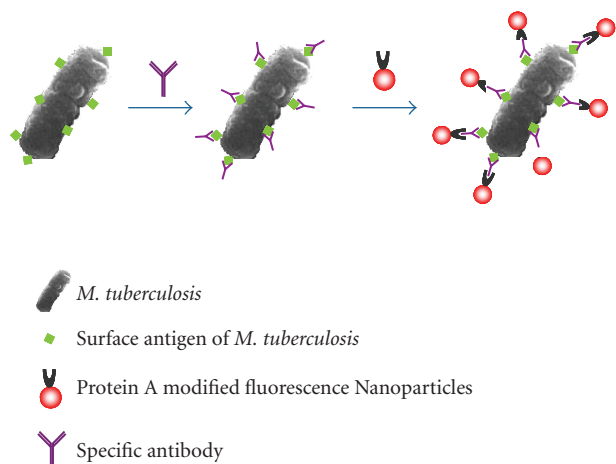


FIGURE 2: Schematic representation of the principle of the detection of *M. tuberculosis* with the fluorescent nanoparticle-based indirect immunofluorescence assay.

in improving detection sensitivity in many aspects and very suitable for detection of bacteria with higher sensitivity. As another advantage, due to the protective function of the silica matrix, the nanoparticles are much more photostable than ordinary dye molecules. As shown in Figure 1(c), after continuous intensive illumination with a laser source for 80 seconds, the fluorescence intensities of both RuBpy and FITC dyes were decreased to below 20%, while the fluorescence intensiy of RuBpy-doped nanoparticles remained above 80%.

### 3.2. Covalent immobilization of Protein A on nanoparticles

Covalent attachment of antibodies directly to solid supports via glutaraldehyde, carbodiimide, succinimide ester, and so forth is always found with the loss of biological activity of the antibodies. One of the main reasons for such reduction is attributed to the random orientation of the asymmetric macromolecules on support surface [30]. Several approaches for achieving oriented antibody coupling for good steric accessibilities of active binding sites and increased stability have been developed, including the use of Protein A or Protein G [31], chemical or enzymatic oxidation of the immunoglobulin (IgG) carbohydrate moiety [32], and the use of biotin-avidin or streptavidin techniques [33]. Protein A, a highly stable 42 kDa coat protein extracted from *Staphylococcus aureus*, is capable of binding to the Fc portion of immunoglobulins, especially IgGs, from a large number of species [34]. In our scheme, Protein A was used as an affinitive adsorber to avoid direct attachment of antibody to nanoparticles.

For immobilization of Protein A on the RuBpy-doped silica nanoparticles, the CNBr method was used to activate the surface of silica nanoparticles and then couple the Protein A. The surface coverage of Protein A on the nanoparticles was quantified by the Bradford method, and the average mass of one particle was determined through the viscosity/light scattering method, then the number of Protein A molecules attached to one particle could be calculated. The amount of Protein A immobilized on nanoparticles was calculated approximately as [29]:

$$q = [(C_i - C_t)V]/m, \quad (1)$$

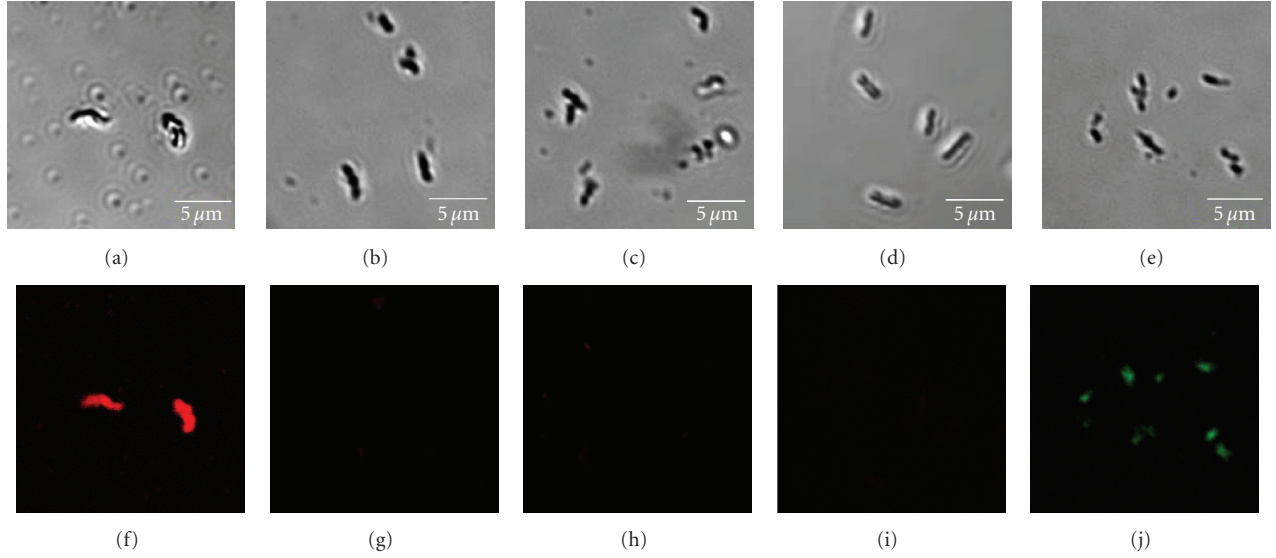


FIGURE 3: The specific, nonspecific interactions, and signal amplification effect of bioconjugated nanoparticles interacted with bacteria. All pictures were obtained with confocal microscopy ( $60\times$  oil), (a)–(e) transmission images, (f)–(j) fluorescence images. (a), (f) *M. tuberculosis* recognized with bioconjugated fluorescent nanoparticles. The bacteria display a bright fluorescence. (b), (g) Control with PBS in place of the primary rabbit anti-*M. tuberculosis* antibody. No fluorescence is associated with the bacteria. (c), (h) Control with rabbit anti-p53 antibody in place of the primary rabbit anti-*M. tuberculosis* antibody. No fluorescence is associated with the bacteria. (d), (i) *E. coli* incubated with bioconjugated fluorescent nanoparticles. No labeling of the bacteria with nanoparticle bioconjugates is observed. (e), (j) *M. tuberculosis* recognized with FITC conjugated rabbit anti-*M. tuberculosis* antibody. The bacteria display a faint fluorescence.

where  $q$  is the amount of Protein A immobilized onto a unit mass of the nanoparticles (mg/mg);  $C_i$  and  $C_t$  are the concentrations of the Protein A in the initial solution and in the supernatant after the immobilization reaction, respectively (mg/ml);  $V$  is the volume of the aqueous phase (ml); and  $m$  is the mass of the nanoparticles (mg).  $C_i$  and  $C_t$  were determined by the Bradford method [28]. The amount of Protein A immobilized on nanoparticles calculated according to (1) in our experiment was  $\sim 0.41$  mg/mg. The average mass of one particle was then determined and calculated as

$$m_i = C/N, \quad (2)$$

where  $m_i$  is the average mass of one nanoparticle (mg);  $C$  is the concentration of the nanoparticle suspension (mg/ml);  $N$  is the number of nanoparticles in a unit volume of suspension liquid (particles/ml), which was calculated through the viscosity/light scattering method [35] as

$$N = \phi / [4/3\pi(d/2)^3], \quad (3)$$

where  $4/3\pi(d/2)^3$  is the average volume of a nanoparticle;  $d$  is the volume-weighted diameter determined by light scattering; and  $\phi$  is the volume fraction of the particles determined by viscosity and calculated as

$$\phi = (h/h_0 - 1)/2.5, \quad (4)$$

where  $h$  is the viscosity of the nanoparticle suspension;  $h_0$  is the viscosity of the solvent without nanoparticles. According

to (2)–(4), the average mass of one nanoparticle calculated was  $\sim 8.8 \times 10^{-17}$  g. So there were  $\sim 3.6 \times 10^{-14}$  mg Protein A on one particle, that is,  $\sim 5.2 \times 10^2$  Protein A molecules on one particle. It provided a foundation for optimal binding of the nanoparticle-Protein A conjugates with the antibody in the later process.

### 3.3. Detection of *M. tuberculosis* in pure culture

A method of fluorescent nanoparticle-based indirect immunofluorescence microscopy (FNP-IIFM) was developed for the rapid detection of *Mycobacterium tuberculosis*. The principle for this method was illustrated in Figure 2. In this scheme, *M. tuberculosis* was first recognized by a rabbit anti-*M. tuberculosis* antibody and then the nanoparticle-Protein A conjugates were used to generate fluorescent signal. To examine the binding of bioconjugated nanoparticles to bacteria, the incubated bacteria were imaged using either fluorescence microscopy or confocal microscopy.

Pure *M. tuberculosis* suspension was first immunodetected with the FNP-IIFM method and the resulting confocal images were shown in Figures 3(a), 3(f). The bacteria displayed a bright fluorescence. This indicated that large quantities of nanoparticles had bound to the *M. tuberculosis* cells. In order to demonstrate whether the binding of bioconjugated nanoparticles to *M. tuberculosis* was solely through the antigen-specific targeting pattern or there were other nonspecific interactions between the Protein A-nanoparticle conjugates and other surface molecules of the bacteria, two controls were set in which the primary antibody was substituted with the following: (1) PBS only; (2) a rabbit anti-p53



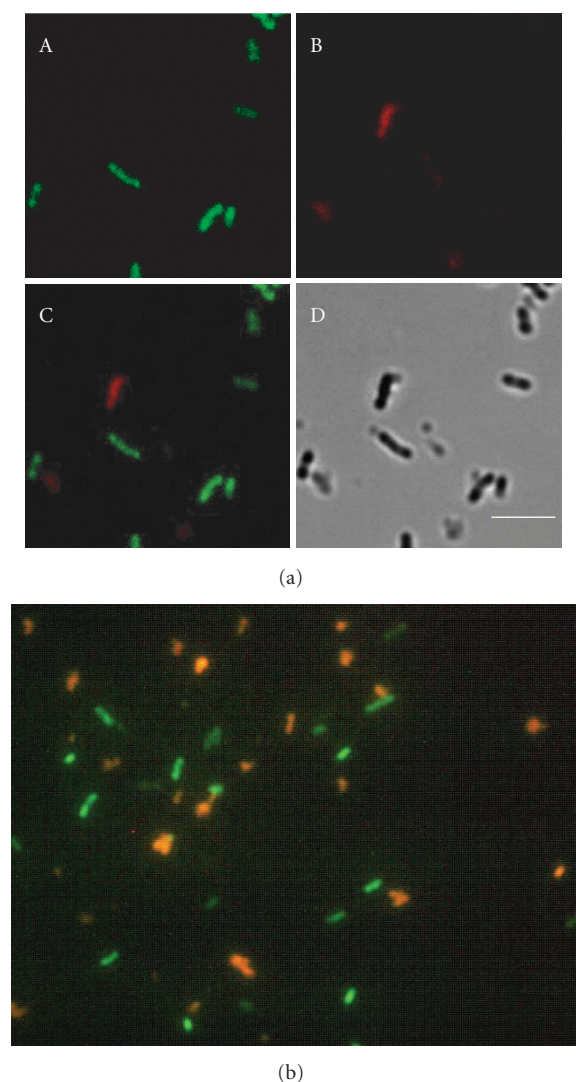


FIGURE 4: Detection of *M. tuberculosis* in mixed bacterial samples with the FNP-IIFM method. A mixture containing  $1.8 \times 10^6$  cells/ml FITC-labeled *E. coli* and  $3.6 \times 10^5$  cells/ml unlabeled *M. tuberculosis* was detected. (a) Confocal microscopic images ( $60 \times$  oil): (A) image obtained after excitation with the 488 nm laser and displayed in the pseudocolor green (FITC signal); (B) image obtained after excitation with the 543 nm laser and displayed in the pseudocolor red (RuBpy-doped nanoparticles signal); (C) overlay of the green channel and the red channel images; (D) transmission image. The confocal images show that there is no colocalization of the red fluorescent nanoparticles with *E. coli* (green). (b) Truecolor fluorescence image ( $100 \times$  oil) with an inverted fluorescence microscope. Green: FITC-labeled *E. coli*; Orange: bioconjugated fluorescent nanoparticles identified *M. tuberculosis*. The differentiation of *M. tuberculosis* from *E. coli* in the mixture with the FNP-IIFM method is good.

antibody. No fluorescence was observed to associate with the *M. tuberculosis* in both controls as shown in Figures 3(b), 3(g) and 3(c), 3(h), suggesting that there was little nonspecific interaction between the Protein A-nanoparticle conjugates and the *M. tuberculosis* cell wall. These results identify that the bioconjugated nanoparticles bind to *M. tuberculosis*

through the antibody-mediated antigen binding pattern. Another bacterium *E. coli* DH5 $\alpha$  was also tested with the FNP-IIFM method. No labeling of the bacteria with the nanoparticle bioconjugates was observed as shown in Figures 3(d), 3(i). The result shows that the anti-*M. tuberculosis* antibody does not cross-react with *E. coli* DH5 $\alpha$ , and the nanoparticle bioconjugates do not attach to *E. coli* DH5 $\alpha$  nonspecifically, which indicates that the FNP-IIFM method can be used to detect *Mycobacterium tuberculosis* in pure culture.

The fluorescence enhancement capability of the bioconjugated nanoparticles label in the FNP-IIFM method has also been investigated. The detection of *M. tuberculosis* with bioconjugated RuBpy-doped nanoparticles was compared with the commercial FITC conjugated rabbit anti-*M. tuberculosis* antibody. The final antibody concentration used in the FITC method was  $25 \mu\text{g/ml}$ . It was 5-fold higher than that used in the FNP-IIFM method. We used higher concentration of antibody in the FITC method because the induced fluorescence signal was too low when the antibody concentration was  $5 \mu\text{g/ml}$ . Figures 3(e), 3(j) showed the confocal images of *M. tuberculosis* recognized by the FITC method. The fluorescence signal from the bacteria recognized with the FITC method (Figure 3(j)) was much weaker than the signal with the FNP-IIFM method (Figure 3(f)). Although the primary antibody used in the FNP-IIFM method was only one fifth of that used in the FITC method, the average fluorescence intensity of *M. tuberculosis* recognized with the FNP-IIFM method was determined to be above five times of that with the FITC method. The experiment reveals the signal advantage that the fluorescent nanoparticles possess over conventional fluorescent dye.

### 3.4. Detection of *M. tuberculosis* in mixed bacterial samples

To evaluate the detection capability of the FNP-IIFM method in complex samples, artificial complex samples consisting of *M. tuberculosis* and *E. coli* were used for test. In order to estimate the accuracy of the detection with the FNP-IIFM method in bacterial mixture, *E. coli* was labeled with FITC to distinguish from *M. tuberculosis* prior to the detection. Then the FITC-labeled *E. coli* was mixed with unlabeled *M. tuberculosis* to constitute the mixed bacterial samples and detected with the FNP-IIFM method. The results obtained with confocal microscopy were shown in Figure 4(a). The image in Figure 4(a)-A showed the FITC fluorescence associated with *E. coli* in the mixture (pseudocolor green, emission filter: BP 505-525 nm). Figure 4(a)-B showed the fluorescence of the bioconjugated RuBpy-doped nanoparticles which had bound to bacteria (pseudocolor red, emission filter: LP 560 nm). If the nanoparticles also attached to *E. coli*, the fluorescence would appear yellow in the overlay image (the combination of green plus red). The overlay image in Figure 4(a)-C showed no colocalization of the red fluorescent nanoparticles with *E. coli*, so the bioconjugated nanoparticles only bound to the *M. tuberculosis*. Besides, the detection was also observed with the less-expensive fluorescence microscopy. As shown in Figure 4(b), the differentiation of *M. tuberculosis* from *E. coli* with the FNP-IIFM method was

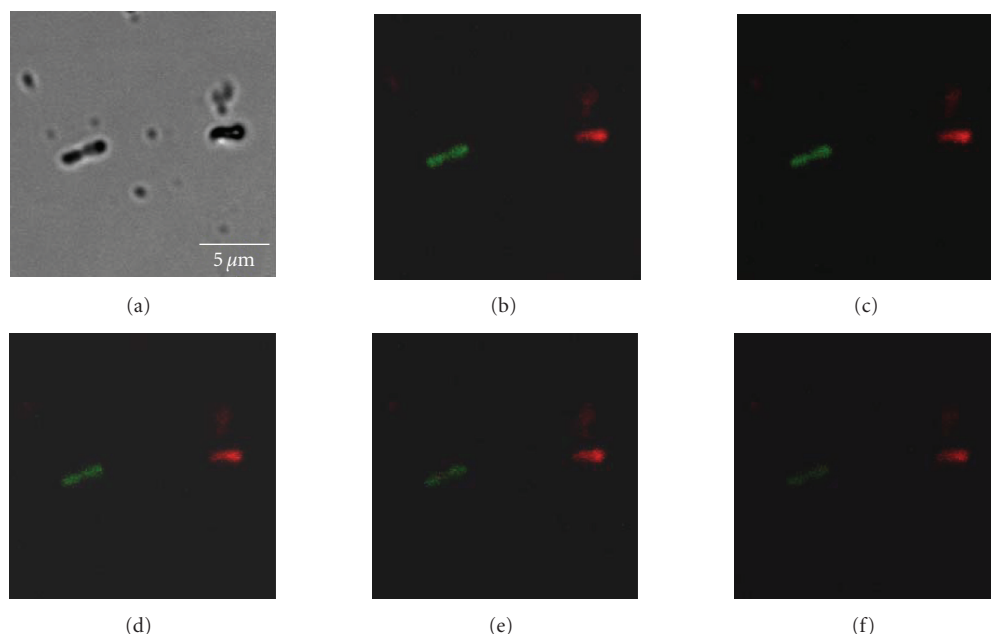


FIGURE 5: Photostability comparing of the fluorescent nanoparticles labeled on *M. tuberculosis* and FITC dyes labeled on *E. coli*. A mixture containing  $1.8 \times 10^6$  cells/ml FITC-labeled *E. coli* and  $3.6 \times 10^5$  cells/ml unlabeled *M. tuberculosis* was detected with the FNP-IIFM method. The slide was successive irradiated with an intensive argon/krypton laser under the confocal microscope ( $60 \times$  oil) for (a) and (b) 0 second, (c) 1 minute, (d) 2 minutes, (e) 4 minutes, (f) 6 minutes. (a) Transmission image, (b)–(f) Fluorescence images. Green: *E. coli*; Red: *M. tuberculosis*. The fluorescence of FITC was dim after being continuously irradiated for 2 minutes while that of the nanoparticles was still bright.

good. These results indicate that the FNP-IIFM method can be used to detect *M. tuberculosis* in mixed bacterial samples.

Meanwhile, the photostability of the fluorescent label in the FNP-IIFM method was also investigated. We compared the photostability of RuBpy-doped nanoparticles bound on *M. tuberculosis* and FITC dyes labeled on *E. coli*. The fluorescence of FITC was dim after being continuously irradiated for 2 minutes while that of the nanoparticles was still bright, as shown in Figure 5. It is demonstrated that the bioconjugated RuBpy-doped silica nanoparticles used in the FNP-IIFM method possess much better photostability in comparison with the FITC dye label.

### 3.5. Detection of *M. tuberculosis* in spiked sputum

In order to demonstrate the usefulness of our method for *M. tuberculosis* detection under clinical condition, *M. tuberculosis* was spiked into sputum and detected with the FNP-IIFM method. The result was compared with unspiked sputum control to make certain whether the *M. tuberculosis* could be detected in the sputum. Sputum from healthy individual was collected and equally divided into two portions. One portion was spiked with *M. tuberculosis*, whereas the other portion was used as the unspiked sample. The spiked sample and unspiked sample were parallelly pretreated and detected by the FNP-IIFM method. For sample pretreatment, we used the NALC–NaOH method to liquefy the sputum. After liquefaction for 15 minutes, the viscosity of the sputum was

greatly decreased. However, there were some visible big agglomerates in both the spiked and unspiked sputum which could neither be liquefied nor be broken up by vigorously vortexing. These big agglomerates caused poor smear quality such as uneven thickness, and had better been removed before immuno-reaction. To remove the big agglomerates, we centrifuged the liquefied sputum samples at low centrifugal speed (1000 rpm, 2 minutes) and disposed the precipitates. The supernatants were detected with the FNP-IIFM method. As we expected, the sputum samples were much complex mixtures containing a great deal of bacteria and impurities shown in Figure 6. In the unspiked sputum sample, no fluorescent bacterium was found as shown in Figure 6(b). It indicates that the bioconjugated nanoparticles have little nonspecific interaction with the sputum components and the oral bacteria. In the spiked sputum sample, we found highly luminescent bacteria in many microscopic fields as shown in Figure 6(a) (the luminescent bacterium indicated by the arrow). By comparing with the unspiked sample, the luminescent bacteria were considered to be *M. tuberculosis* recognized by the bioconjugated nanoparticles. The high intensity of fluorescence associated with the recognized *M. tuberculosis* well distinguished the object bacteria from the complex background. The time needed to finish detecting *M. tuberculosis* with the FNP-IIFM method in sputum is <4 hours after the receipt of specimen (sample pretreatment: <1 hour, immunoassay and smear examination: <3 hours). This result demonstrates that our FNP-IIFM method is useful for rapid detection of *M. tuberculosis* in sputum.

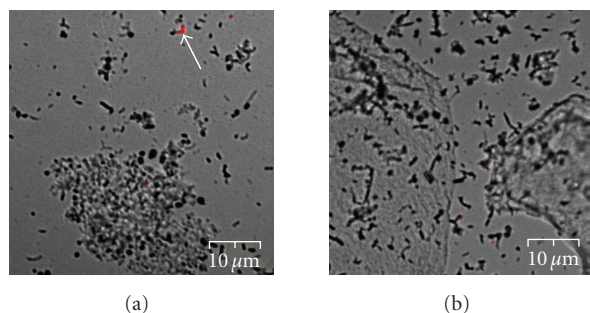


FIGURE 6: Detection of *M. tuberculosis* in spiked sputum. *M. tuberculosis* spiked sputum and unspiked sputum control were detected with the FNP-IIFM method after pretreatment with the NALC-NaOH method. Both images were overlay of the fluorescence channel and the transmitted channel of confocal images ( $60\times$  oil). (a) Sputum spiked with *M. tuberculosis*. Note that a bacterium displays bright fluorescence, indicated by the arrow. (b) Unspiked sputum. No fluorescent bacterium is found.

#### 4. CONCLUSIONS

We have developed a new method for the detection of *M. tuberculosis* using fluorescent nanoparticle-based indirect immunofluorescence microscopy. With this method, *M. tuberculosis* can be detected in both mixed bacterial samples and sputum samples. Total assay time including sample pretreatment is within 4 hours. Comparing with conventional fluorescent dyes, the use of fluorescent nanoparticles as label in immunofluorescence microscopy offers advantages of higher luminescence and higher photostability. This method can integrate with epifluorescent filter techniques to further shorten the time needed for detection. In addition, by substituting the antibody to suit to other bacteria, this technique has the potential to develop to a universal method for detecting a wide variety of bacteria in biomedical and biotechnological areas.

#### ACKNOWLEDGMENTS

The authors thank Dr. Songlin Yi (Hunan Tuberculosis Hospital, Hunan, China) for his kind help on the culture of *M. tuberculosis*. This work was partially supported by the National Key Basic Research Program (2002CB513110), Key Technologies Research and Development Program (2003BA310A16), Key Project of Hunan Province Technology Plan of China (03SSY101), Hi-Tech Research and Development Program of China (863), Grant no. 2003AA302250, Key Project Foundation of China Education Ministry (107084), Program for New Century Excellent Talents in University (NCET-06-0697), National Science Foundation of China (90606003, 20405005), and Outstanding Youth Foundation of Hunan Province (06JJ10004).

#### REFERENCES

- [1] World Health Organization. Global TB Control Report, 2003.
- [2] J. C. Palomino, "Nonconventional and new methods in the diagnosis of tuberculosis: feasibility and applicability in the field," *European Respiratory Journal*, vol. 26, no. 2, pp. 339–350, 2005.
- [3] V. C. C. Cheng, W. W. Yew, and K. Y. Yuen, "Molecular diagnostics in tuberculosis," *European Journal of Clinical Microbiology and Infectious Diseases*, vol. 24, no. 11, pp. 711–720, 2005.
- [4] B. I. Restrepo, D. I. Gomez, G. L. Shipley, J. B. McCormick, and S. P. Fisher-Hoch, "Selective enrichment and detection of mycobacterial DNA in paucibacillary specimens," *Journal of Microbiological Methods*, vol. 67, no. 2, pp. 220–229, 2006.
- [5] Y. J. Yun, K. H. Lee, H. H. Lin, et al., "Detection and identification of *Mycobacterium tuberculosis* in joint biopsy specimens by rpoB PCR cloning and sequencing," *Journal of Clinical Microbiology*, vol. 43, no. 1, pp. 174–178, 2005.
- [6] H. Park, H. Jang, E. Song, et al., "Detection and genotyping of *Mycobacterium* species from clinical isolates and specimens by oligonucleotide array," *Journal of Clinical Microbiology*, vol. 43, no. 4, pp. 1782–1788, 2005.
- [7] S. Y. Lin, W. Probert, M. Lo, and E. Desmond, "Rapid detection of isoniazid and rifampin resistance mutations in *Mycobacterium tuberculosis* complex from cultures or smear-positive sputa by use of molecular beacons," *Journal of Clinical Microbiology*, vol. 42, no. 9, pp. 4204–4208, 2004.
- [8] E. D. Chan, L. Heifets, and M. D. Iseman, "Immunologic diagnosis of tuberculosis: a review," *Tubercle and Lung Disease*, vol. 80, no. 3, pp. 131–140, 2000.
- [9] T. Mustafa, H. G. Wiker, S. G. M. Mfinanga, O. Morkve, and L. Sviland, "Immunohistochemistry using a *Mycobacterium tuberculosis* complex specific antibody for improved diagnosis of tuberculous lymphadenitis," *Modern Pathology*, vol. 19, no. 12, pp. 1606–1614, 2006.
- [10] L. M. Pereira Arias-Bouda, S. Kuijper, H. van Deutekom, et al., "Enzyme-linked immunosorbent assays using immune complexes for the diagnosis of tuberculosis," *Journal of Immunological Methods*, vol. 283, no. 1-2, pp. 115–124, 2003.
- [11] C. Abe, K. Hirano, and T. Tomiyama, "Simple and rapid identification of the *Mycobacterium tuberculosis* complex by immunochromatographic assay using anti-MPB64 monoclonal antibodies," *Journal of Clinical Microbiology*, vol. 37, no. 11, pp. 3693–3697, 1999.
- [12] S. Bhaskar, J. N. Banavaliker, K. Bhardwaj, and P. Upadhyay, "A novel ultrasound-enhanced latex agglutination test for the detection of antibodies against *Mycobacterium tuberculosis* in serum," *Journal of Immunological Methods*, vol. 262, no. 1-2, pp. 181–186, 2002.
- [13] P. V. Baptista, M. Koziol-Montewka, J. Paluch-Oles, G. Doria, and R. Franco, "Gold-nanoparticle-probe-based assay for rapid and direct detection of *Mycobacterium tuberculosis* DNA in clinical samples," *Clinical Chemistry*, vol. 52, no. 7, pp. 1433–1434, 2006.
- [14] E. D. Chan, R. Reves, J. T. Belisle, P. J. Brennan, and W. E. Hahn, "Diagnosis of tuberculosis by a visually detectable immunoassay for lipoarabinomannan," *American Journal of Respiratory and Critical Care Medicine*, vol. 161, no. 5, pp. 1713–1719, 2000.
- [15] M. Pai, S. Kalantri, and K. Dheda, "New tools and emerging technologies for the diagnosis of tuberculosis: part II: active tuberculosis and drug resistance," *Expert Review of Molecular Diagnostics*, vol. 6, no. 3, pp. 423–432, 2006.
- [16] W. H. Tan, K. Wang, X. He, et al., "Bionanotechnology based on silica nanoparticles," *Medical Research Reviews*, vol. 24, no. 5, pp. 621–638, 2004.



- [17] G. Yao, L. Wang, Y. R. Wu, et al., "FloDots: luminescent nanoparticles," *Analytical and Bioanalytical Chemistry*, vol. 385, no. 3, pp. 518–524, 2006.
- [18] S. Santra, K. M. Wang, R. Tapeç, and W. H. Tan, "Development of novel dye-doped silica nanoparticles for biomarker application," *Journal of Biomedical Optics*, vol. 6, no. 2, pp. 160–166, 2001.
- [19] X. J. Zhao, R. Tapeç-Dytioco, and W. H. Tan, "Ultrasensitive DNA detection using highly fluorescent bioconjugated nanoparticles," *Journal of the American Chemical Society*, vol. 125, no. 38, pp. 11474–11475, 2003.
- [20] X. X. He, J. Y. Chen, K. M. Wang, W. H. Tan, and D. L. Qin, "Preparation and properties of Cy3 doped core-shell silica fluorescent nanoparticles," *Chemical Journal of Chinese Universities*, vol. 27, no. 10, pp. 1835–1839, 2006.
- [21] S. Santra, P. Zhang, K. M. Wang, R. Tapeç, and W. H. Tan, "Conjugation of biomolecules with luminophore-doped silica nanoparticles for photostable biomarkers," *Analytical Chemistry*, vol. 73, no. 20, pp. 4988–4993, 2001.
- [22] S. Santra, H. Yang, D. Dutta, et al., "TAT conjugated, FITC doped silica nanoparticles for bioimaging applications," *Chemical Communications*, no. 24, pp. 2810–2811, 2004.
- [23] S. Santra, B. Liesenfeld, D. Dutta, et al., "Folate conjugated fluorescent silica nanoparticles for labeling neoplastic cells," *Journal of Nanoscience and Nanotechnology*, vol. 5, no. 6, pp. 899–904, 2005.
- [24] J. K. Herr, J. E. Smith, C. D. Medley, D. H. Shangguan, and W. H. Tan, "Aptamer-conjugated nanoparticles for selective collection and detection of cancer cells," *Analytical Chemistry*, vol. 78, no. 9, pp. 2918–2924, 2006.
- [25] X. J. Zhao, L. R. Hilliard, S. J. Mechery, et al., "A rapid bioassay for single bacterial cell quantitation using bioconjugated nanoparticles," *Proceedings of the National Academy of Sciences of the United States of America*, vol. 101, no. 42, pp. 15027–15032, 2004.
- [26] L. S. Schlesinger, C. G. Bellinger-Kawahara, N. R. Payne, and M. A. Horwitz, "Phagocytosis of *Mycobacterium tuberculosis* is mediated by human monocyte complement receptors and complement component C3," *Journal of Immunology*, vol. 144, no. 7, pp. 2771–2780, 1990.
- [27] H. M. Cao, *Handbook of Inorganic Compound Synthesis*, vol. 1, Chemical Industry Publishing House, Beijing, China, 1988, (ed. Japanese Society of Chemistry) (in Chinese).
- [28] M. M. Bradford, "A rapid and sensitive method for the quantitation of microgram quantities of protein utilizing the principle of protein dye binding," *Analytical Biochemistry*, vol. 72, no. 1–2, pp. 248–254, 1976.
- [29] H. Yavuz and A. Denizli, "Immunoabsorption of cholesterol on protein A oriented beads," *Macromolecular Bioscience*, vol. 5, no. 1, pp. 39–48, 2005.
- [30] B. Lu, M. R. Smyth, and R. O'Kennedy, "Oriented immobilization of antibodies and its applications in immunoassays and immunosensors," *Analyst*, vol. 121, no. 3, pp. 29R–32R, 1996.
- [31] J. J. Langone, "Applications of immobilized protein A in immunochemical techniques," *Journal of Immunological Methods*, vol. 55, no. 3, pp. 277–296, 1982.
- [32] V. S. Prisyazhnoy, M. Fusek, and Y. B. Alakhov, "Synthesis of high-capacity immunoaffinity sorbents with oriented immobilized immunoglobulins or their Fab' fragments for isolation of proteins," *Journal of Chromatography*, vol. 424, no. 2, pp. 243–253, 1988.
- [33] X. L. Su and Y. Li, "Quantum dot biolabeling coupled with immunomagnetic separation for detection of *Escherichia coli* O157:H7," *Analytical Chemistry*, vol. 76, no. 16, pp. 4806–4810, 2004.
- [34] M. Graille, E. A. Stura, A. L. Corper, et al., "Crystal structure of a *Staphylococcus aureus* protein domain complexed with the Fab fragment of a human IgM antibody: structural basis for recognition of B-cell receptors and superantigen activity," *Proceedings of the National Academy of Sciences of the United States of America*, vol. 97, no. 10, pp. 5399–5404, 2000.
- [35] F. Reynolds, T. O'Loughlin, R. Weissleder, and L. Josephson, "Method of determining nanoparticle core weight," *Analytical Chemistry*, vol. 77, no. 3, pp. 814–817, 2005.



## Research Article

# Preparation and Characterization of Poly(D,L-Lactide-co-Glycolide) Nanoparticles Containing Ascorbic Acid

Magdalena M. Stevanović,<sup>1</sup> Branka Jordović,<sup>2</sup> and Dragan P. Uskoković<sup>1</sup>

<sup>1</sup> Institute of Technical Sciences of the Serbian Academy of Sciences and Arts, 11000 Belgrade, Serbia

<sup>2</sup> Faculty of Technical Sciences, University of Kragujevac, 32000 Čačak, Serbia

Correspondence should be addressed to Dragan P. Uskoković, uskok@itn.sanu.ac.yu

Received 28 March 2007; Accepted 29 June 2007

Recommended by Marek Osinski

This paper is covering new, simplistic method of obtaining the system for controlled delivery of the ascorbic acid. Copolymer poly (D,L-lactide-co-glycolide) (DLPLG) nanoparticles are produced using physical method with solvent/nonsolvent systems where obtained solutions were centrifuged. The encapsulation of the ascorbic acid in the polymer matrix is performed by homogenization of water and organic phases. Particles of the DLPLG with the different content of ascorbic acid have different morphological characteristics, that is, variable degree of uniformity, agglomeration, sizes, and spherical shaping. Mean sizes of nanoparticles, which contain DLPLG/ascorbic acid in the ratio 85/150%, were between 130 to 200 nm depending on which stereological parameters are considered (maximal diameters Dmax, feret X, or feret Y). By introducing up to 15% of ascorbic acid, the spherical shape, size, and uniformity of DLPLG particles are preserved. The samples were characterized by infrared spectroscopy, scanning electron microscopy, stereological analysis, and ultraviolet spectroscopy.

Copyright © 2007 Magdalena M. Stevanović et al. This is an open access article distributed under the Creative Commons Attribution License, which permits unrestricted use, distribution, and reproduction in any medium, provided the original work is properly cited.

## 1. INTRODUCTION

The systems for controlled delivery of the medicaments in the body are causing real revolution in the medicine and pharmacy in the recent years, and all in favor of better medical treatments of the patients [1]. Using the system for the controlled and balanced release of medicaments, opposing to standard and conventional methods, constant and uniform concentration of medicament in the body is achieved throughout longer period of time. Copolymer poly(D,L-lactide-co-glycolide) is used for the controlled delivery of several classes of medicaments like anticancer agents, anti-hypertensive agents, immunomodulatory drugs, hormones, and macromolecules like nucleic acid, proteins, peptides, antibodies, DLPLG nanospheres are very efficient mean of transdermal transport of medicaments in the body, for example, ascorbic acid [2]. DLPLG polymer particles allow the encapsulation of the medicament within the polymer matrix, where the principle requirement for the controlled and balanced release of the medicament in the body is the particle's

ideal spherical shape and narrow distribution of its size. The size and shape of the particles play key role in their adhesion and interaction with the cell. Dynamic of the release (pace and concentration) depends of the morphology, that is, structure of the copolymer. The chemical structures, molecular weight, composition, as well as the synthesis conditions, are parameters which influence the final morphology of the polymer. The direct relation between these parameters and morphology is inadequately examined thus making it a topic of many researches. Depending on the nature and matrix of the selected material, methods of obtaining polymer particles can be divided in general into dispersion of the polymer solution method, polymerization of the monomer method, and coacervation [3–6]. The PLGA spheres obtained with emulsion process are in range of 150–200  $\mu\text{m}$  [7], 45  $\mu\text{m}$  [8], 30  $\mu\text{m}$  [9]. With modified emulsion method, the particle sizes are decreased to 10  $\mu\text{m}$  [10]. Further modification of the process for synthesis of the particles, that is, emulsification solvent evaporation method, the obtained particles are in nanometer scale of 570–970 nm [11] and 244–260 nm

[12–14]. The latest researches in this field indicated the possibility of producing DLPLG spheres with average diameter under 100 nm [15]. Controlling the conditions of obtaining DLPLG by solvent/nonsolvent method, changing the parameters like aging time, after adding nonsolvent, time and velocity of centrifugal processing, it is possible to influence on morphology (size and shape) and uniformity of DLPLG polymer powder [16]. DLPLG powder with short aging time with nonsolvent and longest time and velocity of the centrifugal processing has smallest particles and highest uniformity. DLPLG copolymer has potential to be used for transport of ascorbic acid in the body, thus considerably increasing its efficiency. Ascorbic acid reduces free radicals, and in that way damages created by oxidative stress which is a root cause of, or at least associated with, many diseases are minimized. The aim of this research is obtaining the nanoparticles of copolymer poly(D,L-lactide-co-glycolide) in which ascorbic acid is encapsulated, as well as examining the influence of the synthesis method on morphological characteristics of poly(D,L-lactide-co-glycolide) particles with the different content of ascorbic acid.

## 2. MATERIALS AND METHODS

### 2.1. Materials

Poly(D,L-lactide-co-glycolide) (DLPLG) was obtained from Durect, Lactel, Adsorbable Polymers International and had a lactide to glycolide ratio of 50 : 50. Molecular weight of polymer was 40000–50000 g/mol. Time of complete resorption of this polymer is 4–8 weeks. Molecular weight of ascorbic acid was 176.13 g/mol. Polyvinyl alcohol (PVA) was used with a 98% hydrolyzation degree. All other chemicals and solvents were of reagent grade.

### 2.2. Preparation of nanoparticles

Copolymer powder DLPLG was obtained by means of physical methods from commercial granules using solvent/nonsolvent systems (Figure 1). Commercial granules poly(D,L-lactide-co-glycolide) (0.05 g) were dissolved in 1.5 mL of acetone and, after approximately two hours, 2 mL of methanol was added into solvent mixture. DLPLG precipitated by the addition of methanol and the solution became whitish. The polymeric solution thus obtained was very slowly poured into 20 mL of aqueous PVA solution (0.02% w/w) while continuous stirring at 1200 rpm by a stirrer. After that, the solution was centrifuged and decanted. Time and velocity of the centrifugal processing were 120 minutes and 4000 rpm. PVA is used as a stabilizer which creates negative charge of the DLPLG particles, that is, it creates negative zeta potential [17]. By creating specific zeta potential, PVA brings to reduction of agglomeration of the particles. All used solutions are nontoxic for environment. The ascorbic acid was encapsulated into the polymer matrix by means of homogenization of water and organic phases. The water solution with the variable ratio of the ascorbic acid was added to the polymer solution. This was followed by the precipitation using alcohol methanol. In the particles of DLPLG copolymer,

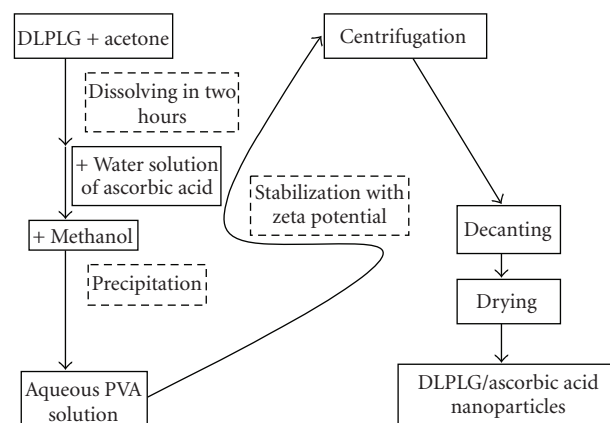


FIGURE 1: Schematics for obtaining of the DLPLG/ascorbic acid nanoparticles.

different concentration of ascorbic acid has been encapsulated with ratios 85% DLPLG to 15% ascorbic acid, 70% DLPLG to 30% ascorbic acid, 50% DLPLG to 50% ascorbic acid, and 30% DLPLG to 70% ascorbic acid.

### 2.3. Infrared (IR) spectroscopy measurements

The quality analysis of the samples was performed with IR spectroscopy. The IR measurements were performed on Perkin-Elmer 983G infrared spectrophotometer, using the KBr pellet technique, in the frequency interval of 400–4000  $\text{cm}^{-1}$ .

### 2.4. Scanning electron microscope (SEM) observation

The morphology of obtained particles of DLPLG was examined by scanning electron microscope (SEM) JEOL JSM-646OLV. The powder samples for SEM analysis were coated with gold using the physical vapor deposition (PVD) process. Samples were covered with gold (SCD 005 sputter coater), using 30 mA current from the distance of 50 mm during 180 seconds.

### 2.5. Stereological analysis

The particle size and morphology were examined using the area analysis method [18, 19] by semiautomatic image analyzer (Videoplan, Kontron), connected with a scanning electron microscope (SEM). From 200 to 300 particles in the SEM were measured and the following parameters were determined: area section Aa, perimeter Lp, maximal diameter of the particle Dmax, feret x and feret y, and form factor (fL) (Figure 2).

### 2.6. Ultraviolet (UV) spectroscopy

Release of the ascorbic acid from DLPLG particles in vitro in physiological solution (0.9% sodium chloride in water) was studied with UV spectroscopy. The UV measurements were

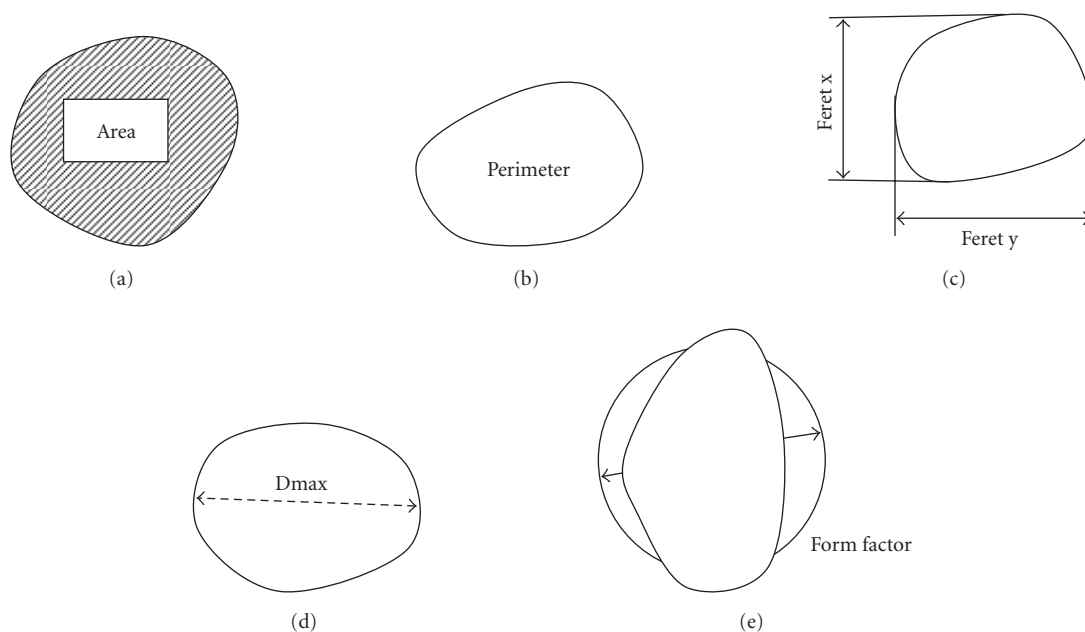


FIGURE 2: Schematics of the stereological parameters: (a) area (Aa); (b) perimeter (Lp); (c) feret x and feret y (d) maximal particle diameter (Dmax); (e) form factor (fL).

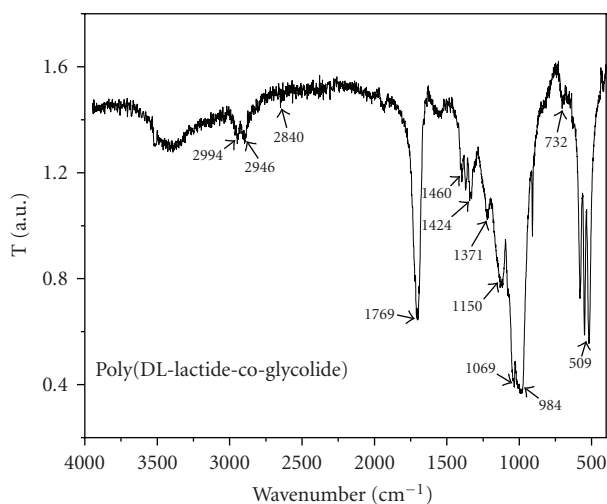


FIGURE 3: IR spectra of the DLPLG nanoparticles.

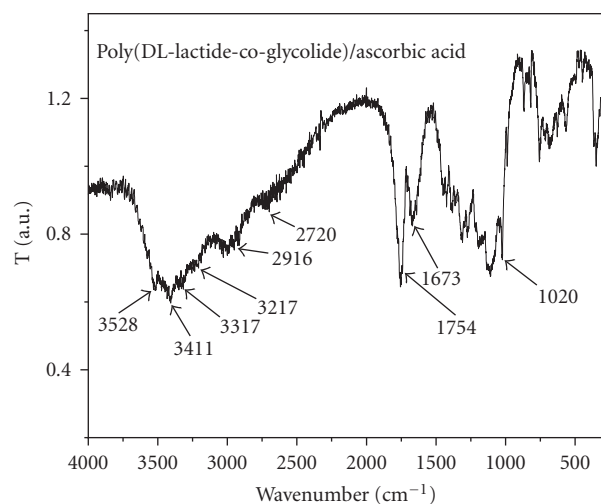


FIGURE 4: IR spectra of the DLPLG/ascorbic acid 85/15% nanoparticles.

performed on Perkin-Elmer Lambda 35 UV-V is spectrophotometer in the frequency interval of 200–400 nm.

### 3. RESULTS AND DISCUSSION

The IR spectra in Figure 3 illustrate all characteristic groups for copolymer poly(D,L-lactide-co-glycolide). The IR spectra of DLPLG show peaks at 2994, 2946, 2840 (CH bend), 1769 (C=O ester), 1460, 1424, 1371 (CH<sub>3</sub>), 1150, 1069 984 (C–O stretch), 732 509 (CH-bend) cm<sup>-1</sup> while the band

on 3100–3600 cm<sup>-1</sup> belongs to the OH group of the water molecule [20].

Comparing the obtained IR spectra for DLPLG and ascorbic acid (Figure 4) with the IR spectra characteristics for ascorbic acid shown in the literature [21, 22], it is confirmed that obtained nanoparticles are composed of poly(D,L-lactide-co-glycolide) and ascorbic acid. Besides the characteristic groups for copolymer DLPLG, the four O–H bands of ascorbic acid could be assigned by means of infrared investigations at 3528, 3411, 3317, 3217 cm<sup>-1</sup>. The spectra show bands that can be assigned to CH<sub>3</sub>,

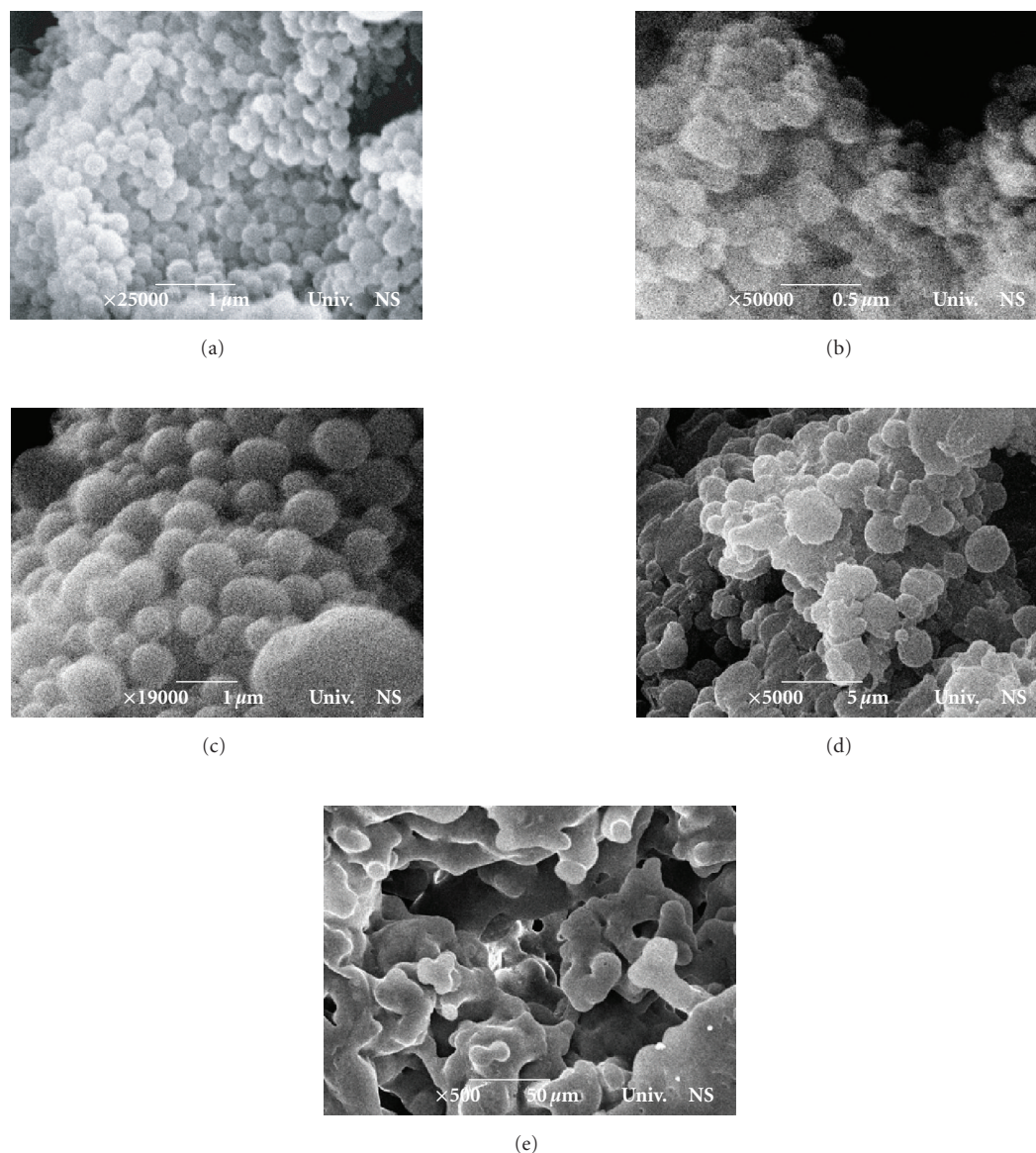


FIGURE 5: SEM images of (a) DLPLG nanoparticles; (b) DLPLG/ascorbic acid 85/15% nanospheres; (c) DLPLG/ascorbic acid 70/30%; (d) DLPLG/ascorbic acid 50/50%; (e) DLPLG/ascorbic acid 30/70%.

$\text{CH}_2$ , or  $\text{CH}$  groups in the ascorbic acid environment at  $2720\text{ cm}^{-1}$  and the spectra also clearly show the band corresponding to  $\text{C}=\text{O}$  groups at  $2916\text{ cm}^{-1}$ . The bands that correspond to the wave number  $1754\text{ cm}^{-1}$  belong to  $\text{C}=\text{C}$  groups,  $1673\text{ cm}^{-1}$   $\text{C}-\text{O}-\text{C}$ , and  $1020\text{ cm}^{-1}$   $\text{C}-\text{O}$ , respectively.

The morphological characteristics of the obtained DLPLG particles, with and without encapsulated ascorbic acid, were examined with a scanning electron microscope. From the SEM recordings of DLPLG particles without ascorbic acid (Figure 5(a)), it is visible that the particles have spherical shape, smooth surface, low level of agglomeration, and high level of uniformity—higher than other samples. From the SEM recordings of the second sample (Figure 5(b)), where DLPLG copolymer has encapsulated

ascorbic acid in ratio DLPLG/ascorbic acid 85/15%, it is visible that particles also have spherical shapes, that is, spherical shape of the initial DLPLG has not been compromised. DLPLG/ascorbic acid 85/15% nanoparticles are uniform with sizes from 130 to 200 nm depending on which stereological parameters are considered ( $D_{\text{max}}$ , maximum diameters, feret X, or feret Y). The particles of the sample DLPLG/ascorbic acid 70/30% (Figure 5(c)) also have spherical shapes, but their sizes are increased. In case of the fourth sample, DLPLG/ascorbic acid 50/50% (Figure 5(d)) uniformity is perturbed, particles have both spherical and irregular shapes and they are much agglomerated. For the fifth sample, DLPLG/ascorbic acid 30/70% (Figure 5(e)), the particles were very much agglomerated, so stereological analyses could not be performed.



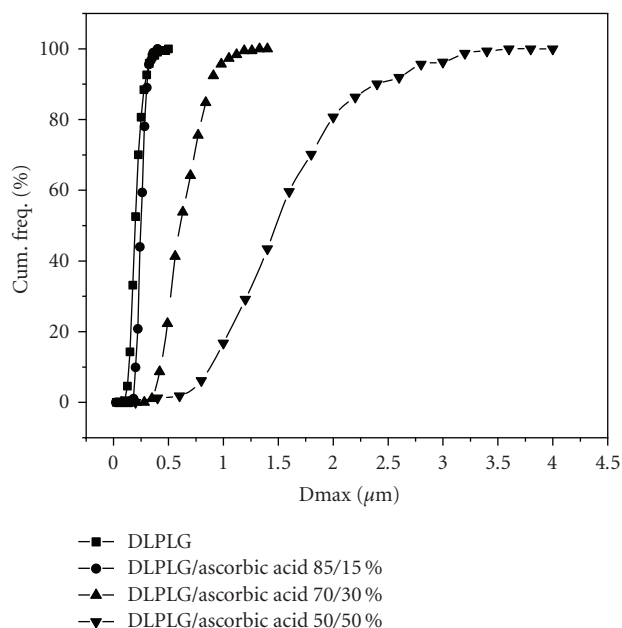


FIGURE 6: Comparative results of the stereological examining of DLPLG particles and particles with different ratio of DLPLG and ascorbic acid, DLPLG/ascorbic acid 85/15%, DLPLG/ascorbic acid 70/30%, DLPLG/ascorbic acid 50/50%, based on maximal diameter of the particle Dmax.

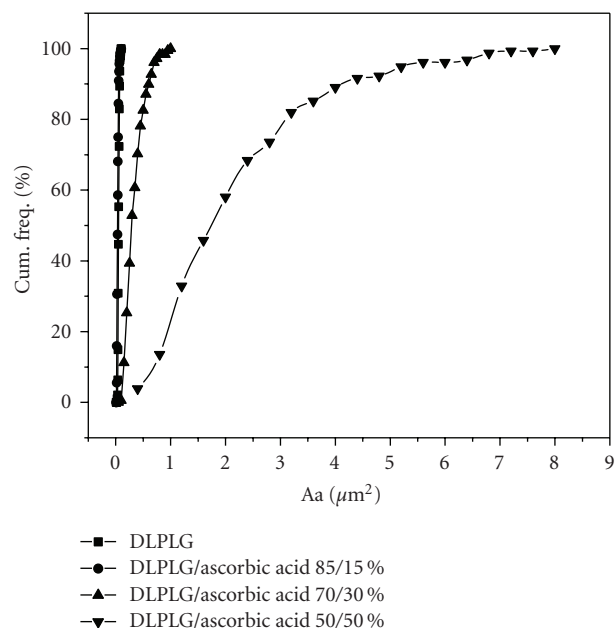


FIGURE 7: Comparative results of the stereological examining of DLPLG particles and particles with different ratio of DLPLG and ascorbic acid, DLPLG/ascorbic acid 85/15%, DLPLG/ascorbic acid 70/30%, DLPLG/ascorbic acid 50/50%, based on area section Aa.

The stereological analysis is giving us the parameters which are characterizing the particle sizes (area section—Aa, perimeter—Lp, maximal diameter—Dmax, and feret's diameters) and parameter which is characterizing the particle shape (perimeter form factor—fL). For all parameters, minimum, maximum, and mean values were recorded and presented in Table 1.

Based on the obtained results of the stereological analysis of DLPLG particles, it is visible that they are uniform, their average mean size varies from 0.15 to 0.23  $\mu\text{m}$  depending on the stereological parameter taken in consideration (Dmax, feret X, or feret Y) (Table 1). Dmax values range from 0.09 to 0.39  $\mu\text{m}$  with particle's mean size 0.23  $\mu\text{m}$  (Figure 6). Figures 7 and 8 present comparative results of DLPLG particles with and without ascorbic acid based on their area section and perimeter form factor.

From the comparative results of the stereological analysis of the area section (Aa) of DLPLG with and without encapsulated ascorbic acid (Figure 7) as well as comparative results of the perimeter form factor (fL), (Figure 8) we can see that DLPLG particles without ascorbic acid have the smallest area section (minimum value for Aa is 0.02  $\mu\text{m}^2$  and maximum is 0.08  $\mu\text{m}^2$ ) and the highest mean value of perimeter form factor which is 0.89. Nanoparticles DLPLG/ascorbic acid 85/15% have minimum Dmax of 0.09  $\mu\text{m}$  and maximum Dmax of 0.49  $\mu\text{m}$ , where their mean size is 0.20  $\mu\text{m}$  (Figure 6). The mean value of the area section is 0.03  $\mu\text{m}^2$  (Figure 7) and of the perimeter form factor is 0.87 (Figure 8). For particles DLPLG/ascorbic acid 70/30%, minimum Dmax is 0.30  $\mu\text{m}$  and maximum Dmax is 2.59  $\mu\text{m}$ , where their mean

size is 0.67  $\mu\text{m}$  (Figure 6), which indicates that the uniformity is decreased and size is increased. The mean value of the area section is 0.41  $\mu\text{m}^2$  (Figure 7) and of the perimeter form factor is 0.77 (Figure 8). For particles DLPLG/ascorbic acid 50/50%, minimum Dmax is 0.28  $\mu\text{m}$  and maximum Dmax is 4.51  $\mu\text{m}$ , where their mean size is 1.60  $\mu\text{m}$  (Figure 6). The mean size of the area section is 2.30  $\mu\text{m}^2$  (Figure 7) and of the perimeter form factor is 0.74 (Figure 8). In case of DLPLG/ascorbic acid 30/70%, the stereological analysis could not be performed.

The release amount of the ascorbic acid from the polymer particles was determined periodically during the eight weeks with UV spectroscopy. A calibration curve of the ascorbic acid in physiological solution at different concentrations has been prepared using the specific absorbance peak of the ascorbic acid at 264 nm.

Figure 9 shows the dependence of the maximum absorption from the degradation time in cases of DLPLG without ascorbic acid, DLPLG/ascorbic acid 85/15%, DLPLG/ascorbic acid 70/30%, and DLPLG/ascorbic acid 50/50%. This absorbance is correlated with the calibration curve and amount of ascorbic acid is determined in percentages. Figure 10 gives cumulative curves of the release of the ascorbic acid in percentages over the period of time of the degradation. Figure 10 also shows the relative review in percentages of the ascorbic acid release in periods of up to two days, 2–11, 11–17, 17–24, 24–31, 31–39, 39–46, and 46–55 days. In the first 24 days of the degradation, for all samples, less than 10% of the encapsulated ascorbic acid have been released. For all

TABLE 1: Results of the stereological analysis of DLPLG and DLPLG/ascorbic acid particles.

Ratio DLPLG/ ascorbic acid	Lp ( $\mu\text{m}$ )			Aa ( $\mu\text{m}$ ) <sup>2</sup>			Dmax ( $\mu\text{m}$ )			Feret x ( $\mu\text{m}$ )			Feret y ( $\mu\text{m}$ )			fL		
	Min	Max	Mean	Min	Max	Mean	Min	Max	Mean	Min	Max	Mean	Min	Max	Mean	Min	Max	Mean
100% DLPLG	0.19	1.12	0.81	0.02	0.08	0.03	0.09	0.39	0.23	0.09	0.25	0.15	0.09	0.28	0.19	0.49	0.91	0.89
85/15%	0.37	1.39	0.70	0.01	0.14	0.03	0.09	0.49	0.20	0.05	0.43	0.15	0.03	0.26	0.13	0.57	1.00	0.87
70/30%	0.95	8.92	2.40	0.06	4.63	0.41	0.30	2.59	0.67	0.17	2.19	0.46	0.17	1.65	0.48	0.48	0.92	0.77
50/50%	1.62	14.23	5.86	0.20	13.25	2.30	0.28	4.51	1.60	0.21	4.13	1.13	0.15	3.10	1.09	0.35	0.97	0.74
30/70%	—	—	—	—	—	—	—	—	—	—	—	—	—	—	—	—	—	—

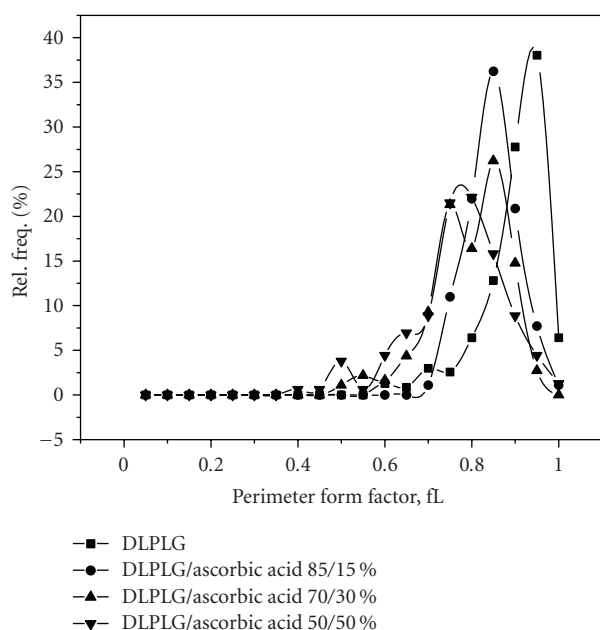


FIGURE 8: Comparative results of the stereological examining of DLPLG particles and particles with different ratio of DLPLG and ascorbic acid, DLPLG/ascorbic acid 85/15%, DLPLG/ascorbic acid 70/30%, DLPLG/ascorbic acid 50/50%, based on perimeter form factor fL.

DLPLG/ascorbic acid samples, the overall quantities of the encapsulated ascorbic acid have been released in 8 weeks of the degradation.

#### 4. CONCLUSIONS

The particles obtained with solvent/nonsolvent physical method and technique of the centrifugal processing have potential use in transdermal systems for controlled delivery of ascorbic acid. It is possible to encapsulate ascorbic acid into DLPLG particles in various concentrations thus producing particles with different morphological characteristics. The nanoparticles of DLPLG/ascorbic acid with lesser ratio of ascorbic acid have higher uniformity, lower level

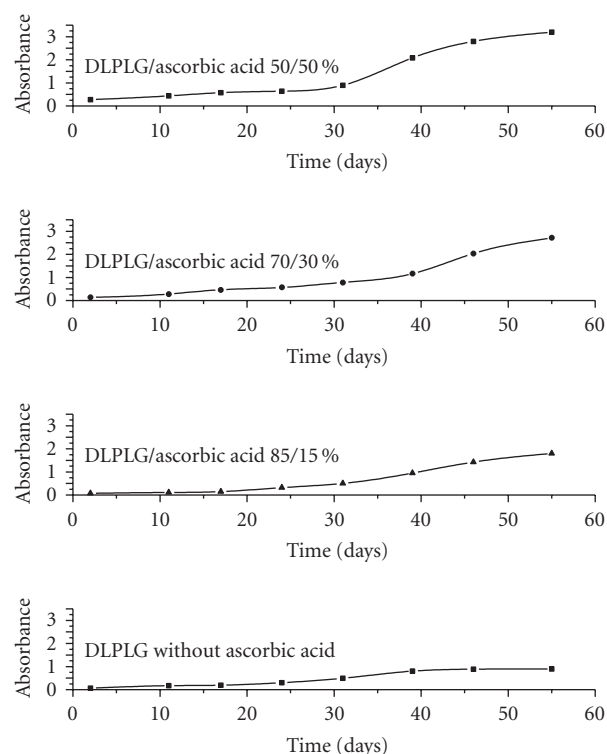
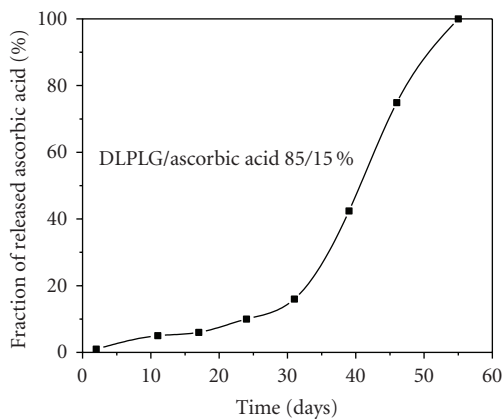


FIGURE 9: Comparative curves for the dependence of the maximum absorbance from the time of the degradation for the DLPLG with and without ascorbic acid.

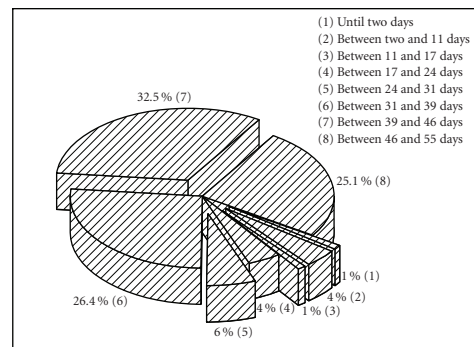
of agglomeration, and smaller sizes. The nanoparticles of DLPLG/ascorbic acid 85/15% have spherical shapes and their sizes are from 130 to 200 nm.

#### ACKNOWLEDGMENTS

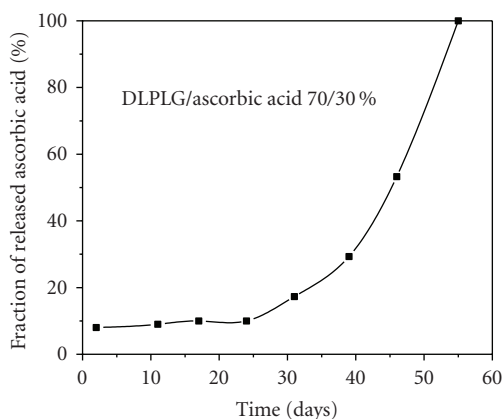
Authors would like to thank Nenad Ignjatović, Zoran Nedić, and Miloš Bokorov for their assistance in the experiment, IR, and SEM analysis. The Ministry of Science and Environmental Protection of Republic of Serbia supports this work through the project no. 142006, and the European Commission through project no. NMP3-CT-2007-032918



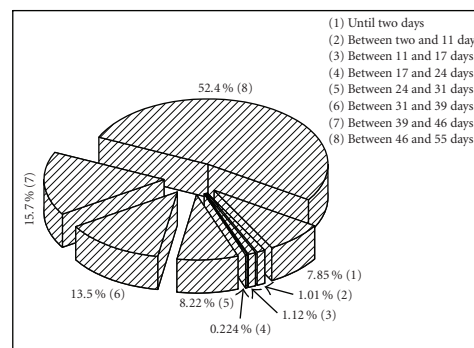
(a)



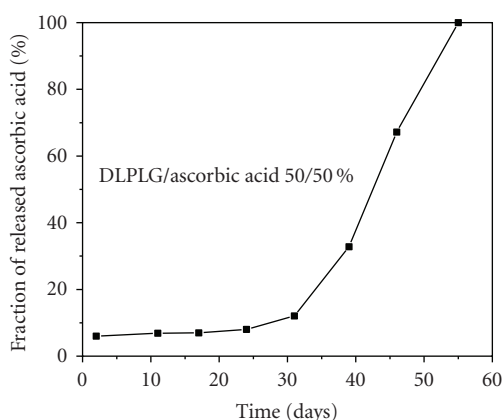
(b)



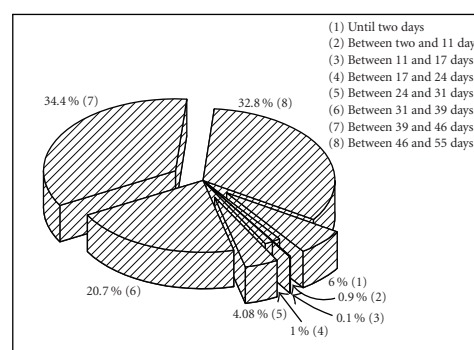
(c)



(d)



(e)



(f)

FIGURE 10: Release of the ascorbic acid in percentages over the period of time of the degradation: cumulative curves and relative review for (a)-(b) DLPLG/ascorbic acid 85/15%; (c)-(d) DLPLG/ascorbic acid 70/30% and (e)-(f) DLPLG/ascorbic acid 50/50% (relative review on figures (b)-(d)-(f): until two days (1), between two and 11 days (2), between 11 and 17 days (3), between 17 and 24 days (4), between 24 and 31 days (5), between 31 and 39 days (6), between 39 and 46 days (7), between 46 and 55 days (8)).

INCOMAT "Creating international cooperation teams of excellence in the emerging biomaterial surface research."

## REFERENCES

- [1] M. Ebbesen and T. G. Jensen, "Nanomedicine: techniques, potentials, and ethical implications," *Journal of Biomedicine and Biotechnology*, vol. 2006, Article ID 51516, 11 pages, 2006.
- [2] T. Yokoyama and C. C. Huang, "Nanoparticle technology for the production of functional materials," *KONA, Powder and Particle*, no. 23, pp. 7–17, 2005.
- [3] C. Thomasin, H. P. Merkle, and B. A. Gander, "Physicochemical parameters governing protein microencapsulation into biodegradable polyesters by coacervation," *International Journal of Pharmaceutics*, vol. 147, no. 2, pp. 173–186, 1997.
- [4] F. Qian, A. Szymanski, and J. Gao, "Fabrication and characterization of controlled release poly(D,L-lactide-co-glycolide) millirods," *Journal of Biomedical Materials Research*, vol. 55, no. 4, pp. 512–522, 2001.
- [5] J. Panyam and V. Labhasetwar, "Biodegradable nanoparticles for drug and gene delivery to cells and tissue," *Advanced Drug Delivery Reviews*, vol. 55, no. 3, pp. 329–347, 2003.
- [6] I. Bala, S. Hariharan, and M. N. V. Ravi Kumar, "PLGA nanoparticles in drug delivery: the state of the art," *Critical Reviews in Therapeutic Drug Carrier Systems*, vol. 21, no. 5, pp. 387–422, 2004.
- [7] Y. S. Choi, S.-N. Park, and H. Suh, "Adipose tissue engineering using mesenchymal stem cells attached to injectable PLGA spheres," *Biomaterials*, vol. 26, no. 29, pp. 5855–5863, 2005.
- [8] V. A. Philip, R. C. Mehta, and P. P. DeLuca, "In vitro and in vivo respirable fractions of isopropanol treated PLGA microspheres using a dry powder inhaler," *International Journal of Pharmaceutics*, vol. 151, no. 2, pp. 175–182, 1997.
- [9] A. L. Daugherty, J. L. Cleland, E. M. Duenas, and R. J. Mersny, "Pharmacological modulation of the tissue response to implanted polylactic-co-glycolic acid microspheres," *European Journal of Pharmaceutics and Biopharmaceutics*, vol. 44, no. 1, pp. 89–102, 1997.
- [10] Y.-I. Jeong, J.-G. Song, S.-S. Kang, et al., "Preparation of poly(DL-lactide-co-glycolide) microspheres encapsulating all-trans retinoic acid," *International Journal of Pharmaceutics*, vol. 259, no. 1-2, pp. 79–91, 2003.
- [11] S.-S. Feng, L. Mu, K. Y. Win, and G. Huang, "Nanoparticles of biodegradable polymers for clinical administration of paclitaxel," *Current Medicinal Chemistry*, vol. 11, no. 4, pp. 413–424, 2004.
- [12] H. Murakami, M. Kobayashi, H. Takeuchi, and Y. Kawashima, "Preparation of poly(DL-lactide-co-glycolide) nanoparticles by modified spontaneous emulsification solvent diffusion method," *International Journal of Pharmaceutics*, vol. 187, no. 2, pp. 143–152, 1999.
- [13] H. Murakami, M. Kobayashi, H. Takeuchi, and Y. Kawashima, "Further application of a modified spontaneous emulsification solvent diffusion method to various types of PLGA and PLA polymers for preparation of nanoparticles," *Powder Technology*, vol. 107, no. 1-2, pp. 137–143, 2000.
- [14] M. N. V. Ravi Kumar, U. Bakowsky, and C. M. Lehr, "Preparation and characterization of cationic PLGA nanospheres as DNA carriers," *Biomaterials*, vol. 25, no. 10, pp. 1771–1777, 2004.
- [15] M. Radić, N. Ignjatović, Z. Nedić, M. Mitrić, D. Miličević, and D. Uskoković, "Synthesis and characterization of biphasic calcium phosphate/poly-(DL-lactide-co-glycolide) biocomposite," *Materials Science Forum*, vol. 494, pp. 537–542, 2005.
- [16] M. Stevanović, N. Ignjatović, B. Jordović, and D. Uskoković, "Stereological analysis of the poly-(DL-lactide-co-glycolide) submicron sphere prepared by solvent/non-solvent chemical methods and centrifugal processing," *Journal of Materials Science: Materials in Medicine*, vol. 18, no. 7, pp. 1339–1344, 2007.
- [17] J. Vandervoort and A. Ludwig, "Biocompatible stabilizers in the preparation of PLGA nanoparticles: a factorial design study," *International Journal of Pharmaceutics*, vol. 238, no. 1-2, pp. 77–92, 2002.
- [18] E. E. Underwood, *Quantitative Stereology*, Addison-Wesley, Reading, Mass, USA, 1970.
- [19] H. E. Exner and H. P. Hougardy, *Quantitative Image Analysis of Microstructures*, DGM Informationsgesellschaft, Oberursel, Germany, 1988.
- [20] M. Kiremitçi-Gümüşderelioğlu and G. Deniz, "Synthesis, characterization and in vitro degradation of poly (DL-lactide)/poly(DL-lactide-co-glycolide) films," *Turkish Journal of Chemistry*, vol. 23, no. 2, pp. 153–162, 1999.
- [21] W. Lohmann, D. Pagel, and V. Penka, "Structure of ascorbic acid and its biological function. Determination of the conformation of ascorbic acid and isoascorbic acid by infrared and ultraviolet investigations," *European Journal of Biochemistry*, vol. 138, no. 3, pp. 479–480, 1984.
- [22] A. Grant, T. J. Wilkinson, D. R. Holman, and M. C. Martin, "Identification of recently handled materials by analysis of latent human fingerprints using infrared spectromicroscopy," *Applied Spectroscopy*, vol. 59, no. 9, pp. 1182–1187, 2005.



## Review Article

# Clinical Potential of Quantum Dots

Arthur M. Iga,<sup>1,2</sup> John H. P. Robertson,<sup>2</sup> Marc C. Winslet,<sup>2,3</sup> and Alexander M. Seifalian<sup>1,4</sup>

<sup>1</sup> Biomaterials and Tissue Engineering Centre, University College London, London WC1E 6BT, UK

<sup>2</sup> Academic Division of Surgical and Interventional Sciences, University College London, London WC1E 6BT, UK

<sup>3</sup> Department of Surgery, Royal Free Hampstead NHS Trust Hospital, London NW3 2QG, UK

<sup>4</sup> Advanced Nanomaterials Laboratory, BTEC, University College London, London NW3 2PF, UK

Correspondence should be addressed to Alexander M. Seifalian, a.seifalian@ucl.ac.uk

Received 12 March 2007; Revised 27 July 2007; Accepted 13 December 2007

Recommended by Marek Osinski

Advances in nanotechnology have led to the development of novel fluorescent probes called quantum dots. Quantum dots have revolutionized the processes of tagging molecules within research settings and are improving sentinel lymph node mapping and identification in vivo studies. As the unique physical and chemical properties of these fluorescent probes are being unraveled, new potential methods of early cancer detection, rapid spread and therapeutic management, that is, photodynamic therapy are being explored. Encouraging results of optical and real time identification of sentinel lymph nodes and lymph flow using quantum dots in vivo models are emerging. Quantum dots have also superseded many of the limitations of organic fluorophores and are a promising alternative as a research tool. In this review, we examine the promising clinical potential of quantum dots, their hindrances for clinical use and the current progress in abrogating their inherent toxicity.

Copyright © 2007 Arthur M. Iga et al. This is an open access article distributed under the Creative Commons Attribution License, which permits unrestricted use, distribution, and reproduction in any medium, provided the original work is properly cited.

## 1. INTRODUCTION

Quantum dots (QDs) are fluorescent semiconductor nanocrystals [1] with diameters of the order of 2–10 nanometers, or roughly 200–10,000 atoms [2]. QDs are made from a variety of different compounds. They are referred to as II–VI, III–V, or IV semiconductor nanocrystals, based on the periodic table groups that these elements are from. Cadmium selenide (CdSe) and Cadmium telluride (CdTe) nanocrystals are examples of QDs which are group II–VI semiconductor nanocrystal. CdSe contains cadmium (Cd) from group II and selenide (Se) from group VI of the periodic table. Their novel optical and physical properties have attracted immense interest in developing them for biological applications that require long-term, multitarget, and highly sensitive imaging. The general structure of QDs comprises an inorganic core, an inorganic shell, and an aqueous organic coating to which biomolecules are conjugated, as shown in Figure 1. Modifications in development can be used to control the size and composition of the nanocrystal core to create specific spectral properties of the QDs.

Developing high-quality QDs cores with a specific wavelength, chemical composition, and size is a prerequisite. Syn-

thesis is achieved by heating appropriate organometallic precursors with stabilizers in high boiling solvents to produce QDs, which can then be dissolved in nonpolar organic solvents to form transparent colloidal QDs dispersions. Organic solvents such as trioctylphosphine oxide (TOPO) and hexadecylamine are commonly used and contain alkyl chains which extend from the QDs surface, rendering the QDs sterically stable as colloids [3]. Altering the size of the QDs core during synthesis helps in tuning the color of emission [4]. The inherent toxicity of the individual ions ( $\text{Cd}^{2+}$ ,  $\text{Se}^{2-}$ , and  $\text{Te}^{2-}$ ) within the cores has been circumvented by growing an inorganic shell, that is, zinc sulphide (ZnS) on top of the CdSe or CdTe nanoparticles [5]. The ZnS shell serves as a barrier whereby the CdSe cannot come in contact with the surrounding solvent and thus dissolve through ionization. Secondly, it improves the quantum yield by passivating the surface nonradiative recombination sites. QDs have been rendered water soluble [6] by providing a shell of functionalized silica, phospholipids micelles [7], or linkers, such as mercaptoacetic acid [5], dihydrolipoic acid [8], or amphiphilic polymers, that is, modified polyacrylic acid [9, 10]. In general, stabilization in aqueous solution is achieved by

coating the QDs in amphiphilic polymers or by ligand exchange.

In order to use QDs in biological applications, QDs have been integrated with biomolecules. QDs are modified with bifunctional or amphiphilic molecules with one end binding or interacting with the QDs surface and the other polar end protruding from the surface [11]. QDs are conjugated electrostatically either directly, between QDs and proteins engineered to incorporate charged domains or via a bridge. Covalent coupling has also been harnessed whereby QDs bioconjugates are bound through carboxylic acids and biomolecules. Stabilization of QDs in aqueous solutions provides some QDs with coats which possess reactive functional groups such as amines, carboxylic acids, alcohols, and thiols [6, 8, 12]. Through these functional groups, covalent conjugation with a variety of biological molecules can be achieved. Once a biological interface has been provided, QDs can effectively and specifically target different biomarkers at cellular, tissue, tumor, and organ levels. The above developmental process has been summarized in Figure 2 and an overview of the current techniques of QDs—conjugate synthesis, biofunctionalization, and bioconjugation has been summarized in Table 1.

## 2. CLINICAL POTENTIAL (IN VIVO APPLICATIONS)

The unique properties of QDs can be put to use in a wide variety of biological applications. A key feature is that they can be modified with a large number of molecules and linkers to optimize their functionality for particular applications. QDs have been used to selectively tag molecules, proteins, and cells [8, 9, 13, 14] of interest. QDs have great potential for use in sentinel lymph node (SLN) mapping which is the mapping of the first tumor draining lymph node, [15–19], diagnostic tools (e.g., imaging), for therapeutic purposes (e.g., drug delivery and cancer treatment) [14], live cell labelling, and tracking over long periods of time [20]. Multicolor in vivo imaging has enabled noninvasive surgeries to be carried out in a way that has not been feasible without QD.

## 3. GUIDING CANCER SURGERY

### 3.1. Type II QDs

When tissues absorb light, there is a possibility that fluorescent light will be emitted. This causes tissue “autofluorescence” which can severely limit signal to background ratio. Some organs have increased green autofluorescent, for example, skin, small intestine, gall, and urinary bladder when excited with blue light. Exciting the gall and urinary bladder with green light will reduce their autofluorescence [21]; however, the use of a near-infrared (NIR) light reduces fluorescence background immensely. Type II QDs emit light within the NIR spectrum and have been used for cancer-guided surgery. Type I QDs structures are composed of CdSe/ZnS or CdTe/ZnS (core/shell) structure whereas Type II QDs structures are composed of CdTe/CdSe (core/shell) or CdSe/ZnTe (core/shell) heterostructures. Type II structures can allow ac-

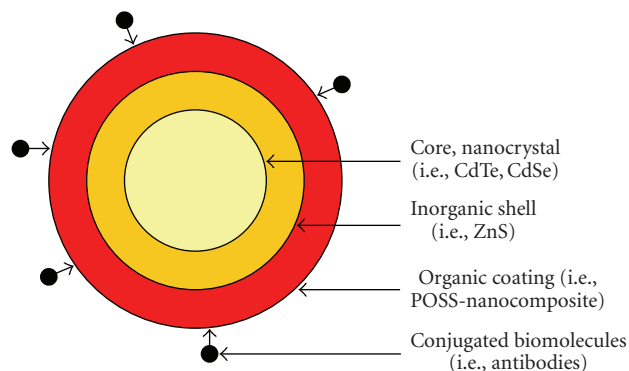


FIGURE 1: General structure of a QDs-modified from [21].

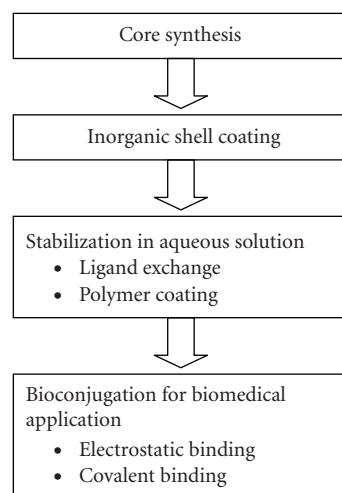


FIGURE 2: Overall development of QDs for biological application.

cess to wavelengths that would otherwise not be available with a single material [32].

### 3.2. Sentinel lymph node mapping

SLN identification and lymphatic mapping are one of the most revolutionary advances in surgical oncology in recent years [33]. Mapping and removal of the SLN provides accurate staging and therapeutic planning, determining the need for adjuvant oncological management [34]. In the USA, lymphatic mapping and SLN biopsy have become the standard of care for melanoma, with increasing acceptance in breast cancer and a growing acceptance in tumors of the gastrointestinal tract [35]. Identification of the sentinel node can be performed by the use of a radioisotope and intraoperative handheld gamma probe, a vital blue dye, or a combination of the two [34]. Current techniques of SLN mapping are limited by unpredictable drainage patterns, high background signal, and the inability to image lymphatic tracers relative to surgical anatomy in real time [15]. Novel fluorescent probes (QDs) have been developed to provide real-time image-guided localization using an NIR fluorescence system which facilitates the resection of the SLN [15–19].

TABLE 1: Overview of current techniques for synthesis, biofunctionalization, bioconjugation of QDs, and their conjugates.

First author	Synthesis	Biofunctionalization	Bioconjugation	Bioapplication
Zhou [22]	ZnS capped	Amphiphilic polymer shell, carboxylic acid, and amine functionalized	Peptide ligand	Selective cell surface and single-molecule imaging
Tortiglione [23]	ZnS capped	Amphiphilic polymer shell, diamino PEG functionalization	Glutathione (GSH)	Biolabelling <i>Hydra vulgaris</i> a freshwater invertebrate
Selvan [24]	Fe <sub>2</sub> O <sub>3</sub> -CdSe magnetic QDs (no ZnS capping)	Silicanization with surface amine groups	Oleyl- <i>O</i> -poly(ethylene glycol)succinyl- <i>N</i> -hydroxysuccinimidyl ester	Cell membrane targeting for biolabelling and imaging of live cells
Kampani [25]	ZnS capped	PEG layer	Biotin-streptavidin complex	Quantitative analysis of viral binding and attachment of human T cell leukemia virus type I
Medintz [26]	ZnS capped	Hexahistidine peptide linker with thiol	DNA oligonucleotides	Genetic analysis
Albuquerque de farias [27]	CdS/Cd(OH) <sub>2</sub> (no ZnS capping)	Glutaraldehyde cross-linking	Anti-A monoclonal antibody	Biolabelling of human erythrocytes
Gao [28]	ZnS capped	Mercaptoacetic acid with bovine serum albumin coating to increase quantum yield and to provide amine and thiol functional groups	None	Potential for molecular sensing
Wolcott [6]	Silica capped	PEG and thiol-terminated biolinkers	Immunoglobulin G proteins	Biolabelling and imaging
Tan [29]	ZnS capped	Chitosan	Human epidermal growth factor receptor 2 antibody	Tracking of RNA delivery
Parungo [19]	CdSe inorganic shell	Oligomeric phosphines	None	Pleural space SLN mapping
Van Tilborg [30]	ZnS shell	Paramagnetic lipid Gd-DTPA-bis(stearylamide)	Human annexin A5 protein molecules	Multimodal detection of apoptotic cells
Jaiswal [8]	Zns shell	Dihydrolipoic acid (DHLLA)	Avidin or antiP-glycoprotein antibody	Long-term imaging of live cells
Dubertret [7]	ZnS capped	Phospholipids	Deoxyribonucleic acid (DNA)	Labelling of <i>Xenopus</i> embryos
Mulder [31]	ZnS shell	Pegylated phospholipids and a Paramagnetic lipid Gd-DTPA-bis(stearylamide)	Arginine-glycine-aspartic acid (RGD) peptides	In viro targeting of human endothelial cells
Bharali [5]	ZnS shell	Mercaptoacetic acid	Folic acid	Imaging of live cells
Wu [9]	ZnS shell	Amphiphilic polymer	Streptavidin or anti-Her2 antibody	Labelling of cancer marker Her2

Tumor staging and treatment planning is improved if assessment of the primary lymph node draining a tumor site is accurate. Gastrointestinal (esophageal, gastric, jejuna, and colonic) and pulmonary SLN mapping have been carried out in in vivo models with a real-time NIR fluorescence imaging system. NIR fluorescent QDs have been used for intraoperative mapping of lymphatic drainage of various organs and for

guiding excision of the primary draining node on a patient-specific basis [15, 18].

### 3.3. Gastrointestinal SLN mapping

In gastrointestinal SLN mapping, injection of 200 pmol of NIR fluorescent QDs into various intra-abdominal organs

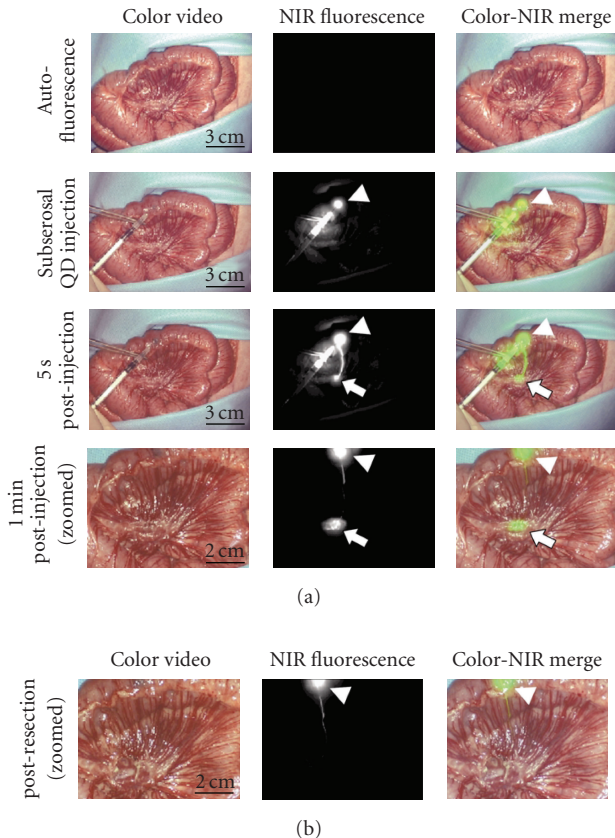


FIGURE 3: NIR fluorescent SLN mapping of the porcine colon. (a) NIR fluorescent images of the surgical field pre-, during, and postinjection of NIR quantum dots. (b) Same image in “(a)” reveals no QDs fluorescence in the area of the excised SLN [15].

identified the SLN in less than 60 seconds and the afferent lymphatics in 100% of the cases [15]. QDs may be engineered to precise sizes which enable localization in the SLN unlike blue dye which contains particles  $<5$  nm that can pass through multiple nodes therefore leading to false-positive results [15]. Examination of the operative site after surgery can be done to ensure successful removal of the lymph nodes. This has been demonstrated in Figure 3 where images after SLN excision in a porcine colon reveal no fluorescence in the area of the excised SLN. However, SLN analysis by the pathologist is facilitated as the QDs help identify the specific part of the SLN that is most likely to contain malignant cells [16].

### 3.4. Pulmonary SLN mapping

In pulmonary SLN mapping, injected QDs identified the SLN within 1 minute, whereas isosulfan blue (the gold standard visible lymphatic tracer) could be visualized in the same node within 4 minutes. In contrast to QDs, isosulfan blue reduces clarity due to extravasation. NIR QDs do not interfere with the visualization of the surgical field as they are invisible to the human eye [18]. NIR fluorescence imaging with QDs in two species demonstrated that the highest superior mediastinal lymph nodes are the SLNs of the pleural

space [19]. Advancement of the NIR fluorescence imaging with QDs indicate a promising future in clinical lymphatic mapping. Table 2 shows various studies using NIR fluorescent QDs in SLN mapping.

## 4. CANCER IMAGING

### 4.1. Strong potential for sensitivity in cancer diagnosis

QDs have been shown to specifically and effectively label molecular targets at cellular level and they have been used as a diagnostic tool for cancer in in vivo studies [14, 36]. In vivo targeting studies of human prostate cancer developed in nude mice showed that QDs probes accumulated in tumors by both the enhanced permeability and retention at tumor sites through antibodies binding to cancer-specific cell surface biomarkers [14]. For active tumor targeting, antibody-conjugated QDs were used to target a prostate-specific membrane antigen (PSMA). Previous research has identified PSMA as a cell surface marker for both prostate epithelial cells and neovascular endothelial cells [37]. Results obtained from QD-PSMA antibody probes injected into the tail vein of a tumor-bearing mouse showed that nanoparticles were delivered and retained by the tumor xenograft [14]. Comparison with other surface modifications of the QDs probe: carboxylic (COOH) group, polyethylene glycol (PEG) groups, and PEG plus PSMA antibody showed, no tumor signals were detected with the COOH probe, only weak tumor signals were observed with the PEG probe (passive targeting) and intense signals were detected in PEG-PSMA antibody-conjugated probe [14]. The above results present new opportunities for ultrasensitive imaging of biomarkers involved in cancer invasion and metastases, as a result alerting clinician to early intervention.

Using QDs, precancerous biomarkers have been investigated in cervical cancers [13]. It is widely accepted among immunohistochemistry studies in the cervix that epidermal growth factor receptor (EGFR) levels demonstrate a statistically significant increase when a lesion progresses from a dysplastic to an invasive lesion [38]. SiHa cervical cancer cells were targeted with QDs conjugated to anti-EGFR antibodies [13]. This showed specific labelling of EGF receptors. Using optical imaging technologies, they postulated that QDs can help visualize changes in the cervical cancer at the molecular level hence the need for early intervention. The ability to image molecular changes will directly affect patient care by allowing earlier detection of disease and identification of specific molecular targets for treatment [39].

## 5. THERAPEUTIC

### 5.1. Photodynamic therapy in cancer treatment

Photodynamic therapy (PDT) has been developed as a novel management technique for a diverse variety of cancers [40]. In conjunction with surgical treatment, PDT has been used successfully in lung cancer and is increasingly being used on gastrointestinal malignancies. This modality is already an established treatment entity in ophthalmology. During PDT,



TABLE 2: Studies using NIR fluorescent QDs (Type II NIR QDs) in SLN mapping, using emission of 840–860 nm wavelength [15–19].

NIR fluorescent Lymph tracer	Model	Tissues/organs	Outcome
Soltesz [15]	Pig	GI tract (gastric, jejunal, colonic)	Identified SLN in less than 1 minute in 100% of pigs
Soltesz [18]	Pig	Lungs	Identified SLN within 5 minutes in 100% of pigs
Parungo [19]	Rat and pig	Pleural space	Demonstrated that station 1 lymph nodes are the SLN of the pleural space in rats and pigs
Kim [16]	Mouse and pig	Limbs (lymphatic flow to axilla and groin)	Identified SLN in 3–4 minutes (percentage not mentioned)
Parungo [17]	Pig	Esophagus	A single SLN was identified within 5 minutes in 100% of pigs

singlet oxygen is generated in the diseased cells by a simple and controllable light-activated process. This process involves a photosensitizer that is capable of absorbing light of an appropriate wavelength and utilizing that energy to excite oxygen to its singlet state which initiates apoptosis of cancer cells [41]. Selectivity is significant in cancer treatment and has been utilized in PDT. Only cells which are simultaneously in contact with the photosensitizer, light and in the presence of oxygen are subjected to the cytotoxic reactions [42]. In the work of Samia et al. [43], CdSe QDs were linked to a silicon phthalocyanine (Pc4) photosensitizer through an alkyl group, and used as a primary energy donor. Excitation of CdSe QDs activated emission of Pc4 photosensitizer at 680 nm, which enabled the use of an excitation wavelength that is not absorbed by the sensitizer. Through the fluorescence resonance energy transfer mechanism from QDs to the silicon Pc4 photosensitizer, oxygen reactive species were generated for photodynamic cancer therapy. Furthermore, the semiconductor nanocrystals alone were found to generate oxygen reactive species without a mediating photosensitizer. In view of their flexible spectral characteristics, QDs can be engineered in size and composition to match those of any PDT photosensitizer and be used as energy donors. Figure 4 shows a summarized mechanism of PDT involving QDs.

## 5.2. Drug delivery

QDs probes have been shown to accumulate in tumors by enhanced permeability and retention at tumor sites or by antibody binding to cancer-specific cell surface biomarkers [14]. Enhanced permeability and retention (EPR) effect is the basis for selective targeting of macromolecular drugs to tumors and the concept is now utilized for selective delivery of many macromolecular anticancer agents [44]. Styrene-maleic acid-doxorubicin micelles utilizing EPR effect have been shown to enhance the therapeutic effects of doxorubicin while reducing toxicity [45]. Polyethylene glycol-liposomes encapsulating doxorubicin were less extensively taken up by the reticuloendothelial system and were able to extravasate through

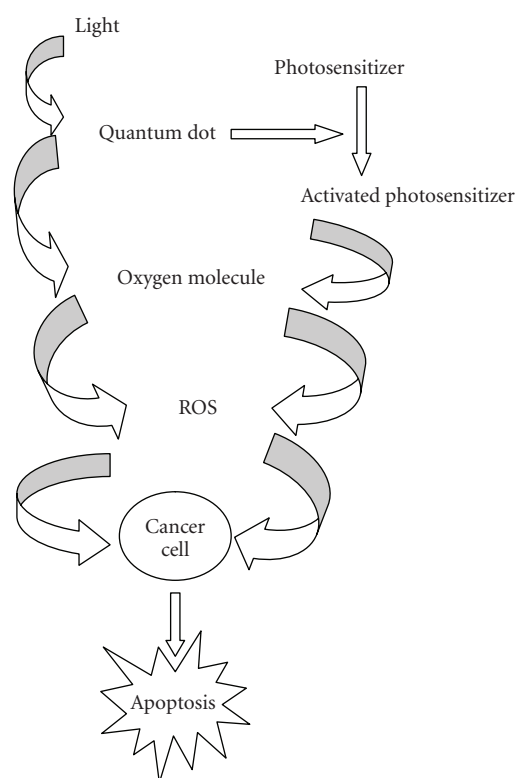


FIGURE 4: Summarized mechanism of PDT involving QDS [43].

“leaky” tumor vasculature resulting into doxorubicin localization in tumor tissue [46]. EPR can deliver therapeutic agents to desired targets while reducing systemic toxicity. Research in drug delivery has benefited from the use of nanotechnology in dendrimers [47] and liposomes [48]. Combining QDs, specifically their ability to bind molecules that recognize cancer cells and a drug, might offer a new strategy for molecular cancer therapy through targeted molecular delivery vehicles.

## 6. QDs AS A RESEARCH TOOL

### 6.1. Bio-sensitive

The rate of success of QDs usage in the laboratory has increased immensely. As a biosensitive tool, detection of single bacteria pathogenic *Escherichia coli* 0157:H7 serotype was made possible with the use of QDs [49]. Under continuous excitation, QDs retained their high fluorescence intensities for hours while organic dyes bleached in seconds, allowing more rapid and accurate identification of *E. coli* 0157:H7 in single-cell fluorescence-based assays. QDs allowed lower limits of detection, which increased sensitivity, and has important implications in the development of any fluorescent immunoassay for bacteria pathogens. QDs-labeled chromatophores have been used as virus detectors to detect H9 avian influenza virus based on antibody-antigen reaction [50]. Selective determination of free cyanide in water with high sensitivity (detection limit of  $1.1 \times 10^{-6}$  M) has been demonstrated via analyte-induced changes in QDs photoluminescence after photoactivation [51].

### 6.2. Bioimaging

QDs have been used to stain *Hydra vulgaris* (a fresh water invertebrate) and study its behavior [23], to image in vivo tumor vasculature in mice [39], and to study vasculogenesis in Zebrafish [52]. Bovine serum albumin-coated QDs have been used as a fluorescent, angiographic contrast agent in the NIR range [39]. Observation of vessels surrounding and penetrating a murine squamous cell carcinoma in a C3H mouse was made possible. Distinction between the superficial vessels associated with the tumor and deep vessels could be made with the deep vessels visible in fluorescence images. Colabelling of Zebra fish embryo's blood vessels with QDs enabled documentation of the embryonic pattern of vasculogenesis as the QDs marked the newly formed vessels [52]. As a result, detailed knowledge about the progression of vascular systems development has been obtained.

### 6.3. Biolabelling

Different groups have successfully demonstrated that QDs can be tagged and incorporated into cells and drugs without affecting their activation and function [20, 27, 53–55]. Up to  $10^8$  QDs could be injected in Zebra fish embryos without malformations or developmental problems during embryogenesis [52]. QDs were used to follow labeled cells during their developmental stages to reveal cellular behavior. Semiconductor nanocrystals have been used for in vivo tracking of cancer cells during metastases. Tumor cells labeled with QDs were used in fluorescence microscopy to study extravasation, a part of metastasis formation at high resolution in living animals [20]. QDs-labeled cells survived the selective pressure of the circulation and managed to extravasate into tissues just as effectively as unlabeled cells. The use of QDs provided the opportunity to simultaneously identify and study the interactions of multiple different populations of tumor cells and tissue cells in a natural tissue environment.

## 7. COMPARISON TO OTHER FLUORESCENT COMPOUNDS

Fluorescent QDs that overcome many of the limitations of organic fluorophores are a promising alternative. Organic fluorophores's excitation and emission wavelengths are dependent on a chemical structure whose tuning to a precise wavelength requires complicated chemistry. The quantum yield of conventional organic fluorophores is usually less than 15% in aqueous environments [21]. QDs have a large absorption cross-section, good quantum yield, and a large saturation intensity that makes them much brighter than fluorescence dyes or fluorescent proteins [56]. QDs have broad-band absorbance to the blue of emission which has been exploited for in vivo applications. Studies have demonstrated that tissue scatter and absorbance may sometimes offset increasing QDs absorption at blue light wavelength and counteract this advantage [57]. However, QDs that emit in the NIR region of the electromagnetic spectrum have been developed for live tissue imaging. Within the NIR of the spectrum there is low tissue scattering and absorption, yielding great tissue penetration depth and optical signal [11].

In the work of Gao et al. [14], sensitivity detection and spectral features of QDs and green fluorescent protein (GFP) were compared by linking translocation peptide HIV Tat to QDs and delivering them into living cancer cells. QDs-tagged cells and the GFP-transfected cells were similarly bright in cell cultures, however only the QDs signal was observed in vivo. GFP signals were not discerned at the injection site. Even if results did not provide an absolute intensity comparison between GFP and QD, they provided a qualitative spectral comparison demonstrating that the emission spectra of QDs could be shifted away from the autofluorescence, allowing spectroscopic detection at low signal intensities [14]. The large Stokes's shift which is the difference between the peak absorption and the peak emission wavelengths enables fluorescent signals from QDs to be easily separated from scattered excited light [13].

QDs are more highly photostable than organic fluorophores. Organic dyes are often photobleached and fade by >90% in less than one minute, whereas QDs are stable for more than 30 minutes under identical experimental conditions [58]. In vivo fluorescence quenching of QDs-micelles and rhodamine green-dextran was compared after 80 minutes of constant illumination at 450 nm under the microscope. The QDs fluorescence intensity remained the same, whereas the dextran had photobleached [7]. While detecting tumor marker CA125 in ovarian carcinoma, Wang et al. [59] compared the photostability of QDs signals and a conventional organic dye fluorescein isothiocyanate (FITC). QDs signals were found to be more specific and brighter than those of FITC, with exceptional photostability during continuous illumination for 1 hour, whereas FITC signals faded very quickly and became undetectable after 24 minutes of illumination. Arguably, the extreme photostability of QDs may have little significance in the context of clinical potential as fluence rates that photobleach organic fluorophores have no place in the clinical settings. The susceptibility of conventional fluorophores to photobleaching limits the fluence

rate that can be applied to a sample and as a result it affects the sensitivity of detection [21]. In order to minimize the potential for toxicity, Kim et al. [16] increased the fluorescence rate, and proportionally decreased the dose of injected QDs. Their photobleaching data suggested that at least a 100-fold lower dose could be used. Although QDs are photostable and they can achieve high-quantum yields in organic solvents, they underperform organic fluorophores as a function of molecular volume. That is, given their size, QDs are much poorer photoluminescence agents than organic fluorophores. In depth, discussions of various properties of QDs in relation to conventional fluorophores have been published [14, 21, 56, 60].

## 8. RECENT DEVELOPMENTS

In the burgeoning field of nanotechnology QDs synthesis, biofunctionalization and bioconjugation techniques are advancing rapidly. Conventionally inorganic cores have been capped with inorganic shells, ZnS; while other techniques of capping the core with cadmium sulphide (CdS), Silicon, CdTe or CdSe to form CdTe/CdSe (core/shell), or CdSe/ZnTe (core/shell) [32, 36, 61] are emerging. CdTe/CdSe (core/shell) or CdSe/ZnTe (core/shell) is expected to have many novel properties that are fundamentally different from CdSe/ZnS (core/shell) or CdTe/ZnS (core/shell) because of their valence and conduction band differences [32]. These properties are being exploited in *in vivo* applications. Water-based synthesis of highly luminescent QDs is a promising alternative to QDs prepared in organic solvents [62–65] in cellular imaging and biolabelling. It offers the advantage of engineering water soluble, stable QDs with smaller hydrodynamic diameters that are easily conjugated to biomolecules. Synthesis of group III–V semiconductor QDs (i.e., InP) as a luminescence probe for imaging in live cells has been reported [5]. Group III–V QDs are potentially less toxic as opposed to II–VI QDs theoretically making them better probes for bioapplications. Drawbacks to utilizing III–V QDs as fluorescent probes are their low quantum yield and laborious synthesis. Future work to harness their full potential will include increasing the quantum yield and minimizing the aqueous size of the quantum dot.

The aqueous size of the QDs should be appropriately matched to the *in vivo* study of interest [16]. Types 11 QDs with aqueous sizes of 15.8–18.8 nm have been used for SLN mapping [15–19]. Recent work of Zimmer et al. [66] demonstrates the synthesis of a size series of (InAs)ZnSe (core) shell QDs that emit in the NIR and exhibit aqueous size of less than 10 nm. These QDs circulated in the blood before they were able to migrate out of the blood vessels and into the interstitial fluid. It is a significant achievement in the development of QD; hence after intravenous injection, they can possibly penetrate most normal organs or micrometastases.

Bimodal nanoparticles consisting of QDs that are encapsulated in a paramagnetic micelle to enable both optical imaging and magnetic resonance imaging (MRI) are being developed [30, 31]. This has potential to detect pathological processes in *in vivo* models and tumor angiogenesis with both intravital fluorescence microscopy and MRI [30, 31].

Various strategies of biofunctionalization and bioconjugation have been developed to generate water-soluble QDs as previously discussed however some have encountered problems. QDs solubilization with mercaptoacetic acid [5, 28] have been reported to cause a drop in fluorescence quantum yields after solubilization and desorption of mercaptoacetic acid has led to aggregation and precipitation of solubilized QDs [28]. Bovine serum albumin has been used to improve the fluorescent intensity of the QDs solubilized in mercaptoacetic acid [28]. Techniques of biofunctionalization and bioconjugation have to (i) be reproducible, (ii) maintain the size of the QDs complex to a minimum, (iii) maintain the photoluminescence properties of the QDs, (iv) provide chemical stability of the QDs complex, and (v) be reliable methods for conjugation to biomolecules.

## 9. DISCUSSION

The future of QDs is promising however there are fundamental questions that still need to be answered. Questions have arisen about their toxicity, long-term *in vivo* stability and metabolic elimination from the body. Prevention of core atoms, Cd atoms, from being accessible to or potentially released in the surrounding environment has been passivated by shelling the core in extra layers of material. Questions regarding biochemical mechanisms of cytotoxicity are slowly beginning to be answered, mechanisms suggested involve production of reactive oxygen species such as free hydroxyl radicals and singlet oxygen [43, 67, 68]. Treatment with N-acetylcysteine (NAC), an antioxidant, has shown to prevent “naked” QD-induced organelle and cell damage which is mediated by reactive oxygen species (ROS) [68]. In the work of Lovrić et al. [68], NAC improved cell survival by reducing concentration of ROS in cell culture medium. NAC further induced the synthesis of glutathione, an effective cellular antioxidant, and possibly improved QDs surface passivation, leading to less damage to the mitochondrial redox system. Understanding the mechanisms of QDs cytotoxicity is significant in order to make use of their potential.

Studies of bovine serum albumin-QDs conjugates have shown bovine serum albumin to provide protection against QDs-induced cytotoxicity [69]. Albumin reduced or eliminated toxicity through possession of peptides responsible for the extracellular antioxidant defense system. However, work on mercapto-undecanoic acid QDs (MUA-QDs) in sheep serum albumin (SSA); showed that MUA-QDs caused cell damage even at low concentrations [70]. Cytotoxicity caused by mercapto-undecanoic acid QDs in sheep serum albumin was attributed to the nonchemical bonds between the SSA and the MUA-QDs. There could be a possibility that MUA QDs capping alone without the QDs caused cell damage as effects of MUA alone on *vero*, *hela* cells and primary human hepatocytes were not assessed. There is a need to evaluate the strength of bonds between the QDs and their surface coatings. Possible enzymatic, physical and chemical degradation of the semiconductor cores upon injection in live animals could occur. Under what shear stress *in vivo* circulatory pressures are the surface coatings likely to hold? Arguably, QDs do not have to be in the circulatory system for

clinical application, however, they may gain access to circulation through blood and lymphatic channels therefore their degradation needs to be assessed.

Polydentate phosphine-coated NIR QDs were found to be stable in 100% serum after incubation for twice the amount of time needed for a typical SLN mapping procedure [16]. There was minimal disruption in the optical properties of the NIR QDs, which is promising for biological applications. Biocompatible polymer such as silicon are safer materials to use for encapsulation and are highly unlikely to degrade [14, 70].

QDs surfaces can control serum lifetime and pattern of deposition [10] which has been exploited in many in vivo applications. Deposition in the reticuloendothelial system is significant for detecting SLNs. Polymer encapsulation with surface PEG groups reduced the rate of organ uptake and improved circulation half-life of QDs, leading to accumulation of the nanoparticles in the tumor [10]. The size of the nanoparticles plays a vital role in avoiding filtration by the reticuloendothelial system. In a similar strategy exploited in drug delivery systems, drug-carrying liposomes are believed to have an increased lifespan partly due to their ability to extravasate through the splenic and liver fenestrae [71].

Different reports have been published highlighting the inertness of QDs in vivo studies where physiological function has not been affected, however lots of gaps exist regarding biodegradation and excretion. Encapsulation of QDs prepared in organic solvents is one of the most widely used methods of abrogating QDs toxicity, however new ways of QDs synthesis and negating QDs toxicity need to be devised. Adding extra coating onto the QDs core improves blood half-life which in essence increases the dissolution. Additional QDs surfaces will not enhance the translation of QDs to the clinical setting as they do not eliminate the toxic cores. Surface coatings and surface modification prior to in vivo application may have a big role to play on QDs degradation or elimination. However, the current state and design of the QDs precludes the elimination of QDs from the body. The ability to functionalize QDs with many different chemical groups increases its aqueous size. This presents an enormous predicament since the core, shell, organic coatings, and functional groups will be larger than the pore size of the endothelium and the renal threshold. To the best of our knowledge there are no in vivo studies on the metabolism and excretion of QD.

The engineering of QDs for biological applications is at its infancy. Progress is being made in designing sizable and biocompatible QDs. As optimism in exploiting QDs clinical potential is high, there is need to assess their cytotoxicity, in vivo distribution, and excretion. A much more work needs to be done to combat QDs inherent toxicity before they are applied in the clinical settings.

In summary, the development of QDs for clinical usage will have to circumvent a few more hurdles to gain recognition as a novel fluorescent probe for SLN, early cancer detection, rapid spread, and therapeutic intervention. The idea of engineering QDs for clinical purposes is not far fetched. The ideal QDs for clinical application would possess non-toxic elements, being chemically stable and with tunable size

to perfectly negate through the endothelial pores, and would need to be completely eliminated from the body. With improvements in nanotechnology, nanotoxicology, and chemistry, some of the above goals could be achieved; however, it will be difficult to replace the toxic core of the QDs without losing the optical properties, or our efforts have to be redirect to less-toxic elements.

## REFERENCES

- [1] J. K. Jaiswal and S. M. Simon, "Potentials and pitfalls of fluorescent quantum dots for biological imaging," *Trends in Cell Biology*, vol. 14, no. 9, pp. 497–504, 2004.
- [2] A. M. Smith, G. Ruan, M. N. Rhyner, and S. Nie, "Engineering luminescent quantum dots for in vivo molecular and cellular imaging," *Annals of Biomedical Engineering*, vol. 34, no. 1, pp. 3–14, 2006.
- [3] X. Gao, L. Yang, J. A. Petros, F. F. Marshall, J. W. Simons, and S. Nie, "In vivo molecular and cellular imaging with quantum dots," *Current Opinion in Biotechnology*, vol. 16, no. 1, pp. 63–72, 2005.
- [4] M. Green, "Semiconductor quantum dots as biological imaging agents," *Angewandte Chemie International Edition*, vol. 43, no. 32, pp. 4129–4131, 2004.
- [5] D. J. Bharali, D. W. Lucey, H. Jayakumar, H. E. Pudavar, and P. N. Prasad, "Folate-receptor-mediated delivery of InP quantum dots for bioimaging using confocal and two-photon microscopy," *Journal of the American Chemical Society*, vol. 127, no. 32, pp. 11364–11371, 2005.
- [6] T. Jamieson, R. Bakhshi, D. Petrova, R. Pocock, M. Imani, and A. M. Seifalian, "Biological applications of quantum dots," *Biomaterials*, vol. 28, no. 31, pp. 4717–4732, 2007.
- [7] B. Dubertret, P. Skourides, D. J. Norris, V. Noireaux, A. H. Brivanlou, and A. Libchaber, "In vivo imaging of quantum dots encapsulated in phospholipid micelles," *Science*, vol. 298, no. 5599, pp. 1759–1762, 2002.
- [8] J. K. Jaiswal, H. Mattoussi, J. M. Mauro, and S. M. Simon, "Long-term multiple color imaging of live cells using quantum dot bioconjugates," *Nature Biotechnology*, vol. 21, no. 1, pp. 47–51, 2003.
- [9] X. Wu, H. Liu, J. Liu, et al., "Immunofluorescent labeling of cancer marker Her2 and other cellular targets with semiconductor quantum dots," *Nature Biotechnology*, vol. 21, no. 1, pp. 41–46, 2003.
- [10] B. Ballou, B. C. Lagerholm, L. A. Ernst, M. P. Bruchez, and A. S. Waggoner, "Noninvasive imaging of quantum dots in mice," *Bioconjugate Chemistry*, vol. 15, no. 1, pp. 79–86, 2004.
- [11] W. Jiang, E. Papa, H. Fischer, S. Mardiyani, and W. C. W. Chan, "Semiconductor quantum dots as contrast agents for whole animal imaging," *Trends in Biotechnology*, vol. 22, no. 12, pp. 607–609, 2004.
- [12] E. R. Goldman, E. D. Balighian, H. Mattoussi, et al., "Avidin: a natural bridge for quantum dot-antibody conjugates," *Journal of the American Chemical Society*, vol. 124, no. 22, pp. 6378–6382, 2002.
- [13] D. L. Nida, M. S. Rahman, K. D. Carlson, R. Richards-Kortum, and M. Follen, "Fluorescent nanocrystals for use in early cervical cancer detection," *Gynecologic Oncology*, vol. 99, no. 3, supplement 1, pp. S89–S94, 2005.
- [14] X. Gao, Y. Cui, R. M. Levenson, L. W. K. Chung, and S. Nie, "In vivo cancer targeting and imaging with semiconductor quantum dots," *Nature Biotechnology*, vol. 22, no. 8, pp. 969–976, 2004.



- [15] E. G. Soltesz, S. Kim, S.-W. Kim, et al., "Sentinel lymph node mapping of the gastrointestinal tract by using invisible light," *Annals of Surgical Oncology*, vol. 13, no. 3, pp. 386–396, 2006.
- [16] S. Kim, Y. T. Lim, E. G. Soltesz, et al., "Near-infrared fluorescent type II quantum dots for sentinel lymph node mapping," *Nature Biotechnology*, vol. 22, no. 1, pp. 93–97, 2004.
- [17] C. P. Parungo, S. Ohnishi, S.-W. Kim, et al., "Intraoperative identification of esophageal sentinel lymph nodes with near-infrared fluorescence imaging," *Journal of Thoracic and Cardiovascular Surgery*, vol. 129, no. 4, pp. 844–850, 2005.
- [18] E. G. Soltesz, S. Kim, R. G. Laurence, et al., "Intraoperative sentinel lymph node mapping of the lung using near-infrared fluorescent quantum dots," *Annals of Thoracic Surgery*, vol. 79, no. 1, pp. 269–277, 2005.
- [19] C. P. Parungo, Y. L. Colson, S.-W. Kim, et al., "Sentinel lymph node mapping of the pleural space," *Chest*, vol. 127, no. 5, pp. 1799–1804, 2005.
- [20] E. B. Voura, J. K. Jaiswal, H. Mattoussi, and S. M. Simon, "Tracking metastatic tumor cell extravasation with quantum dot nanocrystals and fluorescence emission-scanning microscopy," *Nature Medicine*, vol. 10, no. 9, pp. 993–998, 2004.
- [21] J. V. Frangioni, "In vivo near-infrared fluorescence imaging," *Current Opinion in Chemical Biology*, vol. 7, no. 5, pp. 626–634, 2003.
- [22] M. Zhou, E. Nakatani, L. S. Gronenberg, et al., "Peptide-labeled quantum dots for imaging GPCRs in whole cells and as single molecules," *Bioconjugate Chemistry*, vol. 18, no. 2, pp. 323–332, 2007.
- [23] C. Tortiglione, A. Quarta, A. Tino, L. Manna, R. Cingolani, and T. Pellegrino, "Synthesis and biological assay of GSH functionalized fluorescent quantum dots for staining *Hydra vulgaris*," *Bioconjugate Chemistry*, vol. 18, no. 3, pp. 829–835, 2007.
- [24] S. T. Selvan, P. K. Patra, C. Y. Ang, and J. Y. Ying, "Synthesis of silica-coated semiconductor and magnetic quantum dots and their use in the imaging of live cells," *Angewandte Chemie International Edition*, vol. 46, no. 14, pp. 2448–2452, 2007.
- [25] K. Kampani, K. Quann, J. Ahuja, B. Wigdahl, Z. K. Khan, and P. Jain, "A novel high throughput quantum dot-based fluorescence assay for quantitation of virus binding and attachment," *Journal of Virological Methods*, vol. 141, no. 2, pp. 125–132, 2007.
- [26] I. L. Medintz, L. Berti, T. Pons, et al., "A reactive peptidic linker for self-assembling hybrid quantum dot-DNA bioconjugates," *Nano Letters*, vol. 7, no. 6, pp. 1741–1748, 2007.
- [27] P. M. A. de Farias, B. S. Santos, F. D. De Menezes, et al., "Core-shell CdS/Cd(OH)<sub>2</sub> quantum dots: synthesis and bioconjugation to target red cells antigens," *Journal of Microscopy*, vol. 219, no. 3, pp. 103–108, 2005.
- [28] X. Gao, W. C. W. Chan, and S. Nie, "Quantum-dot nanocrystals for ultrasensitive biological labeling and multicolor optical encoding," *Journal of Biomedical Optics*, vol. 7, no. 4, pp. 532–537, 2002.
- [29] W. B. Tan, S. Jiang, and Y. Zhang, "Quantum-dot based nanoparticles for targeted silencing of HER2/neu gene via RNA interference," *Biomaterials*, vol. 28, no. 8, pp. 1565–1571, 2007.
- [30] G. A. F. Van Tilborg, W. J. M. Mulder, P. T. K. Chin, et al., "Annexin A5-conjugated quantum dots with a paramagnetic lipidic coating for the multimodal detection of apoptotic cells," *Bioconjugate Chemistry*, vol. 17, no. 4, pp. 865–868, 2006.
- [31] W. J. M. Mulder, R. Koole, R. J. Brandwijk, et al., "Quantum dots with a paramagnetic coating as a bimodal molecular imaging probe," *Nano Letters*, vol. 6, no. 1, pp. 1–6, 2006.
- [32] S. Kim, B. Fisher, H.-J. Eisler, and M. Bawendi, "Type-II quantum dots: CdTe/CdSe(core/shell) and CdSe/ZnTe(core/shell) heterostructures," *Journal of the American Chemical Society*, vol. 125, no. 38, pp. 11466–11467, 2003.
- [33] A. Torne and L. M. Puig-Tintore, "The use of sentinel lymph nodes in gynaecological malignancies," *Current Opinion in Obstetrics and Gynecology*, vol. 16, no. 1, pp. 57–64, 2004.
- [34] G. Peley, I. Sinkovics, G. Liszkay, et al., "The role of intraoperative gamma-probe-guided sentinel lymph node biopsy in the treatment of malignant melanoma and breast cancer," *Orvosi Hetilap*, vol. 140, no. 42, pp. 2331–2338, 1999.
- [35] J. W. Jakub, S. Pendas, and D. S. Reintgen, "Current status of sentinel lymph node mapping and biopsy: facts and controversies," *Oncologist*, vol. 8, no. 1, pp. 59–68, 2003.
- [36] X. Yu, L. Chen, K. Li, et al., "Immunofluorescence detection with quantum dot bioconjugates for hepatoma in vivo," *Journal of Biomedical Optics*, vol. 12, no. 1, Article ID 014008, 5 pages, 2007.
- [37] S. S. Chang, V. E. Reuter, W. D. W. Heston, and P. B. Gaudin, "Metastatic renal cell carcinoma neovasculature expresses prostate-specific membrane antigen," *Urology*, vol. 57, no. 4, pp. 801–805, 2001.
- [38] A. M. Kersemaekers, G. J. Fleuren, G. G. Kenter, et al., "Oncogene alterations in carcinomas of the uterine cervix: overexpression of the epidermal growth factor receptor is associated with poor prognosis," *Clinical Cancer Research*, vol. 5, no. 3, pp. 577–586, 1999.
- [39] N. Y. Morgan, S. English, W. Chen, et al., "Real time in vivo non-invasive optical imaging using near-infrared fluorescent quantum dots," *Academic Radiology*, vol. 12, no. 3, pp. 313–323, 2005.
- [40] N. L. Oleinick, R. L. Morris, and I. Belichenko, "The role of apoptosis in response to photodynamic therapy: what, where, why, and how," *Photochemical & Photobiological Sciences*, vol. 1, no. 1, pp. 1–21, 2002.
- [41] A. C. S. Samia, S. Dayal, and C. Burda, "Quantum dot-based energy transfer: perspectives and potential for applications in photodynamic therapy," *Photochemistry and Photobiology*, vol. 82, no. 3, pp. 617–625, 2006.
- [42] R. L. Morris, K. Azizuddin, M. Lam, et al., "Fluorescence resonance energy transfer reveals a binding site of a photosensitizer for photodynamic therapy," *Cancer Research*, vol. 63, no. 17, pp. 5194–5197, 2003.
- [43] A. C. S. Samia, X. Chen, and C. Burda, "Semiconductor quantum dots for photodynamic therapy," *Journal of the American Chemical Society*, vol. 125, no. 51, pp. 15736–15737, 2003.
- [44] J. Fang, T. Sawa, and H. Maeda, "Factors and mechanism of "EPR" effect and the enhanced antitumor effects of macromolecular drugs including SMANCS," *Advances in Experimental Medicine and Biology*, vol. 519, pp. 29–49, 2003.
- [45] K. Greish, T. Sawa, J. Fang, T. Akaike, and H. Maeda, "SMA-doxorubicin, a new polymeric micellar drug for effective targeting to solid tumours," *Journal of Controlled Release*, vol. 97, no. 2, pp. 219–230, 2004.
- [46] A. Gabizon and F. Martin, "Polyethylene glycol-coated (pegylated) liposomal doxorubicin. Rationale for use in solid tumours," *Drugs*, vol. 54, supplement 4, pp. 15–21, 1997.
- [47] U. Boas and P. M. H. Heegaard, "Dendrimers in drug research," *Chemical Society Reviews*, vol. 33, no. 1, pp. 43–63, 2004.
- [48] M. S. Arayne and N. Sultana, "Porous nanoparticles in drug delivery systems," *Pakistan Journal of Pharmaceutical Sciences*, vol. 19, no. 2, pp. 158–169, 2006.

- [49] M. A. Hahn, J. S. Tabb, and T. D. Krauss, "Detection of single bacterial pathogens with semiconductor quantum dots," *Analytical Chemistry*, vol. 77, no. 15, pp. 4861–4869, 2005.
- [50] Z. Yun, D. Zhengtao, Y. Jiachang, T. Fangqiong, and W. Qun, "Using cadmium telluride quantum dots as a proton flux sensor and applying to detect H9 avian influenza virus," *Analytical Biochemistry*, vol. 364, no. 2, pp. 122–127, 2007.
- [51] W. J. Jin, M. T. Fernández-Argüelles, J. M. Costa-Fernández, R. Pereiro, and A. Sanz-Medel, "Photoactivated luminescent CdSe quantum dots as sensitive cyanide probes in aqueous solutions," *Chemical Communications*, no. 7, pp. 883–885, 2005.
- [52] S. Rieger, R. P. Kulkarni, D. Darcy, S. E. Fraser, and R. W. Köster, "Quantum dots are powerful multipurpose vital labeling agents in zebrafish embryos," *Developmental Dynamics*, vol. 234, no. 3, pp. 670–681, 2005.
- [53] A. Hoshino, K.-I. Hanaki, K. Suzuki, and K. Yamamoto, "Applications of T-lymphoma labeled with fluorescent quantum dots to cell tracing markers in mouse body," *Biochemical and Biophysical Research Communications*, vol. 314, no. 1, pp. 46–53, 2004.
- [54] E. B. Garon, L. Marcu, Q. Luong, O. Tcherniantchouk, G. M. Crooks, and H. P. Koeffler, "Quantum dot labeling and tracking of human leukemic, bone marrow and cord blood cells," *Leukemia Research*, vol. 31, no. 5, pp. 643–651, 2007.
- [55] N. Manabe, A. Hoshino, Y.-Q. Liang, T. Goto, N. Kato, and K. Yamamoto, "Quantum dot as a drug tracer in vivo," *IEEE Transactions on Nanobioscience*, vol. 5, no. 4, pp. 263–267, 2006.
- [56] F. Pinaud, X. Michalet, L. A. Bentolila, et al., "Advances in fluorescence imaging with quantum dot bio-probes," *Biomaterials*, vol. 27, no. 9, pp. 1679–1687, 2006.
- [57] Y. T. Lim, S. Kim, A. Nakayama, N. E. Stott, M. G. Bawendi, and J. V. Frangioni, "Selection of quantum dot wavelengths for biomedical assays and imaging," *Molecular Imaging*, vol. 2, no. 1, pp. 50–64, 2003.
- [58] X. Gao and S. Nie, "Molecular profiling of single cells and tissue specimens with quantum dots," *Trends in Biotechnology*, vol. 21, no. 9, pp. 371–373, 2003.
- [59] H.-Z. Wang, H.-Y. Wang, R.-Q. Liang, and K.-C. Ruan, "Detection of tumor marker CA125 in ovarian carcinoma using quantum dots," *Acta Biochimica et Biophysica Sinica*, vol. 36, no. 10, pp. 681–686, 2004.
- [60] A. Fu, W. Gu, C. Larabell, and A. P. Alivisatos, "Semiconductor nanocrystals for biological imaging," *Current Opinion in Neurobiology*, vol. 15, no. 5, pp. 568–575, 2005.
- [61] J. H. Warner, A. Hoshino, K. Yamamoto, and R. D. Tilley, "Water-soluble photoluminescent silicon quantum dots," *Angewandte Chemie International Edition*, vol. 44, no. 29, pp. 4550–4554, 2005.
- [62] M. Bäuml, D. Stamou, J.-M. Segura, R. Hovius, and H. Vogel, "Highly fluorescent streptavidin-coated CdSe nanoparticles: preparation in water, characterization, and micropatterning," *Langmuir*, vol. 20, no. 10, pp. 3828–3831, 2004.
- [63] Y. Liu, M. Kim, Y. Wang, Y. A. Wang, and X. Peng, "Highly luminescent, stable and water-soluble CdSe/CdS core-shell dendron nanocrystals with carboxylate anchoring groups," *Langmuir*, vol. 22, no. 14, pp. 6341–6345, 2006.
- [64] C.-L. Wu and Y.-B. Zhao, "CdS quantum dots as fluorescence probes for the sensitive and selective detection of highly reactive HSe<sup>-</sup> ions in aqueous solution," *Analytical & Bioanalytical Chemistry*, vol. 388, no. 3, pp. 717–722, 2007.
- [65] D.-W. Deng, J.-S. Yu, and Y. Pan, "Water-soluble CdSe and CdSe/CdS nanocrystals: a greener synthetic route," *Journal of Colloid and Interface Science*, vol. 299, no. 1, pp. 225–232, 2006.
- [66] J. P. Zimmer, S.-W. Kim, S. Ohnishi, E. Tanaka, J. V. Frangioni, and M. G. Bawendi, "Size series of small indium arsenide-zinc selenide core-shell nanocrystals and their application to in vivo imaging," *Journal of the American Chemical Society*, vol. 128, no. 8, pp. 2526–2527, 2006.
- [67] J. M. Tsay and X. Michalet, "New light on quantum dot cytotoxicity," *Chemistry & Biology*, vol. 12, no. 11, pp. 1159–1161, 2005.
- [68] J. Lovrić, S. J. Cho, F. M. Winnik, and D. Maysinger, "Unmodified cadmium telluride quantum dots induce reactive oxygen species formation leading to multiple organelle damage and cell death," *Chemistry & Biology*, vol. 12, no. 11, pp. 1227–1234, 2005.
- [69] J. Lovrić, H. S. Bazzi, Y. Cuie, G. R. A. Fortin, F. M. Winnik, and D. Maysinger, "Differences in subcellular distribution and toxicity of green and red emitting CdTe quantum dots," *Journal of Molecular Medicine*, vol. 83, no. 5, pp. 377–385, 2005.
- [70] A. Shiohara, A. Hoshino, K. Hanaki, K. Suzuki, and K. Yamamoto, "On the cyto-toxicity caused by quantum dots," *Microbiology and Immunology*, vol. 48, no. 9, pp. 669–675, 2004.
- [71] S. M. Moghimi, A. C. Hunter, and J. C. Murray, "Long-circulating and target-specific nanoparticles: theory to practice," *Pharmacological Reviews*, vol. 53, no. 2, pp. 283–318, 2001.

## Review Article

# Getting Across the Plasma Membrane and Beyond: Intracellular Uses of Colloidal Semiconductor Nanocrystals

Camilla Luccardini,<sup>1</sup> Aleksey Yakovlev,<sup>2</sup> Stéphane Gaillard,<sup>3</sup> Marcel van 't Hoff,<sup>1</sup> Alicia Piera Alberola,<sup>4</sup> Jean-Maurice Mallet,<sup>3</sup> Wolfgang J. Parak,<sup>4</sup> Anne Feltz,<sup>2</sup> and Martin Oheim<sup>1</sup>

<sup>1</sup>INSERM U 603, CNRS UMR 8154, Laboratory of Neurophysiology and New Microscopies, University Paris Descartes, 45 rue des Saints Pères, 75006 Paris, France

<sup>2</sup>ENS-CNRS UMR 8544, Laboratoire de Neurobiologie, Département de Biologie, Ecole Normale Supérieure, 46 rue d'Ulm, 75005 Paris, France

<sup>3</sup>ENS-CNRS UMR 8642, Département de Chimie, Ecole Normale Supérieure, 24 rue Lhomond, 75231 Paris, France

<sup>4</sup>Center for Nanoscience, Ludwig-Maximilians Universität Munich, Amalienstraße 54, 80799 Munich, Germany

Correspondence should be addressed to Martin Oheim, martin.oheim@univ-paris5.fr

Received 13 April 2007; Accepted 12 October 2007

Recommended by Marek Osinski

Semiconductor nanocrystals (NCs) are increasingly being used as photoluminescence markers in biological imaging. Their brightness, large Stokes shift, and high photostability compared to organic fluorophores permit the exploration of biological phenomena at the single-molecule scale with superior temporal resolution and spatial precision. NCs have predominantly been used as extracellular markers for tagging and tracking membrane proteins. Successful internalization and intracellular labelling with NCs have been demonstrated for both fixed immunolabelled and live cells. However, the precise localization and subcellular compartment labelling are less clear. Generally, live cell studies are limited by the requirement of fairly invasive protocols for loading NCs and the relatively large size of NCs compared to the cellular machinery, along with the subsequent sequestration of NCs in endosomal/lysosomal compartments. For long-period observation the potential cytotoxicity of cytoplasmically loaded NCs must be evaluated. This review focuses on the challenges of intracellular uses of NCs.

Copyright © 2007 Camilla Luccardini et al. This is an open access article distributed under the Creative Commons Attribution License, which permits unrestricted use, distribution, and reproduction in any medium, provided the original work is properly cited.

## 1. INTRODUCTION

Semiconductor nanocrystals (NCs) “quantum dots” are increasingly being used in a wide range of biomedical applications, from cell biology to medical diagnostics. They have a core diameter of 2–10 nm and significantly larger hydrodynamic diameter, making them suitable as large yet relatively biocompatible markers, and have remarkable photophysical properties related to quantum confinement effects [1]. Their superior brightness, higher photostability, and narrower spectral emission compared to conventional organic fluorophores have progressively lead biophysicists to adopt them as a new tool for single-molecule imaging, in vitro and in vivo. NCs have become an alternative for organic fluorophores and complementary tool of fluorescent proteins in single-molecule fluorescence and whole-cell labelling assays.

In this review, we focus on the intracellular applications of semiconductor nanocrystals in biological imaging. We first discuss their unique optical properties, we then introduce some considerations on their surface chemistry and we explore in the following sections the different possible strategies to deliver NC inside the cell and to specifically target them to a protein of interest. Finally, we report on recent applications of NCs in whole animal imaging in vivo and address the risk of potential cytotoxicity.

## 2. CHEMICAL AND OPTICAL PROPERTIES

NCs are inorganic particles of 200 to 1000 atoms. NC cores are commonly synthesized from group II-VI (e.g., CdSe, CdS, ZnSe, and CdTe) and III-V (e.g., InAs, InP, and PbS) semiconductor materials. For any energy exceeding the band gap, which depends on the core diameter, absorption of

a photon generates an electron-hole pair, which on recombination results in the emission of a less-energetic photon. Due to their broad absorption spectra, NCs can efficiently be excited with a multitude of laser lines. Variations in the particle composition and size result in different band-gap energies and hence NCs different photoluminescent (PL) emission, ranging from the near UV to the IR (400–1350 nm) [2]. NCs have narrow and symmetric photoluminescence (PL) emission peaks with typical full widths at half maximum (FWHM) of 25–35 nm [3] that facilitate multicolour imaging by allowing efficient single-colour excitation whilst minimizing emission cross-talk [4], see [5] for a critical discussion. Unlike with organic dyes, the PL emission arises from the radiative recombination of an exciton. For NCs, relaxation to the ground state takes  $\sim 10$  nanoseconds, about one order of magnitude longer than singlet-singlet electronic transitions in organic fluorophores. The slow PL decay makes NCs attractive sources for time-gated imaging, which can be used to reduce the relative contribution of cellular autofluorescence to the total collected signal [6]. Figure 1 graphs the evolution of the collected fraction of long-lived NC emission, relative to that of the short-lived autofluorescence for different time gates  $\Delta t$  at a fixed lifetime ratio of 1:10. Larger gates are required to attain the same suppression of background for increasing levels of autofluorescence. For intensity-based detection NCs benefit from their large brightness ( $\epsilon\phi$ ) which results from a 10-to-100 time larger molar extinction coefficients ( $\epsilon \sim 10^5\text{--}10^6 \text{ M}^{-1}\text{cm}^{-1}$ ) than organic dyes [7, 8] at comparable quantum yield  $\phi$ . Finally, due to their significantly higher photostability than organic fluorophores, NCs are attractive for long-period observation (LPO). The resistance to photobleaching results from the deposition of an additional semiconductor shell (e.g., ZnS or CdSe) having a larger band gap than the core. The result is the confinement of the excitons to the core. However, NCs are not completely inert to prolonged illumination. The photophysical properties facilitate LPO at the single-NC level, a particularly interesting property in single-particle tracking (SPT) applications [9], tracing cell lineage [10], and live animal imaging [11], that all combine the demand for imaging small numbers of fluorophores over extended observation periods.

Beyond their established function as molecular markers, NCs are increasingly being used for FRET-based biosensing (see [12] for review). NCs are both a scaffold and central donor for exciting multiple organic acceptor fluorophores in these inorganic/organic hybrid FRET sensors [13–16]. Also, NCs are attractive FRET donors because, through selecting the appropriate size, they can be dialed into almost arbitrary acceptors. The large overlap integrals between donor emission and acceptor absorbance allow for larger FRET efficiencies or transfer over larger donor/acceptor distances. Due to the broad absorption bands and narrow-band emission, one can chose excitation wavelengths minimizing direct acceptor excitation and minimal bleed-through of donor fluorescence into the FRET detection channel.

At the single-NC level, the radiative recombination of the exciton can temporarily be prevented despite ongoing excitation, resulting in intermittent PL emission, known as “blinking” [17]. Blinking results from the stabilization of the exci-

ton at the NC surface and is associated with surface defects. Dark states reduce the duty cycle, complicate the interpretation of intensity-based measurements, and prompt the elaboration of specific algorithms for quantitative SPT [18].

However, blinking can be turned to an advantage in as much as it allows the identification of single NCs and the detection of single-pair FRET (spFRET, Figure 2(a)), as shown on panel (b) between a QD565STV NC donor and an AlexaBiotin organic fluorophore acceptor (Yakovlev, Luccardini, and others’ personal observations). Blinking of neighboring NCs can also be used for ultrahigh resolution studies beyond the classical resolution limit [19] and allows the emission of single particle to be isolated from the crowd. NC detection is not restricted on detecting PL. Their electron density and crystal structure provide sufficient contrast in transmission electron microscopy (EM) [9, 20]. Their use in EM is an additional advantage over labelling samples with conventional dyes that need to be photoconverted or require the addition of electron-dense material to generate contrast on EM images. However, the contrast obtained with NCs is lower than when using Au nanoparticles for immunolabelling.

### 3. NANOCRYSTAL SURFACE CHEMISTRY

Successful cell biological applications of semiconductor NCs had to await the development of reliable protocols for synthesizing water-soluble and colloiddally stable nanoparticles. To be of use in cellular imaging, NCs need to be first rendered water-soluble and nonaggregating and then functionalized to be specifically targeted to a molecule of interest. They should also be stable and ideally have a long shelf life as well as to allow for experiment series under reproducible conditions. The time needed to develop potent solubilization and functionalization strategies justifies the time elapsed after the first proposition of NCs as biological probes [3, 22] and their wider use by the biological community which is only beginning. NCs are synthesised in organic solvents and are subsequently coated with a hydrophobic shell of surfactant trioctyl phosphine oxide (TOPO) to maintain the particles monodispersed in organic solvents. Their water solubility is obtained by capping the NC surface with an additional hydrophilic coating layer. Among the many solubilization strategies that have been designed the most efficient, in terms of colloidal stability and biocompatibility, is at present the amphiphilic polymer coating [23–25]. Particle aggregation can further be reduced through the addition of a polyethylene glycol (PEG) layer, which also minimizes nonspecific interactions [20, 26, 27]. Taken together, the improvements in understanding NC surface chemistry and hence controlling their colloidal properties have prompted an ever increasing number of studies using colloidal semiconductor NCs as PL markers in cell biological applications (see, e.g., [28, 29] for review).

The easier accessibility of extracellular epitopes of cellular membrane antigens readily motivates the increasing number of studies using NCs instead of organic-fluorophore conjugated antibodies as *extracellular* markers in immunofluorescence [9, 30, 31]. Different linkers have been used for functionalizing NCs, including streptavidin [32–34], receptor



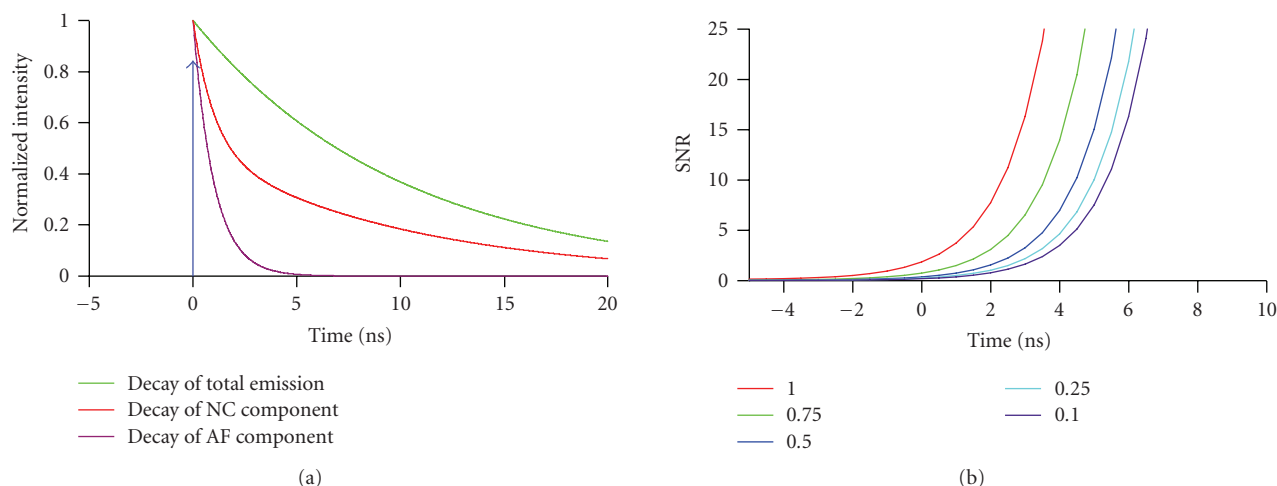


FIGURE 1: Time-gated acquisition of nanocrystal photoluminescence suppresses short-lived autofluorescence, [6]. (a) Schematic representation of the relative timing of the laser pulse (instantaneous, blue), along with the normalized decays of autofluorescence (AF, purple,  $\tau = 1$  nanosecond), NC photoluminescence (NC, green,  $\tau = 10$  nanoseconds), and their sum (red), respectively. (b) Background rejection versus gate time. SNR is the ratio of the integrated signal of the NC divided by the integrated signal of the AF. The numbers/colors represent 5 different ratios  $I_{NC}/I_{AF}$ . To obtain the same SNR at a higher level of AF, a larger time gate is required. The shift in time is relative to the center of a sigmoidal function  $1/(1 + \exp(-T/t))$  that describes detector gating. We assumed a detector on response (10–90%),  $T = 4.4$  nanoseconds. Thus, at  $\Delta t = 0$  detection efficiency is 50%.

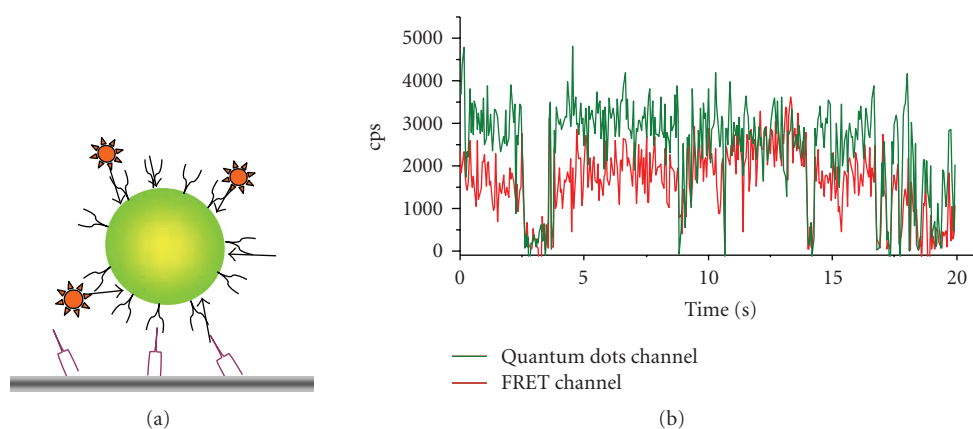


FIGURE 2: Use of blinking to detect single-particle fluorescence resonance energy transfer (spFRET). (a) Schematic representation of the donor/acceptor geometry consisting of a central QD565-ITK/STV donor (green) and biotinylated Alexa594 acceptor (red). NCs were immobilized on glass slides using a biotin-antibody linker. (b) Time-resolved traces of PL intensity simultaneously observed in the donor (D565/20 nm) and FRET channel (D655/40 nm) upon donor 440-nm excitation. The green-emitting NC donor transfers its energy to multiple orange-red fluorescing acceptors. Donor bleed through and acceptor direct excitation are negligible, and contribute less than 0.5% each to the total signal, respectively. Note the concomitant blinking in both channels, indicating no energy transfer when the quantum dot donor is in an OFF state, a hallmark of spFRET [21]. cps = counts per second.

ligands [35, 36], peptides [37], as well as secondary [38] or primary antibodies [39]. The popularity of NCs for studying molecular migration comes, at least in part, from the fact that NCs often offer a viable compromise between the desired stability and the tolerable degree of invasiveness. On the one hand, they are clearly more stable than small organic fluorophores that in turn exert less influence on the bound ligand. On the other hand, over tags offering a comparable long-term stability, such as the much bigger (and hence invasive) fluorescent nanobeads or light-scattering gold particles [40], through their smaller size, so that NCs are less

prone to reduce ligand mobility and access to the binding site.

Despite their obvious advantage for extracellular labelling, four main difficulties are encountered when using NCs for *intracellular* labelling of cytoplasmic constituents in live cells. First, to deliver NCs into the cell, the plasma membrane has to be made transiently permeable for these nanoscale (but in a cellular context yet relatively large) objects, while maintaining the cell intact and viable [41]. Second, as NCs are also unspecifically taken up, probably by a process similar to pinocytosis, any specific uptake has to

dominate over these nonspecific uptake mechanisms to ensure a specific labelling. Pinocytosis occurs in all types of cells, leading to pinosomes which can be bigger than  $1\ \mu\text{m}$  (macropinocytosis). Because their size, macropinosomes provide an efficient route for nonselective endocytosis of solute macromolecules, and hence NCs in solution. Third, once the NCs have penetrated the cell, they must stay monodispersed and reach their molecular target through diffusion or transport. However, nanometric hard particles are frequently recognized as exogenous objects and are engulfed in endo-/lysosomal compartments. Finally, even in the case of a successful cytoplasmic loading, the main obstacle remains the difficulty in addressing NCs to their specific target sites and in removing the unbound NC fraction from the cytoplasm.

#### 4. CROSSING THE PLASMA MEMBRANE

Whole-cell labelling has been demonstrated with biocompatible, but nonfunctionalized (bare) NCs. The addition of NCs to the extracellular medium leads to their spontaneous uptake [28, 42]. Not only specialized macrophages and fibroblasts but also many cells internalize both extracellular particles and fluid via phagocytosis and pinocytosis, respectively. Virtually all cells are able to take up NCs via endocytic mechanisms. This uptake leads to endosomes that are much bigger than the NCs itself (macropinosomes  $>1\ \mu\text{m}$ , clathrin coated pits  $\sim 120\ \text{nm}$ , caveolae  $\sim 60\ \text{nm}$ , and clathrin- and caveolin-independent endocytosis  $\sim 90\ \text{nm}$  [43]). However, these tracks often lead to aggregations of NCs crowded in intracellular compartments (recognized by the absence of blinking). Thus, additional and more specific loading techniques are required for specific NC loading.

Microinjection is a simple tool for loading monodispersed NCs into the cytoplasm [10, 36]. Dubertret and coworkers injected NCs into *Xenopus laevis* oocytes and traced the cell lineage throughout embryonic development. Single-cell electroporation [44] potentially is another technique for loading charged NCs into individual cells, but its efficiency critically depends on the size and charge of NCs (Luccardini and Yakovlev unpublished observations). However, similar to patch clamping or microinjection, it is time-consuming techniques; and more efficient techniques are desirable when the loading of larger cell populations is required.

Bulk electroporation of cell suspensions allows the parallel delivery of NCs into thousands of cells, but has been reported to go along with NC aggregation [36, 45]. This technique probably traps NCs on the plasma membrane where they are endocytosed during the time that is required for the cells to settle on the cover glass before imaging (Luccardini and Yakovlev, personal observations). Thus, the osmotic lysis of pinosomes (Figure 3, upper panel) provides a simple and convenient method to efficiently load monodispersed NCs into many cells simultaneously, under identical conditions. During loading, the cell morphology did not change and plasma membrane integrity and cell viability were not affected through the osmotic shock and inclusion of NCs (Figure 3, lower panel). This technique enabled, for example, the loading of NCs to track single kinesin motors in

live cells [46]. Chemical methods to deliver NCs to the cytoplasm include the use of cationic polymers [36, 45, 47] and cationic lipids [10, 48]. After liposome formation, NCs penetrate the plasma membrane, but accumulation in endosomal compartments is frequently observed [36, 39, 49]. Also, liposome-loaded NCs have been found in late endosomes/lysosomes [50], and in keeping with this observation, tend to concentrate in regions close to the nucleus [10]. Overcoming NC sequestration, encapsulation of NCs in a PEG-grafted polyethylenimine coat has been reported to permit their escape from endosomal compartments [51]. Another possibility for NCs delivery into the cytosol is their conjugation to specific peptide sequences [52, 53], similar to what has been used for the delivery of magnetic nanoparticles [54]. Although this is a particularly interesting and active area of research, and NC translocation to the cytoplasm [55, 56] and specific labelling of intracellular organelles such as mitochondria [36, 57] or the nucleus [36, 45] have been published, the true impact of these studies can only be evaluated with a careful study of the three-dimensional (3-D) intracellular localization of the NCs, for example, combining specific immunostaining and quantitative 3D imaging [35, 58], and careful colocalization analysis [5]. Finally, the conjugation of NCs to membrane-permeable toxins like botulinum toxin should represent an attractive strategy to deliver NC into the cytoplasm, although further work needs to confirm these initial observations.

In summary, while many different strategies of NC loading have been explored and some of them to produce a monodispersed cytoplasmic labelling at least in the cell types studied, the absence of rigorous criteria for successful cytoplasmic loading and the lack of appropriate controls along with the often uncritical and overoptimistic interpretation of intracellular fluorescent puncta make it hard to be directly extrapolated from the published literature on the own experiment. In principle, if NCs are localized in the cytoplasm rather than sequestered in some intracellular compartment, they should be evenly distributed in and randomly diffused throughout the accessible volume; in contrast, many images rather show localized distributions and heterogeneous clusters of different sizes and brightnesses. A definite proof needs SPT and the analysis of single molecule fluorescence. Blinking and consistent diffusion coefficients will clarify if particles are monodispersed and trapped or they can diffuse freely. As yet, it seems safe to say that the uptake and internalization of nanoscale particles into cells has not been completely understood and probably varies both from cell type to cell type. Also, it depends on the surface chemistry of the nanoparticles. Additionally, purification steps could play a crucial role; for example, in determining the concentration of excess ligands in solution.

#### 5. REACHING SPECIFIC INTRACELLULAR TARGETS

Site-specific labelling of intracellular proteins is far more difficult than extracellular target recognition, since the cytoplasm constitutes a crowded molecular environment, containing a plethora of proteins, nucleic acids, and other molecules. So as to achieve specificity in intracellular

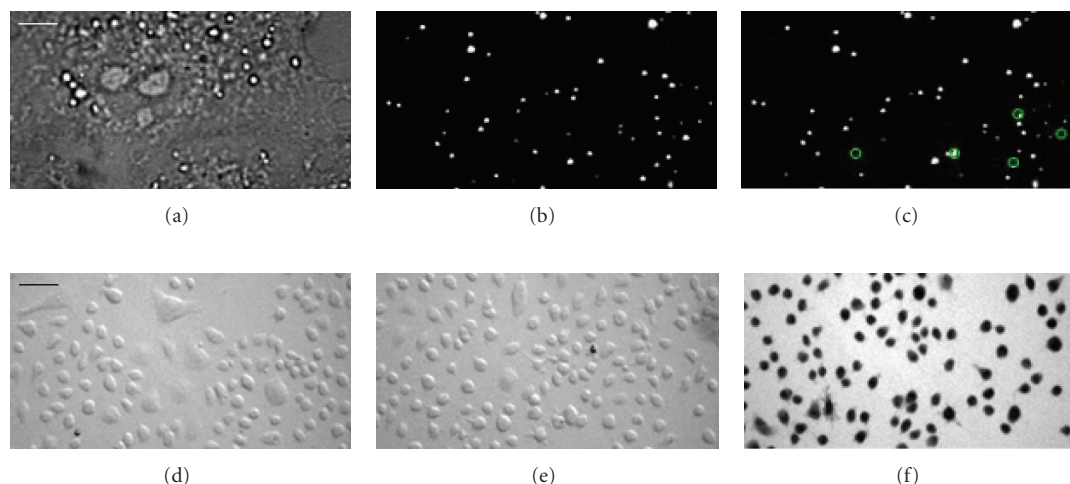


FIGURE 3: Evaluation of cytoplasmic nanoparticle loading in live cells by osmotic lysis of pinosomes. COS-7 cells were incubated in hypertonic solution (10 minutes, 37°C, Invitrogen I-14402) for pinocytic loading of QD565ITK nanocrystals (NCs, Quantum dot corporation). Shifting to hypotonic culture medium caused the osmotic lysis of the internalized pinosomes and release of NCs into the cytoplasm. (a) Bright-field image at  $\times 100$  magnification. Scale bar for (a) to (c): 4  $\mu\text{m}$ . (b)–(c) Epifluorescence images from a time-resolved image stack of the same cell. Green circles identify individual NCs that intermittently changed from ON to OFF state (blinking) between frame 250 (b) and 253 (c). Cell viability following loading was tested using the trypan blue exclusion assay at low magnification,  $\times 10$ . Osmotic shock without (d) and with 1 nM QD565ITK nanocrystals in the extracellular fluid (e) did not compromise cell viability. (f) In contrast, adding ethanol reliably killed cells as reported by the dark trypan blue labelling. Scale bar for (d) to (f): 40  $\mu\text{m}$ .

targeting, tagging strategies rely on specific target recognition (reviewed in [12, 59]). Another requirement for LPO imaging is that the chemical bond linking the cytoplasmic target and the label chosen for its detection is stable over the experiment time.

It is in response to this need that the Tsien laboratory (University of California, Calif, USA) introduced genetically encoded fluorescent proteins in cell biology (reviewed in [60]). An alternative strategy uses self-labelling protein tags. The introduction of a small protein tag or of a unique combination of amino acids on the target protein allows their interaction with a specific fluorophore-bearing substrate, here an NC. Examples of self-labelling protein tags are biarsenical compounds [61, 62], SNAP tag [63], and Halo tag [64]. These approaches are helpful for developing new NC functionalization strategies for specific intracellular targeting.

## 6. WHOLE ANIMAL IMAGING, IN VIVO

Compared with applications to subcellular imaging in cell biology, NC-based whole-animal imaging has developed very fast [65]. Due to their long-wavelength emission, brightness, and long-term photostability, NCs are ideal probes for sensitive in vivo imaging in deep tissues of small animals or imaging superficial tissue layers of larger species [11]. The possibility of synthesizing NCs emitting in the infrared wavelengths minimizes scattering, optimizes depth penetration and allows discrimination against collagen autofluorescence and thus should permit ultra-deep imaging of “optically thick” tissue [66, 67], provided that cytotoxicity is not an issue (see Section 7).

One of the first live-animal applications of NCs was the selective labelling of tumor vasculature in mice by using PEGylated NCs coated with specific peptidic sequences against vascular markers. In 2002 Åkerman et al. [26] showed in histological staining that after intravenous NC injection, functionalized NCs can be addressed to specific blood vessels. A high level of PEG substitution on top of the functionalization of the NCs reduced their uptake into the endothelial reticulum. One year later, Larson et al. were able to image by multiphoton microscopy NCs through the skin of live mice, in capillaries embedded 100  $\mu\text{m}$  in tissue [4]. Ballou et al. demonstrated the importance of long-chain PEG (5 kDa) coating for increasing the duration of NCs circulating in the blood flow of mice [20]. They were able to detect NCs by noninvasive whole body fluorescent imaging, up to four months after injection. The same report also showed that NCs deposit in liver, skin, and bone marrow in a surface-coating dependent manner and that polymer- and PEG-coated (up to 3,400 Da MW) NCs are cleared from the blood after injection. Gao et al. developed polymer-coated NCs functionalized with a monoclonal antibody directed against prostate cancer cells as a cell-specific marker [68]. After NC injection in mice, transplanted with human cancer prostate cells, they succeeded in specifically detecting and imaging the tumor site. However, as their NCs emitted in the visible spectrum, the authors used spectral unmixing algorithms to detect the NC signal in the presence of autofluorescence. Along these lines, Kim et al. [11] intradermally injected near-infrared-emitting NCs in mice and pigs and imaged sentinel lymph nodes (SNL) one cm deep in tissue. This work enables for the first time SNL mapping and cancer surgery under image guidance. Metastatic tumor cell extravasations

were monitored in mice by intravenous injection of cells labelled with NC, which were examined by fluorescence emission spectroscopy [47]. More recently, Stroh et al. combined NCs and multiphoton intravital microscopy to distinguish in mice tumor vessels from perivascular cells and extracellular matrix [48]. With this approach, they also investigated the ability of NC-loaded silica beads (100–500 nm diameter) to access the tumor and monitored the trafficking of the precursor cells, a promising technique for cancer prevention and treatment.

So et al. designed recently “self-illuminating” NC conjugates permitting in vivo imaging without an external light source; instead, luciferase on the NC surface transfers its excitation to the NC core in a Bioluminescence resonance energy transfer (BRET) assay [69]. Intramuscular or subcutaneous injection in mice of 5 pmol of polymer-coated NCs conjugated to the *Renilla reniformis* luciferase was enough to image a BRET emanating from 3 mm depth tissue, after coelenterazine injection for activation. We note that this study is one of the few applications that used NCs as acceptors rather than donors.

## 7. CYTOTOXICITY

As NCs are increasingly being used as biological photoluminescent probes, in both acute cell assays and chronic, in the entire animal, in vivo, it is important to evaluate if they represent a specific risk of toxicity for the organism under study.

Although probably not classically termed cytotoxicity in a strict sense, one obvious problem resulting from the nanoscopic size of nanoparticles is that NCs can directly affect the biological system under study by impairing the mobility, interaction, binding, or other biological action of the ligand molecule to which they are attached. Hence, any study using NC-conjugated biomolecules must exclude the inhibition of the enzyme, receptor, motor, or other by the NC.

Concerns against the use of semiconductor NCs for cell biological applications go well beyond arguments of steric hindrance. It is well known that  $\text{Cd}^{2+}$  can be released from the CdSe core after oxydative attack (corrosion) [70]. Bare CdSe NCs are particularly harmful in this regard [36, 71], limiting their utility for direct-injection strategies. Additional shells (ZnS) and capping (silanization) can reduce  $\text{Cd}^{2+}$  leakage, and further purification steps can remove already released  $\text{Cd}^{2+}$  [71–73]. In our hands, a supplementary purification step prior to loading NC reduces the toxic action of NCs [74], as measured by a resazurin or cell adhesion assay (Figure 4). Nevertheless, it is important to bear in mind that despite sporadic claims of nanoparticles being indiscriminately harmless [57], there is a general consensus that NC are toxic and that their toxicity depends on their concentration, precise chemical composition, the particle size, colloidal stability, as well as solubilization and functionalization groups. Also, CdSe particles are generally more toxic inside the cell than extracellularly, in line with the known action of  $\text{Cd}^{2+}$  by inhibiting protein synthesis, carbohydrate metabolism and—with time—by its accumulation in kidney and liver [75]. At the same time, the undisputable cytotoxic action of Cd nanoparticles has not precluded acute staining

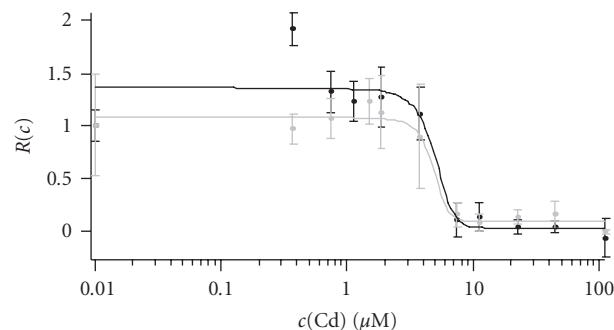


FIGURE 4: Experimental evaluation of cytotoxicity of polymer-coated CdSe nanoparticles. Toxicity to NIH-3T3 fibroblasts of a NC-containing solution was estimated after 48-hour application. Dose-response curve for cell viability was measured with a Resazurin assay [74]. Resazurin is a nonfluorescent dye that is metabolized in functional mitochondria and converted into resorufin which fluoresces red. Black and grey curves show two experiments ( $n = 8$  measurements each). Normalized survival  $R(c)$  after application of a  $\text{Cd}^{2+}$  concentration  $c(\text{Cd})$  was estimated from the change in absorbance of the converted dye measured at 600 nm. Changes in  $R$  became significant at  $c(\text{Cd})$  around 3–5  $\mu\text{M}$ , whereby  $c(\text{Cd})$  refers to the concentration of  $\text{Cd}^{2+}$  on the surface of the CdSe nanoparticles, which accounts for the different toxicity of different-size NCs. This concentration of  $\text{Cd}^{2+}$  corresponds to a concentration of CdSe nanoparticles of 50–70 nm. Similar data was obtained with a cell adhesion assay [71] (not shown). In contrast for free cobalt ions ( $\text{Co}^{2+}$ ), cytotoxic effects became significant at around 50  $\mu\text{M}$  (data not shown).

experiments of cells, because the concentration of NCs can be always kept low enough to prevent immediate cytotoxic damage within the experimental time window, but still high enough for enough fluorescence [4, 20, 39, 45, 47, 50]. However, because of the ligand desorption over time, a simple ligand exchange functionalization is not effective to durably prevent intracellular NC degradation. Since as much as NCs are intrinsically colloiddally unstable and cytotoxic for cells [76], the specific kind of coating is essential for at least retarding the cytotoxic effect [29, 36, 73]. PEG coating can reduce the unspecific uptake of NCs, it reduces their toxic effect for extracellular application at the same initial concentration [29, 71].

For biomedical applications as well as chronic animal experiments, the major healthcare concern of NC labelling is related to the leakage of  $\text{Cd}^{2+}$  into the organism, even at low dose. Extracellular application of CdSe particles already presents a cytotoxic risk because  $\text{Cd}^{2+}$  does not only block  $\text{Ca}^{2+}$  ion channels (like  $\text{Co}^{2+}$  as well, which is released from magnetic NCs) but also it permeates through the channel and enters the cytoplasm. We note that the absence of a visible effect, often based on the detection of cell morphology changes and cell viability assays does not exclude a cumulative poisoning of the organism which first impairs the metabolism of the cells, without being immediately noxious. Interestingly, a similar debate has long haunted the evaluation of nonlinear photodamage caused by two-photon fluorescence excitation, where the introduction of rigorous



physiologically relevant criteria based on microscopic observables like the kinetics of  $\text{Ca}^{2+}$  transients [77, 78] has ended the futile discussion.

In conclusion, more work is needed to critically evaluate the cytotoxicity of NCs, both upon short- and long-term exposure. To better understand the deleterious action of different NCs on the organism under study, standardized samples, experimental conditions, cells, and assays would be a great leap forward and pave the ground for biomedical applications that would additionally benefit from a tight collaboration with toxicologists.

## 8. CONCLUSIONS

In this review, we focus on nanocrystal applications in vivo, both in cell biology and medical diagnostics, and on the potential toxicity of NCs for biological imaging. The advances in understanding NC colloidal properties together with the ability of developing stable surface chemistries has brought about a large choice of functionalization strategies which now offer to biologists a versatile tool kit for many applications that rely on fluorescence and electron microscopy. The main advantages of NCs over conventional organic fluorophores are the possibility to detect easily single molecules, mostly derived from their superior brightness and the long-term photostability; the spectral tunability and narrow-band emission; and, going along with these, the ease of NC use in multicolour fluorescence. However, nanoparticles are not a cure-all. Particularly Cd-based NCs are potentially cytotoxic, and the modulation of their optical properties (e.g., their intrinsic fluorescence intermittency) through their local chemical environment (see, e.g., [79]) needs to be considered in each application.

## ACKNOWLEDGMENTS

Work in laboratories related to this article was partially funded by the French Ministry of Research and Technology (Action Concertée Incitative (ACI) Nanosciences), by the GIP-ANR Nanoscience Program (PRA-PNANO-051 "NanoFRET"), and the European Union (NanoInteract to W. J. Parak). C. Luccardini initially recipient of a postdoctoral research fellowship financed by the European Union. (Long-Period Observation of Single Biomolecules by Novel Non-Invasive Fluorescence Lifetime Imaging Nanoscopy (FLIN), STRP NMP4-CT-2004-013880 to M. Oheim) is now a Fondation pour la Recherche Médicale (FRM) fellow and A. Yakovlev is a postdoctoral fellow of the Centre National de la Recherche (CNRS to A. Feltz). S. Gaillard acknowledges support from the GIP-ANR. Marcel van 't Hoff's work is financed by a Marie-Curie Research-training Grant (From FLIM to FLIN, FP6-2005-019481 to M. Oheim). C. Luccardini, A. Yakovlev, S. Gaillard, J.-M. Mallet, W. J. Parak, A. Feltz, and M. Oheim are members of the "NanoFRET" consortium, supported by the Groupement d'Intérêt Publique-Agence Nationale de la Recherche, Programme Nanosciences et Nanotechnologies (GIP-ANR PNANO).

## REFERENCES

- [1] P. Alivisatos, "Colloidal quantum dots. From scaling laws to biological applications," *Pure and Applied Chemistry*, vol. 72, no. 1-2, pp. 3-9, 2000.
- [2] S. Kim, B. Fisher, H.-J. Eisler, and M. Bawendi, "Type-II quantum dots: CdTe/CdSe(core/shell) and CdSe/ZnTe(core/shell) heterostructures," *Journal of the American Chemical Society*, vol. 125, no. 38, pp. 11466-11467, 2003.
- [3] W. C. W. Chan and S. Nie, "Quantum dot bioconjugates for ultrasensitive nonisotopic detection," *Science*, vol. 281, no. 5385, pp. 2016-2018, 1998.
- [4] D. R. Larson, W. R. Zipfel, R. M. Williams, et al., "Water-soluble quantum dots for multiphoton fluorescence imaging in vivo," *Science*, vol. 300, no. 5624, pp. 1434-1436, 2003.
- [5] M. Oheim and D. Li, "Quantitative co-localisation imaging: concepts, measurements, and pitfalls," in *Imaging Cellular and Molecular Biological Function*, F. Frischknecht, J. Pawley, and S. Shorte, Eds., pp. 115-153, Springer, Berlin, Germany, 2007.
- [6] M. Dahan, T. Laurence, F. Pinaud, et al., "Time-gated biological imaging by use of colloidal quantum dots," *Optics Letters*, vol. 26, no. 11, pp. 825-827, 2001.
- [7] W. C. W. Chan, D. J. Maxwell, X. Gao, R. E. Bailey, M. Han, and S. Nie, "Luminescent quantum dots for multiplexed biological detection and imaging," *Current Opinion in Biotechnology*, vol. 13, no. 1, pp. 40-46, 2002.
- [8] W. W. Yu, L. Qu, W. Guo, and X. Peng, "Experimental determination of the extinction coefficient of CdTe, CdSe, and CdS nanocrystals," *Chemistry of Materials*, vol. 15, no. 14, pp. 2854-2860, 2003.
- [9] M. Dahan, S. Lèvi, C. Luccardini, P. Rostaing, B. Riveau, and A. Triller, "Diffusion dynamics of glycine receptors revealed by single-quantum dot tracking," *Science*, vol. 302, no. 5644, pp. 442-445, 2003.
- [10] B. Dubertret, P. Skourides, D. J. Norris, V. Noireaux, A. H. Brivanlou, and A. Libchaber, "In vivo imaging of quantum dots encapsulated in phospholipid micelles," *Science*, vol. 298, no. 5599, pp. 1759-1762, 2002.
- [11] S. Kim, Y. T. Lim, E. G. Soltesz, et al., "Near-infrared fluorescent type II quantum dots for sentinel lymph node mapping," *Nature Biotechnology*, vol. 22, no. 1, pp. 93-97, 2004.
- [12] K. E. Sapsford, L. Berti, and I. L. Medintz, "Materials for fluorescence resonance energy transfer analysis: beyond traditional donor-acceptor combinations," *Angewandte Chemie International Edition*, vol. 45, no. 28, pp. 4562-4589, 2006.
- [13] A. R. Clapp, I. L. Medintz, J. M. Mauro, B. R. Fisher, M. G. Bawendi, and H. Mattoussi, "Fluorescence resonance energy transfer between quantum dot donors and dye-labeled protein acceptors," *Journal of the American Chemical Society*, vol. 126, no. 1, pp. 301-310, 2004.
- [14] A. R. Clapp, I. L. Medintz, H. Tetsuo Uyeda, et al., "Quantum dot-based multiplexed fluorescence resonance energy transfer," *Journal of the American Chemical Society*, vol. 127, no. 51, pp. 18212-18221, 2005.
- [15] I. L. Medintz, A. R. Clapp, F. M. Brunel, et al., "Proteolytic activity monitored by fluorescence resonance energy transfer through quantum-dot-peptide conjugates," *Nature Materials*, vol. 5, no. 7, pp. 581-589, 2006.
- [16] I. L. Medintz, J. H. Konnert, A. R. Clapp, et al., "A fluorescence resonance energy transfer-derived structure of a quantum dot-protein bioconjugate nanoassembly," *Proceedings of the National Academy of Sciences of the United States of America*, vol. 101, no. 26, pp. 9612-9617, 2004.

- [17] M. Nirmal, B. O. Dabbousi, M. G. Bawendi, et al., "Fluorescence intermittency in single cadmium selenide nanocrystals," *Nature*, vol. 383, no. 6603, pp. 802–804, 1996.
- [18] S. Bonneau, M. Dahan, and L. D. Cohen, "Single quantum dot tracking based on perceptual grouping using minimal paths in a spatiotemporal volume," *IEEE Transactions on Image Processing*, vol. 14, no. 9, pp. 1384–1395, 2005.
- [19] M. P. Gordon, T. Ha, and P. R. Selvin, "Single-molecule high-resolution imaging with photobleaching," *Proceedings of the National Academy of Sciences of the United States of America*, vol. 101, no. 17, pp. 6462–6465, 2004.
- [20] B. Ballou, B. C. Lagerholm, L. A. Ernst, M. P. Bruchez, and A. S. Waggoner, "Noninvasive imaging of quantum dots in mice," *Bioconjugate Chemistry*, vol. 15, no. 1, pp. 79–86, 2004.
- [21] M. T. Fernández-Argüelles, A. Yakovlev, R. A. Sperling, et al., "Synthesis and characterization of polymer-coated quantum dots with integrated acceptor dyes as FRET-based nanoprobe," *Nano Letters*, vol. 7, no. 9, pp. 2613–2617, 2007.
- [22] M. Bruchez Jr., M. Moronne, P. Gin, S. Weiss, and A. P. Alivisatos, "Semiconductor nanocrystals as fluorescent biological labels," *Science*, vol. 281, no. 5385, pp. 2013–2016, 1998.
- [23] X. Gao, L. W. Chung, and S. Nie, "Quantum dots for in vivo molecular and cellular imaging," *Methods in Molecular Biology*, vol. 374, pp. 135–146, 2007.
- [24] T. Pellegrino, W. J. Parak, R. Boudreau, et al., "Quantum dot-based cell motility assay," *Differentiation*, vol. 71, no. 9–10, pp. 542–548, 2003.
- [25] C. Luccardini, C. Tribet, F. Vial, V. Marchi-Artzner, and M. Dahan, "Size, charge, and interactions with giant lipid vesicles of quantum dots coated with an amphiphilic macromolecule," *Langmuir*, vol. 22, no. 5, pp. 2304–2310, 2006.
- [26] M. E. Åkerman, W. C. W. Chan, P. Laakkonen, S. N. Bhatia, and E. Ruoslahti, "Nanocrystal targeting in vivo," *Proceedings of the National Academy of Sciences of the United States of America*, vol. 99, no. 20, pp. 12617–12621, 2002.
- [27] R. A. Sperling, T. Pellegrino, J. K. Li, W. H. Chang, and W. J. Parak, "Electrophoretic separation of nanoparticles with a discrete number of functional groups," *Advanced Functional Materials*, vol. 16, no. 7, pp. 943–948, 2006.
- [28] W. J. Parak, T. Pellegrino, and C. Plank, "Labelling of cells with quantum dots," *Nanotechnology*, vol. 16, no. 2, pp. R9–R25, 2005.
- [29] E. Chang, N. Thekkekk, W. W. Yu, V. L. Colvin, and R. Drezek, "Evaluation of quantum dot cytotoxicity based on intracellular uptake," *Small*, vol. 2, no. 12, pp. 1412–1417, 2006.
- [30] S. J. Rosenthal, I. Tomlinson, E. M. Adkins, et al., "Targeting cell surface receptors with ligand-conjugated nanocrystals," *Journal of the American Chemical Society*, vol. 124, no. 17, pp. 4586–4594, 2002.
- [31] M. Howarth, K. Takao, Y. Hayashi, and A. Y. Ting, "Targeting quantum dots to surface proteins in living cells with biotin ligase," *Proceedings of the National Academy of Sciences of the United States of America*, vol. 102, no. 21, pp. 7583–7588, 2005.
- [32] X. Wu, H. Liu, J. Liu, et al., "Immunofluorescent labeling of cancer marker Her2 and other cellular targets with semiconductor quantum dots," *Nature Biotechnology*, vol. 21, no. 1, pp. 41–46, 2003.
- [33] C. Bouzigues, S. Levi, A. Triller, and M. Dahan, "Single quantum dot tracking of membrane receptors," *Methods in Molecular Biology*, vol. 374, pp. 81–92, 2007.
- [34] D. S. Lidke, P. Nagy, T. M. Jovin, and D. J. Arndt-Jovin, "Biotin-ligand complexes with streptavidin quantum dots for in vivo cell labeling of membrane receptors," *Methods in Molecular Biology*, vol. 374, pp. 69–80, 2007.
- [35] D. S. Lidke, P. Nagy, R. Heintzmann, et al., "Quantum dot ligands provide new insights into erbB/HER receptor-mediated signal transduction," *Nature Biotechnology*, vol. 22, no. 2, pp. 198–203, 2004.
- [36] A. M. Delfus, W. C. W. Chan, and S. N. Bhatia, "Probing the cytotoxicity of semiconductor quantum dots," *Nano Letters*, vol. 4, no. 1, pp. 11–18, 2004.
- [37] F. Pinaud, D. King, H.-P. Moore, and S. Weiss, "Bioactivation and cell targeting of semiconductor CdSe/ZnS nanocrystals with phytochelatin-related peptides," *Journal of the American Chemical Society*, vol. 126, no. 19, pp. 6115–6123, 2004.
- [38] M.-V. Ehrensperger, C. Hanus, C. Vannier, A. Triller, and M. Dahan, "Multiple association states between glycine receptors and gephyrin identified by SPT analysis," *Biophysical Journal*, vol. 92, no. 10, pp. 3706–3718, 2007.
- [39] J. K. Jaiswal, H. Mattoussi, J. M. Mauro, and S. M. Simon, "Long-term multiple color imaging of live cells using quantum dot bioconjugates," *Nature Biotechnology*, vol. 21, no. 1, pp. 47–51, 2003.
- [40] L. Cognet, C. Tardin, D. Boyer, D. Choquet, P. Tamarat, and B. Lounis, "Single metallic nanoparticle imaging for protein detection in cells," *Proceedings of the National Academy of Sciences of the United States of America*, vol. 100, no. 20, pp. 11350–11355, 2003.
- [41] B. D. Chithrani, A. A. Ghazani, and W. C. W. Chan, "Determining the size and shape dependence of gold nanoparticle uptake into mammalian cells," *Nano Letters*, vol. 6, no. 4, pp. 662–668, 2006.
- [42] J. K. Jaiswal, E. R. Goldman, H. Mattoussi, and S. M. Simon, "Use of quantum dots for live cell imaging," *Nature Methods*, vol. 1, no. 1, pp. 73–78, 2004.
- [43] R. G. Parton and K. Simons, "The multiple faces of caveolae," *Nature Reviews Molecular Cell Biology*, vol. 8, no. 3, pp. 185–194, 2007.
- [44] J. Rathenber, T. Nevian, and V. Witzemann, "High-efficiency transfection of individual neurons using modified electrophysiology techniques," *Journal of Neuroscience Methods*, vol. 126, no. 1, pp. 91–98, 2003.
- [45] F. Chen and D. Gerion, "Fluorescent CdSe/ZnS nanocrystal-peptide conjugates for long-term, nontoxic imaging and nuclear targeting in living cells," *Nano Letters*, vol. 4, no. 10, pp. 1827–1832, 2004.
- [46] S. Courty, C. Luccardini, Y. Bellaiche, G. Cappello, and M. Dahan, "Tracking individual kinesin motors in living cells using single quantum-dot imaging," *Nano Letters*, vol. 6, no. 7, pp. 1491–1495, 2006.
- [47] E. B. Voura, J. K. Jaiswal, H. Mattoussi, and S. M. Simon, "Tracking metastatic tumor cell extravasation with quantum dot nanocrystals and fluorescence emission-scanning microscopy," *Nature Medicine*, vol. 10, no. 9, pp. 993–998, 2004.
- [48] M. Stroh, J. P. Zimmer, D. G. Duda, et al., "Quantum dots spectrally distinguish multiple species within the tumor milieu in vivo," *Nature Medicine*, vol. 11, no. 6, pp. 678–682, 2005.
- [49] W. J. Parak, R. Boudreau, M. Le Gros, et al., "Cell motility and metastatic potential studies based on quantum dot imaging of phagokinetic tracks," *Advanced Materials*, vol. 14, no. 12, pp. 882–885, 2002.
- [50] K.-I. Hanaki, A. Momo, T. Oku, et al., "Semiconductor quantum dot/albumin complex is a long-life and highly photo-stable endosome marker," *Biochemical and Biophysical Research Communications*, vol. 302, no. 3, pp. 496–501, 2003.
- [51] H. Duan and S. Nie, "Cell-penetrating quantum dots based on multivalent and endosome-disrupting surface coatings,"

- Journal of the American Chemical Society*, vol. 129, no. 11, pp. 3333–3338, 2007.
- [52] B. C. Lagerholm, “Peptide-mediated intracellular delivery of quantum dots,” *Methods in Molecular Biology*, vol. 374, pp. 105–112, 2007.
- [53] G. Iyer, F. Pinaud, J. Tsay, et al., “Peptide coated quantum dots for biological applications,” *IEEE Transactions on Nanobiotechnology*, vol. 5, no. 4, pp. 231–238, 2006.
- [54] M. Lewin, N. Carlesso, C.-H. Tung, et al., “Tat peptide-derivatized magnetic nanoparticles allow in vivo tracking and recovery of progenitor cells,” *Nature Biotechnology*, vol. 18, no. 4, pp. 410–414, 2000.
- [55] L. C. Mattheakis, J. M. Dias, Y.-J. Choi, et al., “Optical coding of mammalian cells using semiconductor quantum dots,” *Analytical Biochemistry*, vol. 327, no. 2, pp. 200–208, 2004.
- [56] J. B. Delehanty, I. L. Medintz, T. Pons, F. M. Brunel, P. E. Dawson, and H. Mattoussi, “Self-assembled quantum dot-peptide bioconjugates for selective intracellular delivery,” *Bioconjugate Chemistry*, vol. 17, no. 4, pp. 920–927, 2006.
- [57] A. Hoshino, K. Fujioka, T. Oku, et al., “Physicochemical properties and cellular toxicity of nanocrystal quantum dots depend on their surface modification,” *Nano Letters*, vol. 4, no. 11, pp. 2163–2169, 2004.
- [58] W. R. J. Funnell and D. Maysinger, “Three-dimensional reconstruction of cell nuclei, internalized quantum dots and sites of lipid peroxidation,” *Journal of Nanobiotechnology*, vol. 4, pp. 1–10, 2006.
- [59] I. Chen and A. Y. Ting, “Site-specific labeling of proteins with small molecules in live cells,” *Current Opinion in Biotechnology*, vol. 16, no. 1, pp. 35–40, 2005.
- [60] J. Lippincott-Schwartz and G. H. Patterson, “Development and use of fluorescent protein markers in living cells,” *Science*, vol. 300, no. 5616, pp. 87–91, 2003.
- [61] B. A. Griffin, S. R. Adams, and R. Y. Tsien, “Specific covalent labeling of recombinant protein molecules inside live cells,” *Science*, vol. 281, no. 5374, pp. 269–272, 1998.
- [62] S. R. Adams, R. E. Campbell, L. A. Gross, et al., “New biarsenical ligands and tetracysteine motifs for protein labeling in vitro and in vivo: synthesis and biological applications,” *Journal of the American Chemical Society*, vol. 124, no. 21, pp. 6063–6076, 2002.
- [63] A. Keppler, S. Gendreizig, T. Gronemeyer, H. Pick, H. Vogel, and K. Johnsson, “A general method for the covalent labeling of fusion proteins with small molecules in vivo,” *Nature Biotechnology*, vol. 21, no. 1, pp. 86–89, 2003.
- [64] Y. Zhang, M.-K. So, A. M. Loening, H. Yao, S. S. Gambhir, and J. Rao, “HaloTag protein-mediated site-specific conjugation of bioluminescent proteins to quantum dots,” *Angewandte Chemie International Edition*, vol. 45, no. 30, pp. 4936–4940, 2006.
- [65] H. C. Fischer, L. Liu, K. S. Pang, and W. C. W. Chan, “Pharmacokinetics of nanoscale quantum dots: in vivo distribution, sequestration, and clearance in the rat,” *Advanced Functional Materials*, vol. 16, no. 10, pp. 1299–1305, 2006.
- [66] M. Oheim, E. Beaurepaire, E. Chaigneau, J. Mertz, and S. Charpak, “Two-photon microscopy in brain tissue: parameters influencing the imaging depth,” *Journal of Neuroscience Methods*, vol. 111, no. 1, pp. 29–37, 2001.
- [67] P. Theer and W. Denk, “On the fundamental imaging-depth limit in two-photon microscopy,” *Journal of the Optical Society of America A*, vol. 23, no. 12, pp. 3139–3149, 2006.
- [68] X. Gao, Y. Cui, R. M. Levenson, L. W. Chung, and S. Nie, “In vivo cancer targeting and imaging with semiconductor quantum dots,” *Nature Biotechnology*, vol. 22, no. 8, pp. 969–976, 2004.
- [69] M.-K. So, C. Xu, A. M. Loening, S. S. Gambhir, and J. Rao, “Self-illuminating quantum dot conjugates for in vivo imaging,” *Nature Biotechnology*, vol. 24, no. 3, pp. 339–343, 2006.
- [70] N. Zaitseva, L. Manna, F. Leon, D. Gerion, and C. Saw, “Precipitation of se crystals from solutions of CdSe nanocrystals,” *Advanced Materials*, vol. 17, pp. 1321–1324, 2005.
- [71] C. Kirchner, T. Liedl, S. Kudera, et al., “Cytotoxicity of colloidal CdSe and CdSe/ZnS nanoparticles,” *Nano Letters*, vol. 5, no. 2, pp. 331–338, 2005.
- [72] S. T. Selvan, T. T. Tan, and J. Y. Ying, “Robust, non-cytotoxic, silica-coated CdSe quantum dots with efficient photoluminescence,” *Advanced Materials*, vol. 17, no. 13, pp. 1620–1625, 2005.
- [73] T. Zhang, J. L. Stilwell, D. Gerion, et al., “Cellular effect of high doses of silica-coated quantum dot profiled with high throughput gene expression analysis and high content cellomics measurements,” *Nano Letters*, vol. 6, no. 4, pp. 800–808, 2006.
- [74] J. O’Brien, I. Wilson, T. Orton, and F. Pognan, “Investigation of the alamar blue (resazurin) fluorescent dye for the assessment of mammalian cell cytotoxicity,” *European Journal of Biochemistry*, vol. 267, no. 17, pp. 5421–5426, 2000.
- [75] R. Nath, R. Prasad, V. K. Palinal, and R. K. Chopra, “Molecular basis of cadmium toxicity,” *Progress in Food and Nutrition Science*, vol. 8, no. 1–2, pp. 109–163, 1984.
- [76] J. Lovrić, H. S. Bazzi, Y. Cuie, G. R. A. Fortin, F. M. Winnik, and D. Maysinger, “Differences in subcellular distribution and toxicity of green and red emitting CdTe quantum dots,” *Journal of Molecular Medicine*, vol. 83, no. 5, pp. 377–385, 2005.
- [77] H. J. Koester, D. Baur, R. Uhl, and S. W. Hell, “Ca<sup>2+</sup> fluorescence imaging with pico- and femtosecond two-photon excitation: signal and photodamage,” *Biophysical Journal*, vol. 77, no. 4, pp. 2226–2236, 1999.
- [78] A. Hopt and E. Neher, “Highly nonlinear photodamage in two-photon fluorescence microscopy,” *Biophysical Journal*, vol. 80, no. 4, pp. 2029–2036, 2001.
- [79] S. Hohng and T. Ha, “Near-complete suppression of quantum dot blinking in ambient conditions,” *Journal of the American Chemical Society*, vol. 126, no. 5, pp. 1324–1325, 2004.



## Research Article

# Blue-Emitting Small Silica Particles Incorporating ZnSe-Based Nanocrystals Prepared by Reverse Micelle Method

Masanori Ando, Chunliang Li, Ping Yang, and Norio Murase

*Photonics Research Institute, National Institute of Advanced Industrial Science and Technology (AIST), Kansai Center, 1-8-31 Midorigaoka, Ikeda 563-8577, Osaka, Japan*

Correspondence should be addressed to Norio Murase, n-murase@aist.go.jp

Received 16 May 2007; Revised 17 December 2007; Accepted 24 December 2007

Recommended by Marek Osinski

ZnSe-based nanocrystals (ca. 4–5 nm in diameter) emitting in blue region (ca. 445 nm) were incorporated in spherical small silica particles (20–40 nm in diameter) by a reverse micelle method. During the preparation, alkaline solution was used to deposit the hydrolyzed alkoxide on the surface of nanocrystals. It was crucially important for this solution to include  $\text{Zn}^{2+}$  ions and surfactant molecules (thioglycolic acid) to preserve the spectral properties of the final silica particles. This is because these substances in the solution prevent the surface of nanocrystals from deterioration by dissolution during processing. The resultant silica particles have an emission efficiency of 16% with maintaining the photoluminescent spectral width and peak wavelength of the initial colloidal solution.

Copyright © 2007 Masanori Ando et al. This is an open access article distributed under the Creative Commons Attribution License, which permits unrestricted use, distribution, and reproduction in any medium, provided the original work is properly cited.

## 1. INTRODUCTION

Development of bright and stable phosphors is increasingly required in many fields. The II–VI semiconductor nanocrystals (NCs) such as ZnSe and CdTe attract much interest as novel bright phosphors with tunable photoluminescence (PL) wavelength [1] for possible uses including biological labeling [2–6], display, and lighting devices [7–9]. For biological labeling, fluorophores are bound to biological molecules as fluorescent markers. It is possible to monitor the position and movement of virus and various materials by the PL of fluorophores. So far, organic fluorescent dyes were widely used for such biomarkers [2, 10]. However, the emission wavelengths of these dyes are normally close to the excitation wavelengths, and therefore different excitation wavelengths are required for getting multiple colors. Moreover, deterioration and PL quenching of organic dyes occur in a short time of irradiation. For displays and lightings, currently commercialized phosphors are mostly rare earth ion-doped and transition metal ion-doped oxides [11]. These phosphors are highly stable; however, it is not easy to control the emission wavelength. In addition, they show a long decay time of PL (ca. 1 millisecond) because of a forbidden character of the

transition. This slow decay causes the saturation of PL intensity when the excitation light intensity is increased.

The techniques to prepare highly luminescent and monodispersed semiconductor NCs have much advanced in this decade. They are organic solution method [12] and aqueous solution method [13]. Bright PL is obtained by capping the NCs with surfactants which deactivate the unpreferably PL-quenching surface defects. Aqueous solution method has several advantages over organic solution method: (1) highly luminescent NCs can be synthesized at lower temperature ( $\sim 100^\circ\text{C}$ ) using a relatively safe and simple system; and that (2) the prepared water-dispersible NCs have higher stability of PL intensity in water and better compatibility with sol-gel fabrication.

We have reported the preparation of highly luminescent CdTe NCs [14] and ZnSe-based NCs [15–17] by the aqueous solution method. The PL wavelengths of these NCs depend on the band gap ( $E_g^*$ ) which can be controlled by the composition and size of the NCs. The PL wavelength and efficiency of the NCs are almost independent of the excitation wavelength. The emission wavelength can be far from the excitation wavelength. Therefore, various PL colors are obtainable from various NCs using a single excitation



wavelength. Compared with organic dyes, semiconductor NCs show much slower PL quenching or photobleaching on irradiation [2, 10]. Furthermore, the II-VI semiconductor NCs have a direct transition band gap and fast PL decay in ca. 10 nanoseconds that is faster than those of rare earth ions and transition metal ions by ca. 5 orders of magnitude. This fast decay of PL leads to high brightness when the excitation light intensity is increased.

Recently, increasing attention has been directed to the semiconductor NCs incorporated in transparent matrices. The incorporation in silica matrices avoids the agglomeration of NCs and improves the long-term stability of PL. Previously, Mulvaney et al. reported the incorporation of NCs in  $\text{SiO}_2$  [18] and  $\text{ZrO}_2\text{-SiO}_2$  [19] matrices by a sol-gel method. They used hydrophobic NCs (CdSe, CdSe/ZnS, and CdSe/CdS) prepared by organic solution method. However, water-dispersible NCs are more compatible with sol-gel method than such hydrophobic NCs. We have developed techniques to incorporate water-dispersible CdTe and ZnSe NCs in three forms of silica matrices (bulk [16, 20, 21], small particles [22, 23], and thin films [24]) and in bulk-form  $\text{Si}_{1-x}\text{Zr}_x\text{O}_2$  matrix [25], by using a sol-gel method. The prepared NC-incorporating phosphors showed bright PL of three primary colors. Among the three forms, small particles are expected to be used as fluorescent markers for biological labeling. Semiconductor NCs have already been reported to be applicable as fluorescent biomarkers [2–6]. There are several advantages in the incorporation of semiconductor NCs in small silica particles, such as protecting the NCs against oxidation and agglomeration, increasing the mechanical stability, and enabling a transfer into various organic and aqueous solvents. Furthermore, the surface of silica particles can be chemically modified to link bioconjugates.

Previously, several groups reported the preparation and PL efficiencies of silica particles incorporating emitting NCs, by chemical growth of silica shell around an NC (PL efficiency up to 18%) [26]; by sol-gel formation of NC-containing layer around a silica particle without containing NCs (PL efficiency up to 13%) [27]; and by reverse micelle method (PL efficiency up to 20%) [22, 23, 28–30]. The reverse micelle method is simpler than the chemical synthetic growth method and has wide controllability of NC concentration in the silica particles. When the NC concentration in a silica particle is high, both the increased emission brightness and decreased blinking of the silica particle can be expected. We have already reported green- and red-emitting silica particles incorporating CdTe NCs which were fabricated by the reverse micelle method [22, 23]. The PL efficiencies reached 27% and 65%, respectively, for green- and red-emitting silica particles. This PL efficiency (65%) is the highest ever reported efficiency for the silica particles incorporating semiconductor NCs. In order to obtain PL of three primary colors for expanding the application range, blue-emitting silica particles are required. However, bright blue-emitting silica particles have not yet been reported to our knowledge. Zinc selenide NCs attract increasing interest because they can be synthesized in organic or aqueous solution and have tunable PL wavelength in blue region [15, 31–33]. Recently, we synthesized highly luminescent ZnSe-based

NCs in blue region by an aqueous solution method [16, 17]. The emission color of ZnSe NCs was shifted from blue-violet ( $\sim 410$  nm) to pure blue ( $\sim 440\text{--}485$  nm) by doping heavy elements such as Cd or Te, because, generally, the  $E_g^*$  of II-VI semiconductor NCs becomes narrower when the constituent elements become heavier. Here we report the preparation of silica particle phosphor incorporating ZnSe-based NCs thus prepared by a reverse micelle method.

## 2. MATERIALS AND METHODS

### 2.1. Chemicals

All chemicals used were of analytical grade or of the highest purity available. Zinc perchlorate, cadmium perchlorate, and thioglycolic acid (TGA) were purchased from Sigma-Aldrich (Miss, USA).  $\text{Al}_2\text{Se}_3$  lumps acquired from CERAC (Wiss, USA) were used to produce hydrogen selenide ( $\text{H}_2\text{Se}$ ) gas. Ammonia water and NaOH solution were purchased from Wako (Osaka, Japan). Deionized water ( $18.3\text{ M}\Omega$ ) was obtained from a Milli-Q water system (Millipore (Mass, USA)).

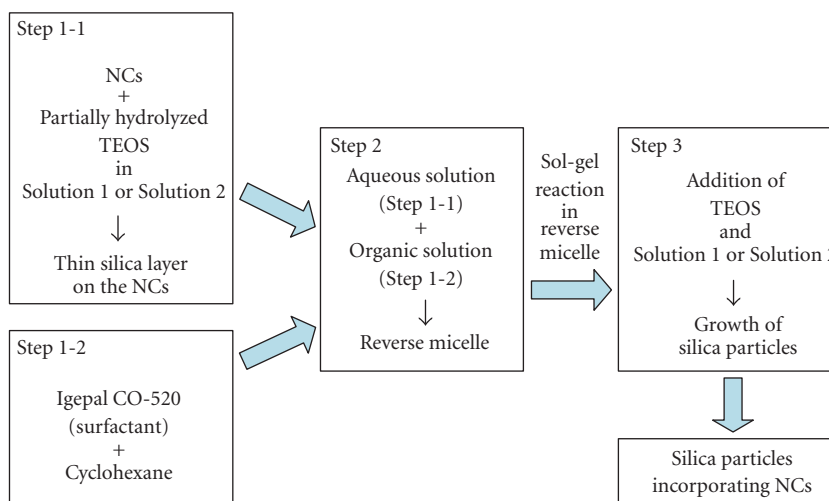
### 2.2. Preparation of ZnSe-based NCs

We have prepared core-shell ZnSe-based NCs by the previously reported aqueous solution method [15–17]. Briefly, the colloidal solutions of ZnSe-based NCs (core) were prepared using zinc perchlorate, cadmium perchlorate, and  $\text{H}_2\text{Se}$  gas. TGA was used as the stabilizing surfactant that caps the NCs. The obtained weakly emitting Cd-doped ZnSe NCs ( $\text{Zn} : \text{Cd} = 95 : 5$  (molar ratio upon synthesis)) was first dispersed in a solution containing cadmium perchlorate and TGA in the dark, and then irradiated with ultraviolet (UV) light (365 nm) in an aqueous solution containing zinc perchlorate and TGA [17]. The ZnS shell was formed on the Cd-doped ZnSe core by the irradiation. Formation of this shell is effective for decreasing the number of surface defects and for increasing the robustness of NCs. As a result, strongly blue-emitting Cd-doped ZnSe/ZnS NCs with a diameter of ca. 4–5 nm were prepared. The PL peak wavelength was 448 nm and PL efficiency was 49% in aqueous solution.

### 2.3. Preparation of silica particles incorporating ZnSe-based NCs by reverse micelle method

Silica particles incorporating ZnSe-based NCs were prepared by the procedure depicted in Scheme 1. Instead of using Solution 1 (diluted aqueous ammonia (6.25%)) described in a previous report for preparing silica particles incorporating CdTe NCs [23], we used Solution 2 (Zn perchlorate, TGA, and NaOH solution ( $[\text{Zn}^{2+}] = 0.261\text{ mol/L}$ , molar ratio of  $[\text{Zn}^{2+}] : [\text{TGA}] = 1 : 2.43$ ,  $\text{pH} \sim 11$ )) for nucleation of silica component to the surface of the particles in Step 1-1 and Step 3. As described below, the Solution 2 was quite effective to retain the emission efficiency of the NCs.

*Step 1-1.* Aqueous solution of the NCs was mixed with alkaline solution of partially hydrolyzed tetraethyl orthosilicate (TEOS). Typically, 1 mL Cd-doped ZnSe/ZnS colloidal solution ( $\sim 3 \times 10^{-5}$  mol particles/L), 1 mL water, 50  $\mu\text{L}$  alkaline



Solution 1: aqueous ammonia  
Solution 2: Zn perchlorate, TGA and NaOH in water

SCHEME 1: Preparation procedure of silica particles incorporating ZnSe-based NCs.

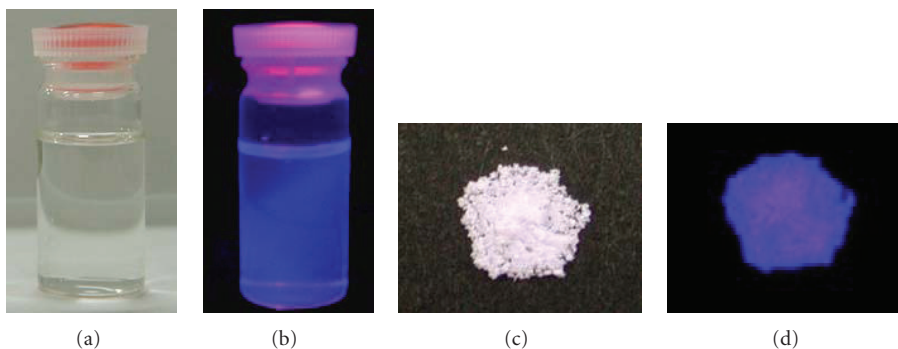


FIGURE 1: Appearance of silica particles incorporating ZnSe-based NCs prepared using Solution 2: (a) cyclohexane solution under visible light, (b) cyclohexane solution under UV light (wavelength: 365 nm), (c) powder under visible light, and (d) powder under UV light (wavelength: 365 nm).

solution (Solution 1 or 2), and 0.15 mL TEOS were mixed in a beaker. The pH of the mixed solution was 9–10. Then the solution was stirred for 2–3 hours to form thin silica layer on the surface of NCs [23].

**Step 1-2.** Nonionic surfactant Igepal CO-520 (polyoxyethylene(5)nonylphenyl ether) was dissolved in hydrophobic cyclohexane. Typically, 2.25 g Igepal CO-520 was dissolved in 12.5 g cyclohexane in a beaker.

**Step 2.** The aqueous solution prepared in Step 1-1 was injected dropwise to the cyclohexane solution prepared in Step 1-2. In this step, reverse micelles containing water droplets dispersing Cd-doped ZnSe/ZnS NCs were formed.

**Step 3.** To grow outermost silica shell further, TEOS (typically 0.3 mL) and alkaline aqueous solution (typically 100  $\mu$ L) were added to the solution prepared in Step 2. Then the solution was stirred for 4 hours.

As a result, silica particles incorporating Cd-doped ZnSe/ZnS NCs were obtained. These silica particles showed

blue PL when irradiated with UV light. Transparent cyclohexane solution of silica particles incorporating NCs was obtained as supernatant by centrifuge of the solution at 4000 rpm.

For comparison, nonluminescent silica particles without containing NCs were prepared using Solution 1 in the similar manner. In Step 1-1, 1 mL diluted NaOH solution (pH~11) was used instead of 1 mL Cd-doped ZnSe/ZnS colloidal solution.

Size distribution of the obtained silica particles was measured by using a dynamic light scattering particle size analyzer (Nikkiso Microtrac Nanotrac 150). Transmission electron microscopy (TEM) of the silica particles was performed at an acceleration voltage of 300 kV by using a Hitachi H-9000. For preparing a TEM specimen, the silica particles were extracted from the supernatant by precipitation with acetonitrile followed by drying in air at  $\sim 40^\circ\text{C}$ . The PL and absorption spectra of the silica particles were measured in

cyclohexane by using conventional fluorescence spectrometer (Hitachi F-4500) and absorption spectrometer (Hitachi U-4000). The PL efficiencies of the solution samples (silica particles in cyclohexane and NCs in water) were estimated by comparison with standard solutions of quinine in aqueous 0.05 M  $\text{H}_2\text{SO}_4$  solution (PL efficiency = 54.6% [34]).

### 3. RESULTS AND DISCUSSION

#### 3.1. Appearance of silica particles incorporating ZnSe-based NCs

After centrifuge in the final step of preparation, the supernatant contained small silica particles and precipitate contained larger silica particles. Both supernatant and precipitate showed bright blue PL. The small silica particles were homogeneously dispersed in the supernatant (cyclohexane solution) at room temperature. The supernatant obtained by using Solution 2 showed brighter PL than that obtained by using Solution 1. Figures 1(a) and 1(b) show the appearance of the silica particles incorporating ZnSe-based NCs prepared using Solution 2 under visible light and under UV light, respectively. The cyclohexane solution was almost colorless and transparent under visible light (see Figure 1(a)) and emitted bright blue PL under UV light irradiation (see Figure 1(b)). On the other hand, the powder of small silica particles extracted from the above supernatant by using acetonitrile was white under visible light (see Figure 1(c)) and emitted blue PL under UV light (see Figure 1(d)).

#### 3.2. Sizes of silica particles incorporating ZnSe-based NCs

Figure 2 shows the size (diameter) distribution of the small silica particles incorporating ZnSe-based NCs in the supernatant, measured by the dynamic light scattering method. The silica particles prepared using Solution 1 and those prepared using Solution 2 gave similar distribution curve of particle size, however, the latter particle size was a little smaller than the former one. Namely, the mean sizes of the silica particles prepared using Solution 1 and that using Solution 2 were ca. 35 and 31 nm, respectively. These two kinds of silica particles had a spherical shape. Nonluminescent silica particles without containing NCs had similar size. A typical TEM photograph of the small silica particles incorporating ZnSe-based NCs in the supernatant is shown in Figure 3. The shape of these small silica particles is spherical and the particle diameters are 20–40 nm, which are in good agreement with those measured by the dynamic light scattering method (see Figure 2). On the other hand, the precipitate after centrifuge in the final step of preparation contained larger silica particles with diameters from a few hundreds nm to 1–2  $\mu\text{m}$ . Such large silica particles also had a spherical shape. The results show that luminescent silica particles with various diameters were formed in the preparation process, and the size selection of silica particles was possible by centrifuge. It was also possible to select the size of silica particles by using syringe filters.

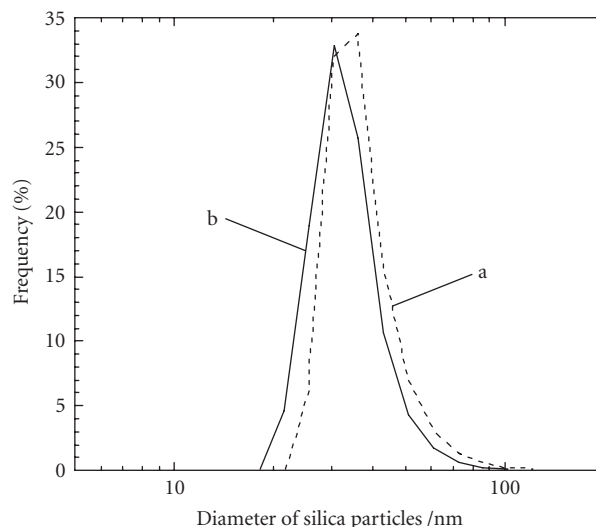


FIGURE 2: Size distribution of silica particles incorporating ZnSe-based NCs measured by dynamic light scattering method: (a) silica particles prepared using Solution 1 and (b) silica particles prepared using Solution 2.

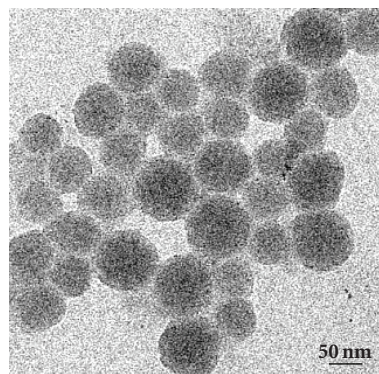


FIGURE 3: TEM photograph of silica particles incorporating ZnSe-based NCs prepared using Solution 1.

#### 3.3. PL spectra, absorption spectra, and PL efficiencies of silica particles incorporating ZnSe-based NCs

Figures 4 and 5 depict the PL spectra and absorption spectra of the small silica particles incorporating ZnSe-based NCs in the supernatant, respectively. The NC-incorporating silica particles prepared using Solution 2 showed an excitonic absorption of the NCs [16, 17] around 420–440 nm. This absorption band was less clearly observed in the NC-incorporating silica particles using Solution 1 and was not seen in the silica particles without incorporating NCs. This suggests that the deterioration of the NCs during incorporation in the silica particles was suppressed by using Solution 2. The PL peak of the NC-incorporating silica particles appeared in the absorption edge region. When the absorbance of the supernatant at the excitation wavelength (350 nm) was adjusted to the same value, the PL intensity of the silica particles prepared using Solution 2 was 2.3 times larger than that of the silica particles prepared using Solution 1 (see Figure 4).

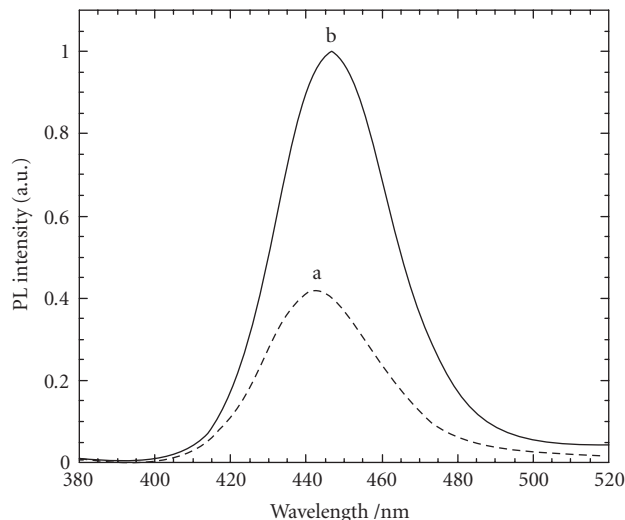


FIGURE 4: PL spectra of silica particles incorporating ZnSe-based NCs in solution: (a) silica particles prepared using Solution 1, (b) silica particles prepared using Solution 2. Excitation wavelength = 350 nm.

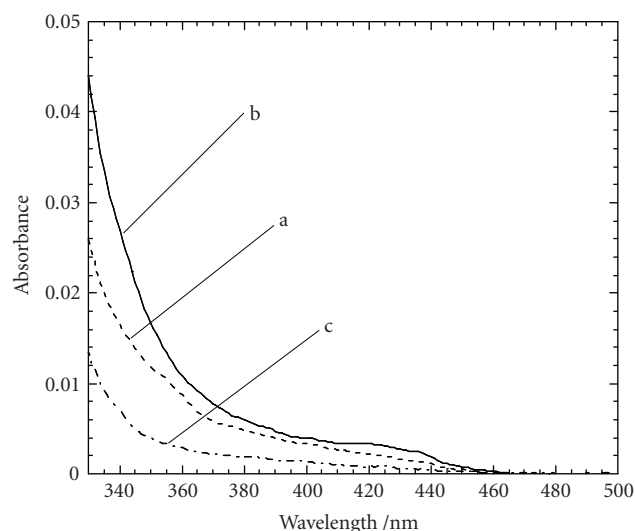


FIGURE 5: Absorption spectra of silica particles with and without ZnSe-based NCs in solution: (a) NC-incorporating silica particles prepared using Solution 1, (b) NC-incorporating silica particles prepared using Solution 2, and (c) silica particles without incorporating the NCs prepared using Solution 1.

As shown in Figure 4, these two PL spectra and that of the initial colloidal solution of NCs had almost the same shape. The widths of the PL spectra were also very close (Table 1). Compared with the initial colloidal solution of NCs, the silica particles showed small blue shift (1–5 nm) of the PL peak wavelength (Table 1). However, the blue shift in the silica particles prepared using Solution 2 was significantly smaller than that in the silica particles prepared using Solution 1. From the PL and absorption spectra, the PL efficiencies of the blue-emitting small silica particles using Solutions 1 and 2 were estimated to be 7 and 16%, respectively (Table 1). As

TABLE 1: PL peak wavelength ( $\lambda_{PL}$ ), spectral width (FWHM), and PL efficiency ( $\eta$ ) of silica particles incorporating the NCs together with the initial colloidal NCs.

No.	(i)	(ii)	(iii)
Sample	Silica particles	Silica particles	Initial NCs
Solution for Steps 1-1 and 3	Solution 1	Solution 2	—
$\lambda_{PL}/\text{nm}$	442.8	446.8	448.0
FWHM <sup>a</sup> /nm	35.2	35.6	35.0
$\eta$ (%)	7	16	49

<sup>a</sup>Full width at half maximum.

exemplified by the preparation of silica phosphor dispersing CdTe NCs [20], the  $\text{Zn}^{2+}$  ions and TGA in Solution 2 prevent the surface of NCs from the deterioration during incorporation into silica particles. This leads to the almost unchanged PL wavelength and high PL efficiency. By contrast, when using the conventional aqueous ammonia (Solution 1), the observed larger blue shift of PL wavelength and lower PL efficiency were derived by deterioration of the NCs such as partial dissolution of the surface part into the surrounding media during incorporation into silica particles.

#### 4. CONCLUSION

We have prepared bright blue-emitting silica particles incorporating core-shell Cd-doped ZnSe/ZnS NCs by a reverse micelle method. When using an alkaline solution containing zinc perchlorate and TGA during silica formation on the surface of NCs, the PL efficiency of the silica particles after preparation reached 16%, which was 2.3 times larger than the PL efficiency of the silica particles prepared by using conventional aqueous ammonia. This is because the TGA-capped ZnS shell of the NCs is retained by the presence of zinc ions and TGA molecules during incorporation in silica particles. As we have already reported the preparation of green- and red-emitting silica particles, three primary emission colors are now obtainable from silica particles incorporating semiconductor NCs. These emitting silica particles are expected to be applicable as fluorescent biomarkers.

#### ACKNOWLEDGMENT

This study was supported in part by the Core Research for Evolutional Science and Technology (CREST) (research area: novel measuring and analytical technology contributions to the elucidation and application of life phenomena), sponsored by the Japan Science and Technology Agency (JST), Japan.

#### REFERENCES

- [1] A. P. Alivisatos, "Perspectives on the physical chemistry of semiconductor nanocrystals," *Journal of Physical Chemistry*, vol. 100, no. 31, pp. 13226–13239, 1996.
- [2] M. Bruchez Jr., M. Moronne, P. Gin, S. Weiss, and A. P. Alivisatos, "Semiconductor nanocrystals as fluorescent biological labels," *Science*, vol. 281, no. 5385, pp. 2013–2016, 1998.



- [3] M. Han, X. Gao, J. Z. Su, and S. Nie, "Quantum-dot-tagged microbeads for multiplexed optical coding of biomolecules," *Nature Biotechnology*, vol. 19, no. 7, pp. 631–635, 2001.
- [4] W. C. W. Chan, D. J. Maxwell, X. Gao, R. E. Bailey, M. Han, and S. Nie, "Luminescent quantum dots for multiplexed biological detection and imaging," *Current Opinion in Biotechnology*, vol. 13, no. 1, pp. 40–46, 2002.
- [5] W. J. Parak, D. Gerion, T. Pellegrino, et al., "Biological applications of colloidal nanocrystals," *Nanotechnology*, vol. 14, no. 7, pp. R15–R27, 2003.
- [6] X. Michalet, F. F. Pinaud, L. A. Bentolila, et al., "Quantum dots for live cells, in vivo imaging, and diagnostics," *Science*, vol. 307, no. 5709, pp. 538–544, 2005.
- [7] N. P. Gaponik, D. V. Talapin, A. L. Rogach, and A. Eychmüller, "Electrochemical synthesis of CdTe nanocrystal/polypyrrole composites for optoelectronic applications," *Journal of Materials Chemistry*, vol. 10, no. 9, pp. 2163–2166, 2000.
- [8] S. Coe, W.-K. Woo, M. Bawendi, and V. Bulović, "Electroluminescence from single monolayers of nanocrystals in molecular organic devices," *Nature*, vol. 420, no. 6917, pp. 800–803, 2002.
- [9] Y. Mori, Y. Arao, K. Tsuchiya, and K. Shimamura, "Photoluminescence properties of ZnS nanoparticles prepared in clay suspension," in *Proceedings of the 58th Divisional Meeting on Colloid and Interface Chemistry*, p. 300, Utsunomiya, Japan, September 2005.
- [10] D. Toomre and D. J. Manstein, "Lighting up the cell surface with evanescent wave microscopy," *Trends in Cell Biology*, vol. 11, no. 7, pp. 298–303, 2001.
- [11] Phosphor Research Society, Ed., *Handbook of Phosphors*, Ohmsha, Tokyo, Japan, 1987.
- [12] B. O. Dabbousi, J. Rodriguez-Viejo, F. V. Mikulec, et al., "(CdSe)ZnS core-shell quantum dots: synthesis and characterization of a size series of highly luminescent nanocrystallites," *Journal of Physical Chemistry B*, vol. 101, no. 46, pp. 9463–9475, 1997.
- [13] A. L. Rogach, L. Katsikas, A. Kornowski, D. S. Su, A. Eychmüller, and H. Weller, "Synthesis and characterization of thiol-stabilized CdTe nanocrystals," *Berichte der Bunsen-Gesellschaft-Physical Chemistry*, vol. 100, pp. 1772–1778, 1996.
- [14] C. Li and N. Murase, "Surfactant-dependent photoluminescence of CdTe nanocrystals in aqueous solution," *Chemistry Letters*, vol. 34, no. 1, pp. 92–93, 2005.
- [15] N. Murase and M. Gao, "Preparation and photoluminescence of water-dispersible ZnSe nanocrystals," *Materials Letters*, vol. 58, no. 30, pp. 3898–3902, 2004.
- [16] C. Li, K. Nishikawa, M. Ando, H. Enomoto, and N. Murase, "Highly luminescent water-soluble ZnSe nanocrystals and their incorporation in a glass matrix," *Colloids and Surfaces A*, vol. 294, no. 1–3, pp. 33–39, 2007.
- [17] C. Li, K. Nishikawa, M. Ando, H. Enomoto, and N. Murase, "Blue-emitting type-II semiconductor nanocrystals with high efficiency prepared by aqueous method," *Chemistry Letters*, vol. 36, no. 3, pp. 438–439, 2007.
- [18] S. T. Selvan, C. Bullen, M. Ashokkumar, and P. Mulvaney, "Synthesis of tunable, highly luminescent QD-glasses through sol-gel processing," *Advanced Materials*, vol. 13, no. 12–13, pp. 985–988, 2001.
- [19] C. Bullen, P. Mulvaney, C. Sada, M. Ferrari, A. Chiasera, and A. Martucci, "Incorporation of a highly luminescent semiconductor quantum dot in  $\text{ZrO}_2 - \text{SiO}_2$  hybrid sol-gel glass film," *Journal of Materials Chemistry*, vol. 14, no. 7, pp. 1112–1116, 2004.
- [20] C. Li and N. Murase, "Synthesis of highly luminescent glasses incorporating CdTe nanocrystals through sol-gel processing," *Langmuir*, vol. 20, no. 1, pp. 1–4, 2004.
- [21] C. Li, M. Ando, and N. Murase, "Preparation and characterization of glass embedding photoluminescent CdTe nanocrystals," *Journal of Non-Crystalline Solids*, vol. 342, no. 1–3, pp. 32–38, 2004.
- [22] S. T. Selvan, C. Li, M. Ando, and N. Murase, "Formation of luminescent CdTe-silica nanoparticles through an inverse microemulsion technique," *Chemistry Letters*, vol. 33, no. 4, pp. 434–435, 2004.
- [23] P. Yang, M. Ando, and N. Murase, "Encapsulation of emitting CdTe QDs within silica beads to retain initial photoluminescence efficiency," *Journal of Colloid and Interface Science*, vol. 316, no. 2, pp. 420–427, 2007.
- [24] P. Yang, C. Li, and N. Murase, "Highly photoluminescent multilayer QD-glass films prepared by LbL self-assembly," *Langmuir*, vol. 21, no. 19, pp. 8913–8917, 2005.
- [25] P. Yang and N. Murase, "Intensely emitting CdTe nanocrystals retained initial photoluminescence efficiency in sol-gel derived  $\text{Si}_{1-x}\text{Zr}_x\text{O}_2$  glass," *Applied Physics A*, vol. 89, no. 1, pp. 189–193, 2007.
- [26] D. Gerion, F. Pinaud, S. C. Williams, et al., "Synthesis and properties of biocompatible water-soluble silica-coated CdSe/ZnS semiconductor quantum dots," *Journal of Physical Chemistry B*, vol. 105, no. 37, pp. 8861–8871, 2001.
- [27] Y. Chan, J. P. Zimmer, M. Strohm, J. S. Steckel, R. K. Jain, and M. G. Bawendi, "Incorporation of luminescent nanocrystals into monodisperse core-shell silica microspheres," *Advanced Materials*, vol. 16, no. 23–24, pp. 2092–2097, 2004.
- [28] S. T. Selvan, T. T. Tan, and J. Y. Ying, "Robust, non-cytotoxic, silica-coated CdSe quantum dots with efficient photoluminescence," *Advanced Materials*, vol. 17, no. 13, pp. 1620–1625, 2005.
- [29] Y. Yang and M. Gao, "Preparation of fluorescent  $\text{SiO}_2$  particles with single CdTe nanocrystal cores by the reverse microemulsion method," *Advanced Materials*, vol. 17, no. 19, pp. 2354–2357, 2005.
- [30] M. Darbandi, R. Thomann, and T. Nann, "Single quantum dots in silica spheres by microemulsion synthesis," *Chemistry of Materials*, vol. 17, no. 23, pp. 5720–5725, 2005.
- [31] X. Zhong, M. Han, Z. Dong, T. J. White, and W. Knoll, "Composition-tunable  $\text{Zn}_x\text{Cd}_{1-x}\text{Se}$  nanocrystals with high luminescence and stability," *Journal of the American Chemical Society*, vol. 125, no. 28, pp. 8589–8594, 2003.
- [32] R. Li, J. Lee, D. Kang, Z. Luo, M. Aindow, and F. Papadimitrakopoulos, "Band-edge photoluminescence recovery from zinc-blende CdSe nanocrystals synthesized at room temperature," *Advanced Functional Materials*, vol. 16, no. 3, pp. 345–350, 2006.
- [33] Q. Zhao and W. Xu, "One-step preparation of ZnSe nanorod aggregates," *Chemistry Letters*, vol. 35, no. 10, pp. 1186–1187, 2006.
- [34] D. F. Eaton, "Reference materials for fluorescence measurement," *Pure and Applied Chemistry*, vol. 60, no. 7, pp. 1107–1114, 1988.